FACULTY OF ENGINEERING
AND ARCHITECTURE

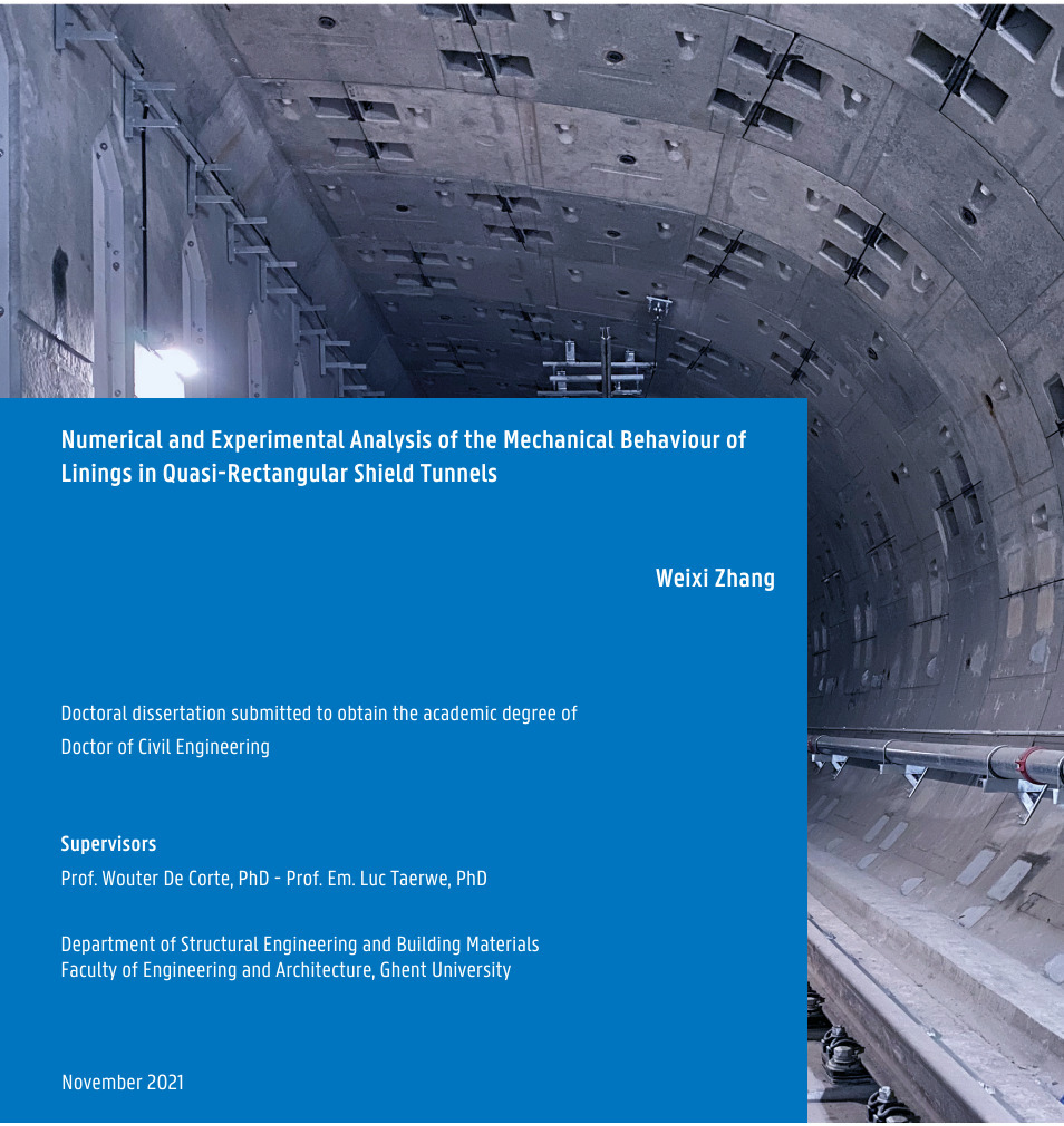

Numerical and Experimental Analysis of the Mechanical Behaviour of Linings in Quasi-Rectangular Shield Tunnels

Weixi Zhang

Doctoral dissertation submitted to obtain the academic degree of
Doctor of Civil Engineering

Supervisors
Prof. Wouter De Corte, PhD - Prof. Em. Luc Taerwe, PhD

Department of Structural Engineering and Building Materials
Faculty of Engineering and Architecture, Ghent University

November 2021

GHENT
UNIVERSITY

FACULTY OF ENGINEERING
AND ARCHITECTURE

Numerical and Experimental Analysis of the Mechanical Behaviour of Linings in Quasi-Rectangular Shield Tunnels

Weixi Zhang

Doctoral dissertation submitted to obtain the academic degree of
Doctor of Civil Engineering

Supervisors
Prof. Wouter De Corte, PhD - Prof. Em. Luc Taerwe, PhD

Department of Structural Engineering and Building Materials
Faculty of Engineering and Architecture, Ghent University

November 2021

GHENT
UNIVERSITY

ISBN 978-94-6355-547-0
NUR 956
Wettelijk depot: D/2021/10.500/95

Members of the Examination Board

Chair

Prof. Filip De Turck, PhD, Ghent University

Other members entitled to vote

Honorary Prof. Adam Bezuijen, PhD, Ghent University
Prof. Geert De Schutter, PhD, Ghent University
Prof. Xian Liu, PhD, Tongji University, China
Prof. Yong Yuan, PhD, Tongji University, China

Supervisors

Prof. Wouter De Corte, PhD, Ghent University
Prof. Em. Luc Taerwe, PhD, Ghent University

Acknowledgement

This dissertation gives a conclusion to my four-year PhD study at Ghent University, which is a unique and unforgettable journey in my life. The peaceful working and natural environment in Ghent gave me the opportunity to sit down and think deeply, ignoring every noise. It led me to roam further academically and, to some extent, changed my “ways of seeing”. I would like to express my appreciation to some people, as my dissertation would not have been completed without their support.

First of all, I would like to show my deepest gratitude to my two supervisors Prof. Luc Taerwe and Prof. Wouter De Corte, who gave me a lot of support, understanding and guidance throughout my PhD research. I can always feel their passion and patience for research and their wisdom and humour for life. All these inspired me to move forward, and made me optimistic and full of energy when I was away from my hometown for four years. It is really my great honour to have worked in their group. I also want to express my appreciation to Prof. Xian Liu at Tongji University, who coordinated the experimental part of my dissertation and encouraged me a lot before and during my PhD study. These valuable insights also enlightened me on many aspects and deserve my most sincere thank you.

During my doctoral study, I have performed extensive experimental investigations. The conducted full-scale experiments form a large part of my dissertation, which would not have been executed without the full help and strong support from the colleagues and technical staff at Tongji University. I want to thank the Ningbo Rail Transit Group and Shanghai Tunnel Engineering Company for providing the technical data and support for my experiments and research related to this innovative tunnel project. I am proud of having been working on that!

I also would like to address my thanks to the staff of the Magnel-Vandepitte Laboratory. I appreciate the mutual help and the valuable friendships between us. Moreover, special thanks to my officemates for their kind supports and suggestions. I can count all the activities we joined together one by one, like the bowling ball, the movie night, the cocktail drinking and the international party. They have made my stay in the lab so unique.

Sincere thanks to my other friends in Ghent, but there are too many to list all. They gave me sound advice related to the life aspect and made my life after work colourful. When I scroll the chatting groups or camera rolls, all the happy memories come back, and, I promise, they will never fade.

A heartfelt gratitude to my parents for the most unselfish supports during these years. I apologise for my absence when studying abroad, but I more strongly felt their unconditional love is everywhere, especially during the Covid-19 pandemic. Particular thanks to my girlfriend, Yiran, for her elegant appearance in my life. I truly hope we will hold hands for every step in the future.

"It is good to have an end to journey toward; but it is the journey that matters, in the end."

-- Ursula K. Le Guin

Weixi Zhang

August, 2021

张维熙

辛丑，凉月，夜

Table of Contents

Summary

With the rapid progress of urbanisation, an increasing number of infrastructure works have been constructed by engineers around the world since the past two centuries, among which there are many tunnels. Due to the advantages compared to other tunnel types, the shield tunnelling method is widely adopted for tunnel construction in cities. These shield tunnels are typically designed in circular shape due to the good mechanical behaviour of the round section. However, with the increasingly high-density utilisation of urban space, more and more city infrastructures are required to be constructed underground. Special-section shield tunnels can be designed to have a configuration that better matches the tunnel purposes, leading to a more effective utilisation of the urban underground space and reducing the number of tunnel excavations or the cost of building refurbishment (repair of local damage due to excessive settlement, foundation strengthening, demolishment and reconstruction etc.). Different special-section shield tunnels have been developed since the 1990s. In 2016, the concept of a quasi-rectangular shield tunnel (QRST) was introduced to further reduce the construction costs and to better solve the problem of subway construction when crossing a dense urban area. QRSTs have various advantages when compared with other special-section shield tunnels or traditional circular tunnels, and they are expected to be used for a wide range of applications. However, there is no specific design standard related to this kind of tunnel. The calculation method for a special-section shield tunnel commonly refers to circular tunnels, and its applicability for the QRST design lacks verification. Therefore, for the new shield tunnel type, the current thesis aims to perform a comprehensive study of the mechanical behaviour of a QRST lining, covering the new joint pattern used in the tunnel, the calculation model, the surrounding pressure distributions and a parametric analysis.

The joints transform the lining into a non-continuous structure, and many accidents initiate from joint's damages. Therefore, the joint is regarded as being the most critical part of a shield tunnel. Due to the section shape of a QRST, its longitudinal joints sustain larger internal forces than in a circular tunnel, and the joint's shear force might have a non-negligible effect on the joint dislocation. A new joint pattern is especially designed to address these problems in QRSTs. Through full-scale tests and FEM simulation approaches, a substantial analysis of the flexural behaviour of the joint is conducted, including the joint's damage process, bearing capacity and the connection of the embedded parts. The proposed joint model provides an efficient approach for exploring the joint's rotational behaviour under different moment-axial force combinations, the lining area influenced by the joint, the segment deflection caused by a joint section, and the potential methods for improving the joint's performance. It is found that a change of the joint section to increase the lever arm between the bolts and the compression zone can improve the joint behaviour the most effectively, resulting in a decrease of the bolt stresses, as well as an increase in the joint's rotational stiffness and bearing capacity. This improvement direction should be preferably considered when redesigning a joint section. Additionally, the joint's shear behaviour under service conditions is explored through full-scale tests. The joint's rotational and shear stiffnesses under varying axial forces are collected and expressed by fitting functions, establishing a database to describe the joint's behaviour.

Regarding the calculation method for a shield tunnel design, there are two main practical methods for a circular tunnel, the modified routine model (MRM) and the beam spring model (BSM). The former requires empirical parameters and a lot of engineering experience. The latter is used for the QRST calculation in the current study. A unique loading frame and experimental program are developed, allowing full-scale point loading tests on a QRST lining and comparisons with the results derived from the proposed model. Additionally, the longitudinal joints of QRSTs are subjected to a wide range of bending moments and shear forces. Their stiffnesses are related to the level of sustained internal forces. An iterative method is presented to simulate the stiffness changes caused by the joint's moment-axial and shear-axial interaction behaviours with the established database from the joint study. The iterative method is proven to be able to provide good results for different load levels, while a constant stiffness based analysis does not. A parametric study reveals that not only the joint's rotational stiffness but also the joint's shear stiffness significantly affects the structural response. They are the most sensitive parameters for a QRST lining, especially for the lining's deformation.

On the other hand, three in-situ tests in soft soils with similar overburdens are organised to provide direct results of the actual pressures around linings. The temporal and spatial distributions of the lining pressures during and after the construction phase are obtained, allowing comparisons with the logs of construction activities and the assumed pressure distributions in the QRST design. Comparing the ratios between the peak pressures and the stable values, the ratio at the top areas can reach a value of 2 while these ratios at the bottom and the waist areas are about 1.5 and 1.3. The effect of the grouting process happening at the shield tail attenuates quickly in the tunnel's longitudinal direction and has an influential range of 9 rings for the considered grouting and soil conditions. The varying and temporary loads of the back-up equipment and carriages inside the tunnel influence the pressures outside the linings with a coincident pace of construction activities. The pressures perform as a counterforce to resist the load from the tunnel, and the surrounding soil behaves like an elastic foundation to hold the tunnel. From the long-term perspective, for the related shallow buried case in soft soils, the influence of the grouting process or other construction loads on the lining pressures needs about 50 days to be relieved, and different grouting strategies will not affect the final pressure distributions. The applicability of the proposed load distributions referring to the design model of circular tunnels is proven.

Finally, with the proposed QRST calculation model and pressure assumptions based on field tests, a comprehensive parametric study is performed to give more practical insight into the QRST lining's structural behaviour, including the comparisons between the point loads in indoor experiments and uniformly varying pressures in a more realistic situation, the detection of the applicability of the MRM method for the QRST design and the effects of varying pressure distributions.

Until now, only a minimum number of lining experiments and field monitoring tests have been conducted for special-section shield tunnels. In the presented PhD thesis, the general mechanical behaviour of a QRST lining with a special joint pattern and embedded parts has been studied comprehensively through experiments and numerical simulations. The results show that large internal forces can be sustained and that new insights are gained on the behaviour of the joints under different loading scenarios. These findings can also be applied to other special-section shield tunnels. The proposed BSM-based calculation model and the assumed pressure distributions in the QRST design are shown to be realistic.

The research findings and methods are believed to be a good reference for studies related to other special-section shield tunnels in the future.

Samenvatting

Door de snelle vooruitgang van de verstedelijking hebben ingenieurs in de afgelopen twee eeuwen over de hele wereld een toenemend aantal infrastructuurwerken aangelegd, waaronder vele tunnels. Vanwege de voordelen ten opzichte van andere tunneltypes wordt de schild-tunnelbouwmethode op grote schaal toegepast in steden. De schildtunnels worden meestal ontworpen met een cirkelvormige dwarsdoorsnede, vanwege het optimale mechanisch gedrag. Nu de stedelijke ruimte echter steeds dichter bebouwd wordt, moeten steeds meer stedelijke infrastructuren ondergronds worden aangelegd. Schildtunnels met speciale doorsnede kunnen worden ontworpen met een configuratie die beter past bij de tunneldoelstellingen, zodat de ondergrondse ruimte in de stad efficiënter kan worden benut en het aantal tunneluitgravingen of de impact op bestaande gebouwen kan worden verminderd. Sinds de jaren negentig zijn verschillende speciale tunneldoorsnedes ontwikkeld. In 2016 werd het concept van een quasi-rechthoekige schildtunnel (QRST) geïntroduceerd om de bouwkosten verder te verlagen en het probleem van de metroaanleg bij het doorkruisen van een dicht stedelijk gebied beter op te lossen. QRST's hebben verschillende voordelen in vergelijking met andere speciale-sectie schildtunnels of traditionele cirkelvormige tunnels, en er wordt verwacht dat ze voor een breed scala aan toepassingen zullen worden gebruikt. Er is echter geen specifieke ontwerpnorm voor dit soort tunnels. De berekeningsmethode voor een schildtunnel met speciale doorsnede is gewoonlijk gebaseerd op deze voor cirkelvormige tunnels, maar de toepasselijkheid voor het ontwerp van QRST's is tot dusver niet geverifieerd. Daarom wordt in onderhavig proefschrift voor dit nieuwe type schildtunnel een uitgebreide studie van het mechanisch gedrag van de QRST-lining uitgevoerd, met inbegrip van het nieuwe verbindingspatroon dat in de tunnel gebruikt wordt, het berekeningsmodel, de drukverdeling op het buitenvlak en een parameterstudie.

De voegen tussen de segmenten maken van de lining een niet-continue structuur, en veel ongevallen zijn het gevolg van beschadigingen aan deze voegen. Daarom wordt de voeg beschouwd als het meest kritieke onderdeel van een schildtunnel. Door de vorm van de doorsnede van een QRST, ondergaan de langsvoegen grotere interne krachten dan in een cirkelvormige tunnel, en ook de dwarskrachten in de voeg kunnen een niet te verwaarlozen effect hebben op het gedrag van de voeg. Om deze problemen in QRSTs op te lossen is speciaal een nieuw voegpatroon ontworpen. Door middel van proeven op ware grootte en FEM simulaties wordt

een fundamentele studie van het buigingsgedrag van de verbinding uitgevoerd, met inbegrip van het schadeproces van de verbinding, de sterkte en de verbinding van de ingebedde delen. Het voorgestelde voegmodel biedt een efficiënte manier voor het onderzoeken van het rotatiegedrag van de voeg onder verschillende moment-langskrachtcombinaties, de beïnvloede oppervlakte, de vervorming van de segmenten veroorzaakt door een voeg en de mogelijke methoden voor het verbeteren van de prestaties van de voeg. Er is gebleken dat een wijziging van de voegdoorsnede om de hefboomsarm tussen de bouten en de drukzone te vergroten, het gedrag van de verbinding het meest effectief kan verbeteren, wat resulteert in een afname van de boutspanningen, alsmede een toename van de rotatiestijfheid en de sterkte van de verbinding. Deze manier van verbeteren moet dan ook bij voorkeur in aanmerking worden genomen bij het ontwerpen van een geoptimaliseerde voegdoorsnede. Bovendien wordt het afschuifgedrag van de verbinding in gebruiksgrenstoestand onderzocht aan de hand van proeven op ware grootte. De rotatie- en afschuifstijfheden van de voeg onder variërende langskrachten worden verzameld en uitgedrukt met behulp van best passende functies, waarmee een database wordt aangelegd om het gedrag van de voeg te beschrijven.

Wat de berekeningsmethode voor het ontwerp van een schildtunnel betreft, zijn er twee belangrijke praktische methoden voor een cirkelvormige tunnel, namelijk het aangepaste routinemodel (MRM) en het balk-verenmodel (BSM). De eerste methode vereist empirische parameters en veel ontwerpervaring. De laatste methode wordt in de huidige studie gebruikt voor de QRST-berekening. Er werden een unieke proefopstelling en een uniek proefprogramma ontwikkeld, waardoor een belastingsproef met puntlasten op ware schaal op een QRST lining kan uitgevoerd worden en vergelijkingen met de resultaten afgeleid van het voorgestelde rekenmodel kunnen worden gemaakt. Bovendien worden de langsvoegen van quasi-rechthoekige tunnels onderworpen aan een breed scala van combinaties van buigende momenten en dwarskrachten. Hun stijfheden zijn gerelateerd aan het niveau van de aangrijpende snedekrachten. Er wordt een iteratieve methode voorgesteld om de stijfheidsveranderingen ten gevolge van het moment-langskracht en dwarskracht-langskracht interactiegedrag van de verbinding te simuleren met behulp van de database die opgesteld werd op basis van het onderzoek op de voegen. De iteratieve methode blijkt aanvaardbare resultaten op te leveren voor verschillende belastingsniveaus, terwijl een analyse op basis van een constante stijfheid dat niet doet. Een parameterstudie toont aan dat niet alleen de rotatiestijfheid van de verbinding, maar ook de afschuifstijfheid van de verbinding de structurele respons aanzienlijk beïnvloeden. Dit zijn dan ook de gevoeligste parameters voor een QRST-lining , vooral voor de vervorming ervan.

Bovendien worden drie in-situ proeven in zachte grond met vergelijkbare bovenbelastingen georganiseerd om directe resultaten te verkrijgen van de werkelijk optredende drukken aan de buitenkant van de lining. De tijdsafhankelijke en ruimtelijke verdelingen van de drukken rond de lining tijdens en na de constructie worden verkregen, wat vergelijkingen mogelijk maakt met de logboeken van de bouwactiviteiten en de aangenomen drukverdelingen in het QRST-ontwerp. Uit een vergelijking van de verhoudingen tussen de piekdrukken en de stabiele waarden blijkt dat de verhouding in de bovenste zones van de lining een waarde van 2 kan bereiken, terwijl deze verhoudingen in de onderste en middelste zones ongeveer 1.5 en 1.3 zijn. Het effect van het injectieproces dat zich voordoet aan de achterkant van het schild verzwakt snel in de lengterichting van de tunnel en heeft een invloedsgebied van 9 ringen voor de hierbij van toepassing zijnde injectie- en grondvoorwaarden. De veranderlijke en tijdelijke belastingen van de technische apparatuur en de transportwagens in de tunnel, beïnvloeden de drukken aan de buitenkant van de linings volgens een tempo dat synchroon verloopt met de bouwactiviteiten. De drukken werken als een tegenrecatie om de belastingen afkomstig uit de tunnel te weerstaan, en de omringende grond gedraagt zich als een elastische fundering om de tunnel vast te houden. Op lange termijn en voor het geval van ondiepe tunnels in zachte grond, heeft de invloed van het injectieproces of andere belastingen in de bouwfase op de drukverdeling op de lining ongeveer 50 dagen nodig om te worden afgebouwd, en verschillende injectiestrategieën zullen de uiteindelijke drukverdelingen niet beïnvloeden. De toepasbaarheid van de voorgestelde belastingverdelingen met betrekking tot het ontwerpmodel van cirkelvormige tunnels is aldus bewezen.

Tenslotte wordt met het voorgestelde QRST rekenmodel en de drukaannames gebaseerd op de veldproeven een uitgebreide parameterstudie uitgevoerd om meer praktisch inzicht te bekomen in het structurele gedrag van de QRST lining, inclusief de vergelijkingen tussen de puntbelastingen in de indoor experimenten en de gelijkmatige drukken in een meer realistische situatie, de evaluatie van de toepasbaarheid van de MRM methode voor het QRST ontwerp en de effecten van variërende drukverdelingen.

Tot nu toe is voor schildtunnels met speciale doorsnede slechts een minimaal aantal experimenten op de voegen en in situ proeven uitgevoerd. In dit proefschrift is het algemene mechanisch gedrag van een QRST lining met speciaal voegpatroon en met ingebedde delen, uitvoerig bestudeerd door middel van experimenten en numerieke simulaties. De resultaten tonen aan dat grote interne krachten kunnen weerstaan worden en duidelijke inzichten bekomen worden in het gedrag van de voeg onder verschillende belastingsscenario's die ook kunnen toegepast worden op andere schildtunnels met speciale doorsnede. Het voorgestelde, op de BSM gebaseerde berekeningsmodel en de aangenomen drukverdelingen van het QRST-ontwerp blijken realistisch te zijn.

De onderzoeksresultaten en -methodes uit dit proefschrift worden verondersteld een unieke referentie te zijn voor toekomstige studies met betrekking tot andere schildtunnels met speciale doorsnede.

Nomenclature

These lists give an exhaustive overview of the symbols and abbreviations used throughout the thesis.

Latin Symbols

A_s	Area size of the reinforcement close to the external surface of the segment (Chapter 2)
A'_s	Area size of the reinforcement close to the internal surface of the segment (Chapter 2)
b_0	Width of a segment (Chapter 4)
c_0	Distance from the centre of the reinforcement layer to the closest segment edge (Chapter 4)
E_s	Elastic modulus of steel of the reinforcement close to the external surface of the segment (Chapter 2)
E'_s	Elastic modulus of steel of the reinforcement close to the internal surface of the segment (Chapter 2)
E_{sec}	Elasticity modulus of the segment section (Chapter 2)
F_{jh}	Horizontal load in the joint experiment (Chapter 2)
G_{js}	Dead load of a joint segment (Chapter 2)
h_0	Segment thickness (Chapter 2)
h_e	Eccentricity of the combined effect of the moment and axial force at the joint section (Chapter 2)
h_{est}	Offset distance of the horizontal loads from the central axis of the specimen (Chapter 3)
I_{sec}	Inertia moment of the segment section (Chapter 2)
K_{lat}	Coefficient of lateral pressure (Chapter 4)
K_{lm}	Rotational stiffness of the longitudinal joint (Chapter 2)
K_{ls}	Shear stiffness of the longitudinal joint (Chapter 3)
K_{res}	Coefficient of subgrade reaction (Chapter 4)
M_{C1}	Bending moment of a longitudinal joint without circumferential joints stiffness consideration (Chapter 6)
M_{C2}	Bending moment of a longitudinal joint's segment bodies without circumferential joints stiffness consideration (Chapter 6)
M_{jt}	Bending moment value at the joint section (Chapter 2)
M_{O1}	Bending moment of a longitudinal joint with circumferential joints stiffness consideration (Chapter 6)
M_{O2}	Bending moment of a longitudinal joint's segment bodies with circumferential joints stiffness consideration (Chapter 6)
N_{jt}	Axial force value at the joint section (Chapter 2)

P_{jc}	Reaction force at the vertical supports in joint experiment (Chapter 2)
P_{jv}	Vertical load in joint experiment (Chapter 2)
Q_{js}	Shear force value at the joint section (Chapter 3)
R_{hsoil}.	Coefficient of horizontal subgrade reaction (Chapter 4)
v_{r1}	Variation of the joint opening at the inner side of the segment (Chapter 2)
v_{r2}	Variation of the joint opening at the outer side of the segment (Chapter 2)
u_{js}	Joint dislocation (Chapter 3)
w_J	Joint deflection (Chapter 2)
w_M	Deflection caused by the bending moments along the segment (Chapter 2)
w_R	Deflection caused by the caused by the joint rotation (Chapter 2)

Greek Symbols

ε_s	Strain of the reinforcement close to the external surface (Chapter 4)
ε_s'	Strain of the reinforcement close to the internal surface (Chapter 4)
ξ	Coefficient of bending moment transfer (Chapter 6)
ξ_{AFR}	Coefficient of axial force redistribution (Chapter 6)
ξ_{BMR}	Coefficient of bending moment redistribution (Chapter 6)
η	Stiffness reduction factor (Chapter 6)
θ_{js}	Joint rotation (Chapter 2)
λ_{CAF}	Axial force ratio of a longitudinal joint with circumferential joints stiffness consideration (Chapter 6)
λ_{CBM}	Bending moment ratio of a longitudinal joint with circumferential joints stiffness consideration (Chapter 6)
λ_{OAF}	Axial force ratio of a longitudinal joint without circumferential joints stiffness consideration (Chapter 6)
λ_{OBM}	Bending moment ratio of a longitudinal joint without circumferential joints stiffness consideration (Chapter 6)

Abbreviations

BSM	Beam spring model
CBMR	Coefficient of bending moment redistribution
CBMT	Coefficient of bending moment transfer
CAFR	Coefficient of axial force redistribution
DIJP	Ductile iron joint panel
DPLEX	Developing parallel link excavation
FEM	Finite element modelling
KD	Key designation
MRM	Modified routine model
QRST	Quasi-rectangular shield tunnel
SRF	Stiffness reduction factor

Glossary

Annular gap	Space between the surrounding excavated soil and the outer surface of the segments.
Characteristic value of a material property	The value of a material property having an a priori specified probability of not being attained in the supply produced within the scope of the relevant material standard.
Characteristic value of an action	Principal representative value of an action.
Circumferential joint	Joint between two adjacent segmental rings; also known as ring joint.
Grouting process	Process of filling the annular gap with mortar or blowing pea gravel (or other composites as in case of two-component grouting) in order to produce a frictional connection between the subsoil and the segmental lining.
Design value of an action	Value obtained by multiplying the representative value by the partial safety factor, corresponding to the design situation considered.
Design value of material or product property	Value obtained by dividing the characteristic value of the material or product property considered by a partial safety factor or, in particular circumstances, by direct determination.
Lining	A casing of brick, concrete, shotcrete, iron, steel, or wood placed in a tunnel or shaft to provide final everlasting bearing structure of underground space and/or to finish the interior.
Longitudinal joint	Joint between adjacent segments belonging to the same ring; also known as segmental joint and radial joint.
Ring model	Simplified numerical or analytical model, based on beam theory and using simplified approaches for simulating the surrounding soil, used to calculate the internal ring forces (axial force, bending moment and shear force).
Segment length	Mean segment length measured along the segment mean curved plane.
Segment thickness	Distance between the inner and outer sides of the lining segment.
Segment width	Dimension of the segment ring in its centre axis in the longitudinal direction of the tunnel.
Shield	A movable steel tube, framework, or canopy shaped to fit the excavation line of a tunnel and used to provide immediate support for the tunnel and protect the men excavating and providing the long-term support. May be fitted with a cutting device for excavating the tunnel lining.
Shield tail	An extension to the rear of the shield skin which supports soft soils enabling the tunnel primary lining to be erected within its protection.
Shield tunnel	A tunnel bored by a shield.
Tail void	Annular space between the outside diameter of the shield and the extrados of the segmental lining.
Tunnel boring machine (TBM)	The machine used to excavate tunnels with generally a circular cross section.

Tunnel overburden	Clear soil cover over the crown of the tunnel lining.
Tunnel segment	Curved prefabricated element that composes the tunnel lining rings

Chapter 1

General introduction

1.1 Shield tunnels

With the rapid urbanisation process, an increasing number of underground infrastructure works have been implemented worldwide in the past decades, including underwater tunnels, subway transit systems, and mountain tunnels. The most common options of tunnel construction are: (1) excavated tunnel, (2) cut-and-cover tunnel, (3) bored tunnel, (4) immersed tunnel, and (5) submerged floating tunnel. Excavated tunnelling method is mainly adopted in a hard rock situation rather than in soft soils. Although cut-and-cover tunnelling is widely accepted as an approach for the passage connecting the main tunnel structure and the ground surface, its use in a city centre usually results in traffic blocks and possibly dramatically increases the cost of building refurbishment (repair of local damage due to excessive settlement, foundation strengthening, demolishment and reconstruction etc.). Immersed tunnels and submerged floating tunnels can only be adopted for a river crossing tunnel, and subsidiary constructions might be needed, such as a dry dock or cofferdam. Therefore, the bored tunnelling method is one of the most appropriate options for tunnel construction in the city, especially in soft soil areas.

Shield Tunnel boring machines (TBM) have become one of the preferable methods for constructing underground infrastructures in urban areas, as the induced disturbances at the surface and damages to existing buildings during the construction can be reduced significantly. Figure 1.1 shows the typical layout of a shield TBM. The general principle of the shield is based on a cylindrical steel assembly pushed forward in the direction of tunnel axis while excavating the soil at the same time. The shield secures the excavated void until the preliminary or final tunnel lining is installed. The shield has to withstand the pressure of the surrounding soil and prevent the migration of groundwater (Suwansawat, 2002). The machine advances and gets the thrust force on the cutter head by pushing with jack thrust cylinders against the precast concrete segments that are automatically put in place by an erector. The cutter head is driven by a hydraulic torque machine, and the excavated soil is collected into a muck box and transported by a belt conveyor. The tunnel construction is performed in a differentiated sequence: after completing the advance corresponding to the ring width, the TBM stops excavating and starts assembling the segments. The jacks then push against the newly placed ring, initiating a stroke for the next construction step.

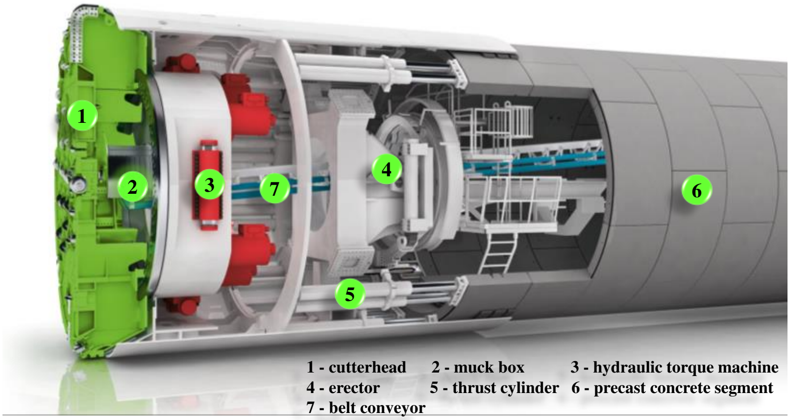

Figure 1.1 General structure of a shield TBM (Brabant and Duhme).

Shield tunnels are typically designed in circular shape due to the good mechanical behaviour of the round section. However, with the increasingly high-density utilisation of urban space, more and more city infrastructure, including railways, roadways, water supply systems, sewerage, electric power lines, and telecommunication networks, must be constructed underground to preserve urban landscapes and protect the environment. Special-section shield tunnels can be designed to have a configuration that better matches the tunnel function and purpose, allowing a more effective utilisation of the underground space and possible reduction of the number of tunnel excavations. Different tunnel types with special cross-sections have been developed since the 1990s, including multiple-circular tunnels and rectangular tunnels. In 2016, the concept of a quasi-rectangular shield tunnel (QRST) was introduced to further reduce the construction costs and solve the problem of subway construction when crossing beneath a dense urban area. Unlike traditional circular tunnels, the QRST with improved cross-sectional shape makes two-way subway transportation in one tube possible, as shown in Figure 1.2.

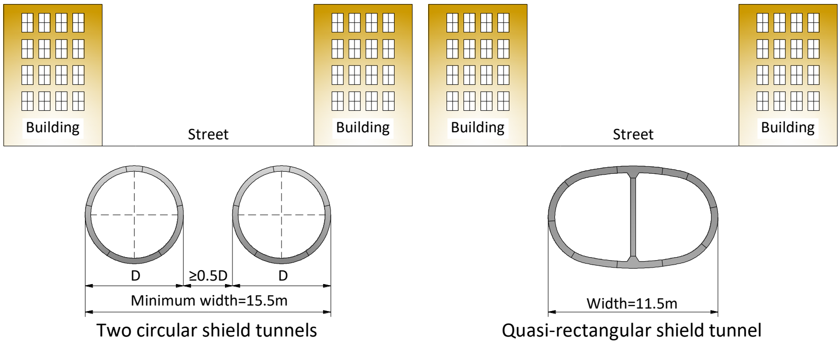

Figure 1.2 Comparison of two circular single-track tunnels and a quasi-rectangular double-track tunnel.

In comparison to a large-diameter circular shield tunnel, the underground space efficiency can be increased by 20%, and the buried depth can be decreased significantly (Zhu et al., 2016; Liu et al., 2018b). Compared to other special-section shield tunnels, the following advantages of a QRST are emphasised: easier control of the surface subsidence when compared to that of a double-O tube (DOT) in relation to improper backfilling grouting and the concave shape of the shield machine (Chow, 2006; Ye et al., 2015), and the low cost of the segment linings due to the use of reinforced concrete compared to the composite steel-concrete segments in the rectangular cross-section tunnels between Rokujizo Station and Ishida Station in Kyoto, Japan, and Hongqiao Linkong 11-3 Connection (Nakamura et al., 2003; Sun et al., 2015). Given the above, QRSTs are expected to be used for a wide range of applications in the future.

1.2 Development of special-section shield tunnels

In 1825, the world's first shield tunnel was built by the hand excavation method and a rectangular shield under the Thames River in London, as shown in Figure 1.3a (Suwansawat, 2002). Since then, the shield tunnelling method has experienced significant developments due to its advantages of small environmental influence in crowded urban areas. At the early stage, open face and hand mining methods were used in shield tunnelling, as shown in Figure 1.3b. New techniques to support the excavating surface, including the slurry method and the soil pressure balanced method, were developed in the 1970s. It was then possible to maintain the stability of the excavation face in extremely soft clay soils (Koyama, 2003). During the same period, new grouting materials, which can harden quickly and maintain plasticity, were used to backfill the void space between the TBM and the lining extrados. In addition, a new tail seal design consisting of wire brushes and special high-viscosity grease between them was developed. All these developments ensured good control of the soil settlements even in complex excavating conditions with the shield tunnelling method and laid a solid foundation for the wide applications of this tunnelling method all over the world (Koyama, 2003).

A circular tunnel shape is usually adopted due to the more favourable stress distribution and construction control when compared to a rectangular one. Therefore, the circular shield tunnels are used preferably and developed rapidly. Until the 1980s, Japan was faced with the urgent needs for infrastructure construction for a dense population in cities, and started focusing on research in the shield boring techniques for special-section tunnels to achieve better utilisation of the urban underground space and a lower cost of building refurbishment. Shield tunnels with different sections were developed and came into use consecutively. Among all these special-section shield tunnel techniques, the DOT tunnel was introduced from Japan to China for subway constructions in Shanghai at the beginning of the 21st century. Up to now, the special-section shield tunnels are only used in Japan and China. Based on the tunnel section shape, the already constructed special-section shield tunnels can be divided into multiple-circular tunnels (including DOT tunnels), rectangular tunnels and circular-based rectangular tunnels.

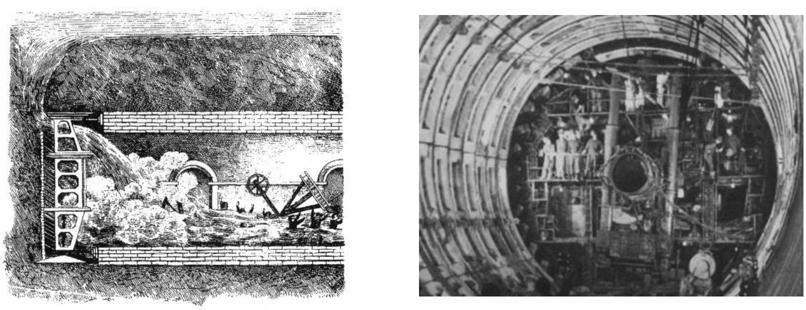

(a) (b)

Figure 1.3 Early-stage shield tunnel construction: (a) the first shield tunnel in the world in 1825 (underneath the Thames River) (Maidl et al., 2013); (b) the first shield tunnel conducted in China in 1965 (Dapu Road tunnel in Shanghai) (Zhu, 2018).

Two circular single-track shield tunnels are needed in a subway line passing through a city centre, and there is a minimum distance requirement between the two tunnels. In order to decrease the tunnels' total width, the idea of a multiple-circular tunnel was first put forward to fulfil a single tunnel accommodating two tracks, as shown in Figure 1.4. In the 1990s, the multiple circular tunnels were successfully applied in Japan and then introduced into China in the 2000s. However, the concave shape of the shield machine caused a complicated construction control of backfilling grouting and TBM turning, resulting in potentially large surface subsidence (Chow, 2006; Ye et al., 2015). There has been no new application of multiple-circular tunnels in Japan since 2005, and their applications in China are limited.

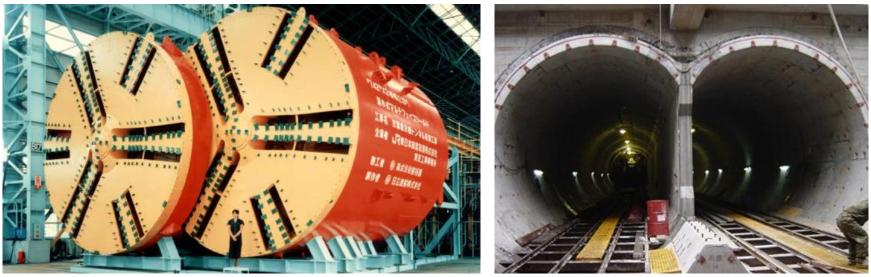

(a) (b)

Figure 1.4 Example of a DOT shield tunnel: (a) a TBM (Ye, 2018); (b) a constructed tunnel (Zhu, 2018).

A rectangular shield tunnel has a simple section and is used for vehicle traffic, pedestrian passage, pipe gallery and cable trench. In practice, the section is designed with a rounded rectangle, which is preferable to a square or oblong shape for reducing the bending moment at the corners. However, unlike using simple spoke-shaped rotating cutter heads in circular or multiple-circular shield tunnels, rectangular tunnels require special techniques to achieve full-section cutting. The introduction (in 1987) and the preliminary test (in 1990) of the developing parallel link excavation (DPLEX) are the key to the successful implementation of the full-section cutting (see Figure 1.5a). The DPLEX technique employs a series of rotating shafts whose cranks are kept parallel. A cutter frame equipped with this shaft and crank system can make a parallel link motion, making it possible to cut a tunnel with a cross-section analogous to the shape formed by the cutter bits (Kashima et al., 1996; Koyama, 2003). The cutting technique also has the advantage of a cutter torque reduction due to many shafts replacing a single spoke in circular tunnels or several spokes in multiple-circular tunnels. In 1994, the first rectangular shield tunnel with DPLEX (size: 4.2 m × 3.8 m) was constructed for a drainage line in Narashino, Japan. In 2003, the first rectangular shield tunnel for double-track rail transport (size: 9.9 m × 6.5 m) was constructed between Ishida Station and Rokujizo Station in Kyoto, Japan, showing a great development potential for rectangular tunnels. This tunnel used composite segments and cast iron segments (Nakamura et al., 2003). In 2013, another large-section rectangular shield tunnel project (size: 10.3 m × 7.1 m) was finished between Shibuya Station and Daikan-Yama Station in Tokyo, Japan. The segments were made from concrete except for the one, used as interior column in the middle of the tunnel section, which is made from steel-concrete composite. However, the concrete segments consisting of tunnel crown were reinforced by textile fabric at the inner surface to avoid cracking. These milestone projects briefly sketch the development of rectangular shield tunnels. Although the use of composite segments or reinforcing materials can ensure a large section for the double-track traffic, the rectangular tunnels have shortcomings in relation to project cost and constructing process when compared with a shield tunnel with only reinforced concrete segments. These drawbacks restrain the wide application of the rectangular shield tunnels and need to be resolved.

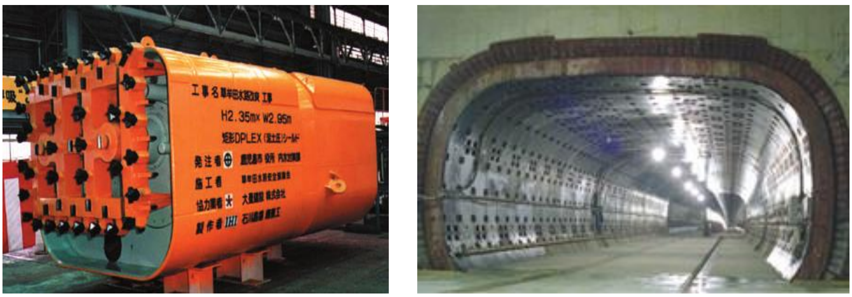

(a) (b)

Figure 1.5 Example of a rectangular shield tunnel: (a) a TBM with a PDLEX cutter head; (b) a constructed rectangular shield tunnel (Zhu, 2018).

In order to keep a good balance between the underground space utilisation and lining's structural performance, the shape of the special-section shield tunnels was further improved in the 2000s. Several arcs were used to shape a tunnel section outline similar to a rectangular one. These arcs were clipped from different circles but connected at their tangent points to keep the stress uniformly changing along the lining circumference. The circular-based section took advantage of the good mechanical performance of a circular shape and made the use of only reinforced concrete (including steel fibre reinforced concrete) segments possible, as shown in Figure 1.6. In 2008, a railway project using a circular-based rectangular shield tunnel with eight reinforced concrete segments (size: 9.7 m × 8.4 m) was constructed between Meiji-Jingumae Harajuku Station and Shibuya Station in Tokyo, Japan. In 2012, a circular-based rectangular connecting tunnel for the subway between Kotake-Mukaihara Station and Senkawa Station in Tokyo, Japan (size: 5.5 m × 6.6 m) was constructed with six reinforced concrete segments.

(a) (b)

Figure 1.6 Example of the shield tunnel with a circular-based section: (a) a TBM; (b) the tunnel's reinforced concrete lining (Zhu, 2018).

Apart from the above rectangular and circular-based rectangular shield tunnels in Japan, there were a few applications in other areas around the world. With the rapid economic development in recent decades, China is faced with a similar problem of city construction as before in Japan. In 2015, China's first rectangular shield tunnel was constructed for a 28 m long passage for Hongqiao Linkong 11-3 Connection in Shanghai, China, adopting six steel-concrete composite segments (size: 9.7 m × 8.4 m), as shown in Figure 1.7a. Based on the project experience, in 2016 and 2017, two circular-based rectangular reinforced concrete shield tunnels were successively applied in Ningbo and Yulin. The former has a quasi-rectangular shape (size: 11.5 m×6.9 m), composed of ten reinforced concrete segments and one reinforced concrete interior column. It was used for the double-track subway transit in crowded city areas and is the subject of the current study. The latter used eight segments to consist of a horseshoe-shaped section (size: 10.6 m×11.5 m), as shown in Figure 1.7b, and served as a railway tunnel (Li et al., 2017).

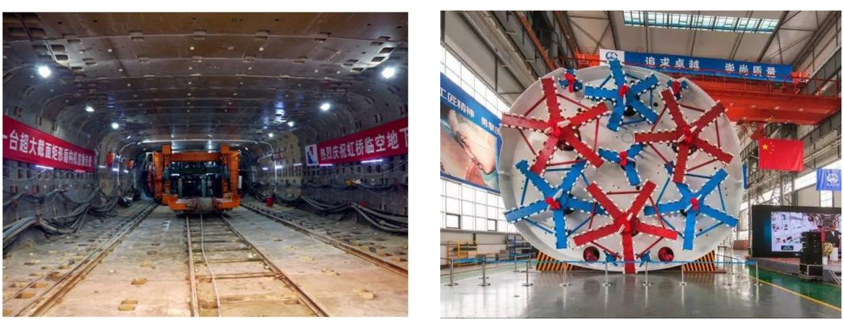

(a) (b)

Figure 1.7 The special-section shield tunnel project in China: (a) Hongqiao Linkong 11-3 Connection in Shanghai; (b) the TBM of the horseshoe-shaped railway tunnel in Yulin.

It can be found that the initial motivation for special-section shield tunnels is to maximize the utilisation of the urban underground space and minimise the excavation area for a minor influence on surrounding buildings. Due to the dense population in Japan, its techniques for special-section shield tunnels are the most developed and advanced. With the development of cutting techniques, the tunnel section shape gradually evolved from multiple-circular shapes to rectangular shapes, and then to circular-based rectangular shapes. Due to the advantages of high space utilisation, small disturbance of tunnel construction and good structural performance (Ye, 2018), the circular-based rectangular section has been regarded as one of the best options for a section outline, and successfully introduced into recent engineering projects. Concerning other areas around the world, as their population density is relatively small or their city spatial structure is relatively loose, the demand for special-section shield tunnels is not as active as in Japan and China. However, due to various advantages of the special-section shield tunnels, they are undoubtedly expected to contribute more to city and transportation development in the future all over the world.

1.3 Introduction of the QRST project

When a shield tunnel crosses a city centre, the choice of the cross-section for the tunnel affects the extent of environmental influences and building refurbishment. In Ningbo, China, a series of subway projects has been planned to meet its rapid urban development. Some planned subway lines travel beneath the old town area, where historical buildings and heavy overpass traffic exist. The complex surroundings and high environmental protection requirements invoke the introduction of QRSTs. This new shield tunnel pattern shows great advantages in making full use of underground space, minimising the cost of building refurbishment and effects on surroundings, and building a double-track tunnel all at once (Zhu et al., 2016). Due to the lack of references, a demonstration project of the QRSTs is applied in the Jiangshan Town, Yinzhou District, Ningbo for the terminal part of Ningbo Metro Line 3. The current research is based on this Ningbo QRST project.

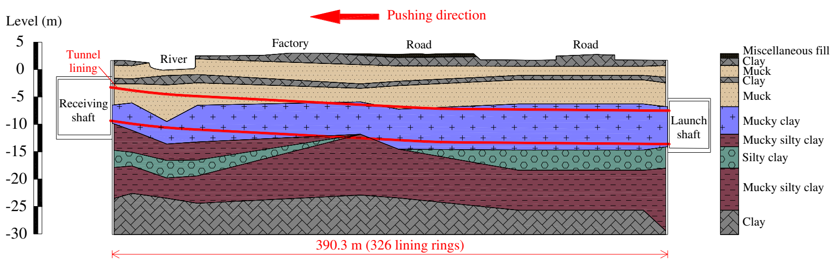

Figure 1.8 Longitudinal profile of the Ningbo QRST project.

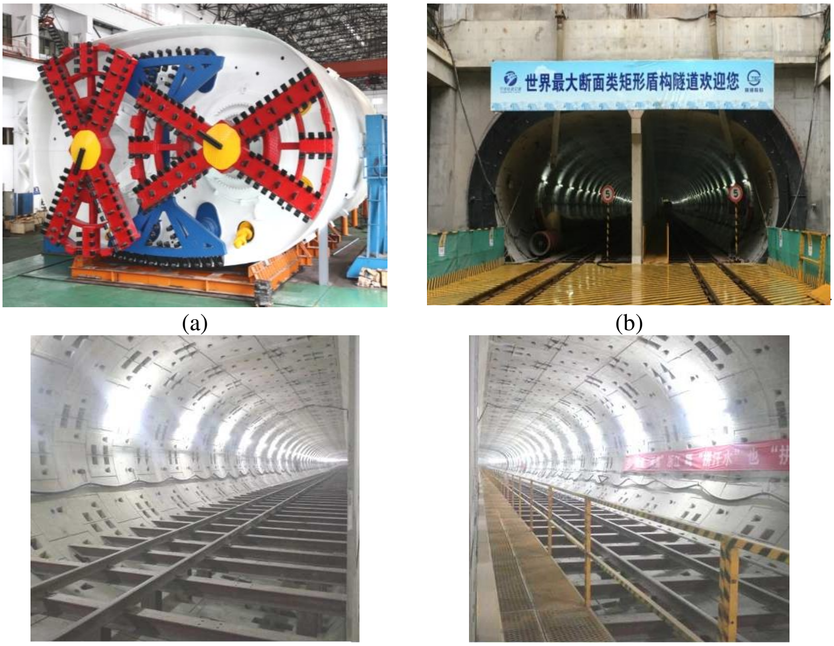

(a) (b) (c) (d)

Figure 1.9 Ningbo QRST project: (a) the TBM; (b) the outside view of the constructed tunnel; (c) the inside view for the left side; (d) the inside view for the right side.

The tunnel length is 390.3 m, including 326 lining rings with an overburden from 2.50 to 10.46 m, as shown in Figure 1.8. The tunnel slope gradient is controlled within 35‰, and the minimum curve radius of the tunnel line is 400 m. The QRST shield tunnel was bored by an 11.83 m × 7.27 m TBM, as shown in Figure 1.9a. The constructed tunnel is shown in Figure 1.9b, c and d. A typical lining structure of the QRST is presented in Figure 1.10. The tunnel construction adopts a staggered assembly, alternating Pattern A and Pattern B linings, and these two lining patterns are symmetrical with respect to the interior column. The structure is composed of ten segments and an interior column (LZ). The segments include two T-shaped blocks (T1 and T2), three C blocks (C1, C2 and C3), three standard blocks (B1, B2 and B3), a contiguous block (L) and a top block (F). The cross-section has a circular-based shape consisting of four arcs, two with an opening angle of 24 degrees with a 15.45 m radius and two with an opening angle of 156 degrees with a 3.20 m radius. The thickness and width of the segments are 450 and 1200 mm, respectively, while these of the interior column are 350 and 700 mm. The concrete grade of the lining structure is C50 (characteristic cube compressive strength of 50 MPa), and the steel quality is HRB400 (characteristic yield stress of 400 MPa) according to the Chinese Code for Design of Concrete Structures [GB50010] (2011). In each longitudinal joint (connecting segments), two pairs of preinstalled cast iron embedded parts serve as connections, and each pair is connected by two 6.8-M33 (diameter of 33 mm) short straight bolts. Thirty-two inclined bolts (6.8-M30 with a diameter of 30 mm) are provided for the circumferential joint (the joint between rings). The tensile stress and yield stress of these two kinds of bolts are 600 MPa and 480 MPa, respectively. The mixture design of the concrete used for segment casting is cement (360 kg/m^3, CEM I 42.5), fly ash (60 kg/m^3, Class 2), sand (620 kg/m^3), gravel (1150 kg/m^3), water (145 kg/m^3) and admixture (0.8%, by weight of binder).

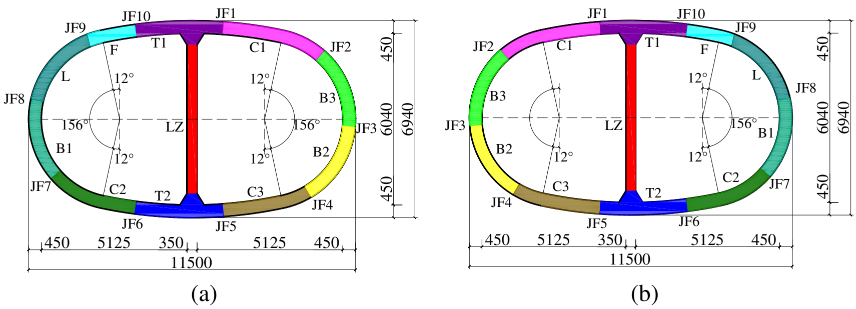

Figure 1.10 Outline of a typical lining structure of the Ningbo QRST: (a) pattern A; (b) pattern B (unit: mm).

1.4 Relevance of calculation model for shield tunnels

1.4.1 General

As the permanent tunnel lining structure, shield tunnel segments account for a large part of the overall budget for a tunnelling project. Shield tunnel lining designs affect not only the quality and durability of tunnel structures but also their economic efficiency (Han et al., 2017). I.T.A. (2000) provides a flowchart of the shield tunnel lining design as shown in Figure 1.11. A tunnel alignment plan and geology of surrounding soils mainly determine the loading conditions. The inner diameter can be derived depending on the function or capacity of the plan-to-built tunnel. With the recommended calculation method for the lining ring from norms and assumed lining conditions, such as the dimension of the lining, the material strength and the reinforcement arrangement, designers are able to compute member forces such as bending moment, axial force and shear force in the lining. The safety of the lining should be checked against the calculated member forces. Parallelly to the calculation of the lining ring, the transient load conditions, such as the segment demoulding, storage, transportation and TBM thrust jack forces, should be checked to ensure the segment safety. If the designed lining is not safe against design loads or not economical, the designer should change the lining conditions and redesign the lining. After the approval from the project administrator, the execution of the construction works can start.

Under a specific load condition and lining condition, the lining's calculation results are used to determine design values of the lining section, which further determine the required concrete compressive strength and type and amount of reinforcement of the precast segments (I.T.A., 2019). Hence, a reasonable calculation model is of great significance for a tunnel design. As so far, different kinds of calculation models for the shield tunnel lining structure have been developed, and they can generally be divided into three categories, analytical solutions, numerical beam models and numerical soil-structure interaction models (Gall et al., 2018). The analytical solution is given through classical mechanical methods. The last two models are numerical approaches, but the main difference between them is whether to regard the tunnel as a three-dimensional problem or not.

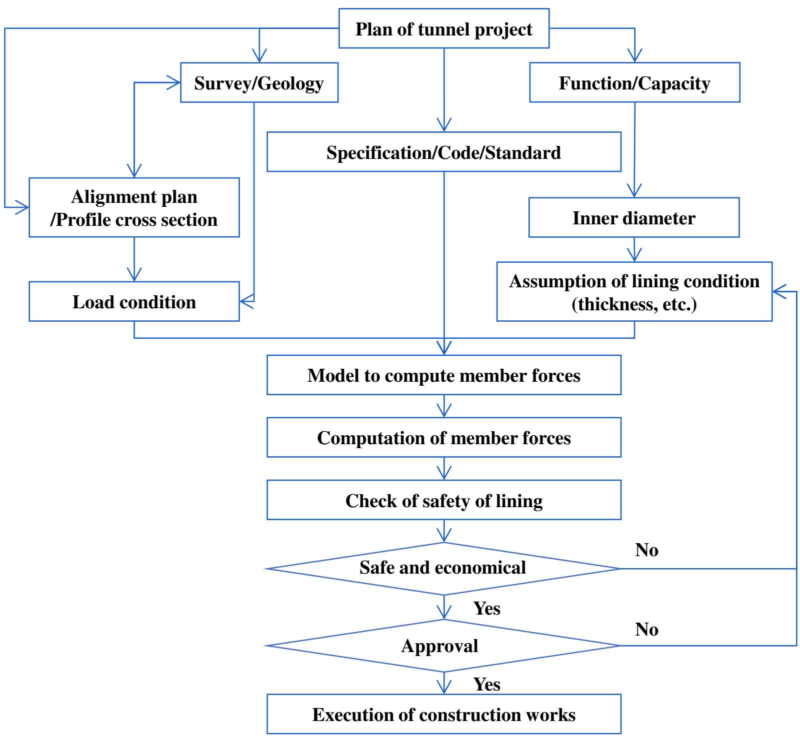

Figure 1.11 Flow chart of shield tunnel design (I.T.A., 2000).

1.4.2 Analytical solution

Although the shield tunnel is apparently a 3D structure, the segmental lining system is usually treated as a plane strain condition, and most calculation models focus on the tunnel transverse section (I.T.A., 2000; Bakker, 2003; Huang et al., 2012). Schmid (1926) proposed the first two-dimensional analytical solution for the lining forces in an elastic continuum. Schulze and Duddeck (1964) published the analysis method for an embedded ring model with limited cover based on the beam theory. These solutions have been continuously improved through considering the elliptical deformation of the tunnel lining, the geometrical nonlinearity of the elastic continuum, the ring rigidity reduction caused by the existence of longitudinal joints and the interaction between soil and structure (Windels, 1967; Wood, 1975; Duddeck and Erdmann, 1985; Duddeck, 1988). However, the lining in these solutions is modelled by a continuous beam without longitudinal joints and circumferential joints, and a linear elastic behaviour of lining and soil are assumed. In recent years, different analytical methods were developed to consider the effect of joints (Blom, 2002; Ding et al., 2004; Groeneweg, 2007; Do et al., 2014c; Zhang et al., 2017). It has to be noted, although there are analytical solutions for the lining structure with longitudinal joints, that numerical approaches are generally introduced to deal with the complex process of these solutions and the problems caused by the changes of joint locations.

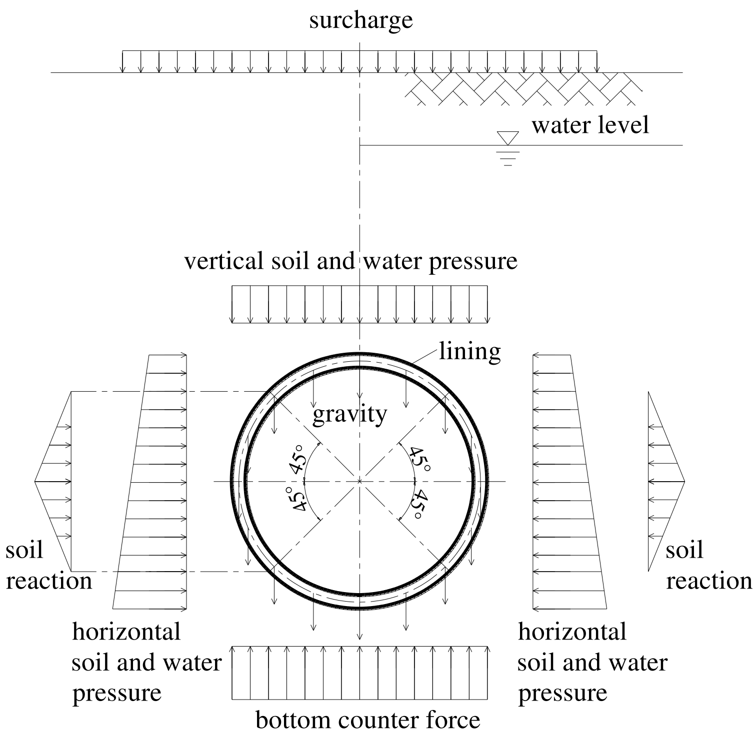

Figure 1.12 Pressure distributions used in elastic equations (I.T.A., 2000; J.S.C.E., 2007).

Considering the above problems, (I.T.A., 2000) and J.S.C.E. (2007) suggest a practical and straightforward method for calculating lining internal forces for a continuum circular tunnel, where the joint existence is ignored. As shown in Figure 1.12, the assumed pressure distribution consists of a uniform vertical pressure from soil and groundwater, linearly varying lateral pressure (by multiplying the vertical pressure by a coefficient), lining dead weight, and a triangular-shaped horizontal soil reaction caused by the lining deformation. The analytical bending moments, axial forces and shear forces from each of the pressures are solved by a series of elastic equations. The total internal forces can be calculated by summing up.

Through the above-introduced analysis methods, although a rigidity reduction for the idealised continuum ring can be introduced to compensate for the deformation difference from a segmented ring (Peck et al., 1972; Wood, 1975), only the internal forces in one ring can be obtained. J.S.C.E. (1977) first proposed the modified routine model (MRM) with an empirical coefficient to redistribute the bending moment for an overall consideration of the effects of the existence of the longitudinal joints in the targeted ring and the unaligned longitudinal joints in the nearby rings. A part of the bending moment at a joint section is regarded to be transferred to its neighbouring segment sections, and the adjusted moment values in joint and segments are used for design. In this way, the two-dimensional solution gives overall internal forces in multiple rings. Due to the quick calculation and long-term accumulated experience from projects, the MRM is a preferred design method in practice (Koyama, 2003; Ye et al., 2014; Zhang et al., 2019b).

1.4.3 Numerical beam model

Given the existence of the longitudinal and circumferential joints, segmental linings are a non-continuous structure. The effects of the joints on internal forces and lining displacements are significant and should be carefully taken into account in design (Lee and Ge, 2001; Lee et al., 2001; Klappers et al., 2006; Teachavorasinskun and Chub-uppakarn, 2010). In the numerical beam method, the cross-section of a segmental lining is modelled by a series of beams, and the lateral soil bedding condition can be simulated by springs with a "compression-only" feature (Gall et al., 2018). The segments are connected by longitudinal joints, which can be modelled by hinges (Tang, 1988) or springs tied at segment ends (Liu and Hou, 1991; Koyama, 2003), as shown in Figure 1.13. The former model treats the joints as free hinges and therefore is named the multiple-hinged ring model, but it cannot reflect the actual structural behaviour and is not commonly used (Zhang et al., 2020). In the latter model, rotational and shear stiffness values can be attributed to the springs to represent the relation between the joint rotational angle and bending moment and the relation between the joint dislocation and shear force. Because the lining and the soil are characterised by a series of beams and springs, this method is commonly referred to as the beam spring model (BSM) method (I.T.A., 2019). The joint's rotational performance is expressed by a stiffness value in the BSM method. Therefore, the determination of this value can significantly influence the calculation results (Lee et al., 2001; Blom, 2002). In early studies, the rotational stiffness of lining joints was considered as a constant parameter (I.T.A., 2000; Lee et al., 2001; Ding et al., 2004). However, many studies and experiments have shown that there are a number of influential factors on the rotational stiffness in longitudinal joints, such as their inability to transfer tensile stress, the different section sizes, the number of bolts and the structural geometries (Ye et al., 2014; Li et al., 2015a; Majdi et al., 2016). The rotational stiffness is also related to the level of the internal forces, including both axial forces and bending moments (Majdi et al., 2016; Jin et al., 2017). A bilinear or multi-linear constitutive relation to describe the joint rotational behaviour can be obtained based on experiments or numerical approaches (Blom, 2004; Zhong et al., 2006; Arnau et al., 2012). Concerning the shear stiffness, as the shear force in circular shield tunnels is small, research related to the joint's shear-resistance behaviour is limited. The joint's shear stiffness was associated with the compressive force at the joint and was affected by the joint structural details, such as the tongue and groove structure (Lan et al., 2009; Zhu et al., 2017). It was suggested to divide the development of shear-caused dislocations into three stages (Guo et al., 2011; Yan et al., 2011). Generally, the current studies focus on the joints' failure characteristics and damage processes under a shear force.

On the other hand, like the analytical solution, the BSM is a two-dimensional model with a plane strain condition in the transverse section for the lining and the soil, which cannot represent circumferential joints or staggered arrangements of segments between rings. However, with the idea of springs standing for circumferential joints, a BSM with multiple ring structures is used to consider the coupling effects between rings, as shown in Figure 1.13b (I.T.A., 2019). In this way, the circumferential joints can be modelled by shear springs in the radial and tangential directions (Koyama, 2003). Under the pressure distributions in Figure 1.12 or more complex pressure distributions, lining internal forces can be quickly calculated using the numerical approach. The BSM method is commonly applied in tunnel lining design as recommended by many current tunnel lining design standards (I.T.A., 2000; A.F.T.E.S., 2005; A.A.S.H.T.O., 2010; Ö.V.B.B., 2011a; D.A.U.B., 2013; B.S.I., 2016; J.S.C.E., 2016) and studies (Koyama, 2003; Do et al., 2014c; Ngan Vu et al., 2017; Chen et al., 2020).

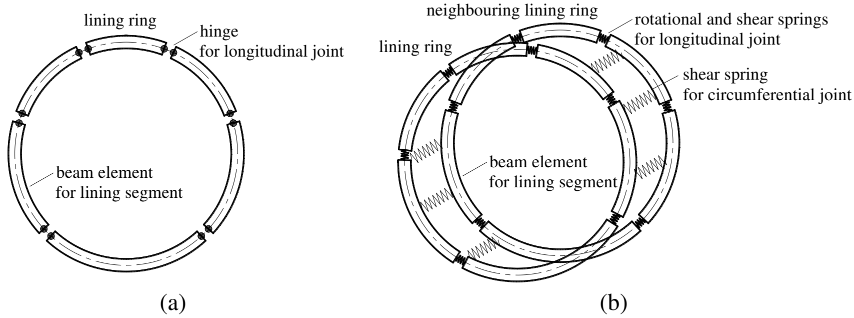

Figure 1.13 Numerical beam model: (a) multiple-hinged ring model; (b) BSM.

1.4.4 Numerical soil-structure interaction model

I.T.A. (2019) states that a two-dimensional calculation approach is generally sufficient for a continuous linear structure that does not contain sudden changes in cross-sectional geometry or high concentrations of loadings, such as crosscuts that intersect the main tunnel. Three-dimensional techniques, such as finite element modelling (FEM), finite difference modelling and discrete element modelling, are generally used for more complex geometries and loadings. FEM is the most used option to model the linings and their surrounding soils (Bakhshi and Nasri, 2013), as shown in Figure 1.14. This method can predict both the ground deformations and lining behaviour, including the post peak behaviour of steel and concrete and stress redistributions resulting from lining deformations (Ö.V.B.B., 2011b). FEM analysis techniques can also be used to represent the tunnelling process, different geologic formations or external loads within proximity of an existing structure (A.F.T.E.S., 2005). When the axial forces and bending moments developed in the ling are determined, the precast segments can therefore be designed with a moment-axial force diagram (I.T.A., 2019). This design process is the same as the aforementioned analytical solutions and numerical beam methods.

On the other hand, this numerical approach needs much computational effort and is time-consuming (Anh and Sugimoto, 2020). Hence, basic simplifications, such as the joint's structural details and soil properties, are unavoidable. Only the analysis for a specific and critical loading case is conducted with this method in current studies (Do et al., 2014b; Li et al., 2015c; Galván et al., 2017; Kavvadas et al., 2017; Gall et al., 2018). It can be found that the FEM calculation is generally used for verification or research purposes. Additionally, in the current design framework considering serviceability and ultimate limit states, it is difficult to assign appropriate factors to the different types of loading when performing a FEM analysis.

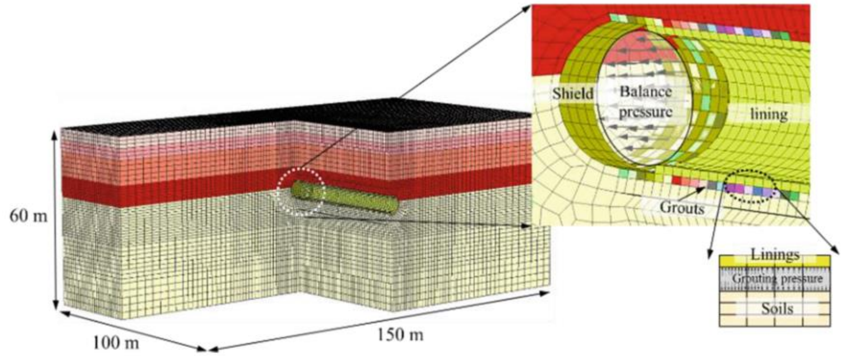

Figure 1.14 Example of the FEM model for shield tunnel construction (Qiao et al., 2018).

1.4.5 Pressure distributions

As shown in Figure 1.11, one of the key points in shield tunnel lining design is to determine the pressure on the tunnel lining reasonably and accurately. Therefore, more specific information about the pressures is needed. Many researchers (Atkinson and Potts, 1977; Nomoto et al., 1999; Mashimo and Ishimura, 2003; Kim and Eisenstein, 2006; Leung and Meguid, 2011; Lin et al., 2015) have studied soil pressures on shield tunnel linings. The soil pressure on the segments depends on the soil type, the construction parameters and the contact characteristics between the segments and the soil. In design practice, the soil pressure is separated into vertical and horizontal pressures (I.T.A., 2000; Koyama, 2003), as shown in Figure 1.12. when following the most commonly adopted methods for shield tunnel lining design, or the MRM and the BSM methods. Since the horizontal soil pressure is derived from the vertical soil pressure by multiplying by a lateral coefficient, it is critical to determine the vertical soil pressure. Currently, the whole overburden theory is commonly used for vertical soil pressure calculation in a shallow tunnel, while Terzaghi’s formula is used to consider the contribution of soil’s shear resistance in good ground conditions or when the tunnel is deep.

Apart from the soil pressure from the surrounding soils acting on the lining, construction loads caused by the backfilling grouting process are also an essential factor affecting tunnel linings, as reported in (Bezuijen et al., 2004; Hashimoto et al., 2005; Hashimoto et al., 2008; Talmon and Bezuijen, 2009; Bilotta and Russo, 2013; Liang et al., 2017; Gil Lorenzo, 2019). The size of the TBM is larger than the external dimension of the lining structure, with a difference of up to 18cm (Thewes and Budach, 2009). A gap between the linings and the soil occurs when the TBM proceeds. In order to minimise the influence of the gap on the soil settlement affecting the surrounding buildings, the synchronous backfilling technology was developed where grout is ejected from the grouting holes into the concurrently produced gap along the proceeding TBM (Shirlaw et al., 2004). It is found that the grouting process has a non-negligible effect on the pressures exerted on the linings when the TBM is advancing, and this effect decreased with the drilling distance increasing. The pressures on the linings when the shield tail was passing by are affected by many factors, such as grouting materials and construction parameters. Localised large grouting pressures might result in concrete cracking, local damage of the segments, leakage at the joints and even a reduction of lining safety, durability and serviceability, meaning that more attention should be paid to the construction load caused by the grouting process when designing a lining structure (Zou and Zuo, 2017; Chen et al., 2018; Teachavorasinskun, 2018; Liu et al., 2019). Additionally, some researchers (Sramoon et al., 2002; Mashimo and Ishimura, 2005; Han et al., 2017) pointed out that the tail brush pressure was a significant type of load during the linings' pushing-out process due to its considerable magnitude, more than four times the theoretical soil pressure in some case studies. In order to consider the grouting pressure, a triangular load distribution is recommended by Working Group No. 2 of I.T.A (2000), where the peak value and the triangle load effecting area are not explicitly stipulated. However, all these studies or standards focus on circular tunnels, and there is no specific instruction for special-section tunnels.

1.5 Research scope and methodology

1.5.1 Lacunae of current knowledge

It is widely acknowledged that a special-section shield tunnel has various advantages when compared with a circular one. However, there are no specific standards or design guidelines related to this kind of tunnel. The calculation method for a special-section shield tunnel commonly refers to circular tunnels, and its applicability for the QRST design lacks verification. As mentioned, there are two main practical calculation methods for a circular shield tunnel design, the MRM method and the BSM method. The former requires empirical parameters and a lot of engineering experience. It seems that the latter is the only suitable method for a QRST calculation in practice. Hence, more insights into the application of the BSM method in the QRST case are excepted.

The joints divide the lining into a non-continuous structure. Once the joint has been installed, its retrofit or repair will be difficult and sometimes impossible. Therefore, the joint is regarded as being the most critical part, whose failure will result in water leakage, rebar corrosion and even structural collapse. The rotational behaviour of the longitudinal joint has been profoundly investigated during the past decades but is mostly limited to joint patterns in circular tunnels. Due to the section shape of a QRST, its longitudinal joints sustain larger internal forces than in a circular tunnel, and the joint's shear behaviour under service conditions is non-negligible. A new joint pattern is specially designed to address these problems in QRSTs. However, the mechanical performance of this new joint pattern is unclear, and the stress level of joints at different positions varies significantly. This may raise a problem of selecting the parameters when the BSM is used by designers. The stiffness value e.g. is unreliable by lack of experimental verification and it varies with different internal force combinations. The effect of different joints' stress levels on the structural behaviour has not been investigated. A reasonable method for dealing with the moment-axial and shear-axial interactions in different longitudinal joints becomes a main concern for the QRST lining calculation, and the resulting difference from a constant stiffness value is worth a study.

Although the BSM method has been widely used in practice for the circular shield tunnel design, its applicability for the tunnel with a special section still needs verification. An indoor full-scale lining experiment can help to obtain the precise lining's mechanical behaviour under clearly defined loading conditions. Therefore this experimental method is regarded as being the most convincing approach to investigate the lining's structural performance. Until now, only an extremely limited number of full-scale experiments has been conducted for special-section shield tunnel linings. So far, a profound comparison between experiments and predictions from the BSM method for a special-section shield tunnel is, to the knowledge of the author, lacking, and it is worth an investigation about the applicability of the BSM method for the design work related to special-section shield tunnels.

In addition, the lack of knowledge also applies to the pressure distributions around a special-section shield tunnel, although in current design, identical pressure distributions as in a circular tunnel are assumed. The surrounding pressures from soils or grouting materials play an important role in the structural calculation and segment section design, which is highly related to the project safety and cost. Hence a reasonable pressure assumption is of great significance. However, research about the spatial and temporal development of the surrounding pressures during a construction process and service stage of a non-circular tunnel is scarce.

1.5.2 Research goals

Based on the lacunae of current knowledge, the research goals of this study include the following aspects of the QRSTs:

- Validation of the applicability of the new joint type used in the QRSTs
- Verification of the proposed calculation model based on BSM method
- Derivation of realistic pressure distributions around linings through on-site tests

1.5.3 Research scope

The scope of this thesis is to perform a comprehensive analysis of the mechanical behaviour of a QRST lining. It includes the following aspects:

- A comprehensive study of the new joint pattern used in the QRSTs through a series of full-scale tests (flexural and shear behaviour) and elaborate FEM (flexural behaviour)
- A calculation model for a QRST lining based on the BSM method and its verification
- A comparison of the pressure distributions between reality and design assumptions in a shallow overburden QRST case
- A parametric study related to various loading conditions and comparison with the MRM method

As a new type of shield tunnel, the QRST lining is comprehensively studied in this work, covering the joint's behaviour, calculation model, pressure distribution and parametric analysis. However, it has to be recognised that it is impossible to cover all the aspects of the structural behaviour of a QRST shield tunnel lining within the scope of a single PhD thesis.

1.5.4 Methodology

Firstly, through full-scale tests and FEM simulation approaches, a substantial study into the flexural behaviour of the joint specially designed for the QRSTs is conducted, including the joint's damage process, bearing capacity and the connection of the embedded parts. Additionally, the joint's shear behaviour under service conditions was explored through tests. The joint's rotational and shear stiffnesses under varying axial forces are collected and expressed by fitting functions, establishing a database to describe the joint behaviour.

Secondly, based on the BSM method, a calculation model for QRST is proposed, using an iterative method considering the combination of axial forces, shear forces and bending moments in different longitudinal joints. The established database from the joint study is used to serve as an input to verify the iterative function in the proposed QRST model. A unique loading frame and experimental program are developed, allowing full-scale point loading tests on a QRST lining and comparisons with the results derived from the BSM-based QRST model.

Additionally, three in-situ monitoring tests are carried out for shallow-buried QRSTs in soft soils to provide direct results of the actual pressures around linings. The measurement protocol for the field tests is elaborately designed and implemented. Correspondingly the tunnel construction is recorded in detail to capture the pressure changes during the execution of the experiments and compare with the assumed pressure distributions in the QRST design.

Finally, with the proposed QRST calculation model and pressure assumptions based on field tests, a comprehensive parametric study is performed to investigate the QRST lining's structural behaviour, covering the effects of the indoor point loads, circumferential joints and various design loads.

1.6 Outline of this thesis

This PhD thesis includes seven chapters. Figure 1.15 displays the structure of this thesis and the title of each chapter. The current Chapter 1 gives a general introduction about the development of special-section shield tunnels, project background, relevant calculation models for shield tunnels, and this PhD research content.

Part A: Calculation model consists of three chapters. Firstly, due to the new joint pattern used in the QRSTs, the joint's moment-axial interaction behaviour and bearing capacity are comprehensively studied through both testing and simulation approaches in Chapter 2. Following that, Chapter 3 focuses on the joint's shear behaviour under varying axial forces. Finally, with the support of these two chapters, a BSM-based calculation model for the QRSTs is developed with an iterative method to consider each joint's flexural and shear behaviour in Chapter 4. The proposed model is verified through a unique indoor full-scale experiment on a tunnel lining, with exactly known point loads allowing precise observations of the structural behaviour.

Parallel to Part A, three in-situ tests in soft soils with similar overburdens but different construction parameters were organised to investigate the pressure changes. These are presented in **Part B: Surrounding pressures** (Chapter 5). The temporal and spatial distributions of the lining pressures during and after the construction are obtained, allowing comparisons with the assumed pressure distributions in the QRST design.

Based on the research of Parts A and B, a series of parametric studies is conducted for this new shield lining pattern in **Part C: Parametric analysis** (Chapter 6), including the comparisons between the point loads in indoor experiments and uniformly pressures in a more realistic situation, the investigation of the applicability of the MRM method for the QRST design and effects of varying pressure distributions.

Finally, a summary of this thesis and general conclusions are given in the last chapter, Chapter 7, together with some ideas and suggestions for the further development of the presented topic.

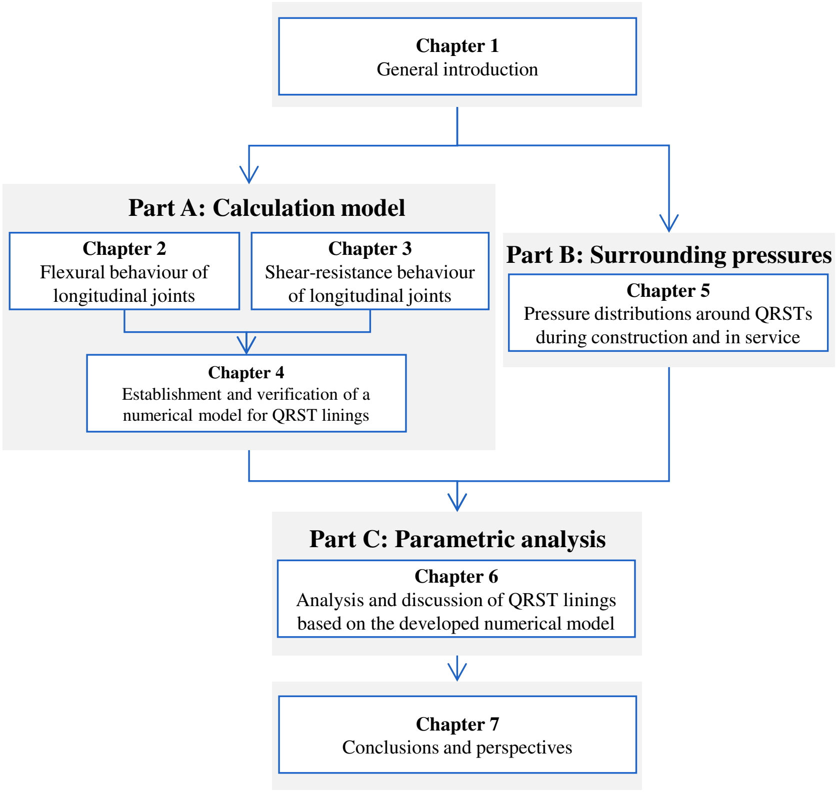

Figure 1.15 Outline of the thesis.

Chapter 2

Flexural behaviour of longitudinal joints

2.1 General introduction

The mechanised shield tunnelling method has the advantage of a smaller environmental influence when compared with conventional tunnelling methods (e.g., open-cut method and blasting), and it has been widely used in urban underground space construction, from drainage tunnels to subway tunnels (Lee and Ge, 2001; Do et al., 2014b). Longitudinal joints between segments divide the cross-section of a lining structure into several parts. For a specific lining shape and a given lining thickness, the joint configuration is the main factor affecting the overall lining stiffness and its deformations (I.T.A., 2000; Lee et al., 2001; Blom, 2002; Do et al., 2014a; Li et al., 2014). The joint rotates under the effect of bending moments, resulting in rigid body displacements of the segments, which contribute a non-negligible part to the tunnel lining's overall deformation (Liu et al., 2016; Liu et al., 2017a). Controlling the overall deformation is an essential performance assessment index. The joint design affects the structural deformation and, in turn, affects the lining thickness. Moreover, the longitudinal joint is also the most critical part, as the lining failure is initiated by joint damage, which causes water leakage and other detrimental distress (Yu et al., 2013; Li et al., 2015a; Liu et al., 2016; Liu and Sun, 2020). Therefore, the choice of the joint type is of great importance when a shield tunnel is designed.

A QRST with an improved cross-sectional shape makes two-way subway transportation in one tube possible, which can reduce the construction costs and the environmental impact (Zhu et al., 2016; Liu et al., 2018a; Liu et al., 2018b). However, the bending moment range in the longitudinal joints of a QRST is larger than in a conventional circular tunnel. In order to increase the joint's rotation resistance performance, a joint type with ductile iron joint panels (DIJPs) is adopted in QRSTs. Although the joint flexural behaviour has an important influence on the lining's structural deformation, there are only a few studies on the joint behaviour of this new joint type. Moreover, the behavioural insight for this joint is necessary for its further application in QRSTs or other special-section shield tunnels with large bending moments.

In this chapter, firstly, the joint type used in QRSTs is introduced, including the joints before and after bolt position improvements. Secondly, the experiments to investigate the bearing capacity, the damage process, the DIJPs' connecting conditions for this joint type under combined axial and bending loads are presented. Moreover, a nonlinear 3D finite element model for the local joint behaviour is introduced and verified by joint tests. Following that, within the bending moment range under normal service conditions, more aspects related to the influence of the internal forces at the joint vicinity and the effects of other modifying methods are analysed through the developed joint model. In addition, the influencing area of the longitudinal joint section is analysed, and a comparison with the BSM method for the calculation of joint deflections is conducted. Finally, a cubic polynomial function is proposed to describe the joint rotation development, which could serve as an input to describe the joint's flexural behaviour in full-ring structural calculations of a QRST.

2.2 Bending moment resistance experiment

2.2.1 Introduction of the joint specimens with different bolt positions

There are two types of longitudinal joints for concrete segments connected by bolts, i.e., joints with or without pre-installed panels. In conventional circular shield tunnels, joints without panels are commonly used, as shown in Figure 2.1a and b. In order to avoid damage to the concrete near the joint, the bolt installing hole cannot be very deep in the direction to the outer segment side or very close to the joint section. This means that the possibilities of adjusting the bolt installing hole are very limited. Studies about this joint type have been conducted through experiments, simulations, and theoretical analyses (Li et al., 2015a; b; Majdi et al., 2016; Liu et al., 2017a; Liu et al., 2017b). In the joint type shown in Figure 2.1c, joint panels are embedded into the concrete of the segments with connecting reinforcement. The panels are commonly made from ductile iron (Koyama, 2003), and these DIJPs can be cast into different shapes to achieve a more flexible bolt positioning. Joints with DIJPs have been adopted in water conveyance tunnels (Yan et al., 2011; Jin et al., 2017; Zhou et al., 2019). As small circumferential stresses might occur in water conveyance tunnels due to the changes of the inside water level, more bolts are needed to prevent the joints from opening (Yu et al., 2009; Cao et al., 2012; Zhang et al., 2016). However, few studies have been conducted for this joint type.

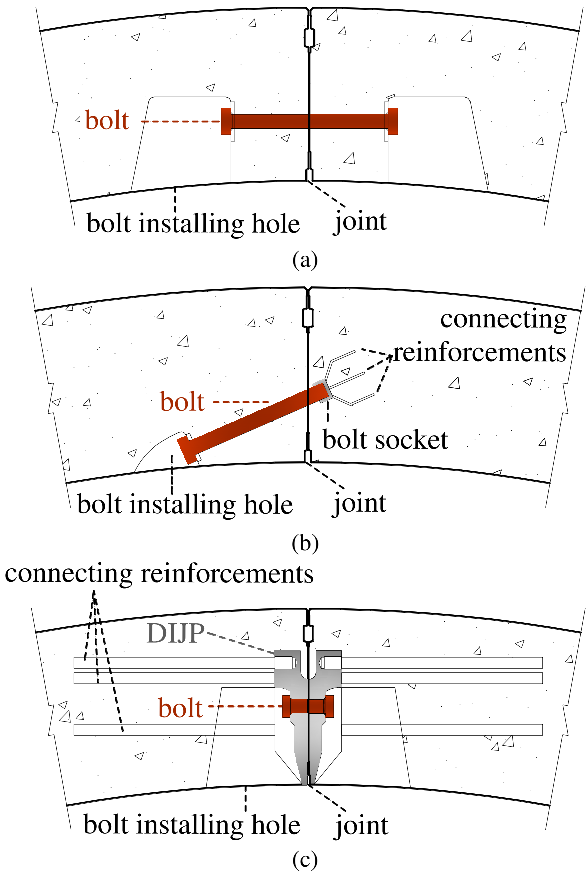

Figure 2.1 Examples of different longitudinal joint types for concrete segments: (a) long straight bolt in a joint without panels; (b) inclined spear bolt in a joint without panels; (c) short straight bolt in a joint with panels.

Unlike a circular lining ring, a quasi-rectangular lining shape has a reduced arching effect due to its small height-to-width ratio (Ding et al., 2020), and as a result, the bending moments in the lining are significantly larger when compared to circular linings with the same buried depth. Additionally, the longitudinal joints of a QRST are subjected to either positive or negative moments, mainly depending on their position in the cross section. Since the shape of a DIJP can be changed to achieve more flexible bolt positionings based on the bending moment type occurring in the longitudinal joint, QRSTs adopt the joint type with DIJPs to resist joint opening and rotation, as shown in Figure 2.1c. As water tightness from the inner segment side is not necessary, and the circumferential stresses are not reduced by the inner water pressure in QRSTs, the joint section design is different from that in water conveyance tunnels. Hence, it is necessary to investigate the flexural behaviour through an experimental approach.

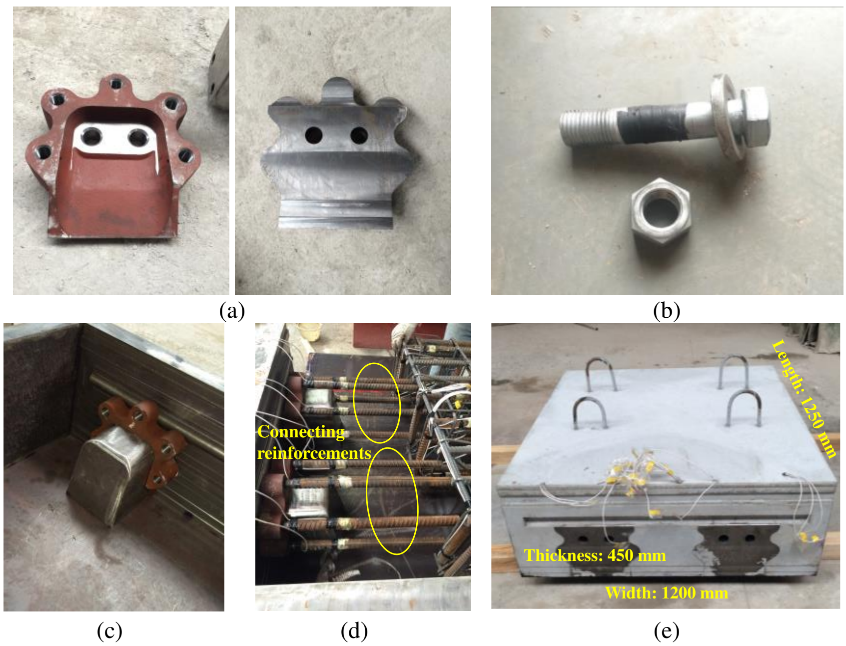

Figure 2.2 Tested segments: (a) ductile iron joint panel (DIJP); (b) bolt with nut and washer; (c) pre-installed DIJP in the casting mould; (d) connecting reinforcements; (e) demoulded segment.

Rotation-resistance tests for longitudinal joints in QRSTs were conducted at the Key Laboratory of Geotechnical and Underground Engineering of the Ministry of Education at Tongji University in 2015. The size of the joint specimens was full-scale, and they were specifically cast for the joint experiments. Given the fact that when the joints of curved or linear lining segments sustain the same axial force and bending moment combinations, the mechanics in the joints can be considered equal (Zhang et al., 2002; Gong et al., 2017), the specimens in the tests were designed as plane rather than curved in order to achieve more precise bending moment values. In addition to this, all the structural details of the joints were retained as they were used in a real tunnel, such as the grooves for the waterproofing belts. Each specimen was composed of two segments, and the size of each segment was 1250 × 1200 × 450 mm (length × width × thickness). Two DIJPs were pre-installed in each segment through five connecting reinforcements.

The DIJPs in adjacent segments were connected by two short straight bolts (diameter of 33 mm, yield stress of 480 MPa, tensile stress of 600 MPa). The adopted concrete class was C50 (characteristic cube compressive strength of 50 MPa). The pre-installed parts and the cast joint segment are shown in Figure 2.2, and the geometric details at the joint section are shown in Figure 2.3.

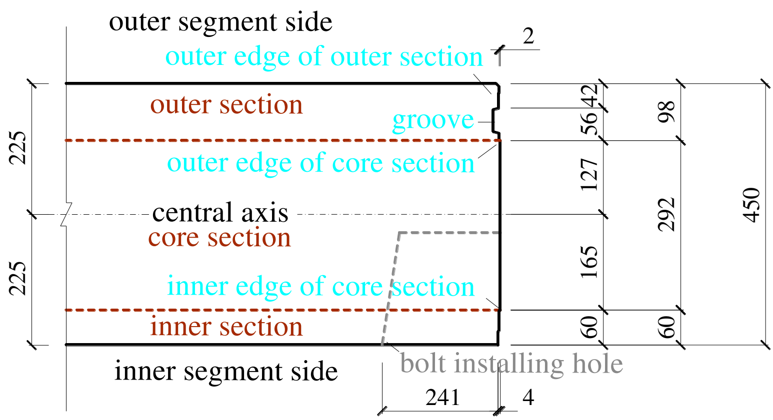

Figure 2.3 Joint section details (unit: mm).

In a shield tunnel, the joints can be subjected to two types of bending moments, which we refer to as positive and negative bending moments. A positive bending moment creates tension at the inner side of the segment and compression at the outer side, while a negative bending moment creates the reverse stress situation. In the test specimens, the original position of the bolt was 200 mm from the inner segment surface, and we define this joint as a Type-A joint. Different from circular tunnels, the horizontal axis of the QRSTs has to be strictly controlled to be parallel to the sea level. As such, most of the longitudinal joints are subjected to either positive or negative moments, depending on their positions in the cross-section. This feature makes an improvement of the bolt position possible based on the occurring bending moment type. Besides the Type-A joint, and in order to increase the distance from the bolts to the compression zone so as to resist a higher bending moment, the bolts were moved 50 mm to the inner side for the joints in the case of a positive bending moment (Type-BPos joint) and 50 mm to the outer side for the joints in the case of a negative bending moment (Type-BNeg joint). The three configurations are shown in Figure 2.4. Each segment had two DIJPs, but only one DIJP of each segment is presented in Figure 2.4 for brevity. Figure 2.5 shows the cross-sections of the DIJPs that are indicated in Figure 2.4. These three configurations were tested to compare the effects of the bolt position improvements.

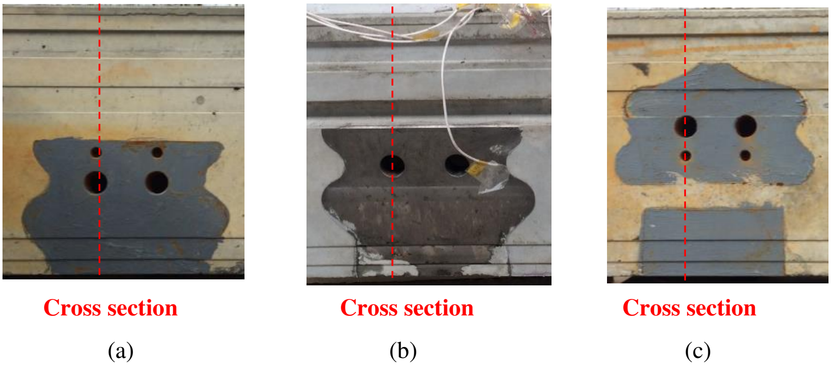

Figure 2.4 Front view of the DIJPs: (a) Type-BPos; (b) Type-A; (c) Type-BNeg.

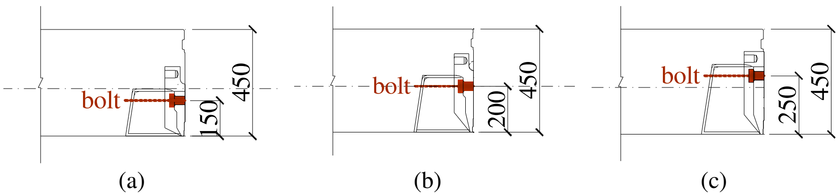

Figure 2.5 Cross-section view of the DIJPs: (a) Type-BPos; (b) Type-A; (c) Type-BNeg (unit: mm).

2.2.2 Test setup

2.2.2.1 Loading procedure

As shown in Figure 2.6, the loading device consisted of a loading frame, vertical and horizontal jacks and loading supports, and was equipped with an electro-hydraulic servo loading system, including three load recorders for the vertical force and four for the horizontal force. The maximum values for the vertical and horizontal loads were 3000 kN and 2000 kN, respectively.

Figure 2.6 Loading system for the rotation resistance experiments.

The ends of the segments were put into steel loading supports, and the gaps were filled with steel plates to ensure the segments were tied to the loading supports, as shown in Figure 2.7. A set of horizontal hinged jacks on the right side provided the horizontal loads F_{jh} through pushing on the loading supports. A steel roller constrained the displacement of the left loading support, but the rotational movement was allowed. Two bottom rollers under the loading supports only balanced the vertical force and allowed the supports to rotate freely. The bending moment was exerted through the vertical jacks and a set of distribution beam.

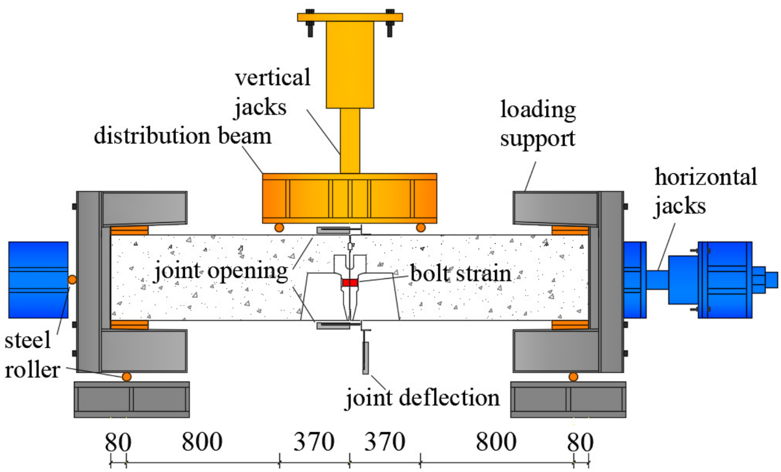

Figure 2.7 Test set-up and layout of the measurement points for joint openings, joint deflections, and bolt strains (unit: mm).

The bending moment M_{js} and axial force N_{js} at the joint can be determined by the vertical loads P_{jv} and horizontal loads F_{jh} through Eq. (2.1), and the bending moment diagram is shown in Figure 8a. Herein, P_{jc} is the reaction force at the vertical supports, equal to the sum of the vertical load P_{jv} and the dead load G_{js}. l_1, l_2, l_3 and l_4 represent the distance from the joint to the vertical load P_{jv}, the distance from the vertical load P_{jv} to the centre of gravity of each segment, the distance from the centre of gravity of each segment to the loading support, and the distance from the loading support to the segment's end, respectively. The distances between the loads are known, and thus, the bending moment at the joint can be calculated. The horizontal loads $F_{jh}$and vertical loads P_{jv}can be adjusted through the electro-hydraulic servo loading system to make the internal forces in the joints equal to the target values.

$$\begin{cases} M_{js} = P_{jv} \cdot (l_2 + l_3) + G_{js} \cdot l_3 \\ N_{js} = F_{jh} \end{cases} \tag{2.1}$$

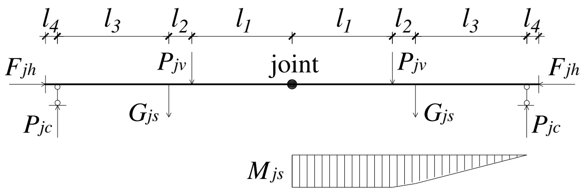

Figure 2.8 Bending moment diagram.

The experimental load cases were divided into two categories. One category related to positive bending moments with the load P_{jv} applied from the outer side of the joint, creating tension at the inner side. The other category related to negative bending moments with the load P_{jv} applied from the inner side of the joint, creating tension at the outer side, as shown in Figure 2.9. Positive bending moments were exerted on Type-A and Type-BPos specimens, while negative bending moments were exerted on Type-A and Type-BNeg specimens.

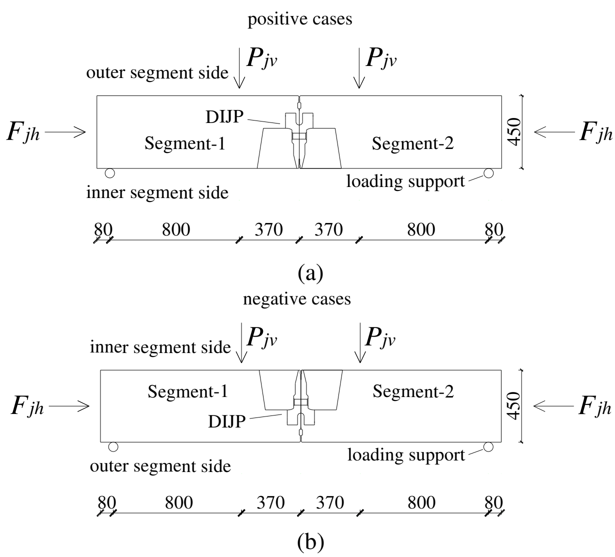

Figure 2.9 Exerted loads and dimensions: (a) positive case; (b) negative case (unit: mm).

The width of the segments and the longitudinal joints in the experiments was 1.2 m, but this width can vary among different shield tunnels. In order to make the results independent of the segment width and comparable to research results from other shield tunnels with different widths, the axial force and bending moment values are presented after normalisation to 1 m width. As such, the units of axial force and bending moments become kN/m and kN·m/m.

Based on the pre-calculation results from the MRM method, which is widely used for the internal force calculations of a circular shield tunnel lining structure (Liu et al., 1991), for most of the positive bending moment cases, the eccentricity of the axial force is around 0.21 m, while for the negative cases, it is generally less than 0.19 m.

The load sequence is as follows. For the positive cases (type-A and Type-Bpos), in the first testing stage, loads P_{jv} and F_{jh} were increased simultaneously in order to achieve a constant eccentricity of 0.21 m up to a horizontal load F_{jh}=1250 kN/m (M_{js}=262.5 kN·m/m). Then, in the second testing stage, only the vertical load P_{jv} was increased to investigate the effect of the bending moment while the axial force remained constant. A similar loading procedure was used for the negative cases (Type-A and Type-BNeg). A constant eccentricity of 0.19 m was achieved there, up to a horizontal load F_{jh}=1625 kN/m (M_{js}=308.8 kN·m/m), after which only the vertical load P_{jv} was increased. The exerted axial forces and bending moments at the joint section are shown in Figure 2.10.

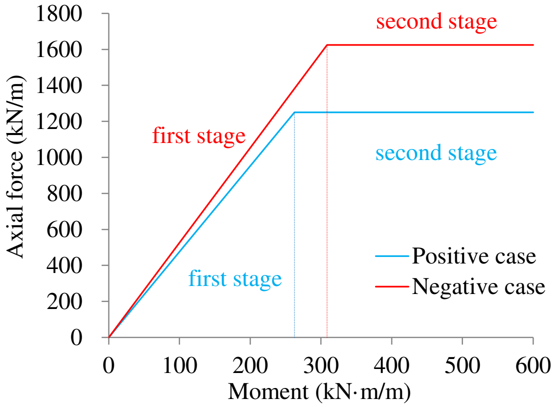

Figure 2.10 Exerted target axial forces and bending moments at the joint section.

2.2.2.2 Measurement layout

During the tests, joint openings, joint deflections, bolt strains, and strains of the connecting reinforcements for the DIJPs and concrete were monitored. Strain gauges were pre-installed on the connecting reinforcements before the DIJP installation. In order to investigate the connection between the DIJPs and the concrete, the gauges were arranged to measure reinforcement strains in one transverse section, as well as along the most stressed reinforcement. The positions and numbers of the measurement points are shown in Figure 2.7, Figure 2.11 and Table 2.1.

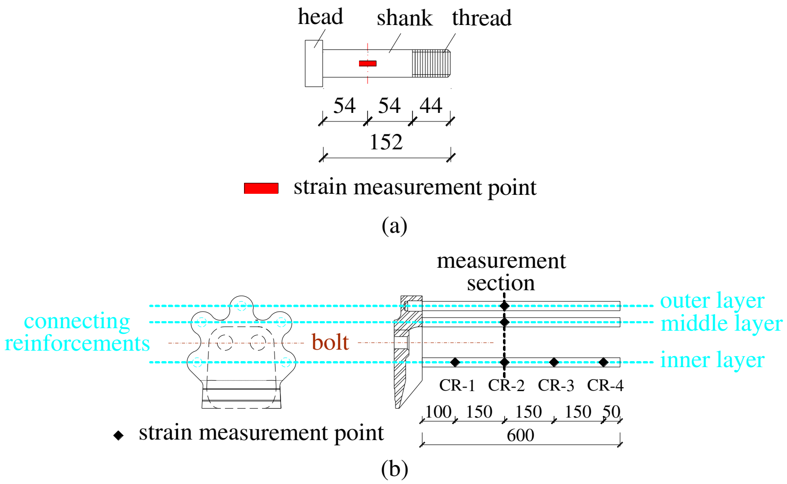

Figure 2.11 Strain measurement points: (a) details of a bolt measurement point; (b) measurement points on the connecting reinforcements (unit: mm).

Table 2.1 List of measurement points in the joint's rotation resistance tests.

Type	Number	Range	Accuracy
Joint opening	4	0–100 mm	0.05 mm
Joint deflection	2	0–100 mm	0.05 mm
Bolt strain	4	0–10,000 με	1 με
Connecting reinforcement strain	9	0–10,000 με	1 με

2.2.3 Results

2.2.3.1 Joint rotations and deflections

The effect of the bolt repositioning on the joint bearing capacity was investigated through the tests. The obtained evolutions of the joint rotation and deflection with increasing bending moments are depicted in Figure 2.12 and Figure 2.13. The joint rotation θ_{js} is calculated through $\theta_{js} = (v_{r1} - v_{r2})/h_0$, where h is the joint height of 450 mm, or the thickness of the joint segment, and v_{r1} and v_{r2} are the variations of the joint opening at the inner and outer side of the segment, which can be obtained from the joint tests.

Key designations (KDs) during the joint damage process (see Table 2.2 and Table 2.3) are indicated with numbers 1 to 5 and 1′ to 5′ in Figure 2.12 and Figure 2.13. For the positive case of the Type-A joint, after the constant axial force at the joint was attained (KD 1), the joint went through core section cracking (KD 2), outer edge contacting (KD 3), outer section cracking (KD 4), crack penetration (KD 5), and concrete crushing (KD 6). When the outer edges of the segments touched each other (KD 3), the outer part of the section started to contribute to the bending moment resistance, and the speed of the joint rotation and deflection evolutions decreased. Once the crushing happened, one of the bolts snapped suddenly. Then, the tensile force in this bolt needed to be sustained by other bolts, and as a result, all bolts failed rapidly. A slightly different sequence was observed for the positive case of the Type-BPos, with the outer edges contacting each other (KD 2′) before core concrete cracking (KD 3′) appeared.

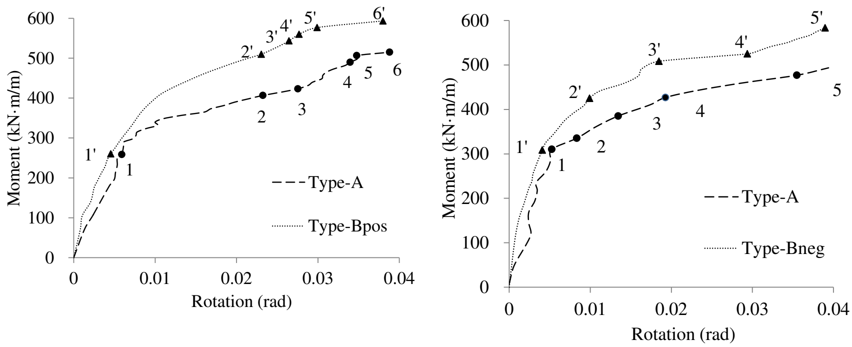

(a) (b)

Figure 2.12 Evolution of the joint rotation with increasing bending moments: (a) positive cases; (b) negative cases.

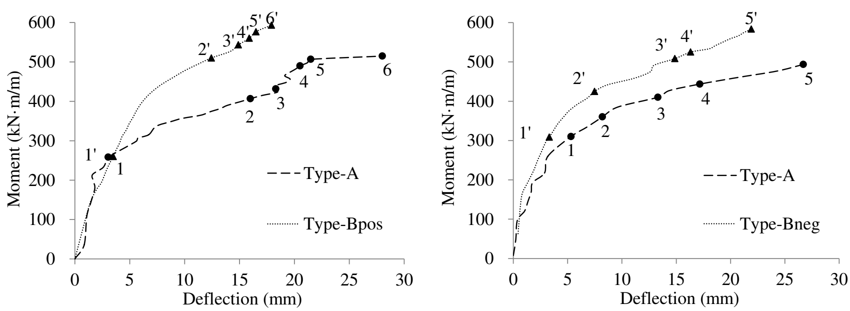

(a) (b)

Figure 2.13 Evolution of the joint deflection with increasing bending moments: (a) positive cases; (b) negative cases.

Table 2.2 Key moments during the damage processes in positive cases (unit: kN·m/m).

Type-A			Type-BPos		
Key Designation	Phenomenon	Value	Key Designation	Phenomenon	Value
1	constant axial force	258.6	1′	constant axial force	260.0
2	core section cracking	**406.7**	2′	outer edge contacting	510.0
3	outer edge contacting	423.3	3′	core section cracking	**543.3**
4	outer section cracking	490.0	4′	outer section cracking	560.0
5	crack penetration	**506.7**	5′	crack penetration	**576.7**
6	concrete crushing	515.0	6′	concrete crushing	593.3

Table 2.3 Key moments during the damage processes in negative cases (unit: kN·m/m).

Type-A			Type-BNeg		
Key Designation	Phenomenon	Value	Key Designation	Phenomenon	Value
1	constant axial force	310.2	1′	constant axial force	308.8
2	core section cracking	**360.2**	2′	core section cracking	**425.0**
3	cracks quickly developing	410.2	3′	cracks quickly developing	508.0
4	crack penetration	**443.5**	4′	crack penetration	**525.0**
5	concrete crushing	493.5	5′	concrete crushing	583.3

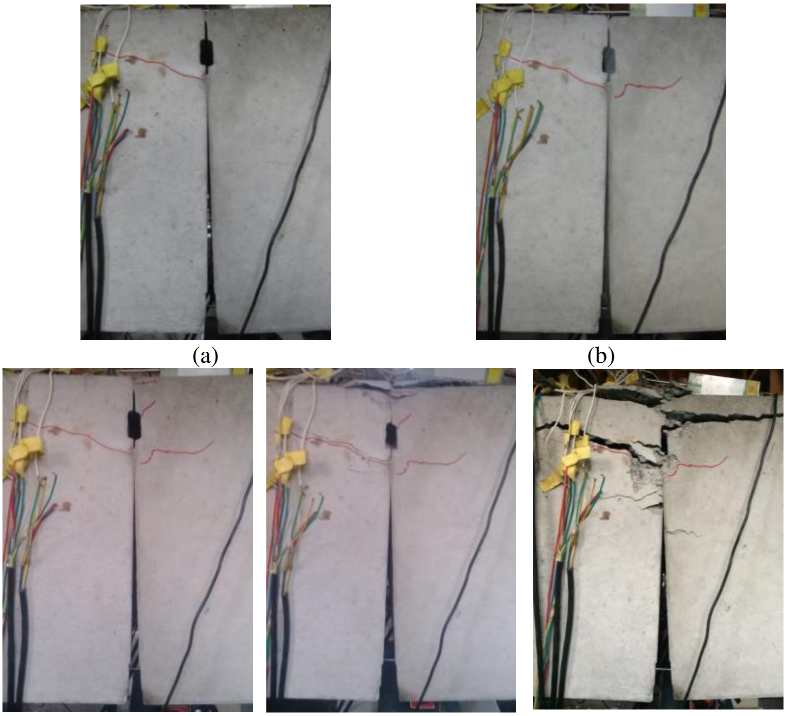

(a) (b) (c) (d) (e)

Figure 2.14 Type-A joint under a positive bending moment: (a) core section cracking; (b) outer edge contacting; (c) outer section cracking; (d) crack penetration; (e) concrete crushing.

For the negative cases, the progressive development of the joint damage included core section cracking (KD 2 and 2′), quickly developing cracks (KD 3 and 3′), crack penetration (KD 4 and 4′), and concrete crushing (KD 5 and 5′), followed by bolt failure. The corresponding bending moments in both the positive and negative cases are summarised in Table 2.2 and Table 2.3, respectively.

The damage processes before and after the improvements are similar, and only pictures of the Type-A joint tests are shown in Figure 2.14 and Figure 2.15. The failure of the DIJP-equipped joints is initiated by core section cracking and terminated by local concrete crushing. The failure mode is similar to that of a column submitted to compound bending with small eccentricity, where the concrete is crushed before the reinforcement starts yielding.

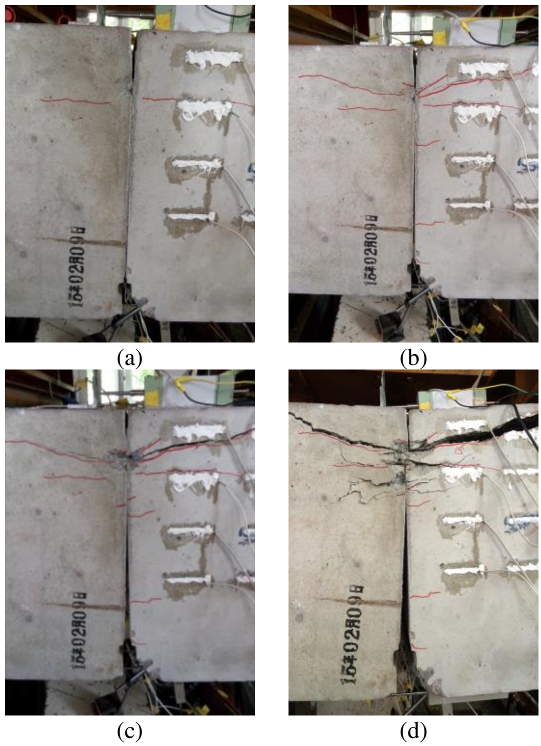

Figure 2.15 Type-A joint under a negative bending moment: (a) core section cracking; (b) quickly developing cracks; (c) crack penetration; (d) concrete crushing.

The noticeable core concrete cracking affects the serviceability of the segmental joint from the long-term view, as water leakage might occur or water might penetrate into the concrete and cause corrosion of the reinforcement. With this key moment chosen as a reference situation, the bolt position improvements (Type-A to Type-B) increase the bending moment resistance values by 33.6% for the positive cases (from 406.7 kN·m/m to 543.3 kN·m/m) and by 18.0% for the negative cases (from 360.2 kN·m/m to 425.0 kN·m/m). As soon as the cracks penetrated the segments, the compressed concrete was crushed quickly. The appearance of such penetrating cracks means that the bearing capacity of the segment is almost reached. With this key moment as a reference, the bolt improvements (Type-A to Type-B) increase the bending moment values by 13.8% for the positive cases (from 506.7 kN·m/m to 576.7 kN·m/m) and 18.4% for the negative cases (from 443.5 kN·m/m to 525.0 kN·m/m). It is obvious that both the joint's resistance to cracking and the ultimate bearing capacity are enhanced due to the bolt positional improvements.

2.2.3.2 Bolt strains

In the tests, after the concrete was crushed, the compressive area moved close to the central axis of the joint section. Due to the reduced lever arm, the joint opening increased considerably, and bolts were rapidly subjected to more tension to balance the moment until they snapped one by one. Due to the stiff contact between the bolt head and the pre-installed DIJP, the bolts were not under pure tension when the joint rotated. Stress concentrations appeared at the transition area between the bolt head and bolt shank, and the bolts failed in this area in the tests, as shown in Figure 2.16.

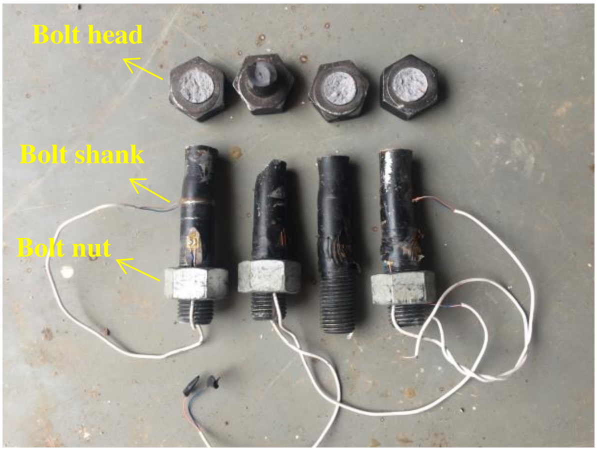

Figure 2.16 Failed bolts in tests.

During the tests, the bolt strains were measured at the middle of the shank, as shown in Figure 2.11a. The bolt strain curves are depicted in Figure 2.17 for the joints with the positional improvement for brevity. In the tests, the recorded strains for different measurement points showed some variation, which was consistent with the observation that bolts broke consecutively and not simultaneously. The bolt strains prior to concrete crushing were much smaller than the yield strain of 2400 με at 300 kN·m/m, which meant that the bolts still had a large strength margin until the concrete was crushed.

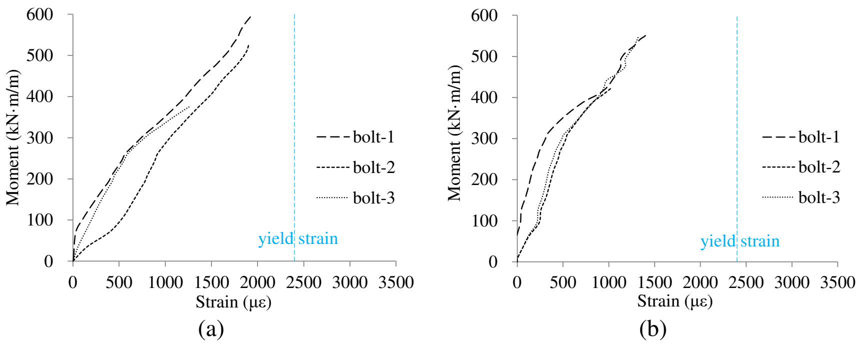

Figure 2.17 Evolution of the bolt strains with increasing bending moments: (a) Type-BPos joint in positive cases; (b) Type-BNeg joint in negative cases.

2.2.3.3 Connecting reinforcement strains

The connecting reinforcements are used to anchor the DIJPs in the concrete, and a reliable connection is essential for the joint safety. As an example, the strains from the Type-A joint under positive bending moments at the measurement points indicated in Figure 2.11b are shown in Figure 2.18. In Figure 2.18a, the strains along the connecting reinforcement at the inner layer, which was the most stressed reinforcement in this test case, are shown. The closer to the joint section, the larger the strains were. For the strains of the connecting reinforcements at different layers, it was obvious that the inner layer resisted most of the tension force, as can be seen in Figure 2.18b. When the bending moment was small, the middle and outer layers were under compression. As the joint was rotating, the connecting reinforcements were gradually submitted to tension forces. For the bending moment equal to 300 kN·m/m, the strains of all connecting reinforcements were smaller than 200 με. Figure 2.19 shows a joint section after testing. Both DIJPs were still in good condition, and few cracks had appeared around them. From this, it can be concluded that the DIJPs, as well as their connections to the concrete, have proved to be reliable, or even slightly over-designed. However, since most tunnel accidents are initiated by joints (Liu and Sun, 2020b), a conservative design is regarded as necessary for QRSTs. Any structural accident in a tunnel will be disastrous, especially for subways in cities. All the current QRSTs keep the longitudinal joints in this pattern. The QRSTs' joint design can be modified to be more economical in the future.

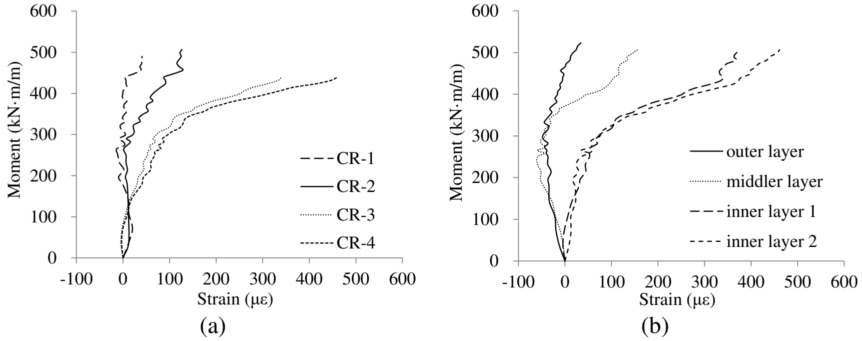

Figure 2.18 Evolution of the connecting reinforcement strains with increasing bending moments: (a) along the inner layer; (b) on different layers at the measurement section.

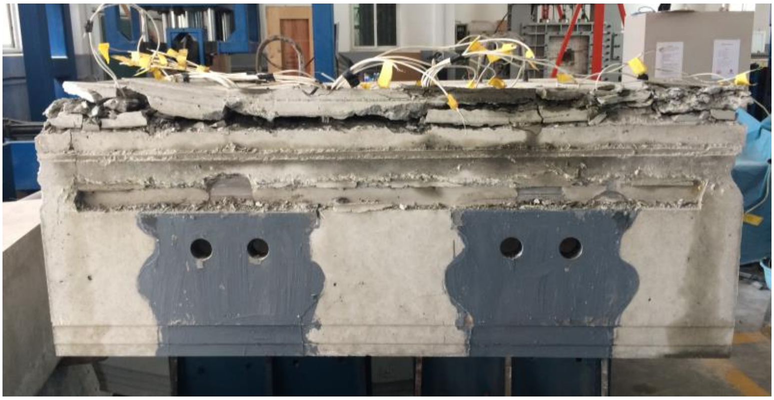

Figure 2.19 Joint section after testing.

2.2.4 Evaluation of the joints with DIJPS applied in QRSTs

The failure of the joints is initiated by concrete cracking at the core section and is terminated by concrete crushing. During this period, the bolts do not yield. This type of joint failure mode is similar to that of a column cross-section with small eccentricity. For the joints under positive bending moments, there is a joint stiffness increase when the outer edges of the segments touch each other. Additionally, the connecting reinforcements between DIJPs and concrete can guarantee the DIJPs' anchorage in the concrete, and components of the DIJPs and their connections in this new joint type are proven reliable.

The design values of the bending moments in QRSTs' longitudinal joints after considering the load safety factors are normally around 300 kN·m under service conditions for an overburden from 7 m to 17 m, or 250 kN·m/m after normalisation (Liu et al., 2018a; Liu et al., 2018c; Zhang et al., 2020). The joint with DIJPs has small rotation and deflection values, showing good performance within the moment range at the normal service level. The bending moment values at which the core concrete cracking appears are larger than 250 kN·m/m, resulting in an acceptable safety factor in practical use. The studied joint pattern is expected to be qualified for the application in QRSTs.

Table 2.4 Comparison between the joints with DIJPs and joints in a conventional circular tunnel in positive cases.

Phenomenon	Bending Moment (kN·m/m)			Rotation (rad)			Deflection (mm)		
	Circular Tunnel	Type -A	Type -BPos	Circular Tunnel	Type -A	Type -BPos	Circular Tunnel	Type -A	Type -BPos
Core concrete cracking	155.0	406.7	543.3	0.030	0.023	0.026	18	16.0	14.9
Crack penetration	200.0	506.7	576.7	0.045	0.035	0.030	28	21.5	16.5

Table 2.5 Comparison between the joints with DIJPs and joints in a conventional circular tunnel in negative cases.

Phenomenon	Bending Moment (kN·m/m)			Rotation (rad)			Deflection (mm)		
	Circular Tunnel	Type -A	Type -BNeg	Circular Tunnel	Type -A	Type -BNeg	Circular Tunnel	Type -A	Type -BNeg
Core concrete cracking	160.0	360.2	425.0	0.040	0.011	0.010	22	8.2	7.3
Crack penetration	200.0	443.5	525.0	0.060	0.023	0.029	31	17.2	16.3

On the other hand, it is worth comparing the performance of a joint with DIJPs to that of the joints commonly used in conventional circular shield tunnels (see Figure 2.1a). From the test results for joints in a conventional circular shield tunnel (Liu et al., 2017b), the bending moments when cracks appeared and cracks penetrated are compared to those from the tests for the joints with DIJPs (see Table 2.4 and Table 2.5). In addition, the corresponding rotation and deflection values are added. It should be noted that no direct comparison is possible, since the segmental thickness is not equal in both tests. Rather, the ratio between the thickness of the segments with DIJPs (450 mm) and that of the conventional joints (350 mm) is 1.29, and correspondingly, the ratio between the moments of inertia is 2.13. In the case of a comparison to the Type-A configuration, the bending moment resistances to cracking and crack penetration of the DIJP joint are more than twice those from the conventional one, which is generally consistent with the inertia moment ratio. After the bolt position improvements (Type-BPos and Type-BNeg), the resistances to cracking and crack penetration are clearly higher. Even under these large bending moments, the improved joints have smaller deflections, which is as, or more, important than the failure loads. Additionally, from Figure 2.12, the slopes of the moment-rotation curves represent the joint rotational stiffness, showing that after bolt position improvements, the rotational stiffness is also increased. All of these observations mean that the bolt position improvements not only contribute to a larger bearing capacity but also to a better structural deformation control. Hence, joints adapted to the sign of the bending moment are preferable in QRSTs, as they can sustain larger bending moments and also reduce overall lining deformations when compared to a single-joint type.

2.3 Numerical study

Due to the high cost of the joint tests, only a limited number of tests can be performed. Hence, a refined nonlinear 3D joint model was developed to analyse the mechanical behaviour of this new type of joint under different loading conditions and the effects of possible modifications. For this, an Abaqus 3D joint model with all structural details was established. As the bearing capacity of this new type of shield tunnel joint had proven to have an acceptable safety factor for its utilisation, its rotational behaviour under normal service conditions is the subject of this section.

2.3.1 Setup of the FEM joint

An Abaqus 3D joint model with all structural details was established. Although a test specimen consisted of two segments, only one half of one segment (Part A) was modelled, taking into account the symmetry of the specimen in order to save calculation time. Hence, the joint model included half of a reinforcement cage (Part B), two halves of bolts (Part C), two steel washers (Part D), and one piece of DIJP (Part E), as shown in Figure 2.20. The other half of the segment was modelled through lateral symmetric boundary conditions. A rigid plate (Part F) and contact conditions allowing for separation were used to represent the other segment and the other halves of the bolts. The model after assembly and boundary settings is shown in Figure 2.21.

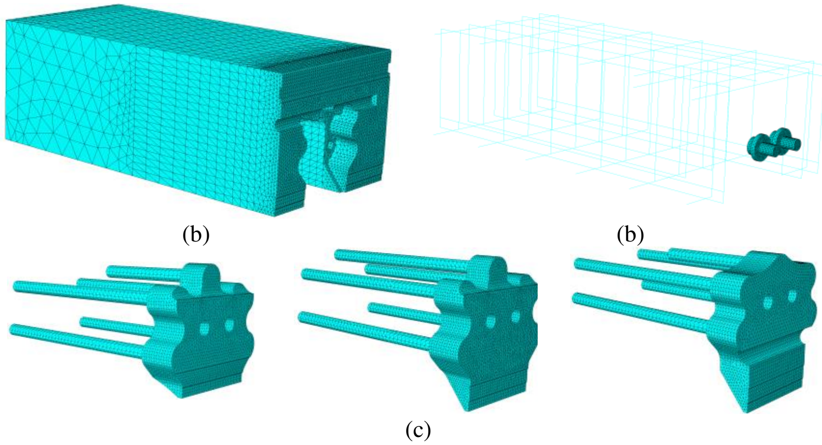

Figure 2.20 Parts in the joint 3D model: (a) one half of a concrete segment (Part A); (b) one half of the reinforcement cage (Part B), two halves of bolts (Part C), and two bolt washers (Part D); (c) different DIJPs (Part E) and connecting reinforcements (Part F).

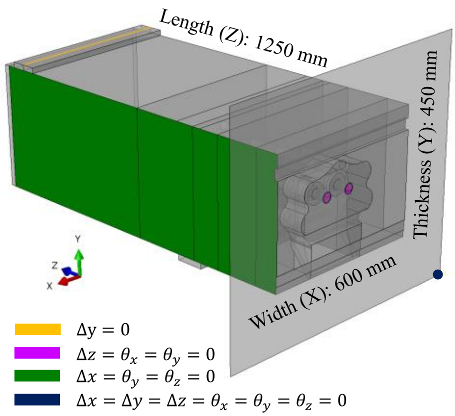

Figure 2.21 Joint model after assembly and boundary settings.

Due to the irregular contact surface between the concrete and the DIJPs in the FEM joint, the tetrahedron element shape was adopted for meshing. The region near the joint section was finely meshed with a 10 mm element size, while the end of the joint segment was relatively coarsely meshed with a 100 mm element size. The total element number of the joint model was about 270,000. The concrete damaged plasticity model (CDP) was used for the concrete modelling, and the elastoplastic constitutive model was used for all other parts. The reinforcing cage was embedded in the concrete as a truss, and the connecting reinforcements of the DIJP were tied to the surrounding concrete. All other contact types in the model were all set as a hard contact (Abaqus, 2018). The different parts and their contact conditions are summarised in Table 2.6.

Table 2.6 Summary of element types and contact properties.

	Part	Type	Contact
A	concrete	deformable 3D	hard contact with G
B	reinforcement cage	truss	embedded in A
C	bolts	deformable 3D	hard contact with D
D	bolt washers	deformable 3D	hard contact with C and E
E	DIJP	deformable 3D	hard contact with A, D and G
F	connecting reinforcements	deformable 3D	tied to A
G	rigid plate	rigid body	-

2.3.2 Comparisons between modelling and testing results

The established model could be used to simulate the joint's rotation-resistance tests from Section 2.2. The same loading processes were exerted in the FEM joint, and the joint openings, joint deflections, bolt strains and the connecting reinforcement strains were retrieved to compare with the measured results in the joint tests.

The development of the joint rotations in the joint model was also calculated via the joint opening values, according to the formula for θ_{js} mentioned in Section 2.2.3.1. The comparison of the calculated values with those obtained from the joint tests is presented in Figure 2.22. In addition, the deflection results are shown in Figure 2.23. The calculations of the negative cases aborted earlier than in the positive cases, which could be explained by the stress concentration and large strain values at the contact surface between the DIJPs and the concrete. Figure 2.22 and Figure 2.23 show that the curves from the proposed joint model are consistent with those from the tests. The evolution of the rotation and the deflection can be well predicted by the simulation approach.

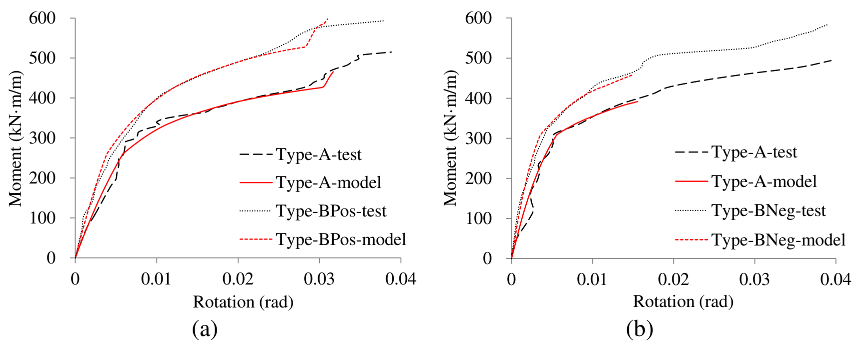

Figure 2.22 Comparison of the joint rotations between tests and simulations: (a) positive cases; (b) negative cases.

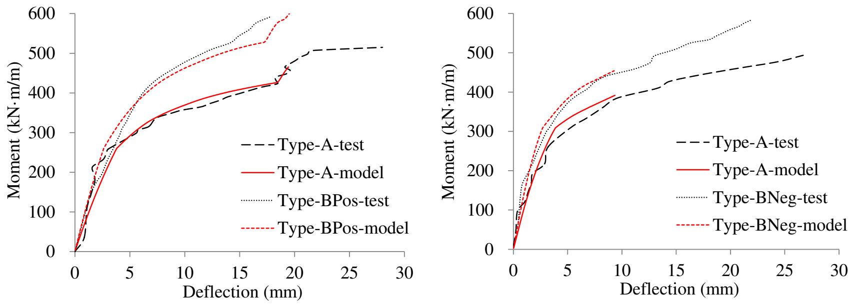

(a) (b)

Figure 2.23 Comparison of the joint deflections between tests and simulations: (a) positive cases; (b) negative cases.

Taking the example of the joints with improved bolt positions, the bolt strain curves from tests and simulations are depicted in Figure 2.24. The bolt strains were measured at the middle of the shank in the joint test, and correspondingly, the bolt strains in the models were also recorded at these locations, i.e., the red circles in Figure 2.25. In the tests, the bolt strains from different measurement points showed a certain variation. However, they were generally similar to those from the joint model, and therefore, the bolt strains from the model can be used to predict the overall bolt strain in reality. Due to the stiff contact between the bolt head and the DIJPs, the bolts were not under pure tension when the joint rotated. As shown in Figure 2.25, the FEM result revealed that stress concentrations appeared at the transition area between the bolt head and bolt shank, which explained the bolts' failure in this area in the tests.

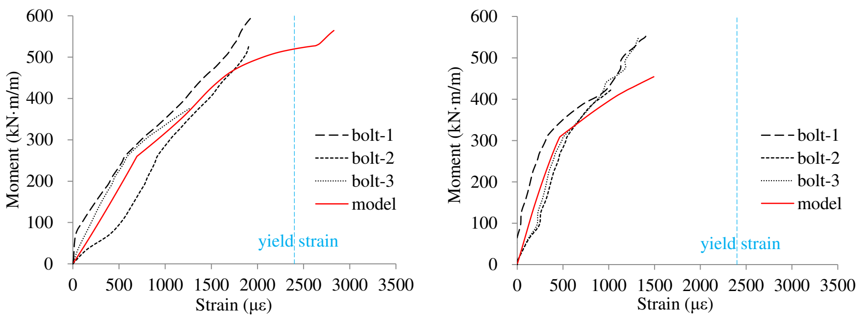

(a) (b)

Figure 2.24 Comparison of the bolt strains between tests and simulations: (a) positive cases; (b) negative cases.

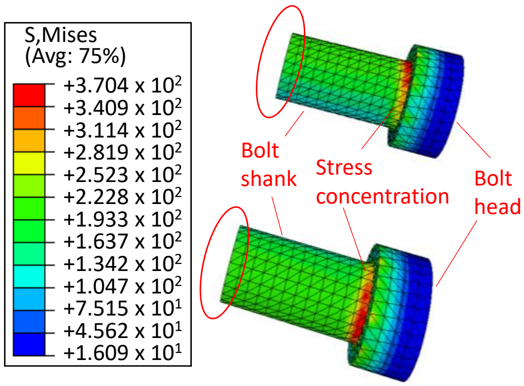

Figure 2.25 Calculated bolt stress concentration in the model.

The connecting reinforcements' strains from the joint test and the joint model of the Type-A joint under positive moments are compared in Figure 2.26. The corresponding measurement positions are shown in Figure 2.11. For the strains along the connecting reinforcement at the inner layer, both the joint test and model indicated that the area close to the joint section sustained relatively high strains. For the strains at different layers, the joint model showed a similar trend to that in tests. Most of the tension force was sustained by the connecting reinforcements at the inner layer. The stress in other connecting reinforcements changed from compressive to tensile with increasing bending moment. The strain curves obtained from the joint model and the tests are generally in good agreement.

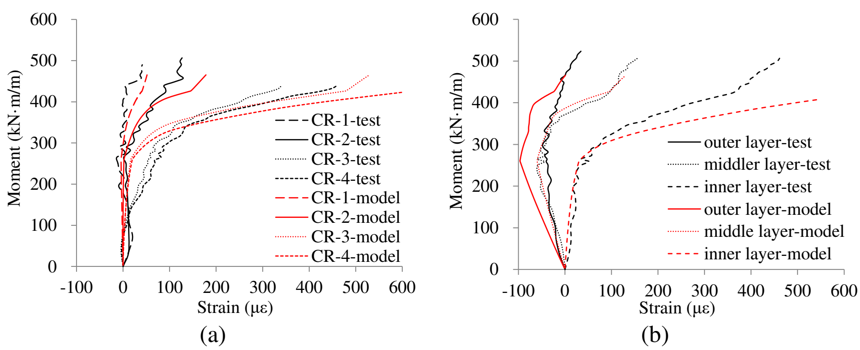

Figure 2.26 Comparison of the connecting reinforcement strains between tests and simulations: (a) along the inner layer; (b) on different layers at the measurement section.

From the comparison, it is found that the proposed joint model well simulated the joint flexural behaviour. The normalized bending moments in the joints of QRSTs are normally within 250 kN·m/m under service conditions (Liu et al., 2018a; Liu et al., 2018c; Zhang et al., 2020), and the calculation results from the proposed joint model can fully cover this bending moment range. On the other hand, the full-scale joint tests have proven that the bearing capacity of the studied joint pattern is quite beyond the 250 kN·m/m bending moment range. The joint pattern with DIJPs is expected to be applied in future QRSTs or similar non-circular shield tunnels. Therefore, considering the significant influence of the longitudinal joints on the lining structural performance, the joint behaviour at the normal service level and possible joint improvements are important for the further applications of this joint pattern. The developed joint model provides an effective and economical approach for studying the joint behaviour and different influencing factors under the service conditions. Some related aspects are discussed in the next section.

2.3.3 Parametric analysis

Different from the joints in conventional circular shield tunnels, the joints in QRSTs are equipped with DIJPs, and the theoretical analysis of their rotational behaviour is complicated. By means of the proposed 3D joint model, more results focusing on the joint rotation within the bending moment range under normal service conditions can be obtained. As the axial forces and bending moments changed together in the first stage of the joint tests, in this parametric analysis, the axial force was kept constant at different levels, and the bending moment increased gradually to investigate the different stages of the joint rotation development. Following that, the influences of the bolts' elongation resistance, concrete properties and height of the core section were analysed.

On the other hand, BSM is a simplified model to calculate the deformations and internal forces in a shield tunnel lining, which has been widely used in tunnel designs (Koyama, 2003). The BSM method regards the lining segments as beams and the longitudinal joints as rotational springs (Ye et al., 2014). However, the existence of the longitudinal joints affects the stress distributions at the vicinity of a joint section, which cannot be considered in the BSM. This aspect might influence the calculated deformations and needs to be studied. In this parametric analysis, the affected length of the stress distributions along the segment caused by the joint section and a joint deflection comparison between the 3D joint model and the BSM method are discussed.

2.3.3.1 Internal forces in the joint's vicinity

The axial force in the considered type of QRSTs generally ranges from 600 to 1000 kN for a segment width under the targeted overburden from 7 m to 17 m (Liu et al., 2018a; Liu et al., 2018c; Zhang et al., 2020). Therefore, the axial force was kept constant at 400, 800, and 1200 kN in the model calculations, or 333, 667, and 1000 kN/m after normalisation.

Figure 2.27 presents the development of joint rotations of the Type-A and Type-B joints as the bending moment increases. Figure 2.28 presents the bolt stress curves for the Type-B joints. The bolt stress curve of the Type-A joint under 667 kN/m axial force is added to compare the effect of the bolt position improvement. Figure 2.29, taking the example of a positive case, shows the stress distributions at the joint section. The rotation evolution was divided into three stages. At the first stage, when the bending moment was small, the rotation curves were similar. This means that joint rotations are not influenced by the axial forces at this stage. It is worth noting that, at this stage, the rotational stiffnesses are quite large and the bolts do not take any force. During this period, the eccentricity h_e resulting from the combined effect of the exerted moment and axial force, as shown in Figure 2.29, is small, and the application point of the resultant force is close to the central axis of the joint section. The whole joint core section is under compression, but its outer side is more stressed than the inner side (stress distribution-1 in Figure 2.29). As the bending moment keeps growing, the eccentricity h_e increases, and the whole core section is not compressed anymore, leading to the joint opening (stress distribution-2 in Figure 2.29). The variation of the joint opening is mainly caused by the compressive deformations. This means that the joint behaviour at this stage is determined by the height of the joint core section. At the second stage, when the neutral axis moves above the bolt axis, the bolts start being tensioned and involved in the joint rotation (stress distribution-3 in Figure 2.29). From Figure 2.27 and Figure 2.28, it can be seen that the bolt stress increases quickly while the rotational stiffness decreases gradually. At the third stage, the eccentricity h_e increases further and exceeds the distance between the edge of the outer section and the joint central axis, namely $h_1 - h_c$ (stress distribution-4 in Figure 2.29). However, the stress distribution in the compression zone at the joint section cannot exceed this distance. From the rotation and bolt stress curves, at this stage, the rotation curve appears to be almost linear, while the bolt stress also follows a linear trend. For the same joint type under different axial forces, the stiffnesses at this stage appear to be similar.

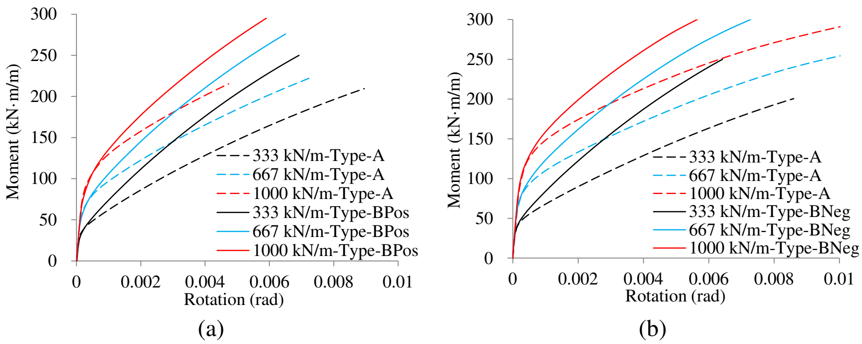

Figure 2.27 Evolution of the joint rotation with increasing bending moment under constant axial force: (a) positive cases; (b) negative cases.

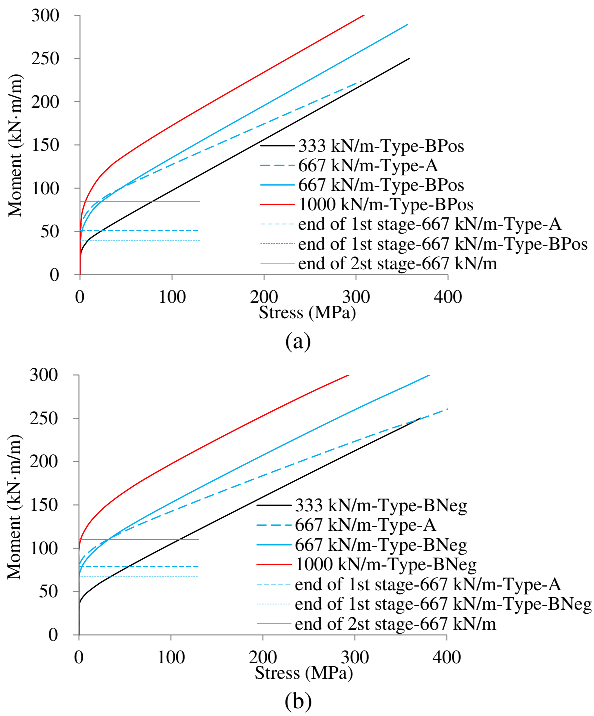

Figure 2.28 Evolution of the bolt stresses with increasing bending moment under constant axial force: (a) positive cases; (b) negative cases.

From Figure 2.29, the bending moment values at the end of the first stage and the second stage can be evaluated. As the stress level at the first stage is not large, based on the assumption of a plane strain distribution, the stress distribution is assumed to have a triangular shape, and it balances the exerted axial force N_{js} and bending moment M_{js}. When the neutral axis is at the bolt axis, the first stage ends.

The corresponding moment value can be calculated with Eq. (2.2). For the end of the second stage, the eccentricity h_e equals $h_1 - h_c$, and the corresponding moment value can be calculated from Eq. (2.3). The bending moments at the ends of these two stages are summarised in Table 6 for all calculated cases. The corresponding eccentricities at the end of the first stage and second stage are k_{1-2} and k_{2-3}, which are expressed as Eq. (2.3) and Eq. (2.4). Only the results for the 667 kN/m axial force cases are added to Figure 2.28 as examples to show the trend of the stress curves at different stages. The calculated bending moments yield good predictions of the transition points between consecutive stages.

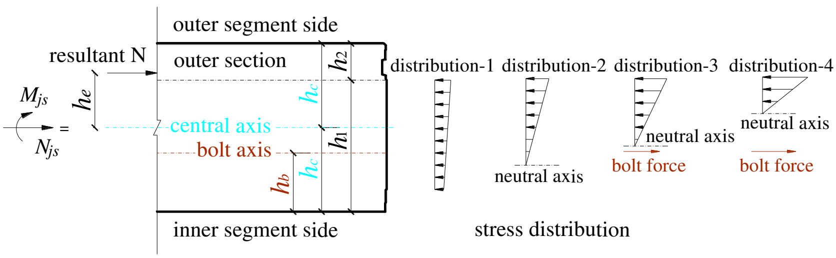

Figure 2.29 Stress distributions at the joint core section in a positive case.

$$M_{1-2} = \left(\frac{2}{3}(h_1 - h_b) + h_b - h_c\right) \cdot N_{js} = \left(\frac{2}{3}h_1 + \frac{1}{3}h_b - h_c\right) \cdot N_{js} \tag{2.2}$$

$$M_{2-3} = (h_1 - h_c) \cdot N_{js} \tag{2.3}$$

$$k_{1-2} = \left(\frac{2}{3}h_1 + \frac{1}{3}h_b - h_c\right) \cdot \tag{2.4}$$

$$k_{2-3} = (h_1 - h_c) \tag{2.5}$$

Table 2.7 Summary of the bending moments at the ends of different stages.

Moment	Axial Force (kN/m)	Positive Cases		Negative Cases	
		Type-A (kN·m/m)	Type-BPos (kN·m/m)	Type-A (kN·m/m)	Type-BNeg (kN·m/m)
End of the first stage	333	25.4	19.9	39.4	33.9
	667	50.9	39.8	78.9	67.8
	1000	76.3	59.7	118.3	101.7
End of the second stage	333	42.3		55.0	
	667	84.7		110.0	
	1000	127.0		165.0	

When the axial force is fixed, at the first stage, the components only providing tensile force, such as bolts, do not contribute to the rotation resistance. Therefore, the joint rotational stiffness is dominated by the height of the core section. At the second stage, the tension-resistant components start working and influence the joint rotations. The bolt position improvements of the Type-B joints increase the distance from the bolts to the compression zone, providing a larger lever arm to balance the exerted moments. Consequently, the bolt stresses decrease under the same bending moment. Meanwhile, the bolt position improvements make the first stage end, as well as the bolts start working, slightly earlier than in the reference Type-A. It is evident that increasing the lever arm has a significant effect on the joint stiffness values. As shown in Table 2.8, by calculating the slope of the curves during the third stage in Figure 2.27, it follows that the rotational stiffness was increased by 67% to 69% for the positive cases and by 97% to 106% for the negative cases.

Table 2.8 Summary of the rotational stiffnesses during the third stage under different axial forces (stiffness unit: kN·m/m/rad, axial force unit: kN/m).

Axial Force	Positive Cases			Negative Cases		
	Type-A	Type-BPos	Increase Rate	Type-A	Type-BNeg	Increase Rate
333	22,591	37,809	67%	17,030	33,490	97%
667	22,069	37,404	69%	16,076	32,598	103%
1000	21,898	37,103	69%	14,604	30,106	106%

On the other hand, it was found that, even under the same axial force, the joint stiffness deviates a lot when different bending moments are applied. Due to the higher number of joints in large-section circular shield tunnels and special-section shield tunnels than in conventional circular tunnels, these joints have different rotational stiffnesses, and the influence of the stiffness differences of these joints on the lining calculation needs to be given due attention.

2.3.3.2 Influence of bolt properties

As mentioned before, improving the bolt positions to increase the lever arm for balancing the exerted bending moment significantly affects the joint rotation behaviour for the second and the third stages. For a fixed distance between the bolts and the core segment edges, the bolt diameter and the number of bolts can be varied to see the influence on the joint rotational behaviour. The essence of these two methods is to enhance the bolts' elongation resistance to a tensile force. The changes of the bolt diameter or the number of bolts might need shape changes of the DIJPs and redesign of the joint. In order to avoid these changes, the Young's modulus of the bolts in the model was adjusted as the only variable to simulate the effect of the enhancement of the bolts' elongation resistance. The bolt diameter of the studied joint was 33 mm, and the Young's modulus was 200 GPa. The Young's modulus was reset to 372 and 661 GPa to simulate the elongation of bolts with 45 and 60 mm diameters under the same tensile force conditions. The increase of the Young's modulus could also be regarded as more bolts to resist the same tensile force. It has to be pointed out that this simplified method aims to simulate the effect of the bolt elongation resistance on joint rotations under a normal bending moment range, rather than the effects related to bolt strength or joint bearing capacity. Only the joint rotations and bolt stresses under the constant 667 kN/m axial force are presented in Figure 2.30 and Figure 2.31.

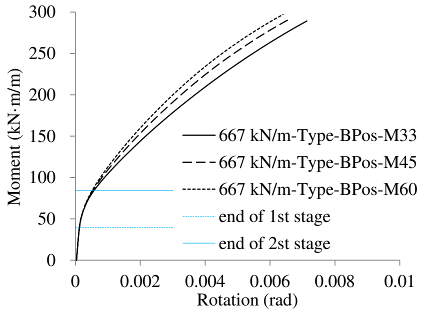

(a)

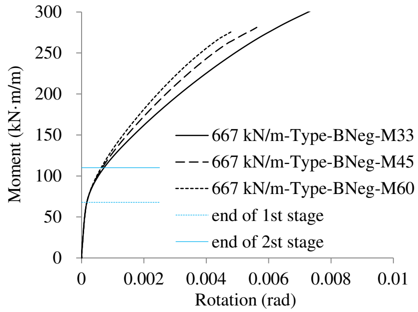

(b)

Figure 2.30 Evolution of the rotations with different Young's moduli: (a) positive cases; (b) negative cases.

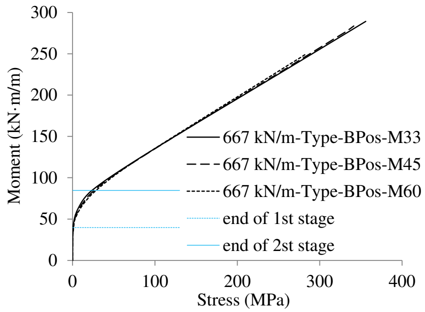

(a)

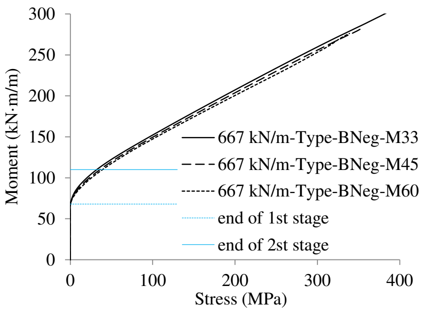

(b)

Figure 2.31 Evolution of the bolt stresses with different Young's moduli: (a) positive cases; (b) negative cases.

The bolts' stress curves for the adjusted moduli are almost identical to those for the original modulus. Due to the modulus increase, identical stresses result in smaller bolt elongations and, consequently, in smaller joint openings. Therefore, the joint stiffness increases, as shown in Figure 2.30. The average rotational stiffnesses during the third stage with the Young's moduli of 372 and 661 GPa are summarised in Table 2.9. For the positive cases, the average stiffness at the third stage increases by 15% and 23%, respectively. Correspondingly, the stiffness increases for the negative cases are 18% and 30%. Based on the model results, the effect of these changes is limited, and when compared to the effect of increasing the lever arm from the Type-A joints to Type-B joints, bolt elongation-resistance enhancement is considered less efficient.

Table 2.9 Summary of the rotational stiffnesses during the third stage with different moduli of the bolts (stiffness unit: kN·m/m/rad, modulus unit: GPa).

Modulus	Positive cases		Negative cases	
	Type-BPos	Increase rate	Type-BNeg	Increase rate
200	37,404	-	32,598	-
372	43,187	15%	38,369	18%
661	45,882	23%	42,492	30%

2.3.3.3 Influence of concrete strength

The effect of concrete strength can be investigated by modifying the concrete strength class. In addition to the design concrete strength class of the segments, C50, the classes C70 and C90 were also investigated. The joint rotation curves and bolt stress curves are shown in Figure 2.32 and Figure 2.33, and only the results under the constant 667 kN/m axial force are presented for brevity. There were only slight rotation differences at the first stage, and the differences were gradually noticeable at the second and the third stages. However, the observed bolt stress curves for C70 and C90 were identical to those for C50. These observations showed that there was little difference between the bolt elongations in these cases and that some differences in the rotation curves occurred for the different concrete classes. The classes C70 and C90 have higher Young's moduli and result in smaller deformations of the compression zone. The average rotational stiffness during the third stage for different concrete classes is summarised in Table 2.10. Compared to the average stiffness at the third stage for the C50 class, the stiffnesses for C70 and C90 increase by 3% and 6%, respectively. The corresponding stiffness increases in the negative cases are 9% and 15%. Within the bending moment range under normal service conditions, the effect of adopting higher concrete classes on the joint deformation is minimal.

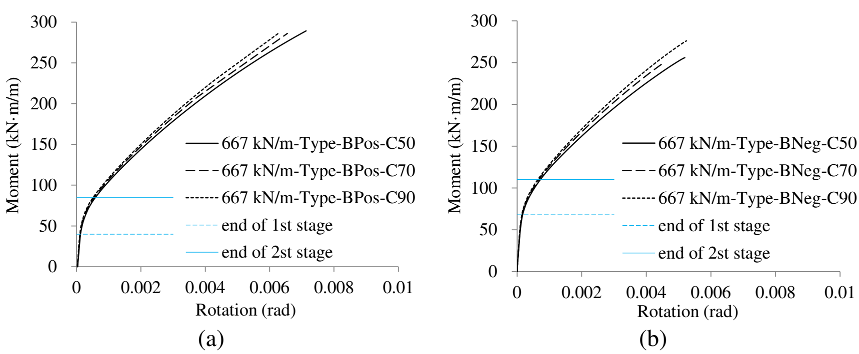

Figure 2.32 Evolution of the rotations with different concrete classes: (a) positive cases; (b) negative cases.

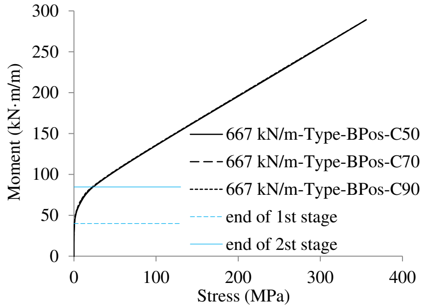

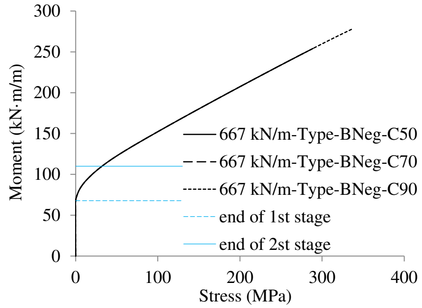

Figure 2.33 Evolution of the bolt stresses with different concrete classes: (a) positive cases; (b) negative cases.

Table 2.10 Summary of the rotational stiffnesses during the third stage with different concrete classes (stiffness unit: kN·m/m/rad, modulus unit: GPa).

Concrete Class	Positive Cases		Negative Cases	
	Type-BPos	Increase Rate	Type-BNeg	Increase Rate
C50	37,404	-	32,598	-
C70	38,431	3%	35,406	9%
C90	39,602	6%	37,342	15%

2.3.3.4 Influence of the height of the core section

The structural details of the joint section are shown in Figure 2.3. In order to further increase the lever arm between the compressive area and the bolts when under an axial force-moment loading case, the details of the joint sections are changed, as shown in Figure 2.34. For the positive cases, the height of the joint's outer section was respectively decreased from 98 mm to 45 mm and to 5 mm. For the negative cases, the height of the inner section was respectively decreased from 60 mm to 22 mm and to 0 mm. All the other aspects related to the detail changes, including contact area and boundary conditions, were correspondingly adjusted. It has to be noted that these structural detail changes only aim to detect the primary effect of increasing the lever arm in order to inspire a possible direction of improvements for the joint section design and that the actual joint improvement should consider many factors, such as changes of the DIJPs' shape, the waterproofing design etc.

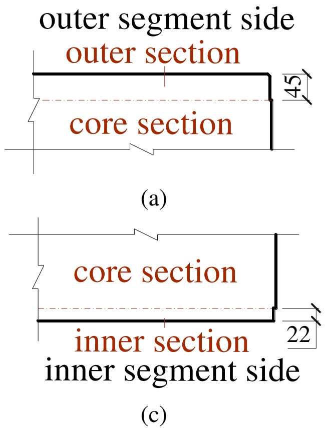

Figure 2.34 Changes of the joint section details: (a) Detail 1 for positive cases; (b) Detail 2 for positive cases; (c) Detail 1 for negative cases; (d) Detail 2 for negative cases (unit: mm).

The joint rotation curves and the bolt stress curves are shown in Figure 2.35 and Figure 2.36. It is evident that the joint stiffness increases considerably, and the rotation-resistance performance is enhanced in both positive and negative cases. Correspondingly, the bolt stresses decrease remarkably. From the previous analysis, the joint section changes could increase the moment values when the first and second stages end. Compared with Figure 2.27, in which the stiffnesses at the first stage were identical, the stiffnesses after detail changes lead to an increase for the stiffnesses at all stages. The stiffness at the first stage is already quite large before changing the core section height, and only the average rotational stiffness during the third stage is summarised and compared in Table 2.11. It is found that improving the lever arm by changing the core section height for balancing the exerted bending moment has a significant effect on the joint's rotational behaviour. However, considering that this change needs to reorganise the joint's waterproof layout, it seems that modifying the bolt positions is a more practical method to increase the lever arm for the studied QRSTs. In the case of a circular shield tunnel, where a longitudinal joint possibly sustains both large positive and negative moments, and bolt repositioning is difficult, managing to increase the core section height is expected to be an efficient method for enhancing the rotational behaviour.

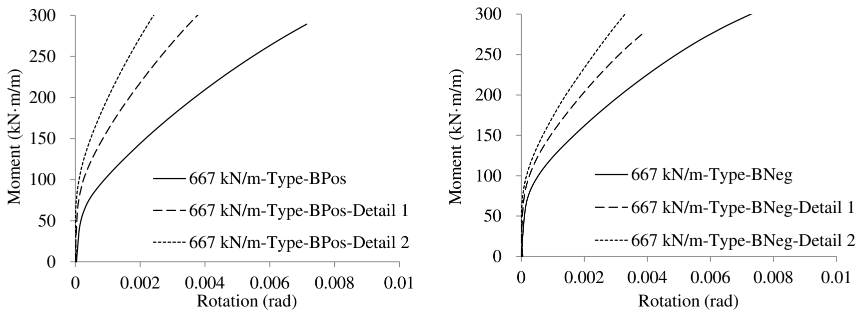

(a) (b)

Figure 2.35 Evolution of the rotations with different joint section details: (a) positive cases; (b) negative cases.

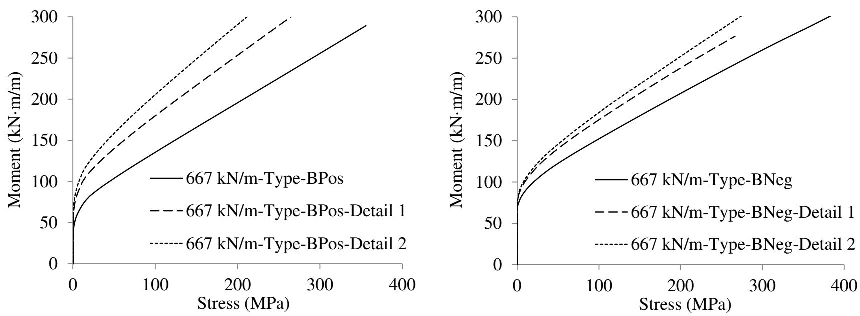

(a) (b)

Figure 2.36 Evolution of the bolt stresses with different joint section details: (a) positive cases; (b) negative cases.

Table 2.11 Summary of the rotational stiffnesses during the third stage with different joint section details (stiffness unit: kN·m/m/rad).

Joint Section	Positive Cases		Negative Cases	
	Type-BPos	Increase Rate	Type-BNeg	Increase Rate
Type-B	37,404	-	32,598	-
Detail 1	59,455	59%	43,073	32%
Detail 2	80,231	114%	57,204	75%

Although an increase of the concrete strength class or the bolt elongation resistance positively influences the joint rotation, adapting the joint section to increase the lever arm between the bolts and the compression zone is the most efficient optimising method. This improvement can be achieved through bolt repositioning or increasing the joint's core section height, which can be considered and chosen based on the bending moments at joint sections and the practical applicability of the improvement.

2.3.3.5 The length affected by the joint section

The segment length in the joint model is 1250 mm, as shown in Figure 2.21, but joint models with another four different segment lengths were also investigated. The segment length was extended to 1550 mm, 1850 mm, 2150 mm, and 2450 mm, respectively, and the corresponding symmetrical boundary conditions were also extended. For the bending moment diagram in Figure 2.8, only the value of l_1 changed while l_2, l_3, F_{jh}, and P_{jv} were kept identical to achieve the same axial forces and bending moments at the joint section in all cases. The joint rotation curves and bolt stress curves derived from different segment lengths under positive and negative bending moments are shown in Figure 2.37, and the results are identical. This means that the segment length does not influence the joint rotational behaviour.

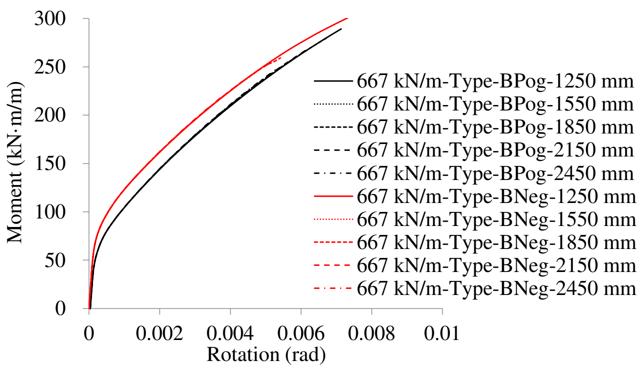

(a)

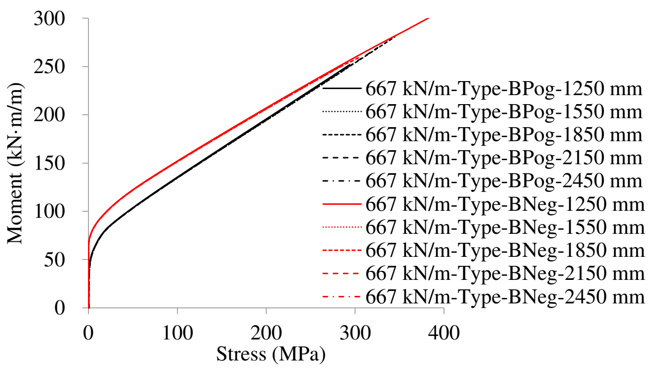

(b)

Figure 2.37 Evolution of the joint rotations and the bolt stresses with different segment lengths: (a) rotation curves; (b) bolt stress curves.

The existence of longitudinal joints in a shield tunnel makes the tunnel lining discontinuous, resulting in large stress concentrations near the joint sections compared to a continuous tunnel lining without longitudinal joints. However, in the joint tests, the locations of the vertical loads are too close to the joint section due to the restrictions of the loading device's size, and the stresses near the joint section are affected by both the existence of the joint and the vertical loads. The actual stress distributions around the joint cannot be obtained in the joint tests, but through the established joint model, the influence of the discontinuity caused by the longitudinal joint can be investigated in the studied loading scenario.

A continuous segment model without a joint section was proposed as a comparison to the established joint model. All the joint structural details were ignored in this segment model, including the groove, DIJP etc. Since there was no longitudinal joint section separating the segment into two pieces, the rigid plate contacting the joint section to simulate the other half of the joint specimen was replaced by a symmetrical displacement control. The other boundary conditions and all the loading procedures in the segment model were kept the same as in the joint model. The segment lengths in this model were the same as those in the joint model, namely 1550, 1850, 2150 and 2450 mm. Figure 2.38 shows an example of the segment model with a length of 2450 mm.

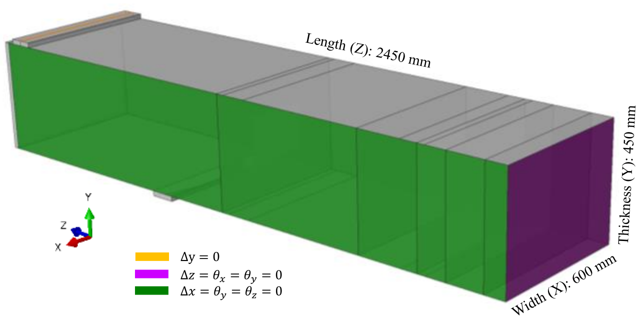

Figure 2.38 Segment model without joint section and corresponding boundary settings.

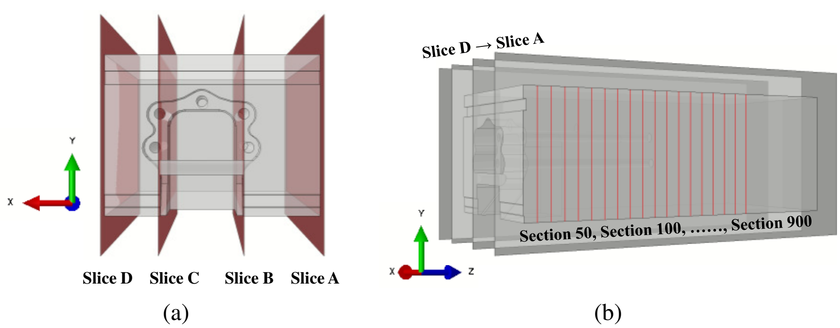

Figure 2.39 Positions of the data retrieving point: (a) Slices A to D along X direction; (b) Section 50 to Section 900 along Z direction.

As the 2450 mm segment length has the longest l_1, which is the distance from the joint to the position of the vertical load as shown in Figure 2.8, and the bending moments along l_1 are constant, the results from the 2450 mm long joint model and the segment model were compared. Four slices (Slices A to D) were chosen in the joint model to retrieve the concrete stresses in the Z-direction, which are the normal stresses along the segment direction in Figure 2.39. For each slice, these Z-direction normal stresses at the points on the sections respectively 50, 100, 150, … , 900 mm away from the joint section (numbered as Section 50, Section 100, … , Section 900) were retrieved to detect the area influenced by the joint section. The Z-direction normal stresses at the same positions in the segment model were depicted as a comparison. The Z-direction stresses from the different sections of the segment model at the bending moments of 40, 120, and 160 kN·m/m are presented in Figure 2.40. It shows a good linear change along the thickness direction, which is the Y direction in Figure 2.38, and the stress distributions at different sections are almost identical at the same bending moment. The stress distributions from the segment model can be compared with those from the joint model.

Four bending moments in the joint model are chosen to compare the stress distributions between the joint model and the segment model, and they are respectively equal to 40, 80, 154, and 200 kN·m/m. The results from Slice D are taken as an example and shown in Figure 2.41. When the moment value is 40 kN·m/m, most of the stresses have a negative value, meaning almost all sections are under compression. For other bending moments, since the moment value increases, all the sections, except Section 50, are under compressive conditions at the outer segment side and under tensile conditions at the inner segment side. However, when a section nearer to the joint is investigated, the stresses there deviate more from the stress distributions retrieved from the segment model. The stresses change dramatically within 200 mm from the joint section, and the stresses beyond this distance tend to become linearly distributed. A considerable stress concentration is found at the height of 325 to 375 mm, the area of the outer edge of the core section as shown in Figure 2.3.

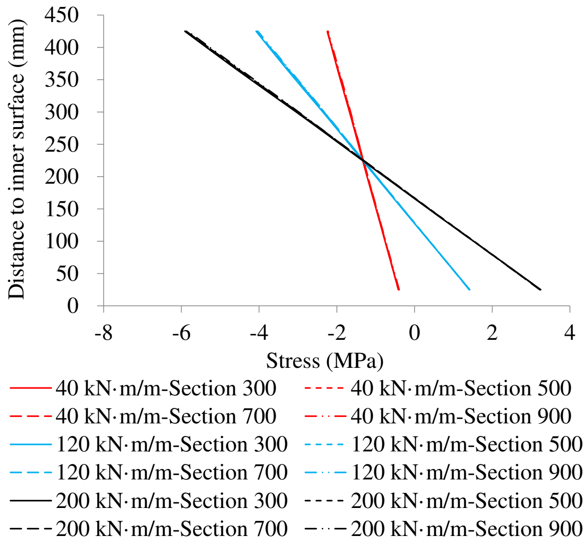

(a)

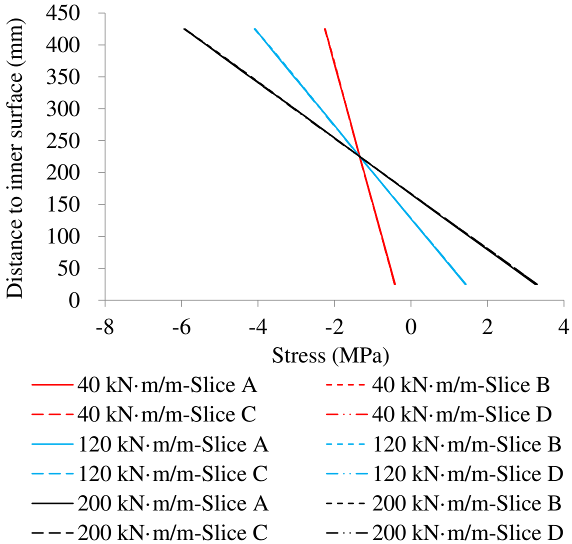

(b)

Figure 2.40 Stress distributions of the segment model at different moments: (a) stresses at Section 300, Section 500, Section 700, Section 900; (b) stresses from Slices A to D.

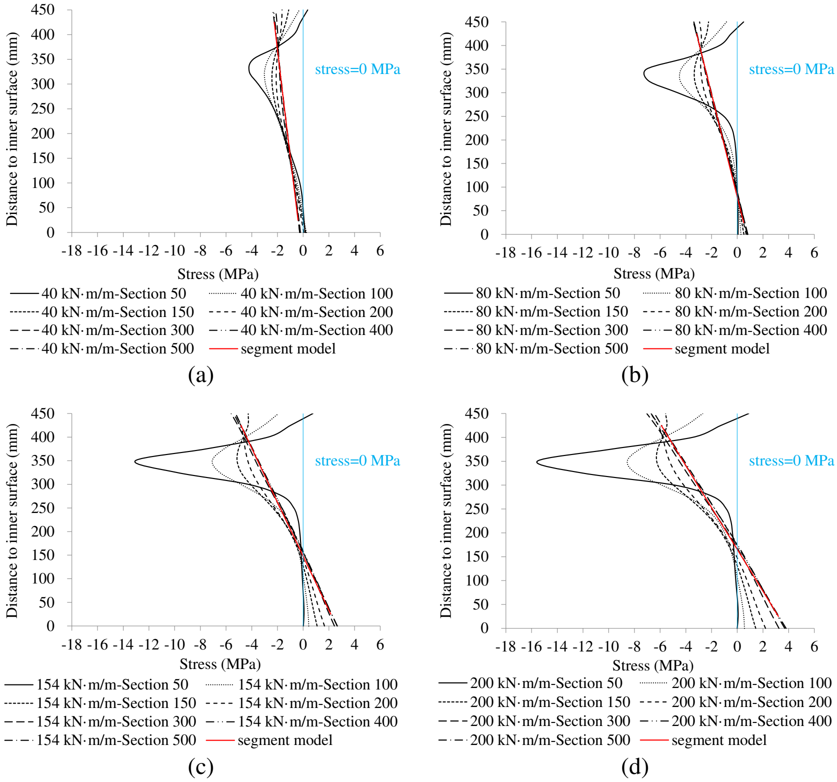

Figure 2.41 Stress distributions from Section 50 to Section 500 in the positive joint model at different bending moments: (a) stresses at 40 kN·m/m; (b) stresses at 80 kN·m/m; (c) stresses at 154 kN·m/m; (d) stresses at 200 kN·m/m.

When the bending moment equals 200 kN·m/m, the stresses of Slices A to D on Sections 200 to 500 are shown in Figure 2.42. The stresses of Slices B and C at the area close to the inner segment side are tensile, and their distributions are different from those in Slices A and D. However, this difference diminishes quickly as the distance to the joint section is beyond 300 mm. The length of the bolt installing hole is 245 mm, as shown in Figure 2.3. The DIJPs are connected with concrete by reinforcements, and these reinforcements sustain large tensile forces from bolts. This means that the existence of DIJPs and bolt installing holes result in large tensile concrete stresses around them. From Figure 2.42, it is found that the influence of the position of the joint section becomes minimal beyond 400 mm, as the stresses at Section 400 are quite similar to those from the segment model.

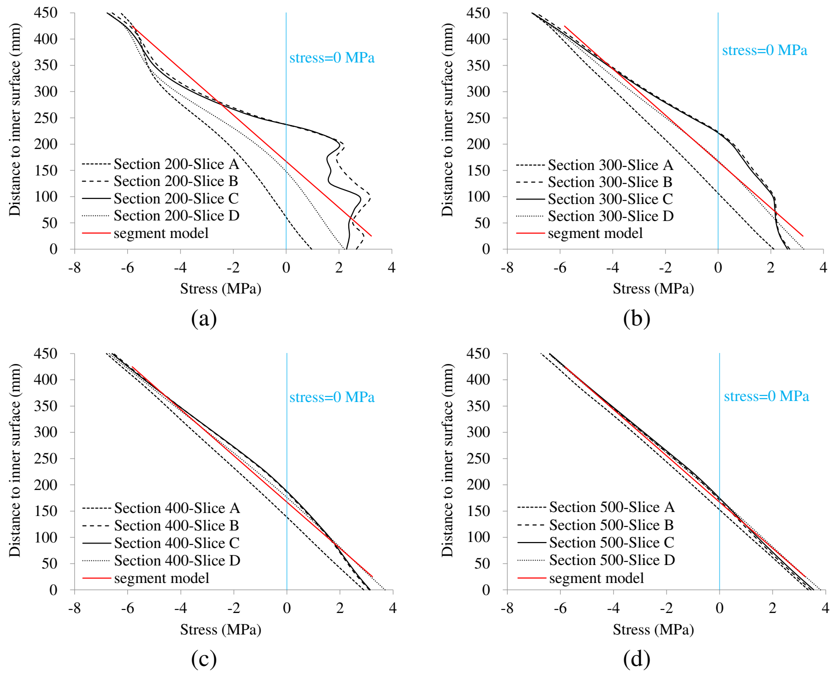

Figure 2.42 Stress distributions from different sections in the positive joint model at a bending moment of 200 kN·m/m: (a) stresses at Section 200; (b) stresses at Section 300; (c) stresses at Section 400; (d) stresses at Section 500.

For the negative cases, four bending moments (respectively 44, 80, 165 and 205 kN·m/m) are chosen to compare the stress distributions from the joint model and segment model as shown in Figure 2.43, taking the example of Slice D. When the bending moment value is 44 kN·m/m, most of the sections are under compression. For other bending moments, all the sections are under tensile conditions at the outer segment side and under compressive conditions at the inner segment side. Similar to the positive cases, the most notable stress changes happen at the area within 200 mm distance to the joint section, and considerable stress concentrations occur at the height of 50 to 100 mm, the area of the inner edge of the core section as shown in Figure 2.3. However, the maximum compressive stresses and the overall compressive situations in negative cases are larger than in positive case, which is most likely caused by the decrease of the compressive area due to the existence of the bolt installing hole.

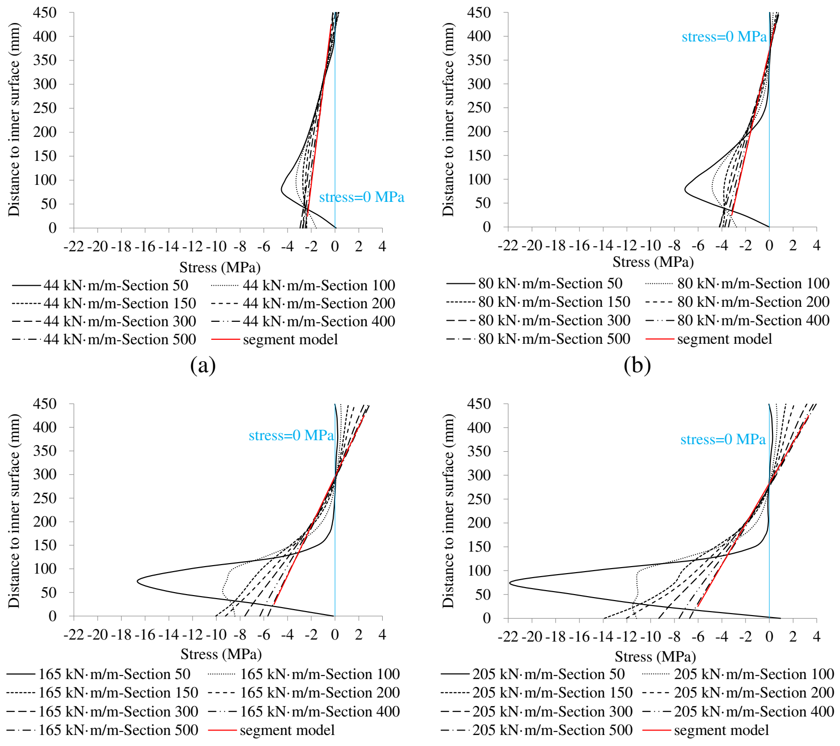

Figure 2.43 Stress distributions from Section 50 to Section 500 in the negative joint model at different bending moments: (a) stresses at 44 kN·m/m; (b) stresses at 80 kN·m/m; (c) stresses at 165 kN·m/m; (d) stresses at 205 kN·m/m.

At the bending moment of 205 kN·m/m, the stresses of Slices A to D from Sections 200 to 500 are also retrieved and presented in Figure 2.44. Compared to Slices A and D at Section 200, the stresses of Slices B and C have higher compressive stresses at the inner side and higher tensile stresses near the outer side. For the compressive area, namely the inner segment side, the DIJP takes more compression, as its stiffness is much higher than that of concrete, leading to higher compressive stresses at the neighbouring Slices B and C. Also, due to the existence of the GIJP, its connecting reinforcements sustain tension from bolts, resulting in higher tensile concrete stresses at the height of 250 mm to 300 mm. These differences between Slices B and C and Slices A and D, are noticeable within 300 mm distance to the joint section, and all the stresses become linear and showed a similar distribution to that from the segment at the section located 500 mm from the joint.

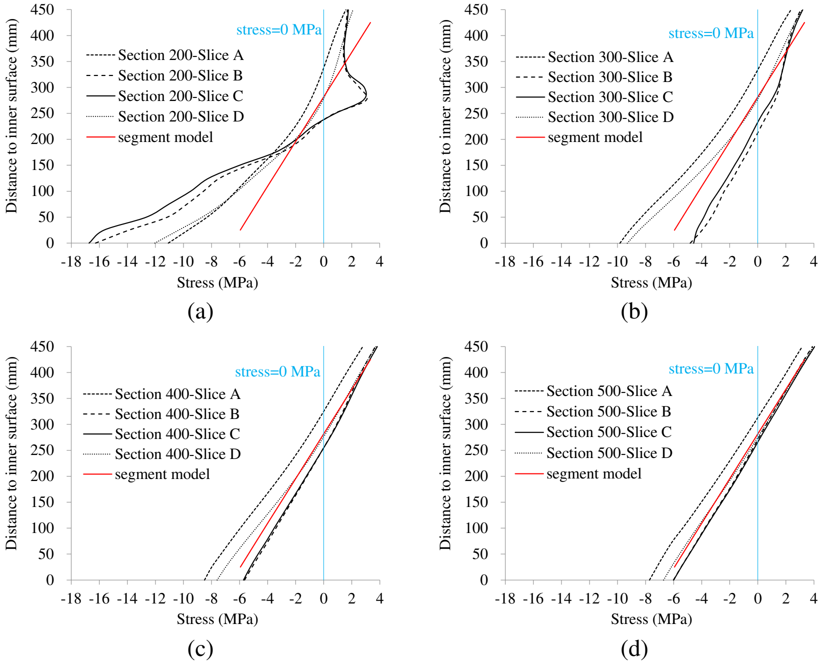

Figure 2.44 Stress distributions from different sections in the negative joint model at a bending moment of 205 kN·m/m: (a) stresses at Section 200; (b) stresses at Section 300; (c) stresses at Section 400; (d) stresses at Section 500.

It can be concluded from the previous comparative analysis that the stresses along the thickness direction change considerably in the area within a 200 mm distance to the joint section. There are notable differences between slices along the width direction of the joint segment, which means the stresses are not uniformly distributed in this direction. It is different from the assumption in the analysis of the joint without DIJPs that the stress along the segment width direction is regarded as uniform. Beyond 300 mm to the joint section, the stresses along the thickness show an overall linear distribution, and the difference between slices becomes small. In addition, for a positive bending moment case, the influenced area by the joint section is about 400 mm, while it is 500 mm for a negative case. The larger influenced area in the negative cases is likely to relate to the decrease of concrete section caused by bolt installing holes, resulting in overall higher stress distributions. On the other hand, in both positive and negative cases, as the connecting reinforcements are located around the installing hole, and they need to sustain the tensile force from bolts, the tensile stresses around the bolt installing hole are larger than in the other areas. In a negative case, the DIJP notably increases the compressive concrete stresses near the inner edge of the joint core section, due to its larger stiffness than concrete. Therefore, although DIJPs make a flexible joint layout and possible bolt position arrangement, the increased tensile stresses and the compressive stresses around DIJPs need more attention and specific stirrup reinforcement is recommended in this area to prevent potential cracks caused by the DIJPs.

2.3.3.6 Comparison with joint deflections calculated by the BSM method

The existence of longitudinal joints in a shield tunnel makes the tunnel lining discontinuous, resulting in large stress concentrations near the joint sections, as discussed in the previous section, and larger structural deformations, when compared to a continuous tunnel lining without longitudinal joints (Blom, 2002; Ye et al., 2014). Since there are several longitudinal joints in a lining ring, the effect of a single joint on the structural deformations is difficult to evaluate. Through the established joint model, the influence of the discontinuity caused by the longitudinal joint can be investigated in the studied loading scenario.

The BSM is a commonly adopted model in a shield tunnel design. In this model, the segment is regarded as a beam. For a longitudinal joint under a combined axial force and bending moment load, the joint is regarded as a hinge spring with the capacity to sustain axial forces and bending moments. The spring allows a relative rotation between the sections of the hinged segments, and the rotation values depend on the defined rotational stiffness and the exerted bending moment. The parameters related to the joint rotational behaviour usually are obtained through experiments or simulation methods. Although the idea of this imaginary spring has been accepted and is commonly used in practical designs, there is no specific background information concerning its accuracy in predicting the deformation caused by joint rotations.

$$w_M = \frac{M_{js}}{E_{sec} I_{sec}} \left(\frac{l_1^2}{2} + \frac{l_2^2}{3} + l_1 \cdot l_2 \right) \tag{2.6}$$

$$w_R = (l_1 + l_2) \cdot \theta_{js} \tag{2.7}$$

$$w_J = w_M + w_R = \frac{M_{js}}{E_{sec} I_{sec}} \cdot \left(\frac{l_1^2}{2} + \frac{l_2^2}{3} + l_1 \cdot l_2 \right) + (l_1 + l_2) \cdot \theta_{js} \tag{2.8}$$

From the perspective of the joint model, the joint deflection can be obtained directly from the model results. From the perspective of the BSM method, the joint deflection can be calculated through a classical method of structural mechanics. The joint deflection w_J consists of two parts, as shown in Figure 2.45. The first part w_M is the deflection caused by the bending moments along the segment, expressed as Eq. (2.6). The second part w_R is caused by the joint rotation given by Eq. (2.7), in which the joint rotation θ_{js} can be retrieved from the joint model.

Then the total joint deflection is found from Eq. (2.8). E_{sec} and I_{sec} are the elasticity modulus and the inertia moment of the segment section. M_{js}, l_1 and l_2 are shown in Figure 2.8.

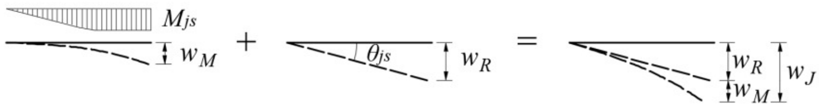

Figure 2.45 Composition of the joint deflection.

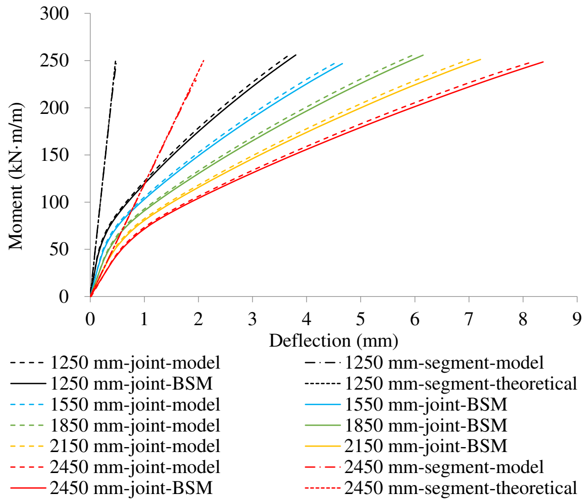

(a)

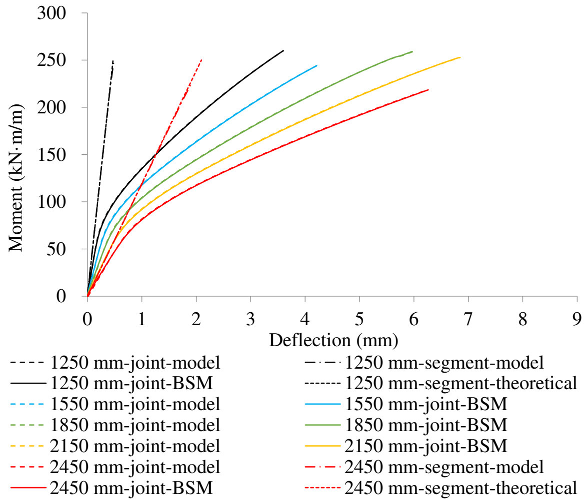

(b)

Figure 2.46 Evolution of the joint defections with different segment lengths: (a) positive cases; (b) negative cases.

For the cases with different segment lengths, the evolutions of the deflections obtained from the joint model and from the BSM method are depicted in Figure 2.46. The deflections at the joint position from the segment model and their theoretical result w_M from Eq. (2.7) are shown as “segment-model” and “segment-theoretical” in Figure 2.46 only for the 1250 mm and 2450 mm segment length cases for brevity. It is clear that they match each other very well.

For the joint deflections from the joint model and the BSM method, the results were very similar. In the positive cases, the bolts were under a large tension force, and the DIJP deformed outward the joint section surface. This makes the calculated joint rotation values slightly higher, which results in a larger deflection value. It might explain the slight deflection deviations in the positive cases. From Figure 2.46, it is clear that the joint deflection caused by the joint rotation accounts for a large proportion of the total deflection. It is a direct proof of the fact that the joint rotational characteristic is one of the critical factors for the shield tunnel lining deformations, and proper choices for the number of joints and their locations also have a significant influence. Additionally, it has to be noted that the joint rotation values in the BSM should be consistent with those from the joint model when the bending moment value increases. Only then, the BSM method can give good predictions for the joint deflections. Although the BSM method is a simplified method for full-ring calculations and is believed to give reliable deformation results, a precise description of the joint rotation behaviour is critical in the application of the BSM method. Otherwise, the BSM cannot give acceptable deformation results.

2.3.4 A polynomial function for the joint’s rotational stiffness

Considering the fact that different axial forces occur in different joints, one moment-rotation curve cannot represent the rotational behaviour of all the joints in a QRST lining. Hence a surface function of the joint’s rotational behaviour is needed. This function should include the axial force and bending moment as variables and cover different axial force and bending moment combinations.

From the verified numerical model and the previous analysis, a cubic polynomial function of bending moments M_{js} (unit: kN·m/m) and axial forces N_{js} (unit: kN/m) was derived for each stage of the joint rotation development for the Type-A and Type-B joints under both positive and negative cases, expressed as Eq. (2.9). With the equations' boundary conditions and continuity conditions, the polynomial coefficients corresponding to the best-fitting results are listed in Table 2.12 and Table 2.13.

$$\theta(M_{js}, N_{js}) = \begin{cases} a_1 M_{js}{}^3 + b_1 N_{js}{}^3 + c_1 M_{js}{}^2 N_{js} + d_1 M_{js} N_{js}{}^2 + e_1 M_{js}{}^2 + f_1 N_{js}{}^2 + g_1 M_{js} N_{js} + h_1 M_{js} + i_1 N_{js} \\ \qquad (M_{js}/N_{js} \le k_{1-2}) \\ a_2 M_{js}{}^3 + b_2 N_{js}{}^3 + c_2 M_{js}{}^2 N_{js} + d_2 M_{js} N_{js}{}^2 + e_2 M_{js}{}^2 + f_2 N_{js}{}^2 + g_2 M_{js} N_{js} + h_2 M_{js} + i_2 N_{js} \\ \qquad (k_{1-2} < M_{js}/N_{js} \le k_{2-3}) \\ a_3 M_{js}{}^3 + b_3 N_{js}{}^3 + c_3 M_{js}{}^2 N_{js} + d_3 M_{js} N_{js}{}^2 + e_3 M_{js}{}^2 + f_3 N_{js}{}^2 + g_3 M_{js} N_{js} + h_3 M_{js} + i_3 N_{js} \\ \qquad (k_{2-3} < M_{js}/N_{js}) \end{cases} \tag{2.9}$$

Table 2.12 List of coefficients and goodness of fit: positive cases.

Coefficient	Type-A			Type-BPos		
	Stage			Stage		
	1	2	3	1	2	3
a	2.37×10^{-10}	1.05×10^{-9}	3.54×10^{-10}	6.80×10^{-10}	3.36×10^{-10}	1.18×10^{-10}
b	0.00	-3.90×10^{-12}	-4.80×10^{-13}	0.00	-5.46×10^{-13}	-1.41×10^{-13}
c	-3.08×10^{-11}	-6.29×10^{-10}	-9.08×10^{-11}	-1.19×10^{-10}	-1.94×10^{-10}	-2.76×10^{-11}
d	7.54×10^{-13}	9.28×10^{-11}	8.63×10^{-12}	9.23×10^{-12}	2.41×10^{-11}	3.27×10^{-12}
e	1.22×10^{-8}	5.09×10^{-7}	3.43×10^{-9}	5.90×10^{-8}	2.23×10^{-7}	9.58×10^{-9}
f	0.00	4.72×10^{-9}	1.37×10^{-9}	0.00	8.13×10^{-10}	7.45×10^{-10}
g	-3.94×10^{-10}	-1.00×10^{-7}	-9.58×10^{-9}	-1.15×10^{-8}	-3.50×10^{-8}	-7.28×10^{-9}
h	2.08×10^{-6}	1.32×10^{-5}	4.15×10^{-5}	5.68×10^{-6}	6.74×10^{-6}	2.52×10^{-5}
i	0.00	-8.50×10^{-7}	-4.44×10^{-6}	0.00	-6.31×10^{-8}	-2.40×10^{-6}
R-square	0.999	1.00	1.00	0.999	1.00	11.00

Table 2.13 List of coefficients and goodness of fit: negative cases.

Coefficient	Type-A			Type-BNeg		
	Stage			Stage		
	1	2	3	1	2	3
a	3.65×10^{-10}	2.59×10^{-9}	1.27×10^{-9}	5.74×10^{-11}	2.86×10^{-10}	2.51×10^{-10}
b	0.00	-9.53×10^{-12}	-1.87×10^{-12}	0.00	-1.60×10^{-12}	1.48×10^{-14}
c	-8.17×10^{-11}	-1.20×10^{-9}	-3.90×10^{-10}	-1.90×10^{-11}	-1.54×10^{-10}	-3.92×10^{-11}
d	4.36×10^{-12}	1.86×10^{-10}	4.21×10^{-11}	1.11×10^{-12}	2.82×10^{-11}	4.46×10^{-13}
e	3.94×10^{-8}	4.53×10^{-7}	-2.33×10^{-7}	2.30×10^{-8}	1.68×10^{-7}	-4.72×10^{-8}
f	0.00	9.14×10^{-9}	-1.06×10^{-9}	0.00	3.01×10^{-9}	8.93×10^{-10}
g	-3.69×10^{-9}	-1.30×10^{-7}	4.51×10^{-8}	-1.77×10^{-9}	-4.61×10^{-8}	2.21×10^{-9}
h	2.58×10^{-6}	2.35×10^{-5}	6.01×10^{-5}	2.06×10^{-6}	1.29×10^{-5}	2.91×10^{-5}
i	0.00	-2.47×10^{-6}	-8.52×10^{-6}	0.00	-1.10×10^{-6}	-3.78×10^{-6}
R-square	0.998	1.00	1.00	0.998	1.00	1.00

The proposed cubic polynomial functions fit the rotations well, and a comparison of the joint rotations between the proposed joint model and fitting results is shown in Figure 2.47. Their differences are shown in Figure 2.48. Combined with Eq. (2.9), the joint's rotational stiffness k_{lm} under a bending moment M_{js} and an axial force N_{js}, as shown in Figure 2.49, can be determined by Eq. (2.10).

$$K_{lm}\left(M_{js}, N_{js}\right) = \frac{M_{js}}{\theta\left(M_{js}, N_{js}\right)} \tag{2.10}$$

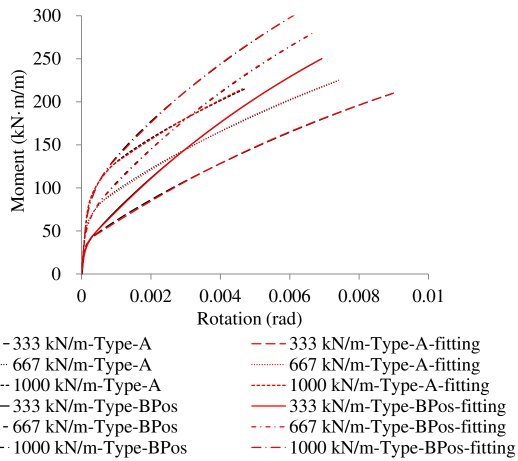

(a)

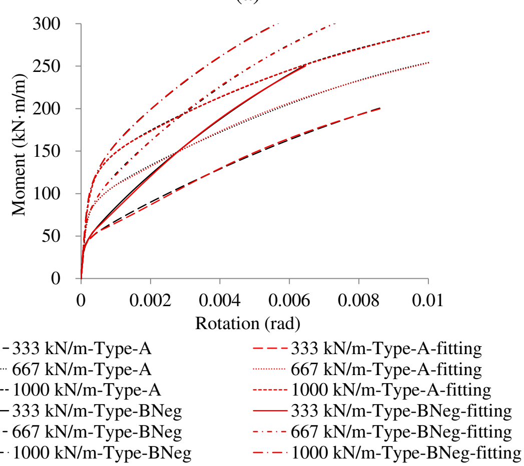

(b)

Figure 2.47 Comparison of the joint rotations between the proposed joint model and fitting results: (a) positive cases; (b) negative cases.

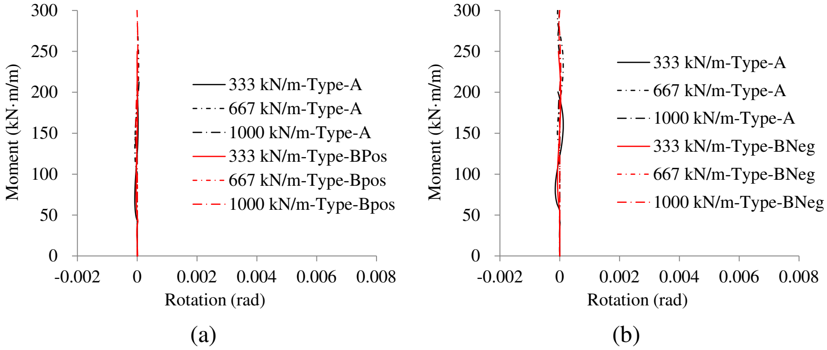

Figure 2.48 Differences of the joint rotations between the proposed joint model and fitting results: (a) positive cases; (b) negative cases.

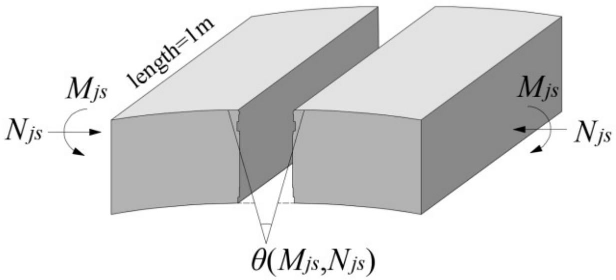

Figure 2.49 Illustration of the joint rotation under a combined bending moment and axial force.

These functions are expected to be used as an input in the full-ring structural calculation of QRSTs to describe the joint's rotational behaviour. Although these functions and coefficients are related to the specific geometry of the QRST under consideration, a precise depiction of the joint's behaviour is important for investigating the mechanical performance of QRSTs and the influence of the joint's moment-axial force interaction behaviour on a full-ring calculation.

2.4 Summary and conclusions

For the longitudinal joints with DIJPs used in QRSTs, joint tests and FEM simulations were conducted to investigate the joint behaviour before and after the bolt position improvements. The joint model provides an efficient approach for exploring the influence of the internal forces in the joint's vicinity. A parametric analysis is conducted to detect other possible improvement methods for the joint design, including increasing the concrete strength class, enhancing the bolt elongation resistance, and changing the joint details. In addition, the area influenced by the existence of the longitudinal joint section is analysed, and a comparison with the BSM method for joint deflection calculation is conducted. The following conclusions can be drawn:

(1) The failure of the joints is initiated by concrete cracking at the core section and is terminated by concrete crushing. The bolts only yield after concrete crushing. The failure mode of the joint type is similar to that of a column cross-section subjected to a normal force with small eccentricity. The joint's resistance to cracking and the ultimate bearing capacity are both enhanced after bolt position improvements. Additionally, during the damage process, the connecting reinforcements between DIJPs and concrete can guarantee the DIJPs' anchorage in the concrete, and the components of the DIJPs and their connections in this new joint type are proven to be reliable. The joint with DIJPs has an acceptable safety factor in the practical use and shows good performance within the moment range at the normal service level. The studied joint pattern is expected to be qualified to be applied in QRSTs.

(2) For a given axial force, the joint stiffness changes with increasing bending moments and its behaviour can be divided into three stages. At the first stage, the whole joint core section is under compression, and bolts do not contribute to the rotation resistance. The joint behaviour is governed by the structural details of the core section. At the second stage, the bolts start being tensioned. The bolt stress increases fairly quickly while the rotational stiffness decreases gradually. At the third stage, the lever arm exceeds the distance from the edge of the outer section to the joint central axis. The evolutions of the joint rotation and the bolt stress appear to be almost linear.

(3) Although an increase of the concrete strength class or the bolt elongation resistance has a positive influence on the joint rotation, a change of the joint section to increase the lever arm between the bolts and the compression zone can improve the joint behaviour the most effectively, resulting in a decrease of the bolt stresses, as well as an increase of the joint rotation stiffness and the joint bearing capacity. This improvement direction should be preferably considered when designing a joint section, and it can be achieved through bolt repositioning or increasing the joint's core section height based on the practical applicability.

(4) The stresses along the thickness direction change considerably in the area within a 200 mm distance to the joint section. There are notable differences between slices along the width direction of the joint segment, which means the stresses are non-uniformly distributed in the segment width direction, which is different from the assumption in the analysis of the joint without DIJPs that the stress along this direction is regarded as being uniform. Beyond 300 mm to the

joint section, the stresses along the thickness show an overall linear distribution. In the positive bending moment case, the area influenced by the joint section is about 400 mm. In the negative bending moment case, the decrease of the concrete section caused by bolt installing holes results in an overall higher stress distribution and a larger influenced area of 500 mm. In addition, although the use of DIJPs makes a flexible joint layout and bolt position arrangement possible, the increased tensile stresses and compressive stress concentrations around DIJPs and bolt installing holes need more attention, and specific stirrup reinforcement is recommended in this area.

(5) The joint deflection caused by the joint rotation accounts for a large proportion of the total deflection, which is direct proof that the joint rotational characteristic is one of the critical factors for shield tunnel lining deformations. A precise description of the joint rotation behaviour is critical in the BSM method. Only then, the BSM method can give good predictions for joint deflections.

(6) A cubic polynomial function is proposed to describe the joint rotation development at each stage for the Type-A and Type-B joints under positive and negative cases. The fitting results show a good consistency with the rotations from the joint model, and the proposed functions will serve as an input in the full-ring structural calculation of QRSTs to define the joint's rotational behaviour.

Chapter 3

Shear-resistance behaviour of longitudinal joints

3.1 General introduction

The large shear force at the joint section is a critical characteristic for a non-circular shield tunnel. Ding et al. (2020) have compared a non-circular tunnel to a circular one with an equivalent cross-section area and similar depths in soft soils and found that the radial shear force at the longitudinal joints was about six times that in the circular tunnel, while the axial forces were almost at the same level. The previous studies for the joint's behaviour under a shear force (Guo et al., 2011; Yan et al., 2011; Zhu et al., 2017) mainly focused on the failure characteristics and the damage processes of the joints. However, the joint's shear resistance behaviour at the normal service level did not draw enough attention. For a QRST, the shear force in the joint is large and the resulting dislocating deformations cannot be neglected. In addition, a proper stiffness value for the joint type in QRSTs is necessary. Therefore, in this chapter, shear resistance experiments of the longitudinal joints in QRSTs were carried out within the possible combinations of shear and axial force under normal service conditions. Firstly, the test setup is introduced, and then the joint dislocations and bolt strains from the tests are presented and analysed. Finally, a linear fitting function is generated to define the shear stiffness in the studied range.

3.2 Shear resistance experiment

3.2.1 Test setup

Full-scale experiments of the longitudinal joints used in QRSTs were carried out at the State Key Laboratory of Disaster Reduction in Civil Engineering at Tongji University in 2015 to investigate the longitudinal joint's shear resistance behaviour under different axial forces, as shown in Figure 3.1 and Figure 3.2. A tested specimen was composed of three segments. The middle segment (Segment-2) had the bolt installing holes at both ends of the segment. Its length, width and height were 1250, 1200 and 450 mm respectively. The other two segments (Segment-1 and Segment-3) were only half of this length, namely 625 mm, and had the bolt installing holes at one end only. After assembly, the specimen's ends were clamped by steel loading supports, and a set of horizontal jacks on the right side exerted axial forces, as shown in Figure 3.2. Under the specimen, two bottom steel rollers resisted the vertical reaction forces for balancing the force from the vertical jack and the segments' dead loads. The vertical jacks produced shear forces at the two joints through a set of distribution beams. The maximum capacities of the vertical and horizontal jacks were 1000 kN. The bolt strain values from the shear resistance tests are very small, and the main difference between Type-A and Type-B joints is only the bolt position. In addition, the full-ring experiments in the following sections are also based on the segments with Type-A joint. Therefore, only the Type-A joint introduced in the last chapter is used for the shear resistance tests. The influence of the shear stiffness will be investigated through a parameter study in the full ring calculations.

Figure 3.1 Front view of the shear resistance experiment.

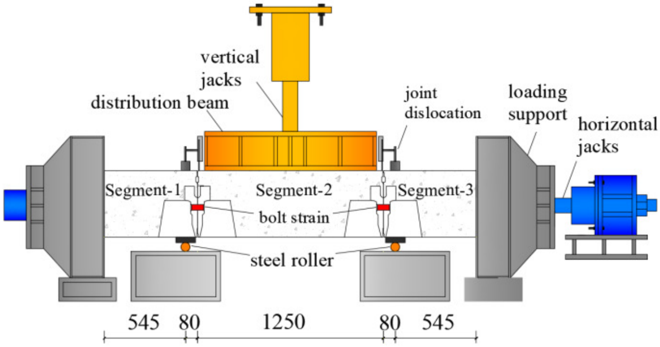

Figure 3.2 Test set-up and layout of the measurement points for joint dislocations, and bolt strains (unit: mm).

The experimental load cases were divided into two categories, outward shear resistance tests and inward shear resistance tests. The outward shear resistance tests related to a vertical load P_{jv} applied from the inner segment side creating an outward movement of Segment-2. The inward shear resistance test related to a vertical load P_{jc} applied from the outer segment side creating an inward movement of Segment-2, as shown in Figure 3.3.

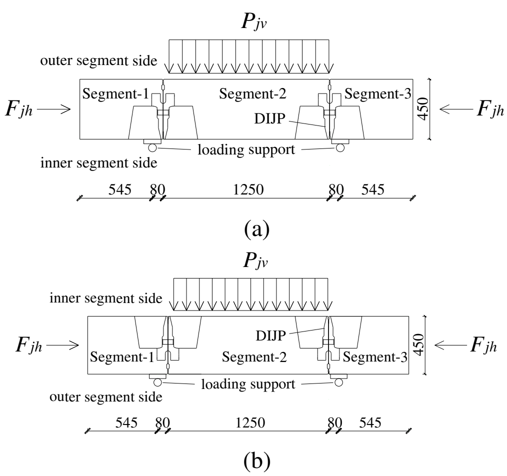

Figure 3.3 Exerted loads in the shear resistance tests: (a) outward shear tests; (b) inward shear tests (unit: mm).

The force diagram of the specimen in the shear tests is shown in Figure 3.4, and the shear force along Segment-2 changes linearly. The force diagram for Segment-3 is shown in Figure 3.4b. Herein, P_{jc} is the reaction force at the vertical supports, equal to the sum of the vertical load P_{jv} and the dead load G_{js}, which can be calculated through Eq.(3.1). l_1 and l_2 represent the distance from the joint to the reaction force P_{jc} and the distance from the reaction force P_{jc} to the centre of gravity of each segment. In order to decrease the bending moment value at the joint section, the axial force is slightly below the central axis of the specimen rather than exactly exerted along it, and h_{est} represents this offset distance. The internal forces at the joint can be calculated through Eq.(3.2). Combined with Eq.(3.1), the axial force N_{js}, shear force Q_{js} and bending moment M_{js} at the joint can be determined by the vertical loads P_{jv} and horizontal loads F_{jh} through Eq.(3.3). The horizontal loads F_{jh} and vertical loads P_{jv} can be adjusted to make the internal forces at the joints equal to the target values.

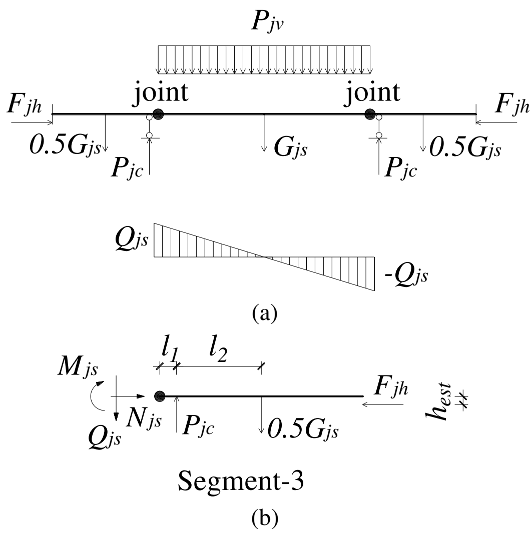

Figure 3.4 Force diagram for the shear resistance tests: (a) exerted forces on the specimen; (b) load analysis of Segment-3.

$$P_{jc} = 0.5 \cdot P_{jv} + G_{js} \tag{3.1}$$

$$\begin{cases} N_{js} = F_{jh} \\ Q_{js} = P_{jc} - 0.5 \cdot G_{js} \\ M_{js} = P_{jc} \cdot l_1 - 0.5 \cdot G_{js} \cdot (l_1 + l_2) - F_{jh} \cdot h_{est} \end{cases} \tag{3.2}$$

$$\begin{cases} N_{js} = F_{jh} \\ Q_{js} = 0.5 \cdot \left(P_{jv} + G_{js}\right) \\ M_{js} = Q_{js} \cdot l_1 - 0.5 \cdot G_{js} \cdot l_2 - F_{jh} \cdot h_{est} \end{cases} \tag{3.3}$$

3.2.2 Loading procedure

From the MRM method's calculation results, the range of axial forces at the joint sections was from 500 to 833 kN/m (600 to 1000 kN before the segment width normalization). It was noticed that the ratios between the shear forces and corresponding axial forces were less than 0.5, and most of these ratios were less than 0.3. Based on the pre-calculation results, five loading cases with different constant axial forces were designed for the shear resistance tests. In each case, the horizontal loads F_{jh} were increased first to make the axial force to attain a target value and then were kept constant. Then, the vertical load P_{jv} started to increase to investigate the effect of the shear force under a given axial force. In the inward shear tests, the ratios between the shear forces and axial forces were designed within 0.3, while those in the outward shear tests were controlled within 0.5. The target axial forces were 500, 583, 667, 750, 833 kN/m in each loading case, and the corresponding designed shear forces are summarized in Table 3.1. In addition, the previous research (Tassios and Vintzēleou, 1987; Buyukozturk et al., 1990; Jiang et al., 2015; Kassem et al., 2017) conducted shear resistance tests for the friction between compressed concrete surfaces and used normal stresses to represent the compression level on the contact surface, namely the axial force in this thesis. The height of the joint's compressed area in the tests equals that of the core section, 292 mm as shown in Figure 2.3. The average normal stress at the joint section is calculated by dividing the corresponding axial force by the area of the core section and they are added in Table 3.1.

Table 3.1 Summary of the loads in shear resistance tests.

Axial force (kN/m)	Normal stress (MPa)	Inward shear test (kN/m)	Outward shear test (kN/m)
500	1.71	150	250
583	2.00	175	292
667	2.28	200	333
775	2.57	225	375
833	2.85	250	417

In order to decrease the bending moments at the joints produced by the shear force and the horizontal load, the steel rollers were located very close to the joints in the horizontal direction and an offset distance h_{est} was arranged between the horizontal load F_{jh} and the specimen's central axis. In the tests, the lengths of l_1, l_2 and h_{est} in Figure 3.4 were set as 80, 232.5 and 20 mm, respectively, from which the bending moment value during the test can be evaluated. Taking the example of the outward shear tests where larger shear force ranges were exerted, the shear force and bending moment in each case are shown in Figure 3.5. It was found that the bending moment range was from -20 to 15 kN·m/m. Although the bending moment at the joint is unavoidable when the shear force Q_{js} changes, its value can be controlled to be very small in the tests. The influence of the bending moment at the joint section will be neglected in the following analyses of the shear resistance tests.

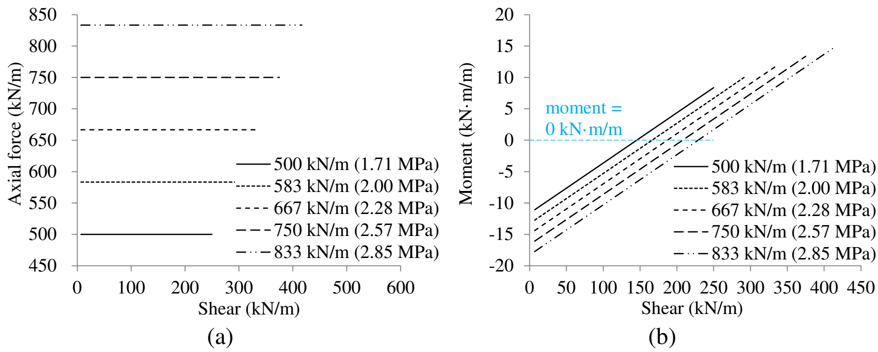

Figure 3.5 Designed internal forces at the joint section in outward cases: (a) axial force and shear force; (b) bending moment and shear force.

3.2.3 Measurement layout

The joint dislocations produced by the shear forces and the bolt strains were measured during the tests. The positions and numbers of the measurement points are shown in Figure 3.2 and Table 3.2.

Table 3.2 List of measurement points of joint's shear resistance tests.

Type	Quantity	Range	Accuracy
Joint dislocation	8	0–100 mm	0.05 mm
Bolt strain	4	0–10,000 με	1 με

3.2.4 Results

Considering the measurement accuracy and the influence of the bending moment when the shear value is small, only the results after 65 kN/m are presented to compare the developments of the joint dislocations under different axial forces.

3.2.4.1 Joint dislocations

The evolution of the obtained joint dislocations from the shear resistance tests are compared in Figure 3.6. As the maximum shear forces were different in the outward and inward cases, the results in the same shear range from 65 to 240 kN/m are shown in more detail. The slope of the dislocation curve is related to the joint shear stiffness, which represents the joint's resistance to the dislocation caused by a given shear force. In both kinds of tests, although there are fluctuations, the joint dislocation generally linearly increases with growing shear force. For the cases with the same axial force, the dislocation values from outward and inward tests are similar to each other. On the other hand, it can be found that the slopes of the dislocation curves are increasing when the axial forces increase. This means that the shear resistance varies with the exerted axial forces at the joint section, and a larger axial force value can help the joint sustain a given shear force with a smaller joint dislocation value.

The required joint dislocation control is 5 mm for the lining construction and 10 mm for the inspections of tunnel acceptance from Code for Construction and Acceptance of Shield Tunnelling method [GB50446] (2017). These permissible values consider the requirement of water sealing performance, the tolerance of segment erections and the influence of possible settlements. The obtained dislocations from the tests are less than 1.2 mm. Although the shear forces in QRSTs are larger than in conventional circular shield tunnels, it is proven that the joint dislocation caused by shear force only accounts for a small proportion of the dislocating requirement and thus will not notably aggravate the dislocation beyond the requirement.

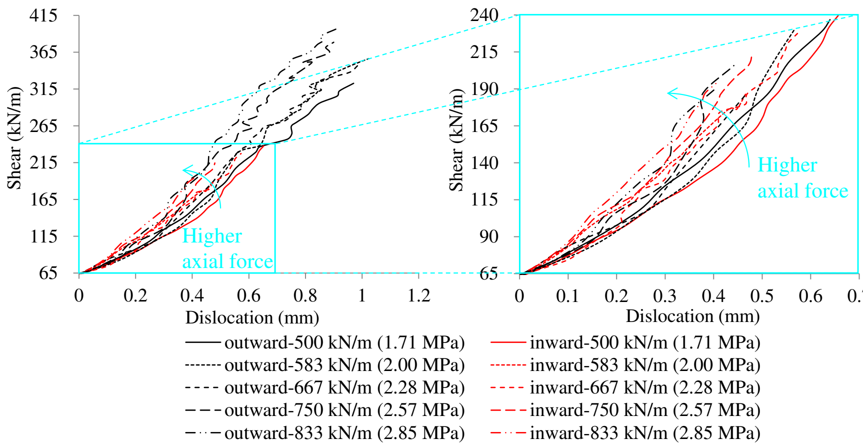

Figure 3.6 Evolution of the joint dislocation with increasing shear force (range from 65 to 415 kN/m and range from 65 to 240 kN/m).

3.2.4.2 Bolt strains

The evolution of the measured bolt strains from the shear resistance tests are compared in Figure 3.7. The results in the shear range from 65 to 240 kN/m are also shown in more detail. Although some strain fluctuations occurred during the tests, the absolute value of the strains were always less than 50 με. For the longitudinal joints in QRSTs, the bolts’ clearance hole is 37 mm while the bolt diameter is 33 mm. The bolt strain measurement point is at the middle of the bolt shank, which is the same as in the moment resistance tests. The strain values are randomly positive and negative in the shear resistance tests, rather than uniformly positive in the tensile condition of the moment resistance tests. 50 με strain value means 10 MPa stress in the bolt, which is small when compared with the yield stress of 480 MPa. So these small fluctuations are regarded as not being caused by the bolt stress increase during the tests. In addition, the bolts' possible dowel action is not considered in the analysis of the shear resistance tests.

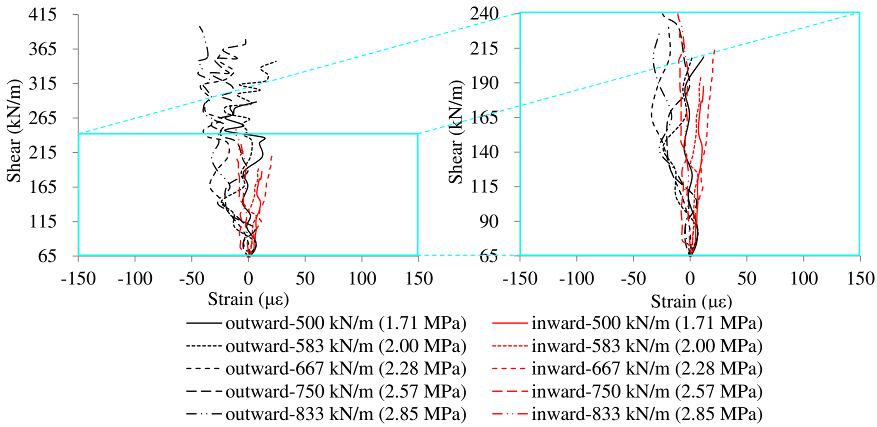

Figure 3.7 Evolution of the bolt strain with increasing shear force (range from 65 to 415 and range from 65 to 240 kN/m).

3.2.5 Analytical formulation of the joint's shear stiffness

The shear stiffness can be calculated by dividing the shear force at the joint by the joint dislocation value. The shear stiffness from outward and inward shear resistance tests are summarized in Table 3.3 and shown in Figure 3.8. As the shear force unit is kN/m, which represents the shear force on 1 m length of the segment, the unit of shear stiffness is expressed in kN/m^2.

Table 3.3 Summary of shear stiffnesses

Axial force (kN/m)	Normal stress (MPa)	Shear stiffness ($10^3 \times$ kN/m^2)	
		Outward shear tests	Inward shear test
500	1.71	289	277
583	2.00	307	305
667	2.28	319	330
750	2.57	345	338
833	2.85	375	363

For the longitudinal joint's geometry in the QRSTs, the shear stiffness values from outward and inward tests are similar, and the range of the stiffness values is from 270,000 to 380,000 kN/m^2 with the related testing conditions. Previous research (Tassios and Vintzēleou, 1987; Buyukozturk et al., 1990; Jiang et al., 2015; Kassem et al., 2017) has shown that the shear stiffness between concrete surfaces increases with the exerted normal stress before considerable slippage happens. In this study, generally, the stiffness values linearly increase with growing axial force or exerted normal force. For a shield tunnel, the longitudinal joint section is identical in every segmental ring, and axial forces can be directly derived from the currently used MRM and BSM methods for designers. Hence the axial force is adopted to propose a linear fitting to match the evolution of the shear stiffness. After fitting, the function of shear stiffness is expressed as Eq.(3.4). Herein N_{js} (kN/m) is the axial force at the longitudinal joint, and K_{ls} (unit: 10^3 kN/m^2) is the shear stiffness. The fitting aims at the targeted axial force range from 500 to 833 kN/m for the overburdens from 7 to 17 m, and is expected to offer stiffness values for the longitudinal joints within this axial force range. For the axial force beyond this, more studies or tests should be conducted to decide the stiffness values. It has to be noted that the constant of 158.67 in Eq.(3.4) might be caused by the prestressed joint's bolts when the test specimen is assembled, and this constant does not stand for the shear stiffness when the axial force is zero. Combined with Eq.(3.4), for a joint under a given axial force N_{js} (unit: kN/m), as shown in Figure 3.9, Eq. (3.5) can be used to calculate the dislocation $u(Q_{js}, N_{js})$ (unit: mm), as a function of the shear force Q_{js} (unit: kN/m), and the shear-dislocation curve will be used as input to the full-ring calculation model to describe the longitudinal joints' shear behaviour.

It has to be stressed that shear resistance tests ignored the joint's bending moments. For an actual situation of the longitudinal joints in a shield tunnel, axial forces, bending moments and shear forces exist at the same time. These three forces vary and have many possible combinations, resulting in complicated testing setup and mechanical analysis. As discussed in the last chapter, the joint rotates with an increasing bending moment, and the joint's compressed area changes simultaneously. This may have an influence on the joint's shear behaviour. In this research, the joint's flexible and shear behaviours are considered individually. Up to now, there are few studies focusing on their interactions, and this aspect will be investigated in the future.

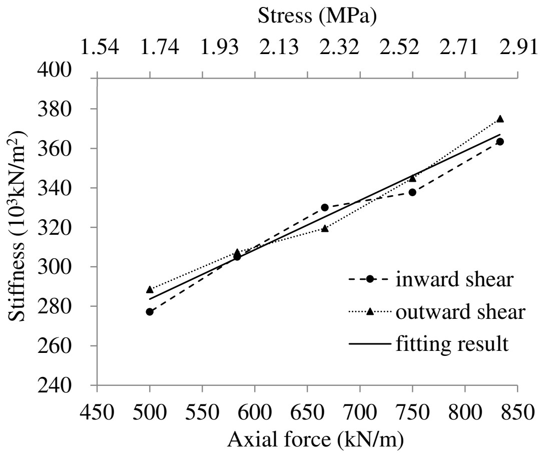

Figure 3.8 Relationship between shear stiffness and axial force.

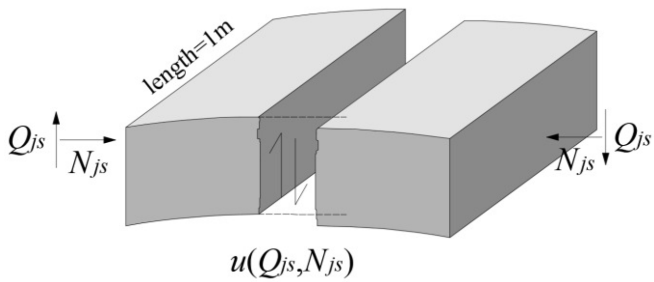

Figure 3.9 Illustration of the joint dislocation under a combined shear and axial force.

$$K_{ls}(N_{js}) = 0.25N_{js} + 158.67 \tag{3.4}$$

$$u(Q_{js}, N_{js}) = \frac{Q_{js}}{K_{ls}(N_{js})} = \frac{Q_{js}}{0.25N_{js} + 158.67} \tag{3.5}$$

As shown in Figure 2.3, the longitudinal joint's section is divided into three parts: outer section, core section and inner section. The core section has a relatively convex surface at the joint section. The type of longitudinal bolt (connecting the circumferential joints) in QRSTs is an inclined spear bolt, as shown in Figure 2.1b. The clearance hole is 36 mm, and the longitudinal bolt has a diameter of 30 mm. The structural details of the circumferential and longitudinal joints in QRSTs are very similar, as shown in Figure 3.10, and the heights of the core sections of the longitudinal joint and the circumferential joint are both equal to 292 mm. Considering the bolts' action is neglected in the current analysis for the shear behaviour, Eq.(3.4) and Eq. (3.5) are also expected to be applicable as a reference to estimate the shear stiffness of the circumferential joints in the following chapters. It is worth noting that the axial force in longitudinal joints in Eq.(3.4) and Eq. (3.5) needs to be replaced by the compressive force in the circumferential joints.

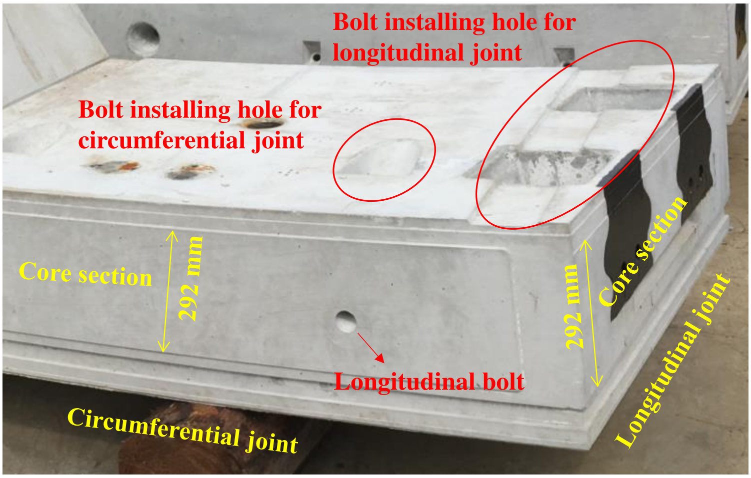

Figure 3.10 Circumferential joint and Longitudinal joint in QRSTs

3.3 Summary

With the focus on the normal service conditions, the outward and inward shear resistance experiments were carried out to investigate the shear behaviour of the longitudinal joints in QRSTs under a combination of shear and axial force. Although the shear forces in QRSTs are larger than in conventional circular shield tunnels, it follows that the joint dislocation caused by the shear force only accounts for a small proportion of the dislocating requirement and thus will not notably aggravate the dislocation beyond the requirement.

Within the axial force range from 500 to 883 kN/m, the stiffness values change from 270,000 to 380,000 kN/m^2, and show an overall linear evolution as the axial force increases. The evolution of the shear stiffness is described by a linear function for the targeted axial force range. On the other hand, as the bolts' action is regarded as having little influence on the current analysis of the joint's shear behaviour, and the section details of the circumferential joints and longitudinal joints in the QRSTs are pretty similar, the obtained experimental results are expected to define the shear resistance behaviour for both longitudinal and circumferential joints in the full-ring calculation model.

Chapter 4

Establishment and verification of a numerical model for QRST linings

4.1 Introduction

The BSM method with constant rotational stiffness is a practical tool for the prediction of the general deformations and bending moments in circular tunnel linings (I.T.A., 2000; Lee et al., 2001; Ding et al., 2004). However, in reality, the rotational stiffness of a segmental joint is not constant, due to nonlinear deformations and local yielding in the vicinity of the joint. These are a result of the specific geometry at the joint, which is related to water-tightness measures and buildability issues (Ye et al., 2014; Li et al., 2015a; Majdi et al., 2016; Jin et al., 2017). For QRSTs, this nonlinearity should not be neglected, as the bending component in the lining is significantly larger compared to circular linings. To date, there are only few studies that have investigated a calculation method for consideration of the joint's nonlinear moment-axial force and shear-axial force interaction behaviour and its consequences on the calculated lining behaviour. In this chapter, an iterative BSM for the prediction of lining deformations and bending moments in a QRST is proposed to tackle this issue, based on rotational stiffness curves derived from 3D FEM of the joints (Chapter 2), and shear stiffnesses substantiated by testing (Chapter 3). The predictions for the lining's performance are validated against unique full ring test results. The relevance of the presented method, compared to a constant joint stiffness approach, is demonstrated. Finally, a parametric study to detect the sensitive parameters for QRSTs is presented.

4.2 Model establishment

4.2.1 General Concept

As mentioned previously, the MRM and BSM methods are the most commonly used calculation methods for shield tunnels in practice. Unfortunately, the MRM method requires a number of empirical parameters, which have to be determined by experience. Moreover, this method does not allow for the precise calculation of the actual distribution of the bending moments (Lee et al., 2001; Koyama, 2003; Hu et al., 2009). Since the BSM method seems the most promising approach, its applicability in special-section shield tunnels is investigated in this chapter.

The segments and columns are simplified as beam elements, with areas and moments of inertia determined according to their specific size and amount of reinforcement. In the current work, the engineering simulation software Ansys is adopted. 960 beam elements have been adopted for the segments in a lining ring. Both rotational and radial shear springs are considered in longitudinal joints and column joints (connecting segments T1 and T2 with the interior column), as shown in Figure 4.1. Additionally, the concept of a rigid zone is adopted in the model, which will be introduced in Section 4.2.3. The established BSM will be verified through an indoor full-scale lining experiment, and finally the mechanical behaviour of a QRST lining can be evaluated with this model.

As the tunnel construction adopts a staggered assembly, with alternating linings of Pattern A and Pattern B, in order to investigate the interaction from neighbouring linings, two more half rings can be added to make a calculation model containing three rings: a front half ring (Pattern B), a middle full ring (Pattern A) and a back half ring (Pattern B), as shown in Figure 4.1. In this way, the effect of neighbouring lining structures is simulated with a minimum length for this kind of staggered assembly. The radial and tangential shear springs are set in the circumferential joints. It has to be noted that the circumferential joints' stiffness needs to be given a value only when it is necessary to consider the effects of the interaction from neighbouring rings.

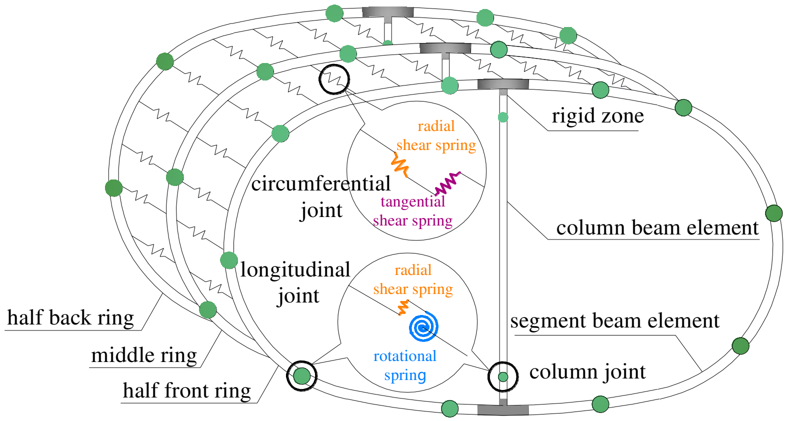

Figure 4.1 Beam-spring model of the QRST linings.

4.2.2 Spring Elements

Accurate prediction of joint deformations is important, as it influences the overall structural deformations and consequently the overall internal forces to a great extent. Controlling the structural deformations is an essential performance assessment index, which often governs the thickness of the lining structure.

Traditionally, in the BSM method, the spring element is given a fixed stiffness value, or given a fixed positive and negative stiffness value for all joints. However, the joint's rotational stiffness value varies under different combinations of bending moments and axial forces, and additionally, the joint's shear stiffness value is also affected by the acting compressive stresses.

The spring used in this paper is a unidirectional element, with a nonlinear generalized force-displacement capability. It has longitudinal and torsional functions in three degrees of freedom. The longitudinal capability is a uniaxial tension-compression function and the torsional capability is a purely rotational function. In a state of plain strain, this spring element consists of a pair of nodes, which are at the same spatial position, as shown in Figure 4.2. Each node has three degrees of freedom, i.e., two translational modes and one rotational mode, all in plane. K_θ, K_n and K_s, respectively, represent the rotational, tangential and radial stiffness. In the current case, a rotational spring and a translational spring are considered in the longitudinal joints and two translational springs in different directions in the circumferential joints. Obviously, a coordinate transformation of the spring elements needs to be taken into account.

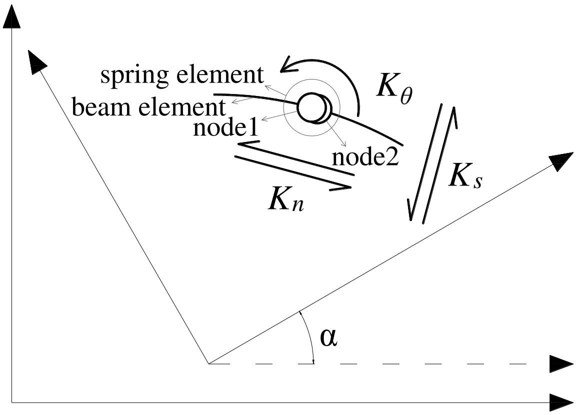

Figure 4.2 Illustration of a general spring element.

The related joint stiffnesses have been analysed in Chapters 2 and 3. The rotational stiffness and shear stiffness values can obtained through Eq. (2.10) and Eq. (3.4). For the column joints, the core section height is 338 mm while these of the segmental and circumferential joints are 292 mm due to the existence of the waterproofing grooves, as shown in Figure 2.3 and Figure 3.10. As the rotational stiffness is proportional to the third power of the section height, the column joints' rotational stiffness is evaluated from Eq. (2.10) and a magnification of $(338/292)^3 = 1.55$ is obtained. The shear stiffness is related to the compressive stress, and the column joints' shear stiffness is determined by Eq. (3.4) and a magnification of $292/338 = 0.86$ is obtained The specific study for the column joints is not conducted considering the fact that the model results are insensitive to the column joints' parameter as shown in Section 4.7.

4.2.3 Rigid Zones

The T-shaped segments (T1 and T2 in Figure 2) have a transition function to connect the segments with the interior column, which does not exist in circular tunnels. A proper method to consider the mechanical properties of this connecting area is needed, similar to the calculation of a column and beam joint in frame structure buildings. As such, a concept of rigid connection is introduced into the QRST model and its effects will be discussed later. Based on the Chinese Technical Specification for Concrete Structure of Tall Building [JGJ3-2010] (2010), an illustration of the rigid zone is shown in Figure 4.3 and its size can be determined through Eq. (4.1) to Eq. (4.3). Herein, b_c is the average thickness of the haunch (the top and bottom thicknesses of the haunch are 850 and 350 mm, then b_c equals 600 mm) and h_b is the thickness of the segment (450 mm). Two rigid zones are introduced at the upper and lower T-shaped segments with the following characteristics.

$$l_{h1} = 0.5b_c - 0.25h_b \tag{4.1}$$

$$l_{h2} = 0.5b_c - 0.25h_b \tag{4.2}$$

$$l_{c1} = 0.5h_b - 0.25b_c \tag{4.3}$$

This results in $l_{h1} = l_{h2} = 187.5$ mm and $l_{c1} = 75$ mm.

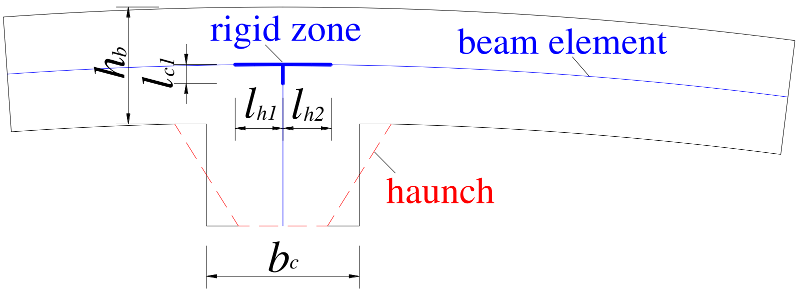

Figure 4.3 Illustration of the characteristics of the rigid zone.

4.2.4 Full-Ring Model Calculation

In the full-ring model, rotational stiffness and radial shear stiffness are considered for the longitudinal joints while radial shear stiffness and tangential shear stiffness are considered for the circumferential joints. The stiffness matrix is $K = [K_{lm}, K_{ls}, K_{ct}, K_{cr}]$ with $K_{lm} = [K_{lm1}, K_{lm2}, \cdots, K_{lm12}]$ representing the rotational stiffness matrix of the moment-rotation curves of the longitudinal joints JF1 to JF12, $K_{ls} = [K_{ls1}, K_{ls2}, \cdots, K_{ls12}]$ representing the radial shear stiffness matrix for the longitudinal joints JF1 to JF12, $K_{cn} = [K_{cn1}, K_{cn2}, \cdots, K_{cnn}]$ representing the tangential shear stiffness matrix of the circumferential joints, $K_{cs} = [K_{cs1}, K_{cs2}, \cdots, K_{csn}]$ representing the radial shear stiffness matrix of the circumferential joints. The number of springs in the circumferential joints can be defined as needed. The positions of the joints (JF), key sections (JM) and key deformation points (ends of line segments D) for the structure are shown in Figure 4.4.

The key sections, except for JM11, are the sections with a relatively large bending moment, which will be decisive for the reinforcement area in the corresponding segments. JM11 experiences a large axial force rather than bending moment and is selected as a key section to represent the stress condition in the interior column. The key deformation points are used to calculate the structural convergence deformation. This convergence deformation is the relative deformation of a pair of specific measurement points. For circular or quasi-rectangular tunnels, the measurement points are usually selected at the ends of the axes crossing the centre of the circular section horizontally and vertically. Positive values correspond to outward deformations, while negative values correspond to inward deformations. According to the Chinese Code for Design of Metro [GB50157] (2013), this convergence deformation should be maximum 3‰ of the corresponding axis length. This means that the deformations of D1, D2 and D3 should be maximum 3‰ of the lengths of D1, D2 and D3, respectively. The coordinate positions of the 11 key sections in Figure 4.4 are summarized in Table 4.1.

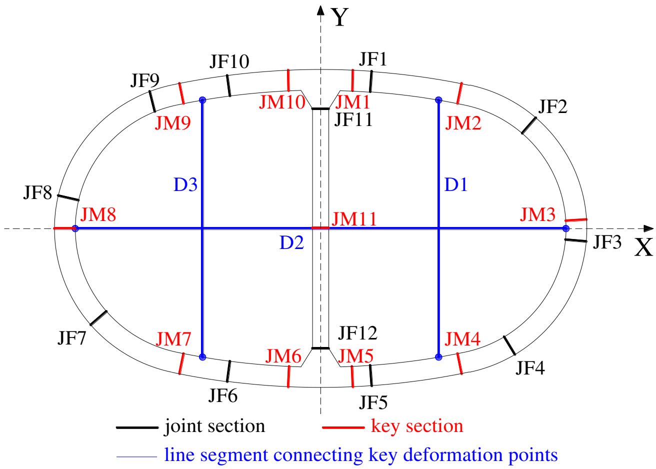

Figure 4.4 Key sections and deformation points for the model calculation.

Table 4.1 The coordinate positions of the 11 key sections.

Key section	X value (m)	Y value (m)
JM1	0.766	3.224
JM2	2.542	3.030
JM3	5.516	0.227
JM4	2.542	-3.030
JM5	0.766	-3.224
JM6	-0.766	-3.224
JM7	-2.637	-3.013
JM8	-5.525	0
JM9	-2.637	3.013
JM10	-0.766	3.224
JM11	0	0

An iterative calculation is used in the full-ring model with a flow chart of the iteration loop shown in Figure 4.5. The calculation results from the current iteration loop are used in the next iteration. The calculation results at the points indicated in Figure 4.4 are used in the criterion for aborting the iteration loop.

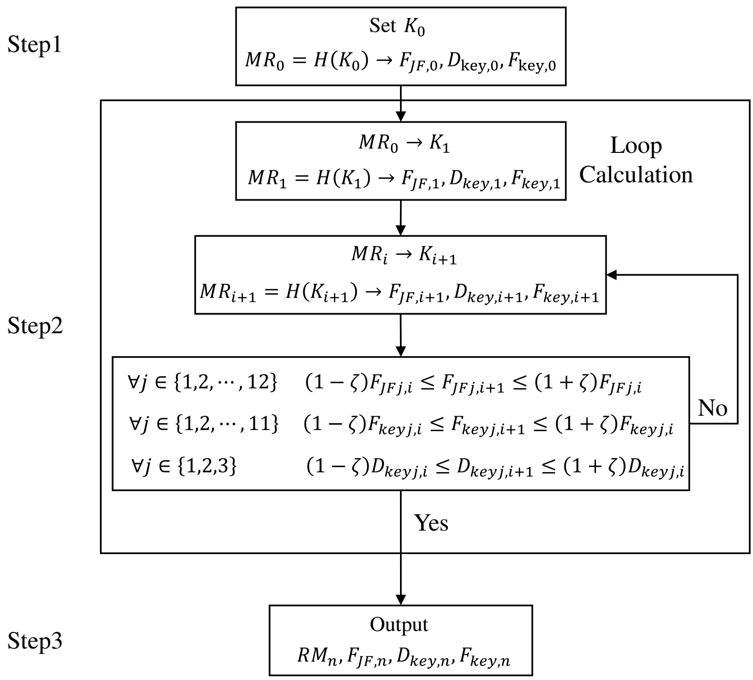

Figure 4.5 Flow chart for the numerical model calculation.

In Figure 4.5, $F_{JF} = [F_{JF1}, F_{JF2}, \cdots, F_{JF12}]$ represents the internal forces in the longitudinal joints JF1 to JF12, including bending moment, axial force and shear force. $F_{key} = [F_{key1}, F_{key2}, \cdots, F_{key11}]$ represents the internal forces in the key sections JM1 to JM11, including bending moment, axial force and shear force. $D_{key} = [D_{key1}, D_{key2}, D_{key3}]$ represents the deformations of the three pairs of the key locations, the right short axis D1, the long axis D2 and the left short axis D3 respectively. MR_i stands for the mechanical response of the QRST lining after i iterations, including internal forces and structural deformations. It can be expressed as $MR_i = H(K_i)$, where $H(K_i)$ is the calculation matrix of the numerical model with the input stiffness matrix K. $F_{JF,i}$, $F_{key,i}$ and $D_{key,i}$ are obtained from MR_i and $F_{JF,i}$ can determine K_{i+1}, which will be used to retrieve MR_{i+1}. Large rotational and shear stiffness values, respectively 10000 kN·m/m/rad and 10000 kN/m^2, are adopted initially to start the iteration loop and avoid non-convergence of the initial calculation caused by unexpected large deformations.

If all the differences for internal forces (F_{JF} and F_{key}) and deformations (D_{key}) between successive steps are smaller than the convergence coefficient ζ, the iteration loop will be broken off and the calculation results in the last iteration will be taken as the final results. In this study, the convergence coefficient ζ is defined as 0.1%.

It has to be noted that the circumferential joints' stiffness is zero for a calculation without the interaction from neighbouring rings. In a calculation considering this interaction, the compressive stress at the circumferential joints is determined by the longitudinal force along the tunnel direction, and the circumferential joints' stiffness is kept at a constant value in every iteration step in Figure 4.5.

4.3 Indoor full ring experiment

4.3.1 Assumed load distributions for a QRST

To the author's knowledge, the load distributions for a non-circular shield tunnel are not specially defined in any design standard. At the design stage for QRSTs, the load assumptions are based on those for circular shield tunnels (Yang et al., 2016; Liu et al., 2018c). Koyama (2003) gave specific calculation methods for the pressure distributions around a circular shield tunnel. There are two modelling methods for the soil and pore water pressures. In the first one, the modelling does not separate the two pressures, while the modelling is separated into the two parts in the second one. In general, the former is applied to a soil with low permeability, such as soft clay soil, and the other is used for a high-permeability soil, such as sandy soil. The soil pressure is divided into vertical and horizontal pressure. Two cases can be assumed for the vertical soil pressure acting on the upper part of the segmental ring, one assuming a full overburden and the other a reduced overburden to take into account the soil's shear strength. The latter is calculated by the Terzaghi's formula. The upward soil pressure from the tunnel bottom is assumed to be distributed uniformly and balances the downward soil pressure in the upper part in magnitude. The horizontal soil pressure is assumed to be a linearly varying load that increases with increasing depth. Hence, the horizontal soil pressure at the top of the ring is derived from the vertical soil pressure multiplied by the coefficient of lateral pressure K_{lat}. The soil reaction is assumed to have a value that corresponds to the local tunnel deformation and displacement, and modelled as soil springs located along the whole periphery of the tunnel. When the water pressure on the tunnel is considered separately, it is assumed to act in the direction of the centre of the ring, increasing with the depth to the ground water level. It has to be noted that, as a shield tunnel typically deforms horizontally, and the deformation value is small, the soil reaction in the practical design can be assumed to be a horizontal soil resisting pressure on both sides in the range of 45° above and below the horizontal tunnel centre line. The distribution of this pressure is an isosceles triangle, and the peak value of this isosceles triangle is calculated by multiplying the lateral deformation of the lining structure by the coefficient of horizontal subgrade reaction R_{hsoil}. These load assumptions are also suggested by the International Tunnelling Association (2000), the Chinese Code for Design of Metro [GB50157] (2013) and the Japanese Standard for Shield Tunneling (2001). In previous studies, similar load distributions also have been used by Lee et al. (2001), Nakamura et al. (2003), Mo and Chen (2008), Hu et al. (2009), and Li et al. (2015c).

Based on the introduced modelling of the pressure distributions for a circular shield tunnel, the pressure distribution for a QRST tunnel in soft soils consists of 5 parts: the vertical pressure on the crown, the horizontal lateral pressure, the dead weight of the lining, the uniform bottom counterpressure (to balance the vertical loads) and the lateral resisting pressure (caused by the lateral structural deformations) as shown in Figure 4.6. The crown pressure is composed of a uniform top pressure and an arc-shaped pressure. The uniform top pressure magnitude is mainly determined by the overburden depth and the surcharge loads on the ground surface. Four arcs compose the outline of a QRST, two of 24 degrees with a 15.45 m radius and two of 156 degrees with a 3.20 m radius. Hence, an arc pressure is caused by the arc shape of the lining at the crown area. Additionally, in the design of a QRST, due to its non-circular shape, a partial offset surcharge is especially considered as an optional pressure, depending on the possible loads or buildings near the tunnel. The lateral pressures are calculated by multiplying the vertical pressure by the coefficient of lateral pressure K_{lat} whose value is obtained from soil property tests. The soil resisting pressure is simulated by a series of soil springs along the whole periphery of the QRST lining. These springs can only sustain pressures, which means that they only take effect when the lining deforms outward into the soil. However, as the resisting pressure caused by the lining deformation is small, in order to make a quick calculation in practice, the soil resisting pressure can also be considered to act in the range of 45° above and below the horizontal centre line. Both the soil spring and the isosceles-triangle pressures are shown in Figure 4.6, but only one of them is chosen in the design. When the water and soil loads are separately calculated for the tunnel surrounded by sandy soils, the water pressure is assumed to be perpendicularly exerted on the lining surface as shown in Figure 4.7, and the value is the hydrostatic water pressure at the corresponding location. As such, the calculations for the vertical pressure on the crown and the horizontal lateral pressure should adopt the soils' submerged weight.

When a deep shield tunnel is planned to be used as a subway, this means deeper elevator shafts and higher evacuation requirements in case of an accident. The total cost of a deep tunnel construction and operation therefore definitely increases. The studied QRSTs are mainly constructed with a shallow overburden, and the design depth of the current QRSTs' applications ranges from 7 m to 17 m. Terzaghi's formula is not necessary to be considered for this depth range when calculating the vertical pressures. So, hereafter, without specific explanation, the vertical pressures are considered to be mainly caused by the soils and the surcharges on the tunnel crown, and Terzaghi's formula is not considered.

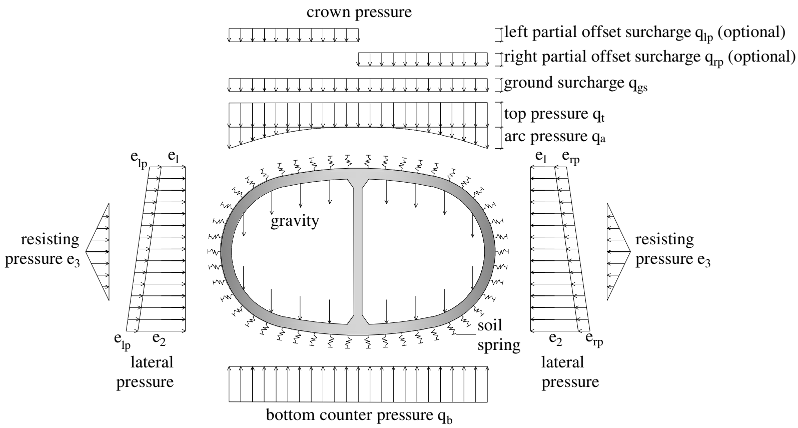

Figure 4.6 Pressure distributions in the design model for a QRST in soft soils.

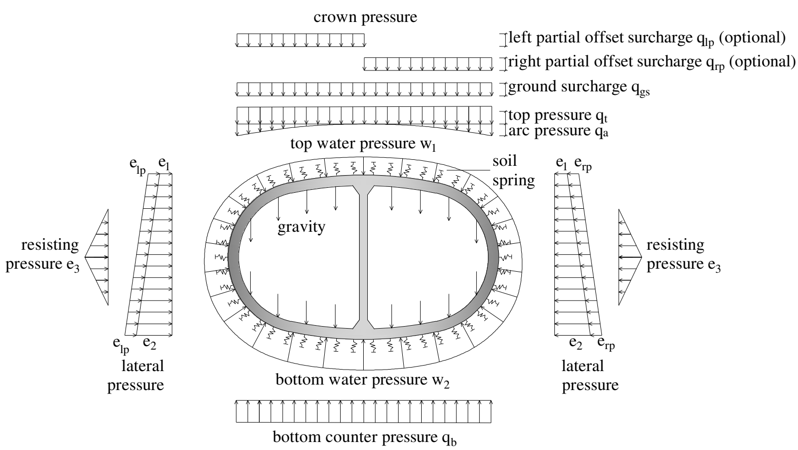

Figure 4.7 Pressure distributions in the design model for a QRST in sandy soils.

4.3.2 Setup of indoor full ring experiment

Indoor full-scale ring experiments allow for a direct evaluation of the mechanical performance of tunnel linings. The loads exerted on the structure are clearly defined, and the measurement results obtained from this kind of indoor experiments are relatively reliable when compared to those from an in-situ tunnel tests. Full-scale ring experiments have been performed for the Green Heart Tunnel in the Netherlands (Blom et al., 1999), the Elbe Tunnel in Germany (Schreyer and Winselmann, 2000), the Shanghai Changjiang Tunnel (Lu et al., 2006), a water storage and sewage tunnel in Shanghai (Huang et al., 2019) and special-section tunnels including rectangular tunnels (Nakamura et al., 2003) and DOT shield tunnels (Moriya, 2000; Chow, 2006). For the tunnels with a new type of cross section or with a large diameter, full-scale experiments are an important way to obtain the mechanical behaviour, providing the necessary parameters for structural design or for verifying the rationality of the calculation method. As a new special-section tunnel, the design model for QRSTs, the applicability of the BSM, which has been widely used in circular tunnels, and the necessary parameters for guiding the structural design, such as the joint's stiffness and the rigid zone, are unclear. Full-scale experiments are needed to lay out the foundation for a design method of QRSTs. In this study, the results from a full-scale ring experiment are used to verify the applicability of the presented model. The full-scale ring experiment contains one ring of the QRST lining, and correspondingly, the model results are taken from the model without circumferential joints, where the circumferential tangential and radial shear stiffnesses are zero.

The indoor full ring experiment was conducted at the Laboratory of Tunnel Components of the Shanghai Tunnel Engineering Company in 2016. A full ring equipped with Type-A longitudinal joints was placed horizontally into a self-balancing steel frame (Figure 4.8a). Every loading point was equipped with two hydraulic jacks with a maximum load output of 2000 kN. A series of steel balls were deployed under the horizontal ring specimen to provide a test condition with negligible friction. During the loading process, 30 loading points were arranged over the circumference to simulate different kinds of loads, such as soil and water pressure and ground surcharge. These loading points were divided into several groups for load applications in different experimental cases. All hydraulic jacks in the same group provided an equal load simultaneously.

During the test, the convergence deformations and displacements of the structure were monitored by 46 displacement transducers. The strains of the rebars and concrete at the key sections were measured by 264 and 224 strain gauges, respectively. Before the formal loading, all loading jacks and measuring meters were calibrated. A pre-experiment was carried out to eliminate the initial gaps between the segments that might have appeared during the assembly. After that, an inspection of the bolts was performed to ensure that all connections were stable to reduce the initial structural deformation.

(a)

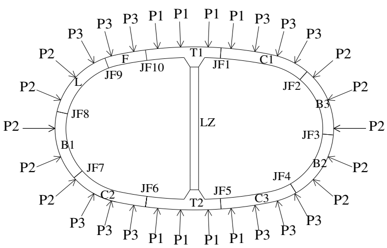

(b)

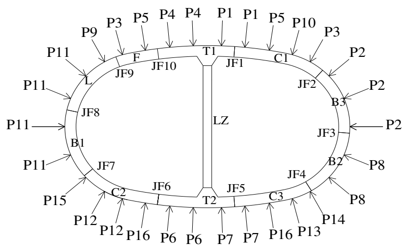

(c)

Figure 4.8 Indoor full-ring experiment: (a) loading frame and full ring experiments; (b) jack distribution for Experimental Cases1 and 2; (c) jack distribution for Experimental Case 3 (see Figure 1.10 for dimensions).

Three experimental cases are selected to compare the results from experiments and the proposed iterative model. In Experimental Cases 1 and 2, the 30 jacks are divided into 3 groups (Figure 4.8b) while 16 groups are used to simulate the load distribution in Experimental Case 3 (Figure 4.8c), in which an extra partial offset surcharge on the left half side of 30 kPa is assumed. This corresponds to the relatively dangerous design condition of the tunnel going partially under a building or when new construction is taking place close to an existing tunnel. A summary of the design parameters and the experimental loads is presented in Table 4.2. The strata surrounding the tunnel is mucky clay and mucky silty clay. The assumed unit weight of the soil is 18 kN/m^3, and the water level is 0.5 m below the ground. In order to use the 30 loading points to simulate the design condition, the principles for deciding on the groups and the values of these loading points include both equivalences of the load distributions on the linings and similarity of the internal forces and deformations between experiment and design. Because the real load exerted on the tunnel and the corresponding structural mechanical behaviour cannot be precisely simulated by the 30 point loads due to the complexity of the soil-structure interaction, plenty of preliminary calculations were made to ensure the internal forces of key sections and displacement of key deformation points (in Figure 4.4) in the tested linings are approximately equivalent to those of an actual tunnel structure under the assumed load distributions shown in Figure 4.6 and

Figure 4.7. This principle of soil load simulation through separate point loads was also adopted in previous full-scale segmental ring experiments (Blom et al., 1999; Schreyer and Winselmann, 2000; Nakamura et al., 2003; Chow, 2006; Lu et al., 2006; Liu et al., 2016; 2017a). The differences in the lining structure's performance between the point loads in the indoor full-ring experiments and the uniformly changing loads in an actual tunnel, and the effect of this loading simulation method will be discussed in Chapter 6.

Table 4.2 Full-scale ring experimental cases.

Experimental Case	Soil overburden (m)	Coefficient of lateral pressure K_{lat}	Ground surcharge	Experimental Load (kN)
1	10	0.7 (soil-water together)	20 kPa	P1 = 300, P2 = 170, P3 = 212
2	17	0.4 (soil-water separately)	20 kPa	P1 = 450, P2 = 250, P3 = 355
3	17	0.7 (soil-water together)	20 kPa and left partial offset surcharge of 30 kPa	P1 = 481, P2 = 227, P3 = 503, P4 = 458, P5 = 344, P6 = 599 P7 = 400, P8 = 486, P9 = 406, P10 = 239, P11 = 255, P12 = 388, P13 = 489, P14 = 40, P15 = 387, P16 = 258

4.4 Comparison between calculation results and indoor full-ring tests

As the point loads in the indoor full-scale ring experiments and the corresponding structural responses are clearly identified, the results from the iterative numerical model under these 30 point loads are compared with those from the experiments.

Based on the measurements and the assumption of plane strain, internal forces at the eleven key sections (See Figure 4.4) in the experiments are calculated through Eq. (4.4) and Eq. (4.5).

$$N = \int_{-h_0/2}^{h_0/2} \sigma[\varepsilon_c(y)]\, b_0 dy + \varepsilon_s E_s A_s + \varepsilon_s' E_s' A_s' \tag{4.4}$$

$$M = \int_{-h_0/2}^{h_0/2} \sigma[\varepsilon_c(y)]\, b_0 y dy + (\varepsilon_s E_s A_s - \varepsilon_s' E_s' A_s')(h/2 - c_0) \tag{4.5}$$

In the formula, h_0, b_0 and c_0 represent the thickness of a segment, the width of a segment and the distance from the centre of the reinforcement layer to the closest segment edge. $\varepsilon(y)$ refers to the concrete strain at different positions in the direction of segment thickness, and $\sigma[\varepsilon(y)]$ refers to the concrete stress corresponding to the concrete strain. ε_s, E_s and A_s refer to the strain of the reinforcement close to the external surface of the segment, the elastic modulus of steel and the area size of the corresponding reinforcement while ε_s', E_s' and A_s' are for the reinforcement close to the internal surface of the segment. The constitutive stress-strain relationship of the concrete is quadratic, while that of the steel rebars is considered bilinear.

Table 4.3 Comparison of bending moments and axial force at key sections (bending moment unit: kN·m/m, axial force unit: kN/m).

Experi-mental Case	Key section	Experiment		Model		Ratio (model/experiment)	
		Bending moment	Axial force	Bending moment	Axial force	Bending moment	Axial force
1	JM1	-241	-526	-235	-529	0.98	1.01
	JM2	198	-523	192	-501	0.97	0.96
	JM3	-101	-599	-95	-589	0.94	0.98
	JM4	206	-493	193	-500	0.94	1.01
	JM5	-236	-540	-235	-528	0.99	0.98
	JM6	-239	-529	-254	-528	1.06	1.00
	JM7	217	-499	171	-499	0.79	1.00
	JM8	-113	-618	-111	-586	0.98	0.95
	JM9	175	-498	164	-502	0.94	1.01
	JM10	-248	-530	-262	-529	1.06	1.00
	JM11	-8	-993	-23	-1038	-	1.05
2	JM1	-313	-853	-312	-809	1.00	0.95
	JM2	303	-774	318	-767	1.05	0.99
	JM3	-192	-887	-168	-925	0.88	1.04
	JM4	297	-801	303	-770	1.02	0.96
	JM5	-296	-870	-305	-810	1.03	0.93
	JM6	-292	-854	-305	-804	1.04	0.94
	JM7	283	-799	297	-764	1.05	0.96
	JM8	-225	-836	-205	-921	0.91	1.10
	JM9	304	-780	276	-771	0.91	0.99
	JM10	-295	-901	-296	-808	1.00	0.90
	JM11	-52	-1731	-46	-1636	-	0.95
3	JM1	-364	-950	-346	-914	0.95	0.96
	JM2	213	-847	220	-876	1.03	1.03
	JM3	-86	-1021	-94	-971	1.10	0.95
	JM4	178	-907	185	-874	1.04	0.96
	JM5	-349	-939	-326	-907	0.93	0.97
	JM6	-229	-855	-243	-905	1.06	1.06
	JM7	348	-874	310	-868	0.90	0.99
	JM8	-263	-1042	-264	-1048	1.00	1.01
	JM9	364	-880	323	-856	0.90	0.97
	JM10	-302	-961	-305	-897	1.01	0.93
	JM11	-99	-1590	-102	-1661	-	1.04

The internal forces and deformations from the experiments and the iterative model under the 30 point loads are listed in Table 4.3, with the ratios of model values to experimental results. From the numerical results, it is found that the errors on the axial forces at most of the key sections are under 5%, while those at the other sections are smaller than 10%. For the bending moments, differences at most of the key sections are within 10%, with the exceptions of the 21% value for JM7 in Experimental Case 1, 12% value for JM3 in Experimental Case 2 and 11% value for JM10 in Experimental Case 3.

When it comes to the structural deformations (in Table 4.4), most of the differences are within the range of 10%, with the exception of measurement D1. This can be attributed to the small value of convergence deformation of measurement D1 in the experiments. Moreover, the absolute errors measured for this measurement point are within 1.50 mm. To get a direct sense of the structural deformations, the measured displacements from the displacement transducers at the measuring points in Experimental Case 1 are compared with the numerical results, as shown in Figure 4.9. The obtained displacements in Figure 4.9 are visualized with a scale factor of 80. Overall, it is found that the calculated deformations from the iterative model and the experimental results are in good agreement.

Table 4.4 Comparison of convergence deformations (unit: mm).

Experimental Case	Convergence deformation	Experiment	Model	Ratio (model/experiment)
1	D1	-4.74	-3.58	0.75
	D2	4.68	4.65	0.99
	D3	-6.92	-7.46	1.08
2	D1	-6.37	-5.42	0.85
	D2	8.44	9.10	1.08
	D3	-12.61	-12.96	1.03
3	D1	-1.87	-0.41	-
	D2	9.24	9.45	1.02
	D3	-19.68	-19.91	1.01

From the comparison of the numerical and experimental results in these three cases with different load levels, concerning the condition without the circumferential joints, the developed model is verified, and it can evaluate the mechanical behaviour of a QRST lining with good accuracy. Concerning the conditions with the circumferential joints, the indoor full-ring experiments are not conducted due to the limitation of the testing device and financial support. However, more analyses related to this aspect are discussed in Chapter 6.

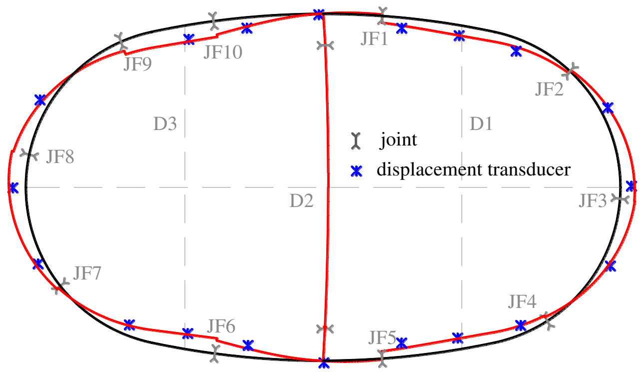

Figure 4.9 Measured deformations from experiment and numerical model in Experimental Case 1.

4.5 Comparison between variable and constant rotational stiffness

In the presented model, the rotational stiffness changes are taken into account through an iterative method. In this section, constant rotational stiffness values for all segmental joints are used to replace the variable stiffness. This allows to investigate the effect of the iterative method on the bending moments at key sections JM1 to JM10 and the convergence deformations at key deformation points D1 to D3. In the following, a range of constant stiffness values in increments of 20,000 kN·m/m/rad is considered, and the differences between the predicted and experimental values from the indoor full ring experiment are recorded. The evaluations show that only values between 40,000 kN·m/m/rad and 100,000 kN·m/m/rad render reasonably good numerical results, as shown in Figure 4.10. Results for axial forces in the linings are not presented in this paper, as no significant differences were found between the iterative nonlinear and constant value predictions.

Firstly, considering the bending moments, Figure 4.10 reveals for a joint stiffness of 100,000 kN·m/m/rad, differences up to 12% in Experimental Case 1, up to 17% in Experimental Case 2, and up to 48% in Experimental Case 3. For the stiffness of 80,000 kN·m/m/rad, the maximum differences in the three cases are respectively 11%, 15% and 42%. Those difference are 12%, 13%, 32% under a stiffness of 60,000 kN·m/m/rad, and 14%, 12%, 21% under a stiffness of 40,000 kN·m/m/rad. This means that if a reasonable constant stiffness value is used, the bending moment differences can be kept within acceptable limits. However, the differences increase with the increase in pressure level around the tunnel linings, and the constant stiffness fitting the experimental results in the best way also changes for the different load cases.

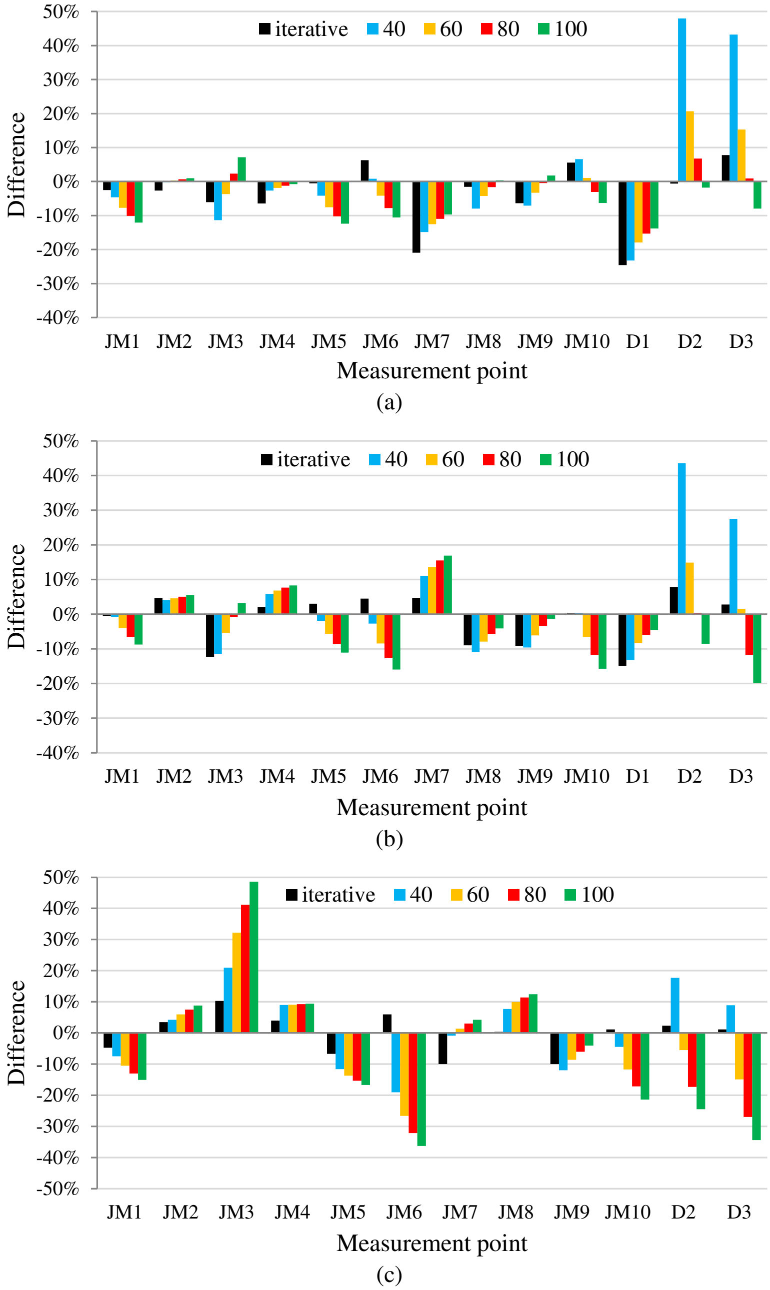

Figure 4.10 Difference comparison between predictions and experiments: (a) Experimental Case 1; (b) Experimental Case 2; (c) Experimental Case 3 (rotational stiffness in 10^3 kN·m/m/rad).

Secondly, considering the key deformations (the differences of the D1 point is not shown due to its small absolute deformation value in Experimental Case 3), Figure 4.10 reveals for a joint stiffness of 100,000 kN·m/m/rad differences up to 13% in Experimental Case 1, up to 20% in Experimental Case 2, and up to 35% in Experimental Case 3. For other joint stiffnesses, the maximum differences are 27% (80,000 kN·m/m/rad Experimental Case 3), 20% (60,000 kN·m/m/rad Experimental Case 1), and 48% (40,000 kN·m/m/rad Experimental Case 1).

In contrast to the previous conclusion for the bending moments, it is evident that the convergence deformations of the key deformation points vary significantly with different stiffnesses. This means that the structural deformation is very sensitive to the rotational stiffness input. If the adaption of a constant stiffness value is not supported by full ring tests, the method of constant rotational stiffness in segmental joints may lead to non-negligible deformation prediction errors. On the other hand, the calculation method presented in this study can consider the joint's nonlinear behaviour. The results obtained by this method can match the experimental results of both deformations and bending moments for all load cases well within the range of about 10% in all but a few measurement points. When the bending moments around the joint's vicinity are large, which may exist in large-diameter and special-section shield tunnels, the joint nonlinear behaviour needs to be considered in the calculation model. In general, it can be concluded that a proper constant joint rotational stiffness is difficult to determine, and its deduced deviations may influence the structural design and safety evaluation. The presented iterative method in this study is able to solve this problem.

4.6 Effect of the joint improvement

The previously introduced indoor full-ring experiments and model calculations used the Type-A joints. In order to detect the effect of the joint improvement, the model results from the Type-A and Type-B joints are compared with the same point loads as in the full-ring experimental cases. A typical bending moment distribution and a typical axial force distribution are shown in Figure 4.11. The bending moments and axial forces along the segments are presented in Figure 4.12 after unfolding the calculation results in function of the angular parameter α. The key sections JM1 to JM 10 and joint sections JF1 to JF 10 are also marked in Figure 4.12. The connecting area means the haunch in Figure 4.3, where the thickness changes and unrealistic bending moments are generated. Hence, the values around the connecting areas of the interior column and segments T1 and T2 are not shown. Due to the small differences between the models with and without joint improvement, only the results from Experimental Cases 2 and 3, where the load levels are relatively large, are presented in Figure 4.3. It can be found that

JM2 to JM4 and JM7 to 9 can generally represent the largest bending moment in the corresponding segments, and their values can affect the segment section design and reinforcement arrangement. JM1, JM5, JM6 and JM10 are mainly used to give bending moment values for the sections of segments T1 and T2. Concerning the joint sections, some are located at positions where the sign of bending moment changes and small bending moments exist, such as JF2 and JF7. However, some joint sections are unavoidably in areas with large bending moments, such as JF3 and JF8.

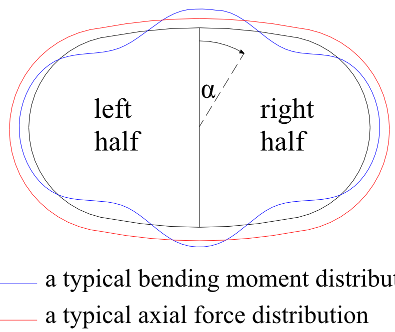

Figure 4.11 Diagram of typical bending moment and axial force distributions.

When the results before and after the joint improvement are compared, generally, the bending moment and axial force ranges are very similar. This means that although the joint improvement can increase the joint's bearing capacity, as presented in Chapter 2, its effect on the internal forces under the current load levels is minimal. Since the key sections JM1 to JM11 are used to determine the section design, the specific bending moments and axial forces at these sections are retrieved and listed in Table 4.5 to investigate the effect of the joint's stiffness enhancement.

For the axial forces, it can be found that they are almost identical before and after the joint improvement, within a 1% difference at all sections. When it comes to the bending moments, the key sections around the interior column (JM1, JM5, JM6 and JM10) show a decrease of up to 6% in Experimental Cases 1 and 2, while the decrease in Experimental Cases 3 is larger, up to 11% at JM6. However, all the waist areas in these three cases (JM3 and JM8) show an increase, up to 8%, except for the 23% increase at JM3 in Experimental Case 3. On the other hand, the positive bending moment sections (JM2, JM4, JM7 and JM9) show little bending moment changes, generally within 3%. The joint improvement makes the areas away from the interior column stiffer, and the stiffness differences between these areas and T segments decrease. This results in the waists sustaining more negative bending moments while the T segments sustaining less. By influencing the stiffness differences between T segments and other areas, the joint stiffness increase can help to decrease the negative bending moments in T segments slightly, where the largest negative moments appear.

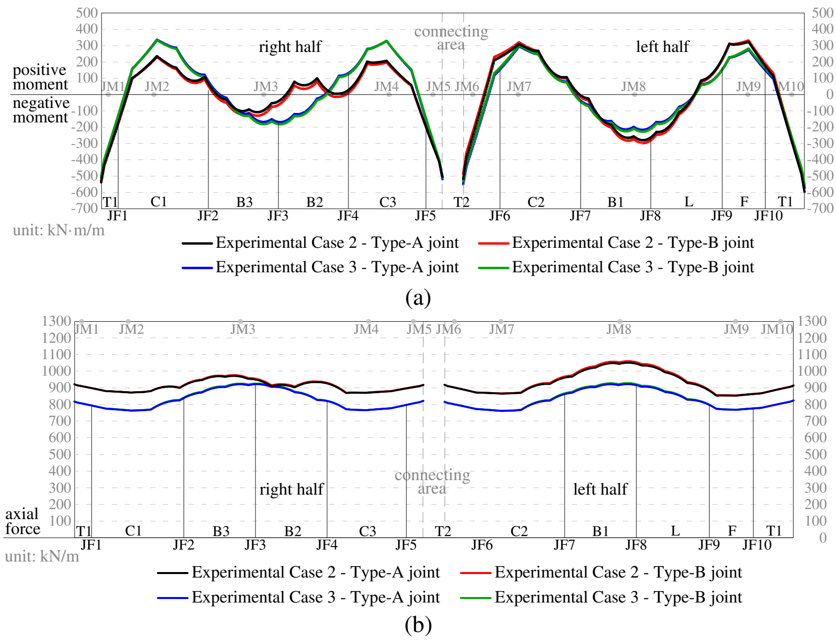

Figure 4.12 Comparison between linings with Type-A joints and Type-B joints in Experimental Cases 2 and 3: (a) bending moments; (b) axial forces.

The bending moments in the joint sections (JF1 to JF10) are compared in Table 4.6. Except for the joints around the waists (JF3 and JF8), generally, all the longitudinal joints in the right half (JF1, JF2, JF4 and 5) sustain less bending moments while the joints in the left half (JF6, JF7, JF9 and 10) sustain more. Based on the fact that the deformations in the left half is more notable than the right half in Figure 4.9 and that the D3 deformation values in Table 4.4 are larger than D1, it can be found that the right half of the QRST lining is stiffer than the left one. When the joint stiffness increases after improvement, the stiffness difference between the left and right halves decreases, which can be confirmed from the decreasing absolute values of D3-D1 in Table 4.7. This stiffness decrease between the two halves can explain that the joints in the left side sustain more bending moments when Type-B joints are used.

Table 4.5 Comparison of bending moments and axial forces at key sections JM1 to JM11 between models with Type-A and Type-B joints (bending moment unit: kN·m/m, axial force unit: kN/m).

Experimental Case	Key section	Model with Type-A joint		Model with Type-B joint		Ratio (Type-B/Type-A)	
		Bending moment	Axial force	Bending moment	Axial force	Bending moment	Axial force
1	JM1	-235	-529	-228	-529	0.97	1.00
	JM2	192	-501	193	-501	1.00	1.00
	JM3	-95	-589	-103	-592	1.08	1.01
	JM4	193	-500	195	-501	1.01	1.00
	JM5	-235	-528	-226	-528	0.96	1.00
	JM6	-254	-528	-240	-528	0.95	1.00
	JM7	171	-499	177	-500	1.03	1.00
	JM8	-111	-586	-117	-590	1.06	1.01
	JM9	164	-502	168	-503	1.03	1.00
	JM10	-262	-529	-250	-530	0.95	1.00
	JM11	-23	-1038	-17	-1031	-	0.99
2	JM1	-312	-809	-307	-810	0.98	1.00
	JM2	318	-767	315	-769	0.99	1.00
	JM3	-168	-925	-182	-929	1.08	1.00
	JM4	303	-770	304	-770	1.00	1.00
	JM5	-305	-810	-297	-809	0.97	1.00
	JM6	-305	-804	-288	-804	0.94	1.00
	JM7	297	-764	303	-765	1.02	1.00
	JM8	-205	-921	-216	-927	1.06	1.01
	JM9	276	-771	283	-772	1.02	1.00
	JM10	-296	-808	-279	-808	0.94	1.00
	JM11	-46	-1636	-34	-1626	-	0.99
3	JM1	-346	-914	-341	-913	0.98	1.00
	JM2	220	-876	216	-876	0.98	1.00
	JM3	-94	-971	-116	-976	1.23	1.01
	JM4	185	-874	175	-876	0.95	1.00
	JM5	-326	-907	-326	-909	1.00	1.00
	JM6	-243	-905	-215	-905	0.89	1.00
	JM7	310	-868	321	-870	1.03	1.00
	JM8	-264	-1048	-282	-1058	1.07	1.01
	JM9	323	-856	332	-858	1.03	1.00
	JM10	-305	-897	-280	-897	0.92	1.00
	JM11	-102	-1661	-74	-1646	-	0.99

From the above analyses, it can be concluded that the joint's stiffness increase influences the bending moment distributions in two ways: (1) a decrease of the stiffness difference between the T segments and other areas, and (2) a decrease of the stiffness difference between the right half and the left half. The former stiffness decrease results in larger moments at the waists and smaller moments in the T segments. The latter results in the joints in the left half sustaining larger moments while the right half joints sustaining smaller ones.

Table 4.6 Comparison of bending moments at joint sections JF1 to JF10 between models with Type-A and Type-B joints (unit: kN·m/m).

Experimental Case	Joint Section	Model with Type-A joint	Model with Type-B joint	Ratio (Type-B/Type-A)
1	JF1	-82	-77	0.93
	JF2	35	30	0.85
	JF3	-95	-103	1.08
	JF4	63	60	0.96
	JF5	-82	-75	0.92
	JF6	106	114	1.08
	JF7	-32	-34	1.09
	JF8	-114	-120	1.05
	JF9	78	78	1.01
	JF10	98	105	1.07
2	JF1	-139	-136	0.98
	JF2	87	77	0.88
	JF3	-168	-182	1.08
	JF4	132	127	0.96
	JF5	-148	-140	0.95
	JF6	170	180	1.06
	JF7	-36	-43	1.20
	JF8	-200	-211	1.05
	JF9	152	153	1.00
	JF10	148	159	1.07
3	JF1	-183	-179	0.98
	JF2	73	58	0.79
	JF3	-42	-65	1.54
	JF4	28	11	0.40
	JF5	-194	-196	1.01
	JF6	237	254	1.07
	JF7	-4	-14	3.61
	JF8	-263	-281	1.07
	JF9	216	215	1.00
	JF10	174	189	1.09

Table 4.7 Comparison of convergence deformations at D1 to D3 between models with Type-A and Type-B joints (unit: mm).

Experimental Case	Convergence deformation	Model with Type-A joint	Model with Type-B joint	Ratio (Type-B/Type-A)
1	D1	-3.58	-3.86	1.08
	D2	4.65	4.27	0.92
	D3	-7.46	-6.48	0.87
	Abs(D3-D1)	3.88	2.62	1.48
2	D1	-5.42	-5.78	1.07
	D2	9.10	7.78	0.85
	D3	-12.96	-10.80	0.83
	Abs(D3-D1)	7.54	5.02	1.50
3	D1	-0.41	-1.69	-
	D2	9.45	7.64	0.81
	D3	-19.91	-15.70	0.79
	Abs(D3-D1)	19.50	14.01	1.39

Table 4.7 summarizes the key deformation points before and after the joint improvement. For point D3, where the most significant deformations occur, the convergence values decrease by 13%, 17% and 21% in the three experimental cases. Although the internal forces are not significantly susceptible to the joint improvement, the convergence deformations are moderated considerably by this improvement in a positive manner. This also proves that the deformation of a QRST lining is sensitive to the joint's rotational stiffness more than its moment distribution.

4.7 Sensitivity study

The mechanical performance of the tunnel lining can be obtained through full-scale ring experiments, but these experiments are difficult to conduct repeatedly. The verified numerical model provides an approach for detecting sensitive parameters and further structural improvements of the QRSTs.

The choice of the configuration of the longitudinal joints is critical for shield tunnel projects (Yan et al., 2011; Caratelli et al., 2018). It influences the lining's mechanical response, including structural deformation and bending moment distribution, and may also affect the safety and applicability of tunnel linings (Koyoma and Nishimura, 1998; Gruebl, 2012; Zhang et al., 2019a). The joint's stiffness is one of the most vital factors for the decision on the joint type (Li et al., 2015b). As a new shield tunnel lining structure, the effect of the longitudinal joint's stiffness needs further investigation. Hereafter, the effects of the longitudinal joint' rotational stiffness, shear stiffness and the size of the rigid zones are analysed and discussed by changing the parameter settings in the model. Additionally, as the column joints' parameters refer to the segmental joints in previous analyses, the model's sensitivity to column joints' stiffnesses is also investigated by modifying the parameter values.

Table 4.8 Ranges of parameters.

Parameter	Range of the magnification factors	Value of x
Rotational stiffness	2^x	-3, -2,-1, 0, 1, 2 ,3 ,4
Shear stiffness	2^x	-3, -2,-1, 0, 1, 2 ,3 ,4
Size of rigid zone	2^x	0, 1, 2 ,3
Column joints' stiffness	2^x	-3, -2,-1, 0, 1, 2 ,3 ,4

In the sensitivity study, the variation tendencies of the structural response are detected by changing various parameter values one by one. Considering only practical ranges for the parameters, the magnification factor ranges for the parametric values are listed in Table 4.8. When one variable is changed, the other parameters remain constant, except that the column joints' rotational and shear stiffnesses change together with the same magnification factor due to the structure's insensitivity to their stiffness changes. The point loads in the indoor full-ring experiments are taken as the basis for the parametric study.

Two convergence deformations (D2 and D3) and six key section bending moments (two at the waists JM3 and JM8, two near the column in each half JM1 and JM10, and two with positive bending moment values in each half JM2 and JM7) are selected as the target objects to detect the effect of the parameter variations. These section choices are determined by the observation that the deformations and internal forces at these sections are relatively large and can act as the main controlling factors for the structural design, as previously introduced. The value of the corresponding input parameter is multiplied by 2^x. The results from magnified or reduced parameters are compared with the results from the original parameters, as shown in Figure 4.13 and Figure 4.14. In the presented graphs, the exponent "x" is the variable on the abscissa axis. The reader should pay attention to the magnification factor of -1 in the abscissa axis of "size of rigid zone" in Figure 4.13 and Figure 4.14. The "-1" indicates no rigid zone in the model in order to compare with the actual range of "x" from 0 to 3.

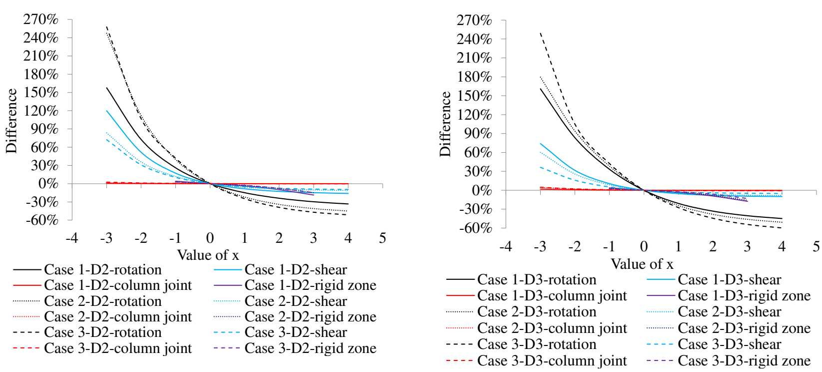

Figure 4.13 Convergence deformations of parameter analysis: (a) D2 (max of long axis deformation); (b) D3 (max of short axis deformation).

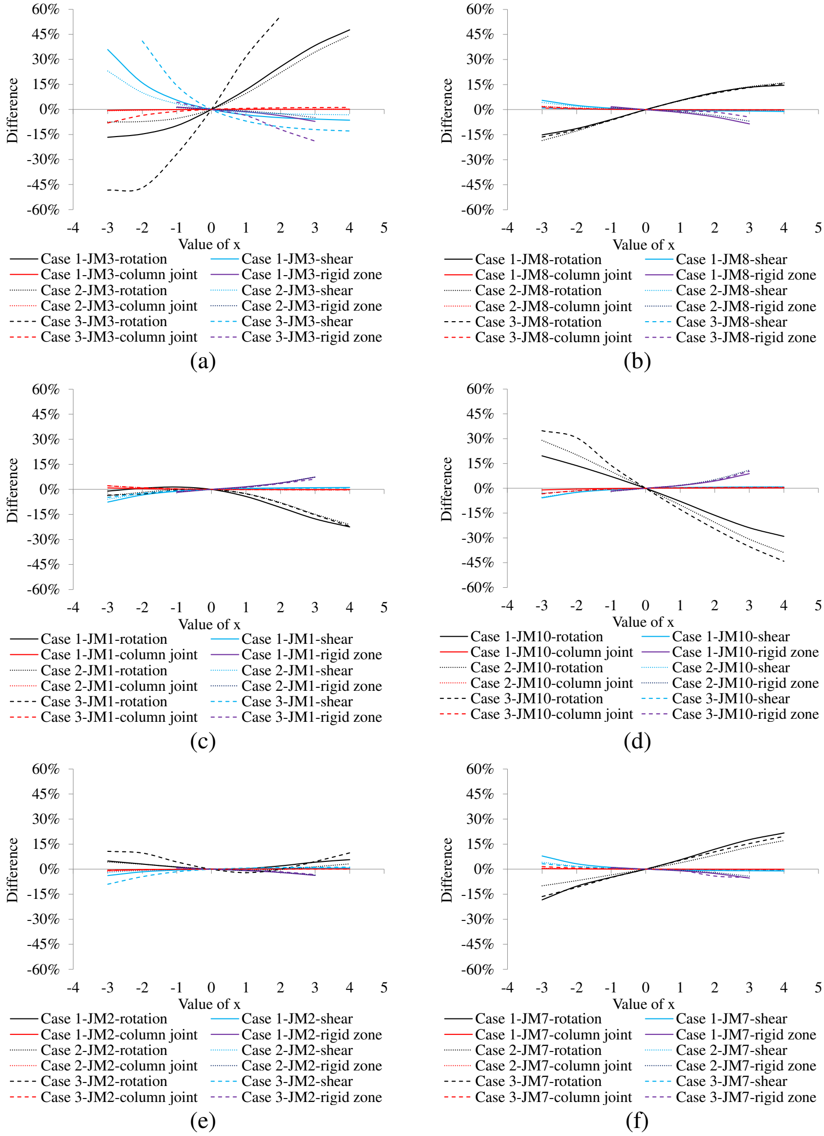

Figure 4.14 Bending moments of parameter analysis: (a) JM3 (max of the negative moment at the right waist); (b) JM8 (max of the negative moment at the left waist); (c) JM1 (max of the negative moment in the right half); (d) JM10 (max of the negative moment in left half); (e) JM2 (max of the positive moment in the right half); (f) JM7 (max of the positive moment in the left half).

When the target object increases in absolute value with the increasing magnification factor, this tendency is represented by ↑, while an opposite tendency is represented by ↓. The slope in the curves represents the change rate, i.e., the level of sensitivity to the relative parameter. Target objects which are very sensitive to a certain parameter are indicated using ↑↑ or ↓↓. Based on the calculation results, the tendencies and sensitivity levels to the parameters are summarized in Table 4.9.

Table 4.9 Summary of the tendency and sensitive level of different parameters.

Target Object	Rotational stiffness	Shear stiffness	Size of rigid zone	Column joints' stiffness
D2 (max of long axis deformation)	↓↓	↓↓	↓	↓
D3 (max of short axis deformation)	↓↓	↓↓	↓	↓
JM3 (max of negative moment at right waist)	↑↑	↓↓	↓	↑
JM8 (max of negative moment at left waist)	↑↑	↓	↓	↓
JM1 (max of negative moment in right half)	-	↑	↑	↓
JM10 (max of negative moment in left half)	↓↓	↑	↑	↑
JM2 (max of positive moment in right half)	-	↑	↓	↑
JM7 (max of positive moment in left half)	↑↑	↓	↓	↓

It can be found that the structural performances are insensitive to the column joint's stiffnesses, as the interior column only sustains very small bending moments and shear forces. Their reference to the segmental joint's stiffness does not influence the full ring calculation results notably, and this reference is acceptable in the model establishment. It is worth mentioning that a change of the size of the rigid zone generally results in a difference within 10% of maximum bending moments and deformations. The effect of the size of the rigid zone is limited, but a choice for the suitable area of the rigid zone also needs due attention for a precise calculation result. When it comes to the rotational and shear stiffnesses, they are the most sensitive parameters for a QRST lining. Both of them influence the structural deformation considerably. It is known that the longitudinal joint's shear stiffness does not significantly affect the behaviour of circular shield tunnels, as small shear forces exist in the longitudinal joint of circular tunnels. However, when it comes to QRSTs, due to the section shape and the existence of the interior column, the shear forces in the longitudinal joints influence the structural deformations a lot. It has to be noted that the joint's shear stiffness in Chapter 3 may be affected by the bending moment, but 50% to 200% shear stiffness changes have very limited influence in this sensitivity study. This proves that the shear stiffness in Chapter 3 is accurate enough for a full-ring calculation. For the bending moments, the rotational stiffness has a more decisive influence at all sections than the shear stiffness, making it the most significant parameter in the sensitivity study. It is also a proof that the stiffness changes in each joint in QRSTs should draw enough attention, and the proposed iterative method to replace the constant rotational stiffnesses is essential for the calculation accuracy.

According to the summary, optimizing the structural performance by adjusting only one parameter is difficult, as increasing the value of one parameter never decreases the absolute values of all target objects. A proper combination of the choices for the parameters is significant for practical design in order to obtain a better structural response.

4.8 Conclusions

The stiffnesses of the joints in a shield tunnel are related to the level of the joints' internal forces. For joints in QRSTs, the joints' rotational and shear deformations are not only affected by bending moments and shear forces in the joints but also by axial forces. Additionally, the longitudinal joints of QRSTs are subjected to a wide range of both bending moments and shear forces. Considering this, a proper numerical model is required for the further study and structural improvement of this new type of tunnel. In this chapter the main achievements and conclusions include:

(1) An iterative incremental method is presented to simulate the stiffness changes caused by the joint's moment-axial force and shear-axial force interaction behaviour. The applicability of the numerical model is verified by comparing the bending moments and deformations in the lining to the results of unique indoor full-scale ring experiments.

(2) The iterative incremental method provides acceptable results for different load levels, while a constant stiffness based analysis does not.

(3) The joint stiffness increase through joint improvement can decrease the stiffness difference between the T segments and other areas, resulting in larger moments at the waist areas while smaller moments occur in the T segments. The joint improvement can also decrease the stiffness difference between the right half and the left half, resulting in larger moments in the joints in the left half while smaller in the right one. Generally, for the overall internal forces in the lining, the effect of the joint improvement is limited, but it can effectively moderate the lining's convergence deformations.

(4) A parametric study reveals that not only the joint's rotational stiffness but also the joint's shear stiffness significantly affects the structural response. They are the most sensitive parameters for a QRST lining, especially for the lining's

deformation. Further optimizing the structural performance by adjusting only one parameter is difficult, and a combination of the choices for the parameters is important for the practical design of QRST linings.

For circular tunnels, only one geometric shape has to be considered. However, for QRSTs, many geometric shapes are possible. Although the analysis presented in this chapter is based on the particular geometry of a metro tunnel in Ningbo, the conclusions could be helpful for other special-section shield tunnels as well, especially where the influence of the nonlinear behaviour of the joints is non-negligible.

Chapter 5

Pressure distributions around QRSTs during construction and in service

5.1 Introduction

The magnitudes and distributions of the pressures around a tunnel lining are the most significant variables in shield tunnel design, as they determine the safety of the lining structure and influence the investment cost of the tunnel project.

Although many studies related to the pressures on tunnel linings have been done and show that the grouting process has a large effect on the exerted pressures (Bezuijen et al., 2004; Hashimoto et al., 2005; Hashimoto et al., 2008; Talmon and Bezuijen, 2009; Bilotta and Russo, 2013; Liang et al., 2017; Gil Lorenzo, 2019), they all focused on circular tunnels. Few literature about the construction load on special-section shield tunnels has been published. The actual pressure magnitudes and distributions as well as the effect of the grouting process are unclear in the case of the QRSTs, and its applied pressure values and distributions typically were based on those of circular tunnels when conducting the structural design. However, the design load for QRSTs has not been verified. On the other hand, so far, a comparison of different grouting strategies and their resulting effects has not been conducted through field tests.

In the current study, three in-situ monitoring tests were carried out for shallow-buried QRSTs in soft soils to provide direct results of the actual pressures on the lining. This is also the first study targeting field tests for special-section shield tunnels. Different grouting strategies were adopted in the test cases to simulate potential practical grouting situations, and the temporal and spatial pressure distributions around linings during and after construction with different grouting strategies are presented. The influences of the inside back-up equipment and transportation carriages on the outside lining pressures are monitored and analysed. For shallow buried QRSTs in soft soils, the applicability of the proposed load distributions in design models is proven through comparing the long-term monitoring results with theoretically predicted pressures. Finally, a combined pressure mode of cosinusoidal pressures and theoretical long-term pressures is proposed to predict the grouting pressure distributions when lining segments are pushed out of the shield.

5.2 Setup of field tests, instrument installations, testing process, grouting situations

5.2.1 Introduction of the project and in-situ tests

For this new special-section shield tunnel, many studies have been carried out, such as the research on the development of the TBM, the design of the lining segments the synchronous grouting techniques, etc. (Liu et al., 2018b). In-situ monitoring tests are also an important part of the research project, aiming to give a clear insight into the load distributions exerted on this new type of lining.

Chenpodu station (in Jiangshan town, Ningbo, China) of Metro Line 3 is the first QRST project in China. Two rings of QRST linings were chosen here for an in-situ monitoring test. The length of the tunnel is 390.3 m with a range of overburden from 2.5 to 10.5 m. The strata driven through by the tunnel machine are muck, mucky clay and mucky silty clay. Their physical and mechanical parameters are shown in Table 1 (Yang et al., 2016). Besides, another in-situ monitoring case was carried out at Dongqianhu station (in Dongqianhu town, Ningbo) of Metro Line 4 with a length of 417.0 m and an overburden from 1.7 to 9.1 m. The main strata around the tunnel are muck and mucky silty clay with the corresponding parameters in Table 5.1. Both of the stations are located on the outskirts of the city with an open space on the ground and relatively low environmental control, which provides good in-situ testing conditions, like the clearly defined load on the top of the tunnel and the possibility for the adjustment of execution parameters.

The tunnel was bored by an 11.83 m × 7.27 m TBM which was specially designed for QRSTs. Based on previous research on the grouting material (Huang, 2016), the adopted material is a mixture of sand, fly ash, bentonite and cement. The properties of the grout are summarized in Table 5.2.

Table 5.1 Physical and mechanical parameters of the strata surrounding the tunnel.

Line	Stratum	Water content (%)	Unit weight (kN/m^3)	Direct shear test	
				Cohesion (kPa)	Internal friction angle(°)
3	Muck	58.0	16.6	14.6	7.7
	Mucky clay	46.2	17.3	14.6	7.8
	Mucky silty clay	40.3	17.9	16.7	8.4
4	Muck	64.3	16.3	9.0	3.3
	Mucky silty clay	37.0	18.0	9.0	2.8

Table 5.2 Properties of the grouting material.

Density (kg/m^3)	Bleeding rate (%)	Fluidity *(cm)	Open time (h)	Slump (cm)		Shear strength (Pa)		Compressive strength at 7 days (MPa)
				0h	8h	0h	4h	
>2000	<1	>20	0-20	14	>5	>300	>800	>0.15

(*) Flow table test according to EN 1015-3

5.2.2 In-situ test procedure

5.2.2.1 Outline of the in-situ monitoring tests

Two in-situ monitoring cases were conducted for Metro Line 3. Ring No.56 was adopted in Field Case 1 for the field test with a 9.12 m overburden depth. The main surrounding soil was mucky clay and only a small area on the lining's top was in muck. 14 sections were selected for the measurement points to obtain the total pressures on the lining's surface (Figure 5.1a). In Field Case 2, ring No.241 was tested. It was covered by 8.30 m soil and surrounded by mucky clay. In this case, after modification of the measurement layout, the number of measurement sections was increased to 18 as shown in Figure 5.1b and 6 points of them were set near the grouting holes from which the grouting material was ejected. A symmetrical and even layout of the measurement points is taken as the basic assumption of the monitoring scheme. Small unavoidable adjustments are made as an exactly symmetrical and evenly distributed measurement location was difficult to arrange due to the dense steel cages and the preinstalled parts in the concrete segments. Finally a measurement point was set within every 1.8 m length along the lining circumference. For Metro Line 4, another field case study was carried out. Rings No.68 and No.69 were taken together in Field Case 3. The measurement layouts on the rings No.68 and 69 were identical to Field Case 2 except for a few points with small adjustments in the practical measurement installation. The rings in Field Case 3 were driven through muck with a soil crown of 8.30 m, identical to Field Case 2. The average density of the soils in these 3 cases was about 17 kN/m^3 and the water levels were all approximately 0.5 m below the ground surface.

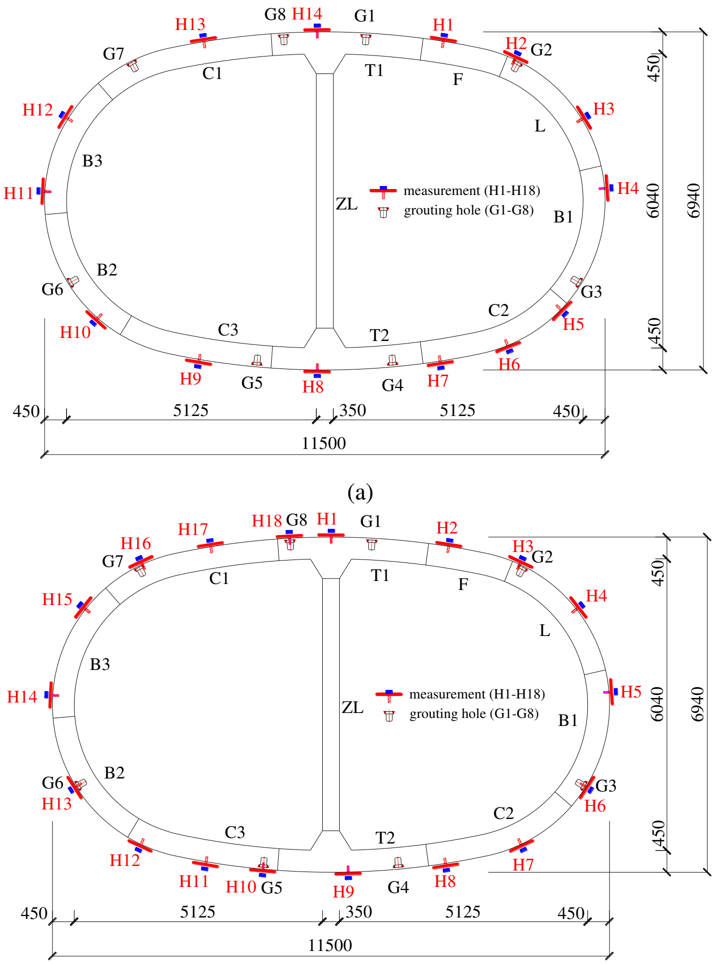

(a)

(b)

Figure 5.1 Layout of measurement points: (a) Field Case 1; (b) Field Cases 2 and 3 (unit: mm).

5.2.2.2 Installation of measurement sensors

Different loads are exerted on the linings, including water pressure, soil pressure, grouting pressure etc. The current field tests focus on the total pressure, namely the sum of all these loads on the linings. All pressures in this study relate to total pressure values if there is no other specification. Soil pressure sensors were used to monitor the changes of the total pressures around the linings and these sensors were installed before concrete casting. The adopted sensor was a pad-type gauge with a 450 mm×350 mm plate and a 1.0 MPa measuring range. Figure 5.2 illustrates the installation of an soil pressure sensor. For this, a customized steel tray was welded to the reinforcement at the measurement position. The sensor was installed on the welded tray. The sensor surface was positioned 5 mm below the linings' outer surface to make space for the protector by adjusting the height of the tray before welding. The connecting cable at the bottom end of the sensor was taped along the steel cage into the cable container which was welded to the reinforcement at the segment inside. Leakage was prevented by rubber seals at the bottom of the tray and at the openings of the cable container. A protector was used to avoid potential damages to the sensor plate during the segment manufacturing and transportation. A cable container accommodated six cables and could be opened after segment curing. Every sensor was checked twice at the segment manufacturing factory, i.e. after the sensor installation and after the segment curing respectively, and twice at the constructing site, i.e. after the transportation to the site and after the assembly in the tunnel respectively. Figure 5.3a and b show the sensor and cable container before the concrete casting, and Figure 5.3c and d show the installed sensor at the outside surface of the segments after curing and the opened cable containers at the inside surface. The output of the sensor is a signal of vibration frequency and can be collected by a manual portable collector and an automatic data logger. They are respectively used for temporary data checks and long-term data collection. The logger can upload the stored data to the internet and remote monitoring is possible.

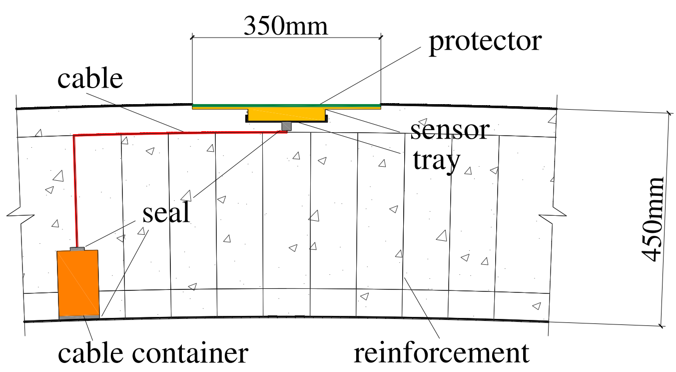

Figure 5.2 Installation of the soil pressure sensor.

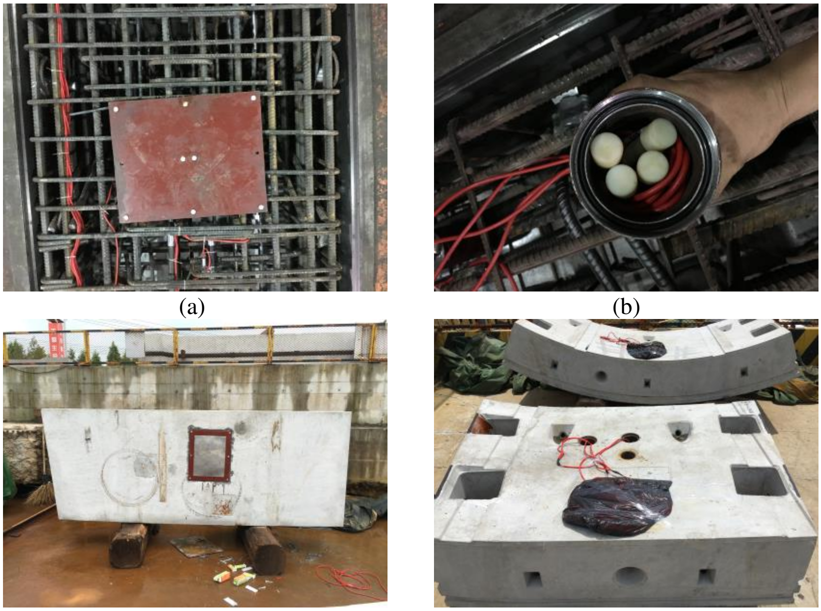

(a) (b) (c) (d)

Figure 5.3 Test segments after curing: (a) installed sensor before casting; (b) installed cable container before casting; (c) sensor at the outside surface after removing the protector; (d) opened cable containers at the inside surfaces.

5.2.2.3 Test procedure and conditions

There are three in-situ cases conducted in this study. The monitoring in Field Case 1 started on 16-01-2016 and stopped on 20-01-2016. During this period, 5 ring drivings were finished. Field Case 2 measured 19 ring drivings from 05-08-2016 to 15-08-2016 while Field Case 3 measured 264 ring drivings from 07-09-2019 to 28-10-2019. During these testing periods, the automatic logger collected the data from the sensors every 5 minutes. In order to obtain a long-term pressure distribution, a second data collection was carried out in Field Case 3 after 4 months of the construction of the tested ring.

There is a certain distance between the outside of the TBM shield and the surface of the tunnel linings. When the TBM is driving forward, a void space, called tail void, is produced due to this distance. This tail void is synchronously backfilled with grouting material. In the case of the QRSTs, the theoretical volume of the tail void is about 6 m^3 for each ring driving. The grouting ratio is defined here to represent the grouting volume in each ring driving and calculated by dividing the actual grouting volume by the theoretical tail void. Previous research (Bezuijen, 2005; Liang et al., 2017) has shown that the pressures on the linings under synchronous grouting were more complex and larger than those during the tunnel operating period, proving the relevance of the current tests. As aforementioned, the selected tested linings were all located in the city suburb and had similar overburdens, providing the environmental conditions to obtain the load distributions under different construction parameters. Hence, in order to clarify the effects of the grouting process and characterize the pressure distributions of QRSTs, different grouting strategies were used in these three cases. Field Cases 1 and 2 had a similar grouting ratio of around 140% while that in Field Case 3 was only 110%. Moreover, the grouting procedures were different in each case. The grout was ejected evenly from eight grouting holes in Field Case 2. In contrast, the top left grouting holes ejected fewer grouting materials in Field Case 1 and the bottom holes ejected fewer in Field Case 3. More details about the grouting situations are presented in Section 5.3.3. The positions of the eight grouting holes can be found in Figure 5.1. Four grouting holes are at the top area with a denser arrangement than the lower four. There are no grouting holes assigned at the waist areas. Instead, the grout at the waists is adjusted by the grout volume ejected from the top holes as the fluid grout tends to flow downwards. Table 5.3 shows an overview of the specific conditions in the three in-situ monitoring tests.

Table 5.3 Overview of the conditions of the in-situ tests.

Field Case	Metro Line	Ring number	Overburden (m)	Grouting ratio	Grouting situation	Duration	
						days	rings
1	3	56	9.12	±140%	Few at top left	4	5
2	3	241	8.30	±140%	Evenly	10	19
3	4	68 and 69	8.30	±110%	Few at bottom	50	261

5.3 Results

Since a relatively normal grouting process in Field Case 2 was adopted, the monitoring results from this case are used in the sections 5.3.1 and 5.3.2 to show a typical pressure distribution around a QRST. The influence of the grouting situations and back-up equipment are analysed in Sections 5.3.3 and 5.3.4. The long-term monitoring results are presented through a comparison with the assumed design load for QRSTs, which are discussed in Section 5.4.

5.3.1 Temporal pressure distributions around the linings

There are three layers of steel brushes on the inside surface of the TBM shield tail. Each layer is enclosed circumferentially to isolate the grease between neighbouring brushes and keep the grease pressure constant. The first two brushes are made of steel wires (Figure 5.4a) and the last one is made of steel plate with higher stiffness to prevent the grout or soil from penetrating into the last grease chamber. The grouting holes (Figure 5.4b) are very close to the last brush to ensure that the grout is immediately backfilled after the linings are pushed out. All these brushes and grease layers work together to fulfil the isolating function of the shield tail and avoid the tunnel linings conflicting with the shield tail directly.

After the shield linings are assembled in the shield, the TBM starts drilling for the space of the next ring. At the same time, the newly assembled linings are pushed into the shield tail. In the case of a QRST construction, the newly assembled ring is firstly pushed to a position in the tail where it touches the steel wire brushes. During the next drilling process, this ring is getting out of the shield tail and the grout starts to exert a pressure on this ring.

(a) (b)

Figure 5.4 Steel wire brushes and grouting holes: (a) Steel wire brushes and inside view on the grouting holes; (b) Outside view on the grouting holes.

The temporal distributions of the pressures on the QRST linings in Field Case 2 are shown in Figure 5.5. Four pressure curves for different positions are presented, including the pressures at the top, waist and bottom, as well as at a point near the grouting hole at the top. The numbers from -1 to 19 at the top of Figure 5.5 represent the number of rings between the tested ring and the TBM shield tail. For example, 5 means that there was a 5-ring distance from the tail to the tested ring. The number -1 means that the tested ring was in the shield and 0 means the TBM tail was passing through the tested ring, i.e. the tested ring was being pushed out. The theoretical pressures from Figure 4.6 for these four measurement points are also shown at the time of 250 h in Figure 5.5.

In practice for Field Case 2, the time needed for each ring driving was different, from 1 hour to 3 hours, depending on the on-site construction conditions. After every driving, around 2 hours were needed for the lining assembly in the shield. Considering other factors, like the construction of the receiving shaft and the transportation control of the dug soil, generally, only 2 rings were executed each day during the measurement period. From the pressure curves, the following can be observed:

(1) Before the time of 10 h, most pressures of the measurement points were close to zero, except for a point with 20 kPa pressure, which means that the loads on the linings when they were in the shield were low.

(2) At 10 h, the tested linings were pushed into the shield tail, starting to have contact with the brush wires. The pressures increased rapidly due to the squeezing of the brushes and the grease between them. As the tested ring kept moving in the shield, the measurement points were not always contacting the brushes and the pressures fluctuated slightly during the following hours.

(3) When the tested ring was pushed through the last brush layer at 15 h, all the measured pressures increased sharply and the peak values of each measurement were similar, between 250 and 300 kPa. The maximum top pressures were nearly twice the theoretical values.

(4) During the following 14-hour standstill, a gradual pressure attenuation was noticed. However the magnitudes of pressure decrease were different, being largest at the top and smallest at the bottom.

(5) During the following drivings, the pressure values were still influenced by the grouting process at the shield tail, but the fluctuation ranges tended to be smaller and smaller with the increase of the distance between the tested ring and the TBM. Small fluctuations could be found at the standstill moments around 35 h. This might be caused by the slight movement of the tested ring when segment assembly is conducted in the shield. This kind of fluctuations tended to be very slight at following standstills.

(6) After the advancement of 9 rings, namely after 120 h, most of the pressure fluctuations during each TBM driving were smaller than 5% of the measured pressure at the corresponding points. It means that the following grouting processes had little influence on the tested ring although slow pressure dissipations (H5, H9 and H18) or increases (H1) still occurred. (7) At the end of the measurement period, the pressures were generally stable and tended to be close to the theoretical pressure values. The pressure at the top almost equalled the static pressure of the whole overburden soil at 141.1 kPa (17 kN/m^3×8.3m).

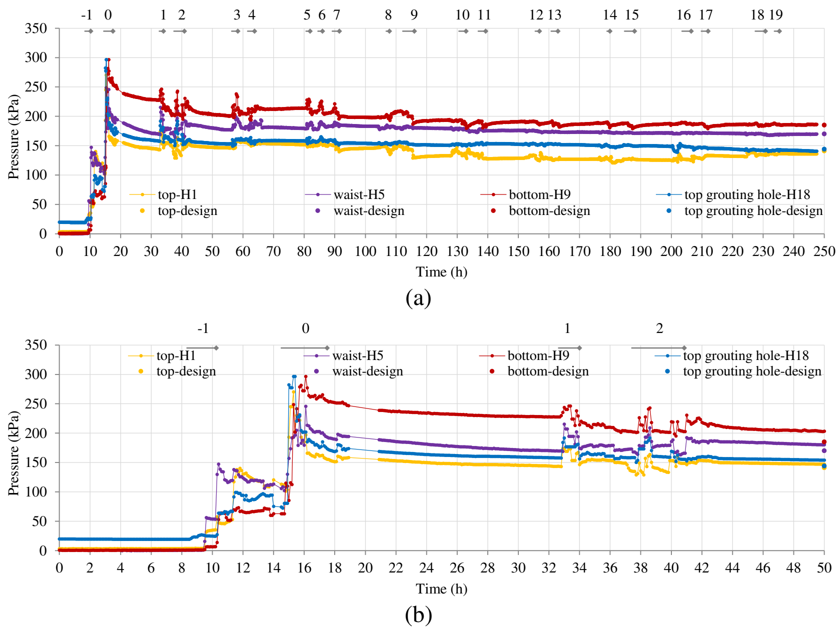

Figure 5.5 Temporal pressure variations of different measuring points in Field Case 2: (a) range from 0 to 250 h; (b) range from 0 to 50 h.

5.3.2 Spatial distributions of the pressures on linings

The spatial pressure distributions around the linings at four different times are depicted and connected with splines in Figure 5.6. These included the time when the tested ring was pushed out from the shield tail, the time when the next driving was conducted after the pushing out of the tested ring, the times when 9 rings and 19 rings had been constructed, or more specifically the times of 15 h, 33 h, 120 h and 240 h in Figure 5.5. Only the pressure values at the measurement points are obtained in the field tests, but a dotted spline is used to connect them for a smooth presentation of the possible pressure distribution. From Figure 5.6, the following phenomena can be observed:

(1) At the time of 15 h when the shield tail was passing through, the grouting load was exerted on the linings directly and the peak pressure appeared at all measurement points. The peak values at the crown and the bottom points were larger than those at the waists due to the layout of the grouting holes, four at the crown and four at the bottom.

(2) For the following drilling stage, at the time 33 h, 18 hours after the tested ring was pushed out, the overall pressures decreased and tended to be evenly distributed, especially at the top area. The decreasing magnitudes at the crown and

the bottom were evident while the waist pressures decreased slightly. The overall pressures at this stage are smaller than when the tested ring was pushed out, which means that the influence of the grouting process decreased quickly along the tunnel longitudinal direction and was very limited for the rings away from the shield tail.

(3) The pressures after 4 and 10 days presented more symmetrical and uniform distributions, and the difference between them were small, which means that the pressures changed slowly to a stable level. From the view of the overall pressure distribution, the deeper the measurement points were, the larger pressures they sustained, which is in agreement with the design load principles for QRSTs in Figure 4.6.

(4) Comparing the ratio between the peak values at 15 h and the stable values at 240 h, these ratios for the top area could reach 2 while these at the bottom and the waist areas were about 1.5 and 1.3, respectively. The grouting pressure had a more significant effect at the top area. Additionally, the pressure difference was large between different points at the top half, which was not observed in previous circular tunnel cases. Perhaps this was due to the fact that a concentrated grouting hole layout was adopted there. This crown pressure distribution might result in large bending moments at the segment T1 (see Figure 5.1 for its position). Moreover, unsymmetrically distributed pressures appeared at the bottom (purple ellipses) and this might cause an overall rotational tendency of the lining structure, resulting in an additional torsion effect during construction. These features are not necessarily considered in circular tunnels. Although the pressure distribution would become more uniform in the long term, the temporally uneven and unsymmetrical pressure distribution should be paid attention to by the designers.

From the in-situ measurement results in Field Case 2, it is obvious that the process of the linings being pushed out of the tail is one of the most critical stages for the construction of QRSTs. The influential range of the grouting process in Field Case 2 is 9 rings. During this period, the grouting process still clearly affected the pressure values although the overall peak pressures tend to decrease and even out.

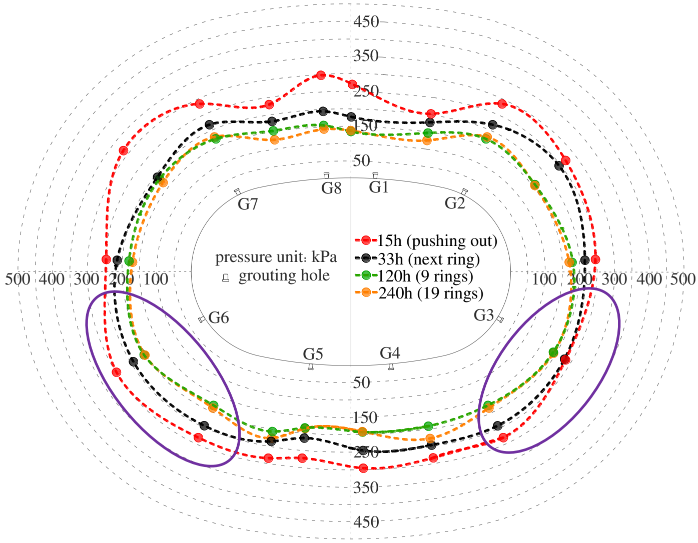

Figure 5.6 Spatial pressure distributions at different stages in Field Case 2.

5.3.3 Influence of grouting situation

Before being pushed out, the linings only experience a low load level in the shield tail. When the last brush layer passes through the tested ring, the grouting pressure is exerted on the linings directly. This process has significant but different effects on the pressures at different measurement points, with the grouting strategy being one of the influential factors. In order to investigate the effect of grouting situations, different grouting ratios and different grout amount assignments are applied as shown in Table 5.3.

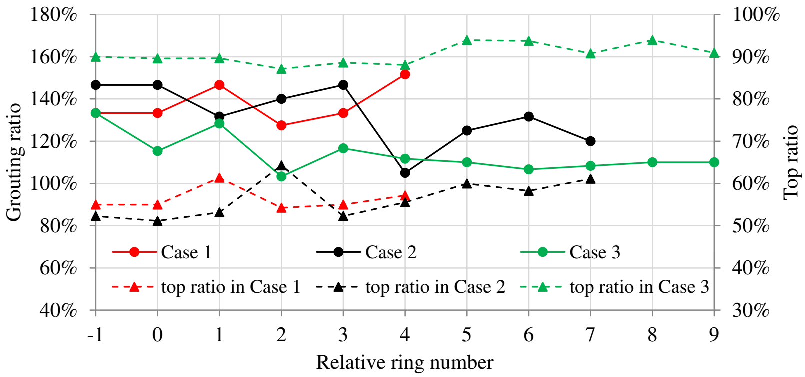

Figure 5.7 Grouting situations in different cases.

According to the daily construction logs, Figure 5.7 shows the records of the grouting ratio in the testing cases. As measurement periods were different in these monitoring cases and the grouting process had a limited influential distance, only related grouting ratios are presented, i.e. 6 rings in Field Case 1, 9 rings in Field Case 2 and 11 rings in Field Case 3. The actual grouting volume should be larger than the theoretical tail void so all the grouting ratios are larger than 100%. In practice, this ratio is changing in every grouting process. It is adjusted based on the daily measured settlements of the nearby surface and buried subsidence points. The abscissa represents the number of rings between the tested ring and shield tail. The numbers -1 and 0 respectively represent the drillings when the tested ring is pushed into the shield tail from the assembly platform and pushed out of the tail. The right ordinate in Figure 5.7 is defined as the top grouting ratio, obtained by dividing the grouting volume injected from the 4 crown grouting holes by the actual total grouting volume.

As Figure 5.7 shows, the grouting ratios in Field Case 1 were between 125% and 150%, generally in the same level of Field Case 2, but they were larger than in Field Case 3 with most ratios below 125%. For the top grouting ratios, a similar range from 50% to 65% was adopted in Field Cases 1 and 2 but this value was quite large in Field Case 3, at around 90%. In Field Case 1, the grouting holes at the top left area were blocked during the drilling process and only a small grout volume was injected from these holes. However, in order to keep the total grouting volume and top grouting ratio, more grout was deliberately injected from the top right holes. The grouting holes were unchoked and worked normally in the following tunnel drillings. For Field Case 3, the grouting ratios were set small to investigate the effects of less grout backfilling on the pressure distributions of this new special-section tunnels. In order to avoid too large immediate settlement of the ground surface on the tested ring, most of the grout was injected from the top grouting holes.

Three moments are selected to compare the differences among the pressure distributions i.e. when the tested ring was pushed out of the shield tail, when the next ring after the tested ring was pushed out and when 9 rings after the tested ring had been pushed out. Due to the monitoring period, the results after 9 rings were not obtained in Field Case 1. The pressures around the linings at these three moments are shown in Figure 5.8.

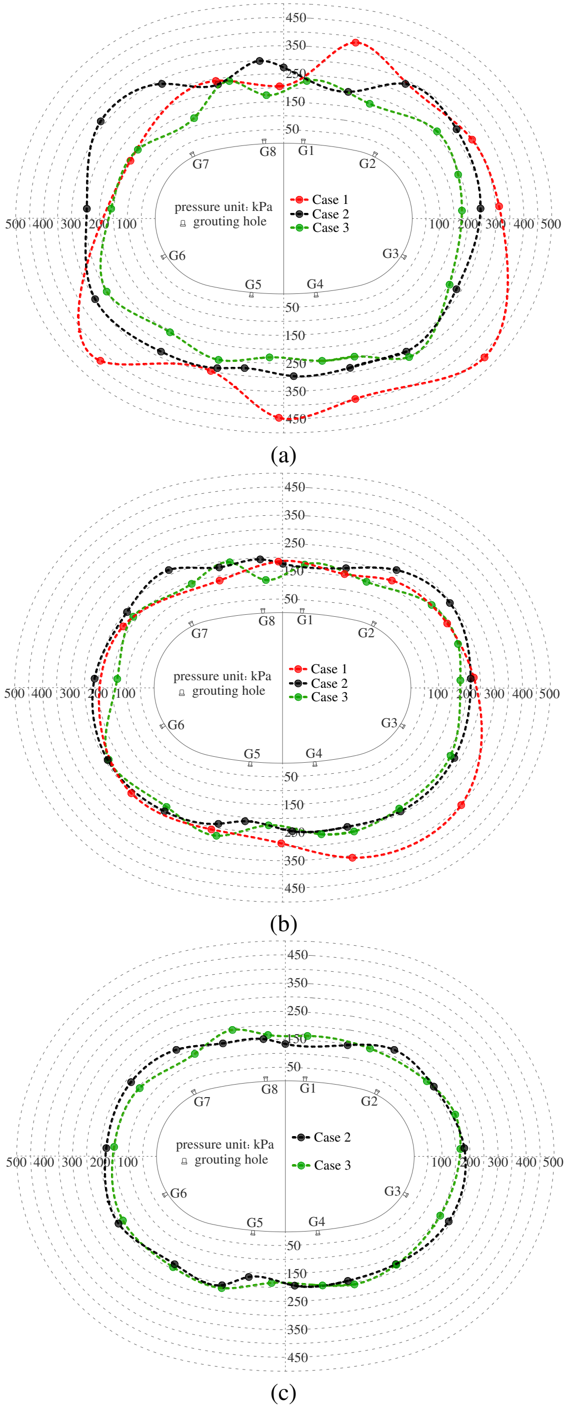

Figure 5.8 Comparisons of pressure distributions in different cases: (a) pushing out of the instrumented ring; (b) pushing out of the next ring; (c) after pushing out of 9 rings.

At the first moment, it is obvious that the pressure distributions were affected by different grouting strategies even with similar overburden depths. From the comparison between Field Cases 1 and 2, it follows that the pressures at the top left area in Field Case 1 were lower than those in Field Case 2 (difference of about 150 kPa) but the reverse phenomenon happened at other areas (larger by more than 200 kPa), resulting in a quite unsymmetrical spatial pressure distribution in Field Case 1. The peak value in Field Case 1 reached 450 kPa or 1.5 times the peak value in Field Case 2 even though a similar total grout volume was injected in these two cases. This means that the grout amount from certain top grouting holes would affect the pressures at the corresponding area considerably and a proper grout assignment for each grouting hole is important. Otherwise, the large peak value and unsymmetrical pattern of pressures might have an adverse influence on the lining structure. Additionally, the soil disturbance caused by this would also influence the surrounding environment. Also, the blocking of the grouting hole should be avoided in construction practice.

When comparing Field Case 2 with Field Case 3, the average pressure level in Field Case 3 was lower than in Field Case 2 due to the lower grouting ratio in Field Case 3. The amount of injected grout at the crown area in Field Case 3 was larger than that in Field Case 2. However, this did not lead to higher pressures at the top area. Conversely, the measured pressure difference between Field Case 2 and Field Case 3 at the top was larger than that at the bottom. In Field Case 3, the pressure magnitudes at the bottom were slightly larger than the average pressure level at the top area. Additionally, the bottom pressures at this moment were also larger than those after a certain time (compared with the curves of Field Case 3 in Figure 5.8b and c). A possible explanation is that the grout from the top grouting holes tended to flow down to backfill the synchronously produced bottom void space, and correspondingly resulted in a pressure loss at the top area. It seemed that the grout backfilling preferentially occurred at the bottom tail void.

Comparing the results in these three cases, it was obvious that the top pressures were all unevenly distributed. The potential risk caused by this situation should be considered in the design practice of QRSTs or other special-section tunnels with similar shape. Among the three cases, the general pressures in Field Case 3 were the lowest. It means that the grouting ratio can affect the pressure levels notably and that the low grouting ratio can help to avoid large structural stresses, leading to a high degree of safety. However, the environmental influence is also a significant concern in practice as the insufficient grout volume will lead to excessive soil settlement and subsidence due to a too large soil stress relief and volume loss. The grouting parameter settings should consider the grouting effect on both the lining response and the environment protection. On the other hand, the relative low pressures at all the sections in Field Case 3 and at the top left in Field Case 1 are the proof that the high squeezing pressure caused by the steel plate of the last brush layer in previous research (Han et al., 2017) does not exist in the case of QRSTs. Otherwise, high pressures would appear in all cases when the steel plate at the shield tail passed through the tested ring.

At the second moment when the ring following the tested ring was pushed out, the pressure distribution in Field Cases 1 and 2 was relatively uniform when comparing with results at the first moment. Field Case 1 still generated smaller pressures at the top left and larger pressures at the bottom right than Field Case 2. The pressure differences between Field Case 1 and Field Case 2 were much smaller than at the first moment. When comparing Field Case 2 with Field Case 3, the overall pressures at the bottom were at a similar level while the top and waist areas in Field Case 2 experienced larger pressures than in Field Case 3. The general pressure difference between Field Case 2 and Field Case 3 at this moment was also smaller than at the first moment. This means that the uneven pressures caused by different grouting strategies disappear considerably already after the drilling of one ring distance and the influence of the grouting process on the tested ring attenuates quickly once the tested ring is pushed out.

At the third moment, only the results in Field Cases 2 and 3 are compared. Although different amounts of grout were adopted, the pressures in Field Cases 2 and 3 had a similar distribution pattern and value ranges. The pressures were generally uniform and symmetrical except for a few measurement points. The top pressure and waist pressure values in Field Case 2 were still larger than in Field Case 3, but remained within 50 kPa difference. The pressure generally went up with the increase of the depth of the measurement points. Even though the pressures at the first moment in Field Case 2 and Field Case 3 deviated a lot, it is obvious that the pressure distributions were tending to stabilize at a similar state in the following days. It means that the different grouting strategies do not affect the final pressure distributions in soft soils from the long-term perspective.

5.3.4 Influence of the back-up equipment and carriages

The results after 9 ring drivings in Field Cases 2 and 3 are compared in the last section. Although the TBM shield is going further and further from the tested ring and the pressures from the outside seem to be stable, the temporary and varying loads of the following tracks, back-up systems and carriage facilities are still exerted from the lining’s inside. These loads result in pressure changes and this phenomenon is monitored and discussed in this section.

When there is a certain distance between the tested ring and the TBM shield, the effects of the grouting process on the pressures around the tested linings become very weak, and the overall pressures appear to be uniformly distributed. On the other hand, since the shield tail of the TBM is followed by a set of back-up equipment and the length of the whole set is tens of meters, and though the grouting process only has a limited influence on the lining pressures, other construction loads are still exerted on the lining's inside surface. The whole TBM consists of two parts. The first part mainly includes the cutter system, the assembling system and the thrust system, which are all located in the shield. The second part is the back-up equipment such as the grout pumps, the soil conveyers, the operating room etc. These are integrated into a working platform which can move as a whole on a track. The track is immediately paved once a new ring is pushed out of the shield tail and the back-up equipment moves forward on it. Behind the back-up equipment, there is a series of carriages for the transportation of the lining segments and the soil dug from the TBM cutter. These carriages stay behind the back-up equipment when the TBM is drilling and the segments are being assembled. After the drilling and assembly, the carriages are trailed into the working shaft to receive the segments for the next ring and to unload the soil by cranes. The construction loads caused by the back-up equipment and the material transportation system were theoretically assumed in shield tunnel analysis by some authors (Kasper and Meschke, 2004; Talmon and Bezuijen, 2013a; b), but measurements of this kind of loads were not conducted before.

In the case of a QRST, the back-up equipment weighs 350 t and its length covers 44 rings behind the shield tail. The back-up equipment is transited on two pairs of tracks, one on each side of the interior column. There are 7 carriages on each pair of tracks, three for segments, three for soil tanks and one for the operating room. The carriages can cover a distance of 20 rings and weigh more than 230 t, including 48 t of segments and 146 t of dug soil (about 80 m^3) and the dead weight of the carriages.

Figure 5.9 shows four pressure curves in Field Case 3 during the period from 100 h to 280 h. At the time of 148 h and 216 h, there were respectively 44 rings and 64 rings between the tested ring and the TBM shield tail. This means that the back-up equipment was certainly on the tested ring before 148 h, the carriages might be on the tested ring from 148h to 216 h and only tracks (carriages occasionally passing by) were on the tested ring after 216 h. As presented in Figure 5.9, the bottom pressure was affected severely by the construction loads caused by the movements of equipment and carriages. This was because these loads are exerted on the bottom directly. In contrast, the other three curves only had notable fluctuations during the period when the carriages were on the tested ring. Also, the fluctuating values, especially at the top area, were smaller than those at the bottom.

During the period from 148h to 216h, the carriages only stayed in the tunnel when the segments were being assembled or the TBM advanced. The pressures showed a cyclic pattern, which matched well with the logs of construction activities. The moments when the fluctuations of these four measurement points happened were equal but the fluctuating directions were different. For the points at the bottom half (H9 and H13), the pressures tended to increase while the opposite happened at the top (H2 and H18). It meant that the cyclic carriage loads on the inside of tunnels induced a new pattern of pressure changes. It was different from the situation when the grouting process actively increased the pressures of all the measurement points from the outside of the tunnel.

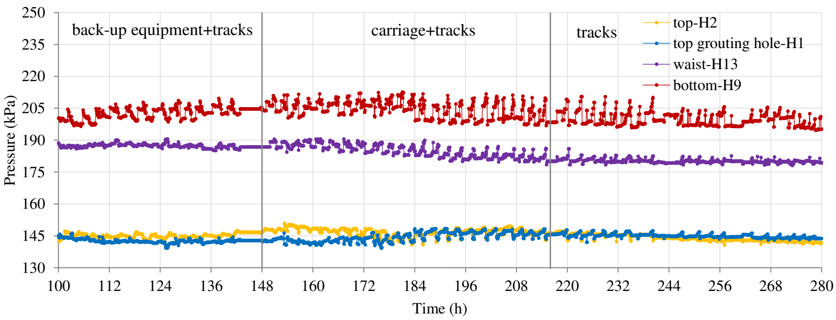

Figure 5.9 Pressure changes of different measuring points in Field Case 3.

In order to give an overall description of the pressure changes of all measurement points, the pressure gradients are introduced here. In previous research (Bezuijen et al., 2004; Gil Lorenzo, 2019) it was observed that the measured pressures around the tunnel linings in their in-situ tests tended to be uniformly distributed and became larger with increasing depth. Eq. (5.1) was put forward to study the variation related to the buried depth of the measurement points.

$$P_{tar} = a_{gra} \cdot D_{tar} + b_{top} \tag{5.1}$$

In Eq.(5.1), P_{tar} (unit: kPa) is the expected pressure of the target point while D_{tar} (unit: m) is the depth of the corresponding point from the top of the lining. An example in the quasi-rectangular case is shown in Figure 5.10. Previous researches focused on gradient a_{gra} to study the pressure changes but less attention was paid to changes of the intercept b_{top}, representing the top pressure value.

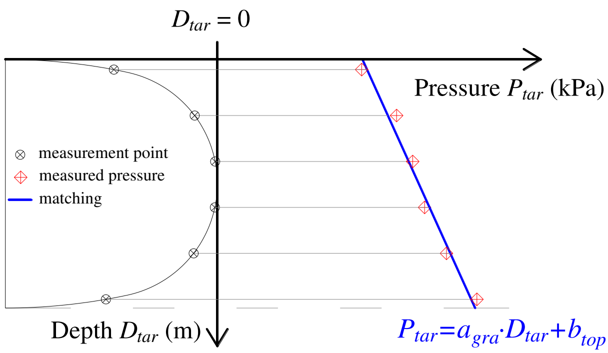

Figure 5.10 Example of the gradient and intercept.

Eq.(5.1) is used to describe the overall pressure distributions for the period from 100 h to 280 h in Field Case 3 and the results, as well as the bottom pressure values calculated through Eq.(5.1), are depicted in Figure 5.11. In this calculation, the monitoring results of the right top and right bottom (H1, H9, H10, H18 in Figure 5.1b) are excluded in the linear matching to avoid calculation errors due to the small depth differences there.

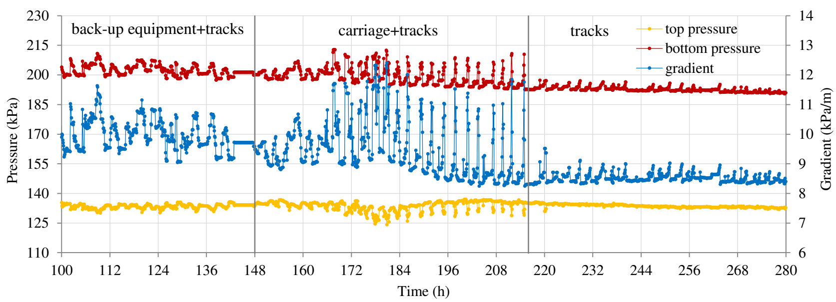

Figure 5.11 Gradient and intercept in Field Case 3.

Through the linear fitting, the top pressures always fluctuate around 135 kPa. This value is close to the whole overburden pressure of 141.1 kPa (17 kN/m^3×8.3m). For the bottom pressure, after 148 h, there is no back-up equipment on the tested ring anymore and the carriages only stay on the tested ring sometimes, which means the loads from the inside decreases. The lowest pressures at the outside bottom also show a decreasing tendency after 148 h. It is clear that the gradients and the bottom pressure go up when the top pressure goes down. The magnitudes of pressure changes depend on the exerted loads. The average load of the carriage is bigger than the back-up equipment and larger fluctuations of gradients and pressures changes are observed during the carriage period. When the TBM is far enough, there are only tracks in the tested ring with occasionally carriages passing by, and the top pressure keeps almost constant and the gradients and bottom pressures slightly increase occasionally. This means that the loads inside the tunnel indeed influence the outside pressures. Although the effect of back-up equipment and carriers only attributes to a maximum of 10% of the theoretical pressures, it needs to be paid attention to in cases of tunnels with extremely shallow overburdens. In addition, this kind of load also might influence the hardening process of the grout material around tunnel linings.

When the carriages move in the tested ring, this temporary and varying load can lead to an overall downward tendency of the lining structure and then result in a pressure decrease at the top and an increase at the bottom. From this prospect, in the current case of shallow soft soil, the outside pressures react with the inside load changes and the surrounding soil behaves like an elastic foundation to hold the tunnel. Then the buoyancy exerted by the surrounding soil should be equal to the whole weight of the tunnel and the temporary loads inside. A direct measurement of the buoyancy proves to be difficult. The dense layout of the 18 measurement points provides the possibility to calculate the buoyancy values. The buoyancy is the vertical resultant force of the surrounding pressures. Every measurement point is assigned a responsible area based on the interval between two neighbouring measurement points and the total pressure on the area can be calculated by multiplying the measured pressure by the corresponding area. Then, only the vertical components were summed up to estimate the buoyancy.

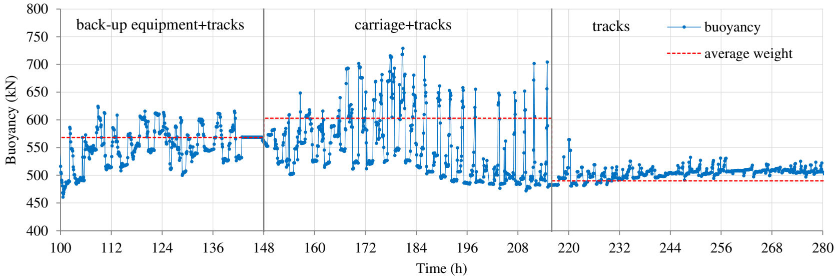

Figure 5.12 Calculated buoyancy in Field Case 3.

The calculated buoyancy is shown in Figure 5.12. The weight of the segments in a ring is 470 kN. The average weight of the back-up equipment on a ring, 1.2m wide, is 78 kN and that of the carriages is 113 kN. Considering the weight of the tracks, pedestrian paths and other temporary installations as 20 kN, the average weight of a lining ring in these three periods are 568kN, 603kN and 490 kN. These average weights are also shown in Figure 5.12 to compare with the calculated buoyancy results. Since the back-up equipment and carriages move on wheels and the loads from the wheels are transited to the tested ring through tracks, the calculated buoyancies were varying, even when only the back-up equipment is slowly moving on the tested ring (from 100 h to 143 h). It can be observed that during the period from 143 h to 148 h when the construction stops for 5 hours the calculated buoyancy approximates the average weight. Since the carriages, whose weight is larger than that of back-up equipment, are pulled forward and backward in the tested ring to transport segments and soils, most of the calculated buoyancy increases a lot when the TBM is drilling between 148 h and 216 h. However, the lowest buoyancy values gradually decrease to the weight of the linings. After 216 h, the buoyancy keeps close to the average weight. Although the exact loads of the equipment and carriages on the tested ring cannot be calculated due to the complexity of the force transfer, the calculated buoyancy fluctuates near the average weights in different stages with the pace of construction activities. The pressures around the linings behave like a counterforce to resist the load from the tunnel rather than an active force exerted on the rings when the lining rings are pushed out.

5.4 Comparison between the proposed design pressures and field monitoring results

5.4.1 Comparison of long-term pressures

The long-term observations for this new type of shield tunnel are compared with the assumed theoretical pressures from the design model in Figure 4.6, and a grouting pressure distribution mode is proposed to predict pressure distributions at the moment of pushing out.

Since a relatively long monitoring period (50 days) and a second data collection (4 months after the lining construction) were conducted in Field Case 3, the monitoring results of this case are selected to present the long-term pressure distributions of QRSTs and to compare with the theoretical pressures calculated on the basis of Figure 4.6. The buried depth is 8.3 m in Field Case 3. The average weight of the soil and the coefficient of lateral pressure K_{lat} are 17 kN/m^3 and 0.7. For the calculation of the triangle-shaped resisting pressure e_3 in Figure 4.6, the lateral deformation of the lining structure refers to the indoor full-scale experiment as introduced in Chapter 4 with an overburden of 10 m, which is 4.68 mm (Liu et al., 2018c). From the site geological survey report, the coefficient of the horizontal subgrade reaction K_{lat} of the related soft soil is 5.1 kPa/mm. Then the peak value of the resisting pressure is approximately 11.7 kPa at each side. The corresponding pressures in the design model from Figure 4.6 are listed in Table 5.4.

Table 5.4 Pressures in the design model (unit: kPa).

Parameter	Top pressure q_t	Arc pressure q_a	Bottom counter pressure q_b	Top value of lateral pressure e_1	Bottom value of Lateral Pressure e_2	Peak value of resisting pressure e_3
Value	141.1	58.8	185.5	98.8	181.1	11.7

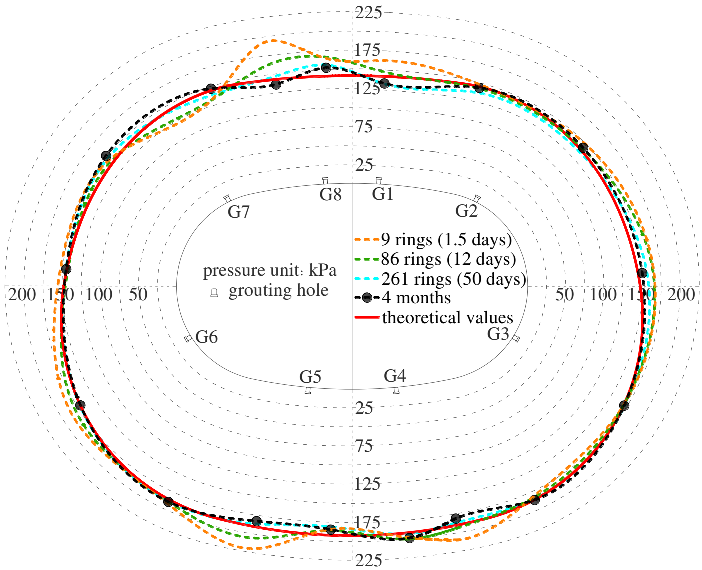

Figure 5.13 Pressures at different times in Field Case 3 and comparison with theoretical pressures.

Figure 5.13 shows the comparison between the theoretical pressure values and the measured long-term pressure values. The measured pressures are selected when the distances between the tested ring and the TBM reaches respectively 9, 86 and 261 rings. The corresponding time values after the tested ring is pushed out, are 1.5, 12 and 50 days. Additionally, the values from the second data collection are presented by black dots in Figure 5.13. Although the grouting process at the shield tail only has limited influence on the tested ring when there is a 9-ring distance to the shield machine, the measured pressures are not fully uniform and some of the values are far different from the theoretical values. After 12 days of lining construction, the load values change a lot at the top and bottom areas and the distribution tends to be more uniform. The differences between the pressures after 50 days and 4 months are much smaller than those between 1.5 days and 12 days or those between 12 days and 50 days. This means that few load changes happen after 50 days. The pressures after 50 days and 4 months are generally equal to the theoretical values retrieved from the load distribution in Figure 4.6, proving the applicability of the proposed load distributions for the design of QRSTs. On the other hand, the speed of the load changes slows down with time and the non-uniform load distribution caused by the grouting process or other construction loads need around 50 days to be relieved in the soft soils in the current case.

5.4.2 Comparison of grouting pressures

Few studies focused on the pressure distributions when the tested ring was pushed out, although the pressures at this moment are larger and less uniform than the theoretical long-term pressures in Figure 4.6. I.T.A. (2000) suggests to consider the grouting pressure on segments as a triangle mode with the maximum value at the grouting hole. Ding et al. (2019) excavated the soils around a scaled QRST after synchronous grouting and found that the average influence range of a single grouting hole is 720mm, taking about 15% of the tunnel circumference. A cosine function was proposed to describe the grouting pressure distribution, but it could not predict the pressures for the areas out of the influence range of grouting holes. Xiao et al. (2016a; 2016b) found that the influence radius of a single grouting hole was 2 m through a field test in Shanghai and proposed to consider the grouting pressure distributions as a combination of a triangular load and the theoretical long-term pressures from the design model. However, this grouting pressure mode was not compared to their field test results.

In this paper, from the aspect of practical monitoring results, the grouting pressure at a certain point on the segment is assumed to be a combination of the theoretical pressures from Figure 4.6 and a cosine function according to Eq. (5.2). Herein, D_{range} and x represent the influence range of a grouting hole and distance (positive value) from a certain point to the corresponding grouting hole, $P_{t,x}$ is the theoretical long-term pressure of this point in Figure 4.6, P_{grout} and $P_{t,gh}$ represent the grouting pressure and theoretical pressure at the corresponding grouting hole. The value of D_{range} is adopted as 15% of the circumference length of a QRST, namely 4.32 m in this case, whose influence radius is close to that found by Xiao et al. (2016a). For example for the grouting hole G7 in Field Case 2: at the moment of being pushed out, the measured pressure is 283.0 kPa and the theoretical pressure from Figure 4.6 is 142.6 kPa. Then the grouting pressure for a certain point near G7 can be expressed as $P_x = P_{t,x} + 140.6 \cdot \cos\frac{\pi}{4.32}x$ with x ranging from 0 to 2.16 m.

$$P_x = P_{t,x} + \left(P_{grout} - P_{t,gh}\right) \cdot \cos\frac{\pi}{D_{range}}x \tag{5.2}$$

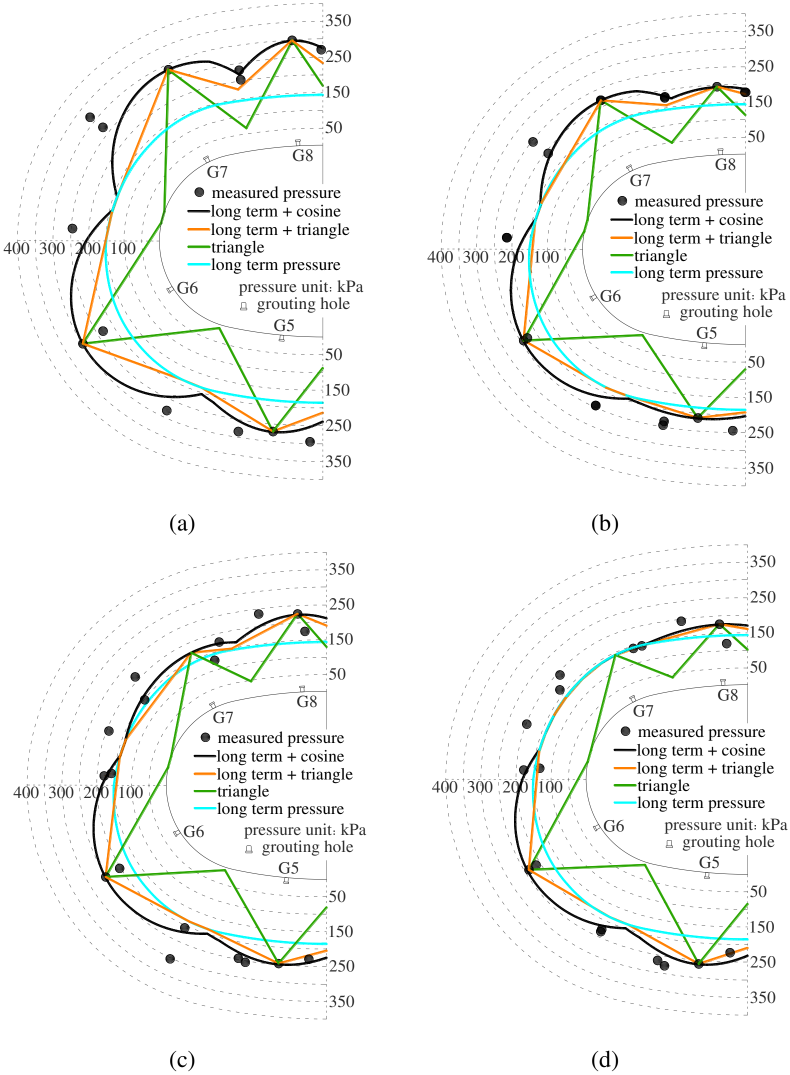

Figure 5.14 Comparison among different grouting pressure distribution modes: (a) Pushing out of the instrumented ring in Field Case 2; (b) Pushing out of the next ring in Field Case 2; (c) Pushing out of the instrumented ring in Field Case 3; (d) Pushing out of the next ring in Field Case 3.

Figure 5.14 shows the comparison between the proposed grouting pressure distribution mode and the measured pressures in Field Cases 2 and 3. The moments when the tested ring and the next ring are pushed out are chosen herein as the grouting process has a relatively strong effect at these moments. Only the left half of the proposed mode is depicted but the measured pressures on the right half are mirrored to the left. Additionally, the triangular mode and the combination mode of triangular and theoretical pressures are also shown in Figure 5.14. Due to the small amount of measurement points at the grouting holes in Field Case 1, its results are not shown here.

The pressures from the triangle mode change considerably around the tunnel linings and they are too non-uniform when compared with the measured results. For the pressures between grouting holes, it cannot replicate the practical values. The same is true for the combination mode of triangular and theoretical pressures. The proposed combination mode of a cosine function and the theoretical pressures gives good predictions for most of the measurement points. Therefore, the proposed grouting pressure mode is recommended to simulate the actual grouting pressure distributions in the segments' construction-stage design.

5.4.3 Relationship with design load of circular tunnels

Generally, the design method for QRSTs mainly refers to that for circular tunnels, including two parts, the pressure distribution and structural calculation. This chapter focuses on the former part. From the long-term perspective, the monitored results coincide well with the theoretical pressures from the design loads referring to circular tunnels, which is a good proof that QRSTs, as well as possibly other special-section tunnels, share the same pressure calculation method as used in the design of circular shield tunnels.

For the construction load, from the in-situ monitoring tests in this chapter and previous studies for circular shield tunnels, the segments sustain the largest pressures when linings are pushed out of shield tail in both quasi-rectangular and circular tunnels. I.T.A. (2000) suggests a triangular distribution mode to be considered in the grouting pressure distribution but few other standards give specific guide for this construction load. The triangular pressure distribution deviates a lot from the field testing results of QRSTs, especially for regions between grouting holes. Based on the monitored pressures, a mode combining cosinusoidal and theoretical long-term pressures is proposed for QRSTs.

On the other hand, some unique aspects might be considered in QRSTs. Unlike the small arc at the waists with a natural good resistance for surrounding pressures, the crown area tends to be flat and is connected with the interior column, resulting in a complex force distribution there. The joint area of column and segments is proven to be a weak part of the lining structure (Liu et al., 2018c). However, non-uniform pressures at the crown are observed in all test cases and the peak pressure is twice as high as the corresponding theoretical pressure. An uneven pressure distribution mode at the crown is suggested for QRSTs. When a certain grouting hole is temporarily blocked or an improper grout volume assignment in grouting holes is conducted, an unsymmetrical pressure distribution appears, possibly inducing local large bending moments in the ring or an additional torque between rings. The potential partial grouting pressure mode is another special feature of QRSTs.

5.5 Conclusions

Three in-situ monitoring tests with different grouting situations for QRSTs in soft soils under shallow overburdens were conducted, and the temporal and spatial distributions of the pressures around the lining structure were measured and analysed. Summarizing the results in this chapter, the following conclusions for QRSTs can be drawn:

(1) The steel brushes and plates in the shield tail have small contributions to the lining pressures. When the lining is pushed out of the shield tail, peak pressures appear and these pressures are primarily caused by the injected grout. The peak pressures at the waists are smaller than those at the crown and the bottom where the grouting holes are concentrated. Comparing the ratios between the peak pressures and the stable values in Field Case 2 with a relatively normal grouting situation, the ratio at the top areas could reach a value of 2 while these ratios at the bottom and the waist areas were about 1.5 and 1.3.

(2) Non-uniformly distributed top pressures are observed in all tests, and these might result in large local bending moments at the crown area. Unsymmetrical pressure distributions appear on the sides of the lining. The left-right unsymmetrical grout assignment would augment this phenomenon. It might cause an overall rotational tendency of the lining structure and lead to an additional torque during the construction. These potential risks are unique concerns for QRSTs and should be specially considered.

(3) The effect of the grouting process happening at the shield tail attenuates quickly in the longitudinal direction as the peak pressures decrease a lot once the tested ring is pushed out. The grouting process during tunnel construction has an influential range of 9 rings. Beyond this range, most of the pressure fluctuations during TBM drillings are smaller than 5% of the corresponding measured pressures. From the long-term perspective, the pressure distributions tend to stabilize at a similar state, and different grouting strategies will not affect the final pressure distributions.

(4) The varying and temporary loads of the back-up equipment and carriages inside the tunnel influence the pressures outside the linings. This kind of load

seems to lead to an overall downward tendency of the lining structure and to result in a pressure decrease at the top and an increase at the bottom. By evaluating the lining buoyancy from the monitoring results, the calculated buoyancy fluctuates around the average weights of the tunnel at different stages and changes with a coincident pace of construction activities. The pressures around the lining perform as a counterforce to resist the load from the tunnel, rather than an active force exerted on the segments, such as when the lining was pushed out, and the surrounding soils would behave like an elastic foundation to hold the tunnel.

(5) For the shallow buried QRSTs in soft soils, the applicability of the proposed load distributions referring to the design model of circular tunnels is proven through comparison with long-term monitoring results. The speed of the pressure changes slows down with the increase of time after the linings are constructed. The influence of the grouting process or other construction loads on the lining pressures needs about 50 days to be relieved.

(6) A pressure mode combining cosinusoidal pressures and theoretical long-term pressures is proposed. It can give relatively good predictions for the grouting pressures when lining segments are pushed out and it is expected to guide the segment design for the construction stage.

Through the three in-situ tests, the influence of grouting situations and the following loads on the pressure distributions of QRSTs, as well as the applicability of the design model for long-term load distributions, are investigated. Additionally, a pressure distribution mode for the construction stage is proposed. However, the research on lining pressures in the conditions of different overburdens or different strata has not been carried out. In the future, further in-situ tests and theoretical analyses for pressure calculations need to be conducted.

Chapter 6

Analysis and discussion of QRST linings based on the developed numerical model

6.1 Introduction

The exerted pressures from the surrounding soils play an essential role in a shield tunnel design, generally determining the stress level in the lining for a specific tunnel shape and then affecting the segment design, such as the related material, size and joint locations. After the verification of the proposed pressure distribution for the QRSTs in Chapter 5, the uniform pressures can replace the point loads to investigate the structural performance under different loading conditions through the proposed QRST model. In this chapter, different pressure settings are assumed to investigate their effects. Firstly, a comparison between the uniform pressures and the point loads in the indoor experiments is made. The deviations caused by the point loads and limitations of this loading method are discussed. Secondly, the circumferential joint stiffness is considered in the three-ring model to simulate the neighbouring rings' influence of a staggered assembly for the QRST segments. The bending moment transfer between rings and a comparison with the MRM method are analysed. Following that, the influence of different parameters related to the assumed pressures and soil reactions is investigated, including the coefficient of lateral pressure, the coefficient of subgrade reaction and the partial offset surcharge. Finally, based on the observed on-site pressures in the field test, a preliminary case study is conducted to evaluate the impact of the synchronous backfill grouting on the segmental lining that is just being pushed out of the shield tail and the influence of different grouting pressure attenuations of the nearby segmental linings.

6.2 Structural analysis with proposed pressure distributions and deviations caused by indoor point loads

Although some indoor full-scale shield tunnel lining tests were done in previous studies (Blom et al., 1999; Schreyer and Winselmann, 2000; Nakamura et al., 2003; Chow, 2006; Lu et al., 2006; Huang et al., 2019), an effective comparison between the point loads in indoor tests and the uniform loads in design models has not been investigated. Therefore, an analysis of the applicability of the indoor point loads is necessary. After the pressure distribution for the case with an 8.30-meter was verified in the last chapter, the assumed pressure distributions in Section 4.3.1 are used in the proposed full-ring calculation model to compare with the corresponding point loads in the indoor experimental cases from Section 4.3.2. The uniform pressure distributions of the indoor Experimental Case 1 and Experimental Case 3 (with left partial offset surcharge of 30 kPa) are illustrated in Figure 4.6, and the pressures in Experimental Cases 2 are shown in Figure 4.7. The corresponding parameters in these three cases are presented in Table 6.1. For a better simulation of the resisting pressures of the reaction from the surrounding soils, these pressures are exerted by the soil springs along the whole periphery of the QRST lining model. These springs can only take effect when the lining deforms outward into the soil. Based on the site geological survey report, the coefficient of subgrade reaction K_{res} of the related soft soil in Experimental Case 1 is 5.1 kPa/mm while that in Experimental Cases 2 and 3 is 7.2 kPa/mm.

Table 6.1 Pressures in the design model for indoor experiments (unit: kPa).

Parameter	Experimental Case		
	1	2	3
Top pressure q_t	200.0	161.0	326.0
Arc pressure q_a	58.8	26.1	58.8
Bottom counter pressure q_b	242.0	143.0	368.0
Top value of lateral pressure e_1	140.0	64.4	249.2 (left), 228.2 (right)
Bottom value of lateral pressure e_2	228.2	86.8	337.4 (left), 316.4 (right)
Top water pressure w_1	-	165.0	-
Bottom water pressure w_2	-	235.0	-
Partial offset surcharge q_p	-	-	30.0

Figure 6.1 presents the comparisons of the unfolded bending moments and axial forces in Experimental Cases 1 and 2, while Experimental Case 3 is shown in Figure 6.2. The bending moments and axial forces at the key sections JM1 to JM10 and convergence deformations at D1 to D3 measurement points are summarized in Table 6.2 and Table 6.3, respectively. In addition, in order to investigate the influence of the lining's dead weight, the corresponding cases without gravity are also calculated. Due to its limited influence, the results are only added in Figure 6.1, Figure 6.2 and Table 6.3 for brevity.

Firstly, considering the axial forces, their values at the key sections JM1 to JM10 in these three experimental cases range from 500 to 600 kN/m, from 750 to 920 kN/m, and from 870 to 1050 kN/m, respectively. In contrast, except for the top area, the axial forces from uniform pressures are generally 150 kN/m larger, or up to 21% difference. When comparing the results with and without the lining's dead weight, only differences of up to 7% (within 50 kN/m) appear at the waist areas, i.e., JM3 and JM8. The uniform pressures have two main differences from the point loads. The first is that the lateral pressures linearly vary with the depth increase, and the second is the lining's dead weight. The point loads cannot simulate these two differences well because of the balance required between the top and bottom areas and the lining's horizontal lying-down position in the indoor experiments. The former factor has a larger influence than the latter. As a large axial force is beneficial to cracking and joint openings, small axial forces are preferable in the point load arrangement to achieve a high safety factor for the section design. On the other hand, the horizontal pressures are calculated by multiplying the vertical pressures by a lateral coefficient less than 1, and therefore the largest axial forces appear at the waist areas.

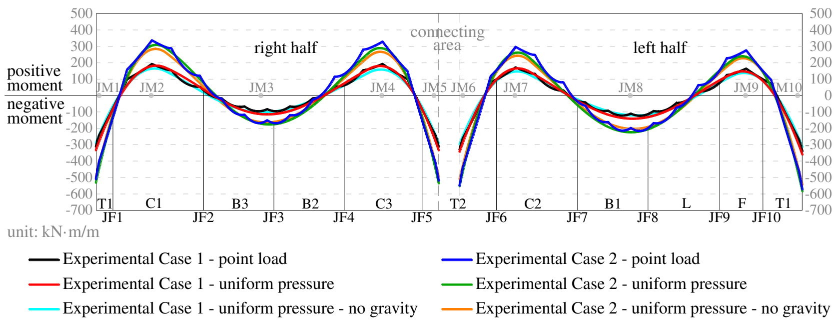

(a)

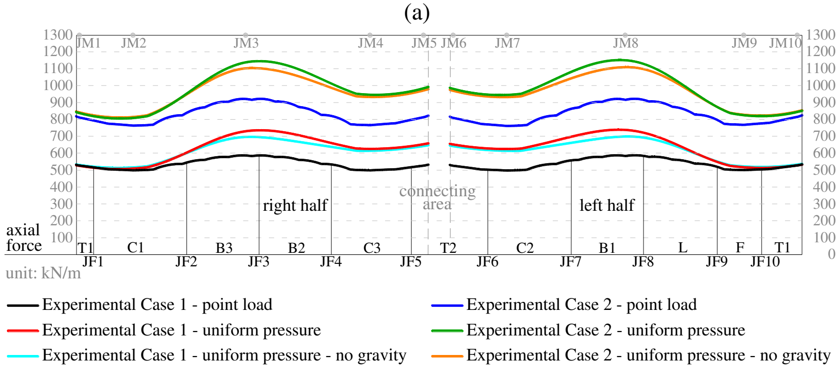

(b)

Figure 6.1 Diagram of the bending moment and axial force in the indoor Experimental Cases 1 and 2: (a) bending moment; (b) axial force.

Secondly, considering the bending moments, it is evident that the moment distributions from uniform pressures are smooth, while those from point loads have inflection points. These bending moment changes are unavoidable as the point loads are perpendicularly exerted on the segment surface, resulting in sudden force changes along the lining. Generally, the bending moment distributions from point loads and uniform pressures are similar in Experimental Cases 1 and 2 with a difference up to 15% except for the key sections with small moment values, like JM3 and JM8, as shown in Table 6.2. However, when it comes to Experimental Case 3, the results from point loads deviate notably from uniform pressures in the right half, up to 49% difference. On the other hand, the differences in the left half are moderate, up to 18%. Due to the partial offset surcharge assumed on the left side, the point loads are preferably arranged to simulate the bending moments in the left lining, and the point loads on the right side are adjusted for the overall structural balance. In addition, the influence of the lining's dead weight on the bending moments is limited, resulting in a difference of up to 7%.

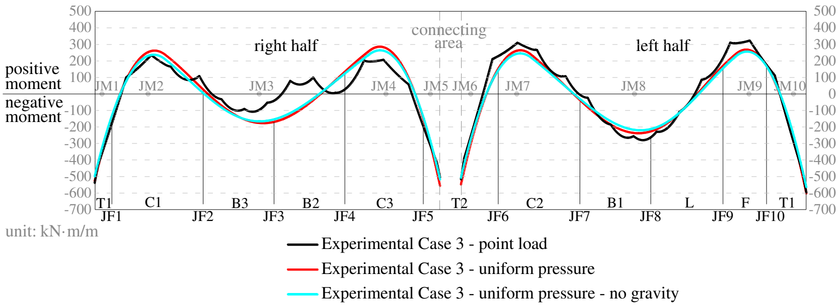

(a)

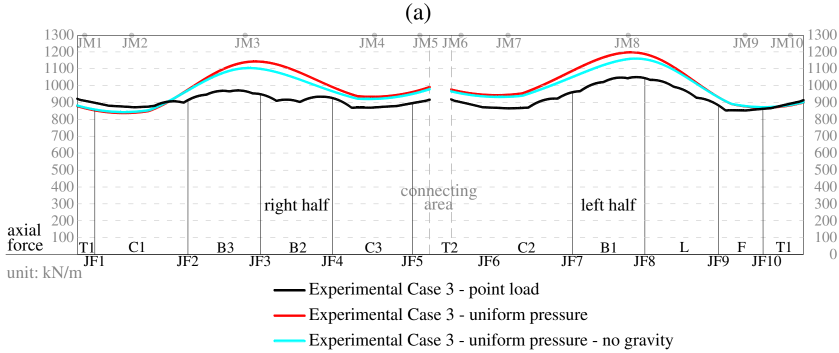

(b)

Figure 6.2 Diagram of the bending moment and axial force in the indoor Experimental Case 3: (a) bending moment; (b) axial force.

Table 6.2 Comparison of bending moments and axial forces at key sections between models with point loads and uniform pressures (bending moment unit: kN·m/m, axial force unit: kN/m).

Experimental Case	Key section	Model with point loads		Model with uniform pressures		Ratio (point loads/ uniform pressures)	
		Bending moment	Axial force	Bending moment	Axial force	Bending moment	Axial force
1	JM1	-235	-529	-268	-527	0.88	1.00
	JM2	192	-501	180	-511	1.07	0.98
	JM3	-95	-589	-114	-733	0.83	0.80
	JM4	193	-500	179	-628	1.08	0.80
	JM5	-235	-528	-267	-655	0.88	0.81
	JM6	-254	-528	-276	-654	0.92	0.81
	JM7	171	-499	165	-627	1.04	0.80
	JM8	-111	-586	-142	-740	0.78	0.79
	JM9	164	-502	145	-518	1.13	0.97
	JM10	-262	-529	-295	-530	0.89	1.00
	JM11	-23	-1038	-17	-1017	-	1.02
2	JM1	-312	-809	-324	-834	0.96	0.97
	JM2	318	-767	299	-811	1.06	0.95
	JM3	-168	-925	-171	-1140	0.98	0.81
	JM4	303	-770	282	-949	1.07	0.81
	JM5	-305	-810	-307	-980	0.99	0.83
	JM6	-305	-804	-288	-975	1.06	0.82
	JM7	297	-764	261	-949	1.14	0.81
	JM8	-205	-921	-224	-1153	0.92	0.80
	JM9	276	-771	236	-827	1.17	0.93
	JM10	-296	-808	-288	-837	1.03	0.97
	JM11	-46	-1636	-32	-1642	-	1.00
3	JM1	-346	-914	-330	-870	1.05	1.05
	JM2	220	-876	255	-842	0.86	1.04
	JM3	-94	-971	-177	-1143	0.53	0.85
	JM4	185	-874	276	-937	0.67	0.93
	JM5	-326	-907	-324	-977	1.01	0.93
	JM6	-243	-905	-285	-968	0.85	0.93
	JM7	310	-868	263	-949	1.18	0.91
	JM8	-264	-1048	-238	-1201	1.11	0.87
	JM9	323	-856	266	-880	1.21	0.97
	JM10	-305	-897	-287	-886	1.06	1.01
	JM11	-102	-1661	-45	-1661	-	1.00

Thirdly, for the convergence deformations at D1 to D3, the differences in Experimental Cases 1 and 2 are generally not more than 20%, while Experimental Cases 3 shows relatively large differences with a relative value up to 56% at D3 measurement. A self-balanced loading is required under the point-load testing situations in indoor experiments. However, the soil springs around the lining periphery can provide passive soil reactions to balance the offset surcharge. This spring simulation method is more realistic for the actual soil conditions around a shield tunnel. It can help to explain the large deformation differences caused by point loads in a situation with an unbalanced load, such as the partial offset surcharge. It is noticed that most of the deformations from the point loads are larger than those from the uniform pressures, which might be explained by the smaller axial forces in the calculations with point loads. When comparing the results with and without the dead weight of the tested ring, the largest difference of 20% appears at D1 measurement in Experimental Case 1.

Table 6.3 Comparison of convergence deformations between the models with point loads and uniform pressures (unit: mm).

Experimental Case	Convergence deformation	Model with point loads	Model with uniform pressures		Ratio	
			With gravity	Without gravity	point loads/ uniform pressures with gravity	uniform pressures without gravity /with gravity
1	D1	-3.58	-3.93	-3.43	0.91	0.87
	D2	4.65	4.81	3.83	0.97	0.80
	D3	-7.46	-7.14	-6.08	1.04	0.85
2	D1	-5.42	-5.32	-4.96	1.02	0.93
	D2	9.10	7.42	6.39	1.23	0.86
	D3	-12.96	-11.21	-9.97	1.16	0.89
3	D1	-0.41	-4.61	-4.25	-	0.92
	D2	9.45	7.96	6.90	1.19	0.87
	D3	-19.91	-12.78	-11.5	1.56	0.90

Based on the above comparisons and discussions, the following conclusions can be drawn. Firstly, gravity has a limited influence on the axial forces and bending moments, up to 7% difference, and a relatively larger influence on the deformations, up to 20% difference. The linearly varying lateral pressures mainly lead to higher axial forces at the bottom area than at the top. Since the balance of the exerted loads is required, a horizontal lying-down position of the tested lining ring with the point-loading method cannot simulate these effects well. Secondly, for the conditions without partial offset loads, overall good bending moment distributions can be achieved through the 30 point loads in the indoor full-ring experiments, with differences within 15% at most of the key sections. The convergence deformations D1 to D3 have a difference within 23%. The indoor point loads can give an acceptable prediction for the bending moment distributions but generally smaller axial forces and larger deformations, resulting in a high safety factor for the lining design. Finally, the partial or unbalancing load is challenging to simulate through a limited number of point loads, such as in Experimental Case 3. The soil reaction is a passive force for the structural balance. Hence, the indoor experimental method introduced in Section 4.3.2 needs further modifications when simulating a situation with large soil reactions.

It has to be noted that, although differences appear between the results from point loads and uniform pressures, the indoor experiments are still a reliable method to verify the proposed full-ring model under a clear loading condition, because it is conservative. These differences are mainly caused by the translation of the actual pressure distributions into exerted indoor point loads. The translation method needs further research in the future, including more point loads, more reasonable load grouping, new devices simulating the soil reactions, and, if possible, a loading device for a vertical ring. On the other hand, despite the limitation of the current indoor experiments, some aspects related to the advantages of loading a horizontal lying-down segmental lining should be stressed. Firstly, a relatively easy segment assembly is allowed considering the condition without the TBM assembling system. It is also true for the installation of the measurement sensors in a horizontal lining. Secondly, in order to avoid high stresses caused by the hard contact between the loading jacks (or their distribution beams) and segments, a proper seat or supporter needs to be explored and installed at the bottom of a vertically standing segmental lining. Thirdly, the lining's failure could turn out to be a dangerous situation in case of a vertical lining test under indoor testing conditions. Large deformation, or even collapse, possibly happens when approaching the damage process of a shield tunnel lining. The bearing capacity and a possible repair method in case of an accident are essential for a tunnel lining. It is obvious that the indoor experiment with a horizontally deployed QRST lining is more reasonable and more feasible with the current test facilities. When further insights into this new lining pattern are needed, experiments with a suitable loading device for a vertical lining erection might be conducted in the future.

6.3 Influence of staggered assembly and bending moment transfer

6.3.1 Effect of staggered assembly

A staggered assembly is a common option in shield tunnel construction (Arnau Delgado, 2012; Gil Lorenzo, 2018). The QRSTs are also staggeringly assembled. Due to the limits of the testing facility, an experiment with a staggered full-scale prototype could not be carried out. In the following section, the staggering effect is discussed using the proposed model in Chapter 4. The shear stiffnesses in radial and tangential directions are taken into account in the circumferential joints in the three-ring model, as shown in Figure 4.1.

The total jack thrust force during the construction remains a residual longitudinal force in shield tunnels. This longitudinal force makes the lining compressed in the tunnel's longitudinal direction and contributes to the circumferential joints' shear stiffness. In previous studies, this force in soft soils was assumed as approximately 15% to 30% of the total thrust of the tunnel boring machine by Liu et al. (2017a), while Galván et al. (2017) regarded 50% of the thrust force as the longitudinal force. Another simulation case study by Arnau and Molins (2012) directly defined a 5,000-40,000 kN range for the longitudinal force in an 11.6-meter diameter tunnel with a 25 m depth. According to the construction data, the total jack thrust force during the construction of a QRST is about 50,000 kN. Herein, 30% of the thrust force is assumed to remain in the tunnel's longitudinal direction, and Eq. (3.4) is adopted to approximate the shear stiffness of 288×10^3 kN/ m^2 under a 519 kN/m compressive force in the circumferential joints. The effect of different stiffness values will be discussed with a parametric study later.

The concept of QRSTs is put forward based on a metro project in soft soils (Yang et al., 2016). Hereafter, the uniform load distribution shown in Figure 4.6 replaces the indoor point loads in the three-ring calculations to better simulate the loads around the QRST lining. Two typical design cases with 7 and 17 m overburdens are used for analysis. All relevant parameters are listed in Table 6.4. The coefficient of lateral pressure is 0.7 from the surrounding soft soils in the current QRST project. As specific horizontal deformation is unknown before calculation, the soil reaction is stimulated by the soil springs around the tunnel lining, with a coefficient of subgrade reaction K_{res} of 5.1 kPa/mm. The effects of coefficient of lateral pressure, soil reaction and partial offset surcharge will be discussed later.

Table 6.4 Pressures in the calculational cases (pressure unit: kPa).

Parameter	Calculational Case	
	1	2
Soil overburden	7.0 m	17.0 m
Coefficient of lateral pressure	0.7	0.7
Surcharge	20.0	20.0
Top pressure q_t	146.0	326.0
Arc pressure q_a	58.8	58.8
Bottom counter pressure q_b	188.0	368.0
Top value of lateral pressure e_1	102.2	228.2
Bottom value of lateral pressure e_2	190.4	316.4

Calculations are made with and without shear stiffness in the circumferential joints. The front and back rings in the model are symmetric to the middle ring relating to the interior column. From the perspective of the middle ring, the relative positions of the neighbouring rings' longitudinal joints are marked in Figure 6.3. The unfolded bending moments and axial forces are compared in Figure 6.4, Figure 6.5 and Figure 6.6. The longitudinal joint locations (JF1 to JF10) in these figures are based on the middle ring, and the positions of its neighbouring rings' longitudinal joints (CJ1 to CJ10) are also marked. In Figure 6.4a, the average values of the bending moments are the mean bending moment of a segment section and its related sections in the neighbouring rings, namely the average bending moment in the middle ring and its front half ring and back half ring. The average axial forces can be obtained in the same way, as shown in Figure 6.4b. The curves of average values with and without circumferential shear stiffness are generally in good agreement with each other. This means that the circumferential shear forces have little influence on the overall bending moments and axial forces in the lining structure model (including all the 3 rings).

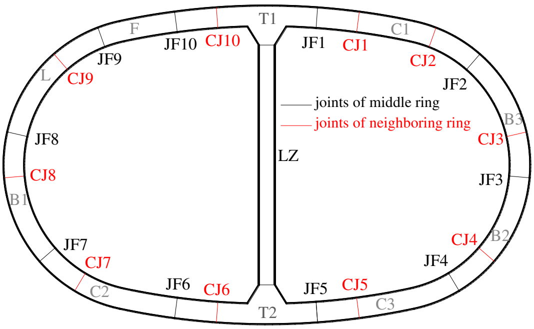

Figure 6.3 Layout of joints in middle and neighbouring rings.

The bending moments and axial forces of the middle ring with and without the circumferential shear are depicted (respectively red and blue curves in Figure 6.5 and Figure 6.6). The bending moments and axial forces of the neighbouring ring under the condition with and without circumferential shear are added for comparison (respectively black curves and green curves in Figure 6.5 and Figure 6.6).

When comparing the results without circumferential joints (blue and black curves), the bending moment values in the middle ring and neighbouring rings are different, caused by the different stiffnesses of the left half and right half. The half without segment F is stiffer than the half with segment F, and this observation has been found in the indoor full-scale tests too. However, the axial forces in the middle ring and neighbouring rings are almost identical. It means that although the longitudinal joints' locations result in a stiffness difference between the left and right compartments, this stiffness difference mainly influences the distribution of bending moments.

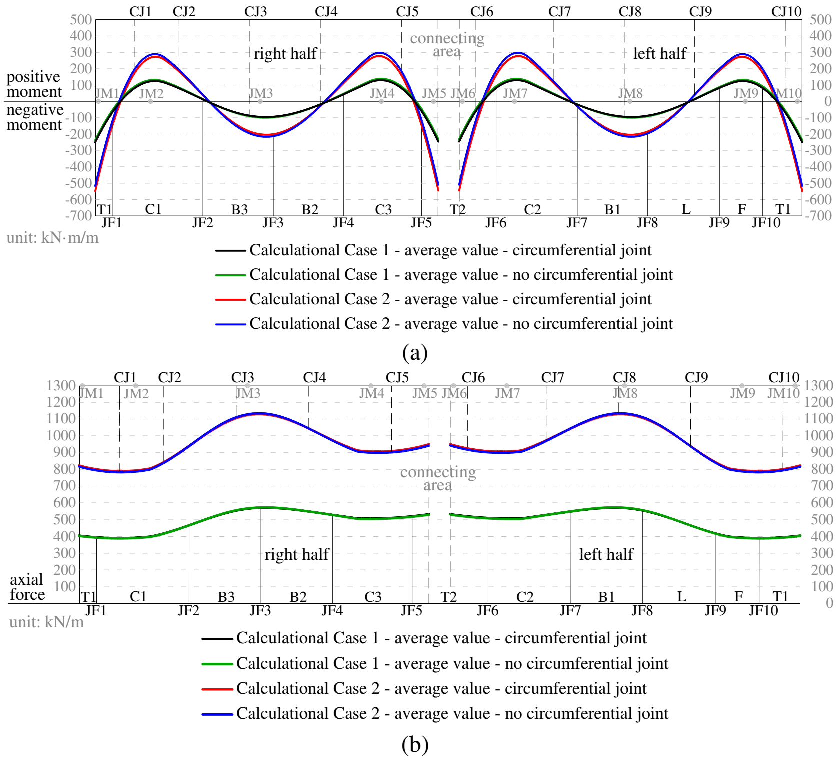

Figure 6.4 Comparison of average bending moment and axial force in the calculational cases with and without circumferential shear stiffness: (a) average bending moment; (b) average axial force.

Considering the bending moments in the middle ring (blue and red curves), they appear to have a different distribution, depending on whether the circumferential shear stiffness is considered or not. For the right half, it is clear that the moment value in the middle ring with circumferential shear stiffness (red) is generally larger than that without circumferential shear stiffness (blue). Meanwhile, a reverse observation is found on the left half. In contrast, when considering the bending moments in the neighbouring rings (green and black curves), the magnitudes on the left half are enlarged by the circumferential shear stiffness, while those on the right half are reduced. It is opposite to the trend in the middle ring and caused by the symmetry between the middle ring and its neighbouring rings. Moreover, for a certain section, when the moment in the middle ring with circumferential joint stiffness (red) is larger than that without circumferential joint stiffness (blue), the moment value at the related section of the neighbouring ring with circumferential joint stiffness (black) is smaller than that without circumferential joint stiffness (green) and vice versa. It is evident that transfer of the bending moment occurs between the rings because of the existence of the circumferential shear. Comparing the bending moment distributions between the middle and its neighbouring rings in the staggered model (red and black curves), the absolute values at the longitudinal joints (red) are smaller than those of the neighbouring segment bodies (black), such as JF1, JF3, JF4, JF5, JF6, JF7, JF8, JF9, JF10. In the longitudinal joints of the neighbouring rings (CJ1 to CJ10), the opposite situation is observed (red larger than black). The stiffnesses of the longitudinal joints are smaller than those of their neighbouring segment bodies. As a result, bending moments are transferred from the weaker area to the stiffer area.

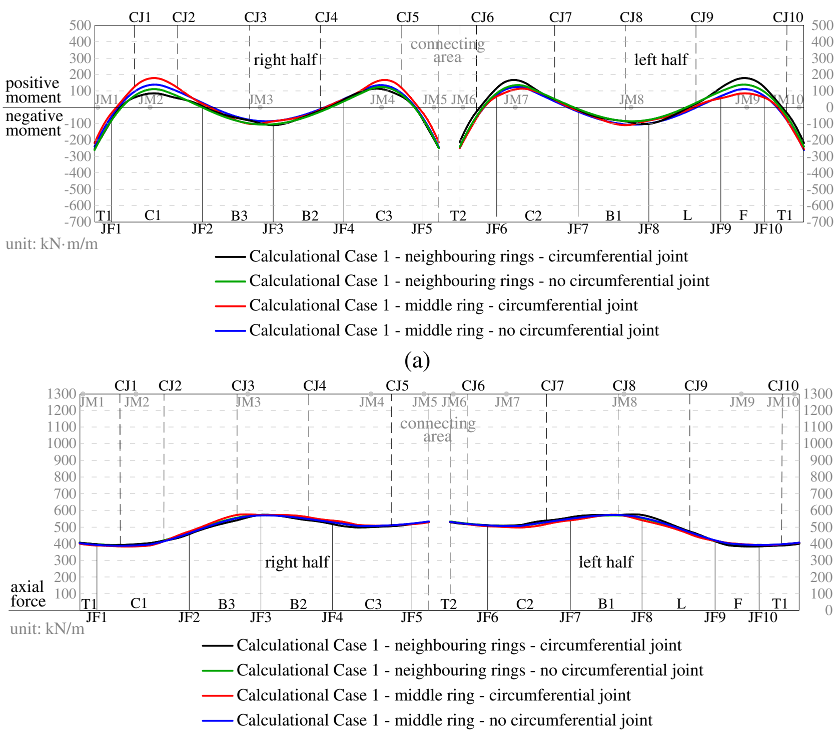

Figure 6.5 Comparison of bending moment and axial force in Calculational Case1 with and without circumferential shear stiffness: (a) bending moment; (b) axial force.

When comparing the bending moments between the left (segments C2, B1, L, F) and right (segments C1, B3, B2, C3) halves, this difference is further magnified after bending moment transfer (red), especially at the sections of segment F. The phenomenon of bending moment transfer in the staggered assembly will increase the maximum positive and negative bending moment values in the whole ring. Meanwhile, the bending moments in longitudinal joint sections become smaller, which is beneficial for the safety of the joints. Relevant specific measures should be taken for the neighbouring segment design, like increasing the amount of reinforcement, to prevent possible cracks at the segment bodies due to the bending moment transfer from longitudinal joints in the neighbouring rings.

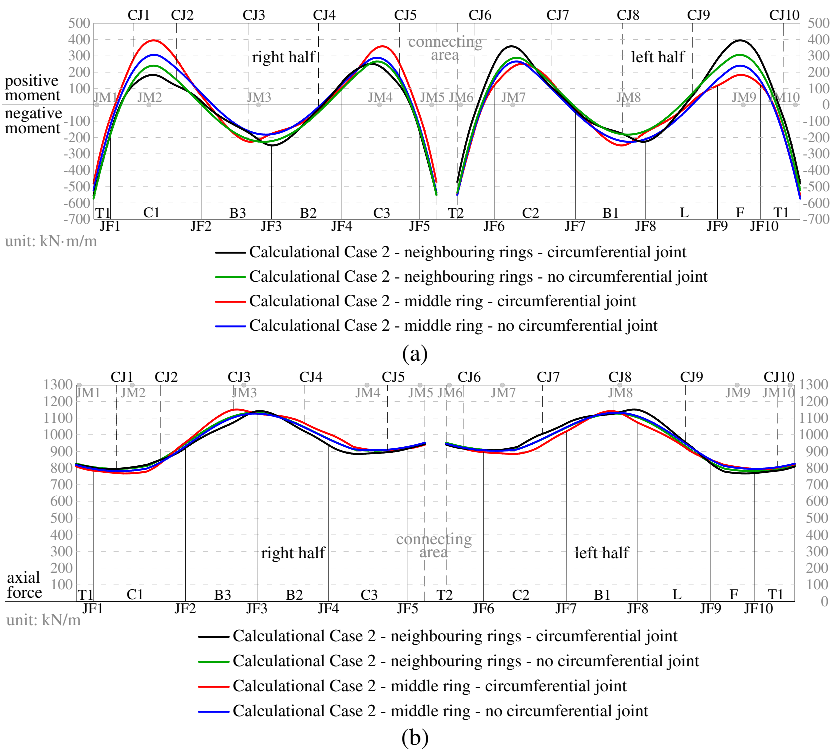

Figure 6.6 Comparison of bending moment and axial force in Calculational Case2 with and without circumferential shear stiffness: (a) bending moment; (b) axial force.

Table 6.5 Comparison of convergence deformations between the models with and without circumferential joints (unit: mm).

Calculational Case	Convergence deformation	Model without circumferential joints	Model with circumferential joints	Ratio (with/ without)
1	D1	-2.97	-3.49	1.18
	D2	3.48	2.99	0.86
	D3	-5.35	-3.67	0.69
	Abs(D3-D1)	2.38	0.18	0.07
2	D1	-5.83	-7.38	1.27
	D2	8.25	6.75	0.82
	D3	-12.06	-7.73	0.64
	Abs(D3-D1)	6.23	0.35	0.06

Regarding the convergence deformations with the circumferential joint stiffness consideration, about 16% of the deformation of the long axis point D2 and about

34% of the left axis short point D3 decrease, as shown in Table 6.5. In comparison, the deformation of the D1 point increases by about 23%. The deformation difference between D1 and D3 remarkably decreases. The deformation increase at D1 point demonstrates that the lining's right half takes more bending moment in a QRST with a staggered assembly than a QRST with a continuously jointed pattern. D3 is the deformation point where the largest deformation appears. The staggered assembly leads to a considerable deformation decrease at this key point, which is beneficial for the deformation control in a QRST design and resulting in higher stiffness of a multiple-ring lining structure than a single ring.

The QRST lining structure is divided into two parts by the interior column, and the different stiffnesses in these two parts are a unique characteristic of QRSTs. The different stiffnesses are essentially caused by the different longitudinal joints' location arrangements in each half, resulting in a non-symmetric distribution of bending moments in the same ring. When the pattern of the staggered assembly is adopted, the bending moment transfer from neighbouring rings to the middle ring, further increases the non-symmetric distribution of bending moments between the left and right halves. As shown in this case, the bending moment in the neighbouring sections of segment F is around twice the bending moment in segment F. Concerning the deformation, the staggering assembly can notably decrease the largest deformation and make the left and right halves deform uniformly.

6.3.2 Bending moment transfer

The longitudinal joints make the lining structure discontinuous, and therefore the deformation at a joint section is different from its neighbouring segment bodies. The phenomenon of bending moment transfer at the joint section is a key characteristic of a staggered tunnel assembly, when compared to a continuously jointed tunnel with the longitudinal joints in each ring at the same positions. A coefficient is defined to evaluate the moment-transfer magnitude in this study. As shown in Figure 6.7, when the circumferential joint stiffness is not considered, the moments at the joint section and its neighbouring segment body are M_{O1} and M_{O2}, respectively. A moment ratio λ_{OBM} of M_{O1} to $M_{O1}+M_{O2}$ can be calculated by Eq. (6.1). Similarly, when the circumferential joint stiffness is considered, a moment ratio λ_{CBM} of M_{C1} to $M_{C1}+M_{C2}$ can be defined by Eq.(6.2) with M_{C1} and M_{C2} representing the moment values of the joint and its neighbouring segments. It has to be noted that the values of $M_{O1}+M_{O2}$ and $M_{C1}+M_{C2}$ are approximately equal, as indicated in Figure 6.4. For a certain longitudinal joint, the moment-transfer magnitude caused by the circumferential joint can be evaluated through ξ_{BMR}, defined by Eq. (6.3). In order to distinguish from the coefficient of bending moment transfer (CBMT) used in MRM as introduced in Chapter 1, the new coefficient is named the coefficient of bending moment redistribution (CBMR), and their difference will be discussed later. By its definition, the CBMR stands for the relative moment ratio changes between the case with circumferential joint stiffness and the case without circumferential joints.

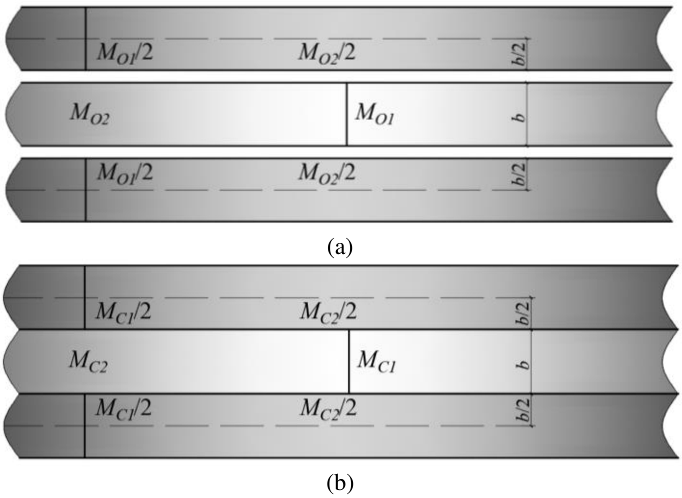

Figure 6.7 Illustration of bending moment distribution around the longitudinal joint area in the BSM method: (a) case without circumferential joint consideration; (b) case with circumferential joint consideration.

$$\lambda_{OBM} = \frac{M_{O1}}{M_{O1} + M_{O2}} \tag{6.1}$$

$$\lambda_{CBM} = \frac{M_{C1}}{M_{C1} + M_{C2}} \tag{6.2}$$

$$\xi_{BMR} = \frac{\lambda_{OBM} - \lambda_{CBM}}{\lambda_{OBM}} \tag{6.3}$$

The CBMRs in Calculational Cases 1 and 2, are listed in Table 6.6. Compared with the results without circumferential joint stiffness, the absolute bending moment values with circumferential joint stiffness decrease, resulting in all positive values of the CBMRs. The joint sections JF2 and JF7 have relatively small bending moment values, and the joint design can easily ensure the safety of these joint sections. For the other joint sections, the range of CBMRs is from 0.2 to 0.3, except for JF5 with a relatively large CBMR value around 0.4. It means that, generally, 20% to 30% of the bending moments at most joint sections are transit to their neighbouring segment bodies with the consideration of circumferential joints.

Table 6.6 Comparison of bending moments at joint sections between models with and without circumferential joints (bending moment unit: kN·m/m).

Calculational Case	Joint Section	Model without circumferential joints		Model with circumferential joints		CBMR ξ_{BMR}
		Bending moment	λ_{OBM}	Bending moment	λ_{CBM}	
1	JF1	-57	0.42	-36	0.32	0.24
	JF2	28	1.03	22	0.74	0.28
	JF3	-84	0.45	-83	0.44	0.02
	JF4	52	0.58	49	0.51	0.12
	JF5	-55	0.47	-27	0.29	0.38
	JF6	87	0.47	73	0.36	0.24
	JF7	-27	0.72	-21	0.58	0.19
	JF8	-99	0.56	-81	0.44	0.21
	JF9	68	0.41	55	0.32	0.23
	JF10	68	0.42	59	0.32	0.23
2	JM1	-126	0.41	-78	0.31	0.25
	JM2	76	0.92	61	0.71	0.22
	JM3	-180	0.45	-177	0.42	0.07
	JM4	129	0.56	109	0.44	0.21
	JM5	-136	0.47	-64	0.28	0.40
	JM6	174	0.47	137	0.33	0.31
	JM7	-44	0.78	-25	0.47	0.40
	JM8	-210	0.57	-167	0.43	0.25
	JM9	154	0.41	118	0.30	0.27
	JM10	143	0.41	119	0.30	0.26

On the other hand, the same calculations can be made for the axial forces under the conditions with and without consideration of the circumferential joints. The ratios λ_{OAF} and λ_{CAF}, and the coefficient of axial force redistribution ξ_{AFR} (CAFR) can be defined in the same way. The results of the axial forces and their transfer situations are listed in Table 6.7. Obviously, the consideration of the circumferential joint does not influence the axial force distributions, and this observation is consistent with the assumption in the MRM method that the axial forces are not transferred between rings.

In order to investigate the changes of CBMRs, different circumferential joint shear stiffness values are used in the three-ring calculations. The stiffness values are magnified by the factors 2, 4 and 8 times and decreased to 1/2， 1/4， 1/8， 1/100 and 1/1000 of the original value (288×10^3 kN/ m^2). The corresponding CBMRs in Calculational Cases 1 and 2 are summarized in Table 6.8 and Table 6.9， respectively. The CBMRs at sections JF1, JF3, JF4, JF5, JF6, JF8, JF9, JF10 are shown in Figure 6.8. The CBMR increases as the circumferential joint stiffness rises. When the stiffness is minimal, for example of 1/1000 of the original value, the moment transfer is not noticeable. However, when the stiffness is defined to be 1/100 of the original value, the CBMRs are around 0.1. It means that the circumferential joint only takes effect when the stiffness reaches a specific value. In the design, the circumferential joint stiffness should be adopted large enough to ensure the transfer. When the magnification factor ranges from 1/8 to 8 (stiffness value 36 - 2304 × 10^3 kN/ m^2), generally covering the possible stiffness values in practice, the CBMRs overall fall into the range from 0.2 to 0.4, except for JF3. It can be found that the increase of the circumferential joint stiffness results in a stronger effect of bending moment transfer. Up to 30% of the joints' moment can be transferred when the stiffness does not deviate too much from the original value, such as from 1/2 to 2 times. Hence 0.3 can be recommended as the CBMR value to evaluate the moment in the segment body in design. Additionally, the CBMR of JF5 can be slightly higher, like around 0.4, while that of JF3 can be slightly lower, like around 0.2.

Table 6.7 Comparison of axial forces at joint sections between models with and without consideration of circumferential joints (axial force unit: kN/m).

Calculational Case	Joint Section	Model with circumferential joints		Model with circumferential joints		CAFR ξ_{AFR}
		Axial force	λ_{OAF}	Axial force	λ_{CAF}	
1	JF1	-469	0.50	-391	0.50	0.00
	JF2	-570	0.51	-475	0.51	-0.02
	JF3	-690	0.50	-575	0.50	0.00
	JF4	-649	0.51	-540	0.51	-0.02
	JF5	-623	0.50	-519	0.50	0.00
	JF6	-607	0.50	-506	0.50	0.01
	JF7	-650	0.49	-542	0.49	0.02
	JF8	-651	0.49	-543	0.49	0.03
	JF9	-503	0.50	-419	0.50	0.00
	JF10	-472	0.51	-393	0.51	0.00
2	JF1	-799	0.50	-788	0.49	0.00
	JF2	-933	0.50	-956	0.51	-0.03
	JF3	-1131	0.50	-1131	0.50	0.00
	JF4	-976	0.50	-1008	0.52	-0.04
	JF5	-931	0.50	-921	0.50	0.00
	JF6	-909	0.50	-898	0.50	0.01
	JF7	-1048	0.50	-1023	0.49	0.02
	JF8	-1115	0.50	-1076	0.48	0.04
	JF9	-853	0.51	-852	0.51	0.00
	JF10	-798	0.50	-798	0.51	-0.01

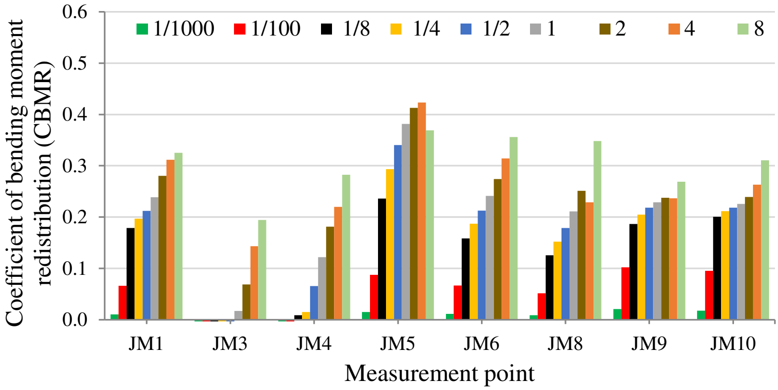

(a)

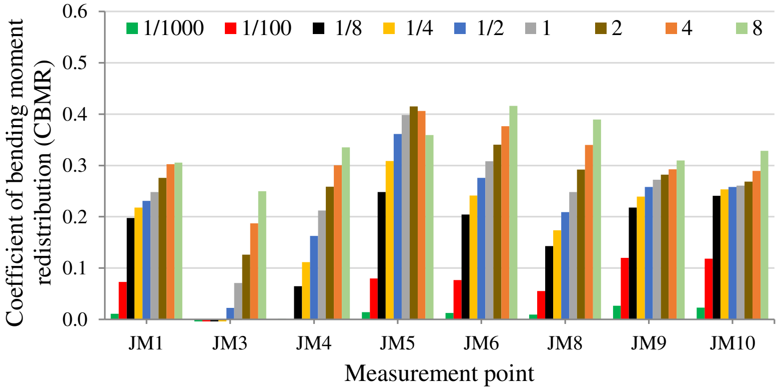

(b)

Figure 6.8 Comparison of CBMR under different circumferential joint stiffnesses: (a) Calculational Case 1; (b) Calculational Case 2.

Table 6.8 CBMR under different circumferential joint stiffnesses in Calculational Case 1.

Joint Section	Magnification factors								
	1/1000	1/100	1/8	1/4	1/2	1	2	4	8
JM1	0.01	0.07	0.18	0.20	0.21	0.24	0.28	0.31	0.33
JM2	-0.01	-0.03	0.08	0.15	0.22	0.28	0.34	0.39	0.48
JM3	-0.01	-0.06	-0.06	-0.06	-0.02	0.02	0.07	0.14	0.19
JM4	-0.01	-0.04	0.01	0.01	0.07	0.12	0.18	0.22	0.28
JM5	0.01	0.09	0.24	0.29	0.34	0.38	0.41	0.42	0.37
JM6	0.01	0.07	0.16	0.19	0.21	0.24	0.27	0.31	0.36
JM7	0.01	0.03	0.08	0.10	0.14	0.19	0.25	0.30	0.36
JM8	0.01	0.05	0.13	0.15	0.18	0.21	0.25	0.23	0.35
JM9	0.02	0.10	0.19	0.20	0.22	0.23	0.24	0.24	0.27
JM10	0.02	0.10	0.20	0.21	0.22	0.23	0.24	0.26	0.31

Table 6.9 CBMR under different circumferential joint stiffnesses in Calculational Case 2.

Joint	Magnification factors								
Section	1/1000	1/100	1/8	1/4	1/2	1	2	4	8
JM1	0.01	0.07	0.20	0.22	0.23	0.25	0.28	0.30	0.31
JM2	-0.02	-0.05	0.06	0.12	0.17	0.22	0.26	0.31	0.40
JM3	-0.01	-0.07	-0.06	-0.02	0.02	0.07	0.13	0.19	0.25
JM4	0.00	0.00	0.06	0.11	0.16	0.21	0.26	0.30	0.34
JM5	0.01	0.08	0.25	0.31	0.36	0.40	0.42	0.41	0.36
JM6	0.01	0.08	0.20	0.24	0.28	0.31	0.34	0.38	0.42
JM7	0.03	0.13	0.25	0.30	0.35	0.40	0.46	0.49	0.51
JM8	0.01	0.06	0.14	0.17	0.21	0.25	0.29	0.34	0.39
JM9	0.03	0.12	0.22	0.24	0.26	0.27	0.28	0.29	0.31
JM10	0.02	0.12	0.24	0.25	0.26	0.26	0.27	0.29	0.33

6.3.3 Comparison between BSM and MRM

In the MRM method, the longitudinal joints are ignored, which influences the structural deformation and the bending moment distribution. For the former aspect, if the longitudinal joints are assumed to have the same stiffness as that of the segment body, the structural deformation cannot be calculated correctly. An average uniform rigidity ring model with a stiffness reduction factor η (SRF) is used to make up for this error. As such, the effective stiffness of the lining structure becomes $(1-\eta)$ times that without stiffness reduction to compensate the deformation caused by the existence of the joints. For the latter aspect, the concept of a coefficient of bending moment transfer ξ (CBMT) is provided by I.T.A. (2000), and is commonly used to determine the bending moment distribution between the joints and their neighbouring segment bodies (Ye et al., 2014; Huang et al., 2019). As shown in Figure 6.9, $(1-\xi)\cdot M$ is taken as the bending moment of the joint section while $(1+\xi)\cdot M$ is taken as the bending moment of the body section, namely the neighbouring segment body.

In the MRM method, the stiffness reduction factor η (SRF) is universally determined by the shape and size of the segments, as well as the profile, number and location of the joints. Although the bending moment redistribution near the circumferential joints is taken into consideration, it is natural that the CBMT ξ changes depending on the stress level of the joint. Additionally, there usually are several longitudinal joints in a lining ring, distributed at different positions. The lining structure with different longitudinal joint positions in each ring is substantially different from a simple continuous ring structure. However, the MRM method just redistributes the moment between rings by the CBMT ξ based on experience. Koyama (2003) and Arnau and Molins (2012) stated that this moment redistribution method physically has no basis, and it is impossible to calculate the actual bending moment distribution through this model. However, considering the convenience of the MRM method, it is still commonly used in the current shield tunnel design. In this section, the applicability of the MRM method for a QRST is discussed.

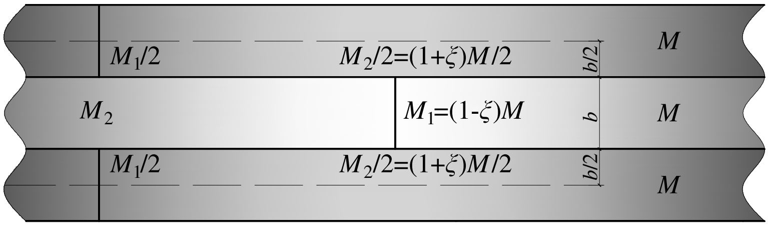

Figure 6.9 Illustration of bending moment transfer in MRM method.

For QRSTs, a series of SRFs are used in the MRM method to obtain the convergence deformations at D1 to D3 points in Calculational Cases 1 and 2. The results with SRFs from 0.55 to 0.80 are compared with those from the established BSM in Table 6.10. For the deformation of the right short axis D1, the SRF needs to be a value between 0.70 and 0.75 to retrieve a similar result. However, it changes to a value between 0.65 and 0.70 for the deformation of the left short axis D3. When it comes to the long axis D2, an SRF of 0.60 can give good predictions. The column pillar divides the lining into two compartments, resulting in a complex deformation in the QRSTs compared to a generally elliptical deformation shape (with the long axis in the horizontal direction) in a circular shield tunnel. Therefore, it can be concluded that different SRFs need to be adopted in the MRM method to simulate the BSM results (underlined and in italics in Table 6.10) for the corresponding deformation points.

Table 6.10 Comparison of convergence deformations between the BSM method and MRM method (unit: mm).

Calculational Case	Convergence deformation	BSM	SRF η in MRM					
			0.55	0.60	0.65	0.70	0.75	0.80
1	D1	-3.49	-4.42	-4.07	-3.77	*-3.51*	-3.28	-3.09
	D2	2.99	3.27	*3.01*	2.80	2.61	2.44	2.30
	D3	-3.67	-4.41	-4.06	*-3.76*	-3.50	-3.27	-3.08
2	D1	-7.38	-9.60	-8.84	-8.19	*-7.62*	*-7.14*	-6.71
	D2	6.75	7.43	*6.85*	6.36	5.93	5.55	5.22
	D3	-7.73	-9.58	-8.81	-8.16	*-7.60*	-7.11	-6.68

Concerning the bending moment distribution, only the results from Calculational Case 2 are used for brevity. The moments from the MRM method with the SRFs of 0 and 0.4 are depicted in Figure 6.10 (black and green curves), and they almost show identical values, indicating that the SRF has little influence on the general bending moment distributions in the MRM method. The average bending moments of the middle ring and its neighbouring rings through the BSM approach (blue) are compared with the MRM results. The MRM method produces smaller moment values around the connecting area but larger values in other areas. This is caused by the fact that the BSM has a larger stiffness difference between the T segments and other areas than the MRM. The average uniform ring rigidity in MRM can only give a general bending moment distribution shape.

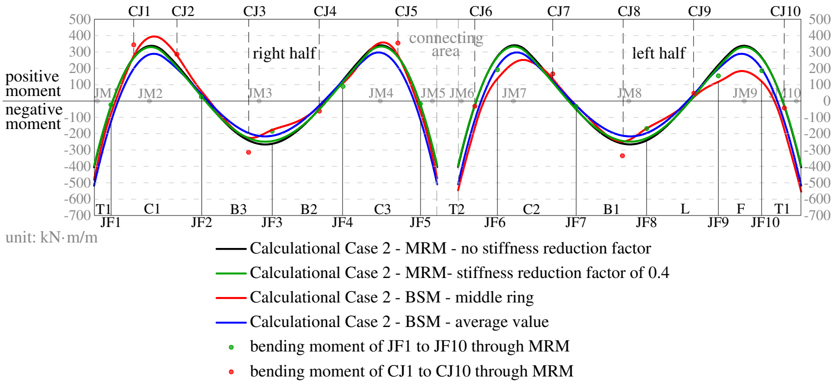

Figure 6.10 Comparison of bending moment between BSM and MRM methods.

Concerning the bending moment transfer, the CBMT ξ is usually set to 0.3 for a traditional circular tunnel in soft soils (Japanese Standard for Shield Tunneling, 2001; Koyama, 2003). A CBMT of 0.3 is also used in the MRM method for QRSTs to compare with the BSM. The comparisons of the bending moments at joint sections (JF1 to JF10) and segment sections around neighbouring joints (CJ1 to CJ10) are listed in Table 6.11 and Table 6.12, respectively. If the absolute value after CBMT adjustment is larger than the BSM result, a "√" mark is added, while a "×" mark is given for a reverse situation. Additionally, the adjusted bending moment values of JF1 to JF10 (green dots) and CJ1 to CJ10 (red dots) are marked in Figure 6.10 to compare with the results of the middle ring (red curve). Firstly, for JF1 to JF10, only half of the results from the MRM can cover those from the BSM (JF3, JF6, JF8, JF9, JF10), but these joint sections have larger bending moment values than those that cannot be covered (JF1, JF2, JF4, JF5, JF7). From the perspective of design, although it can produce safe moment values for the joint section design, they seem too conservative, such as JF6 (137 kN·m/m in BSM versus 191 kN·m/m in RMR) and JF10 (119 kN·m/m in BSM versus 186 kN·m/m in RMR). This means a CBMT value larger than 0.3 is needed in the MRM. Secondly, for CJ1 to CJ10, most MRM results can cover the BSM results except for a few sections with relatively small bending moment (CJ6 and CJ10). However, the same conservative situation also appears, especially for CJ3 and CJ8. These are at the waist area, and the original moment values from the MRM are already larger than from the BSM due to the structural changes caused by the existence of longitudinal joints. However, these moments are further modified through the inherent bending moment transfer in the MRM, finally resulting in 40% larger bending moments than from the BSM method. Considering the bending moments at CJ1 to CJ10, a CBMT value smaller than 0.3 is expected in the MRM. On the other hand, a noticeable issue is that the maximum moment (at section JM2) by the BSM is about 400 kN·m/m, still larger than the maximum bending moment after magnification in MRM, and it leads to an unsafe value from the MRM method for segment design. Although near the joints around 30% bending moment is observed to be transferred to the neighbouring segments in the BSM method, the existence of the longitudinal joints changes the lining structure, and a CBMT of 0.3 in the MRM method cannot give good predictions for the moments around joint sections.

Table 6.11 Bending moment in joint sections JF1 to JF10 through BSM and MRM methods (unit: kN·m/m).

Joint	BSM	MRM		Evaluation
		Original	$1-\xi$	
JF1	-78	-33	-23	×
JF2	61	37	26	×
JF3	-177	-262	-183	√
JF4	109	128	90	×
JF5	-64	-25	-18	×
JF6	137	273	191	√
JF7	-25	-47	-33	×
JF8	-167	-241	-169	√
JF9	118	220	154	√
JF10	119	265	186	√

Table 6.12 Bending moment in segment sections CJ1 to CJ10 through BSM and MRM methods (unit: kN·m/m).

Segment section	BSM	MRM		Evaluation
		Original	$1+\xi$	
CJ1	272	265	345	√
CJ2	280	220	286	√
CJ3	-225	-241	-314	√
CJ4	-29	-47	-62	√
CJ5	282	273	355	√
CJ6	-163	-25	-33	×
CJ7	138	128	167	√
CJ8	-249	-262	-340	√
CJ9	24	37	48	√
CJ10	-176	-33	-43	×

From the above comparisons, it can be concluded that the MRM method gives overestimated results for some joint sections (such as JF6 and JF10) and segment sections (such as CJ3 and CJ8), and that some critical moment values cannot be predicted (such as the positive moment at JM2 in segment C1). Besides, different SRFs are needed for the deformation calculations of D1 to D3. In conclusion, although the MRM method can be used as a preliminary calculation for an overall evaluation of the bending moment distribution and deformation, it cannot directly produce acceptable values for a QRST design.

6.4 Influence of coefficient of lateral pressure

Based on the site geological survey, a coefficient of lateral pressure K_{lat} of 0.7 is adopted in the current calculational cases. In this section, Calculational Cases 1 and 2 are taken as the basis for a parametric study. The coefficient of lateral pressure is reset to 0.4, 0.5, 0.6, 0.8 and 0.9 with all other parameters unchanged to investigate its influence on the calculation results. Examples of the bending moments and the axial forces from 0.4 and 0.9 are compared with the original results from 0.7 in Figure 6.11 and Figure 6.12. Additionally, the result differences between the basic and the reset coefficients of lateral pressure are summarized in Figure 6.13 and Figure 6.14 for bending moment and axial force, respectively.

Concerning the bending moments, the coefficient of lateral pressure has a significant influence. The increase of this coefficient can effectively decrease the absolute moment value, which shows a beneficial effect for lining design. For the soft soils in Ningbo, this coefficient is generally chosen between 0.6 and 0.8. This parameter range produces moment differences around 15% in Calculational Case1 and around 10% in Calculational Case 2 (except for JM8). It is worth pointing out that the key section JM9 in segment F shows a stable moment value. In contrast, the key section JM2 in segment C1 considerably changes. It indicates that the bending moment caused by a lower coefficient is sustained by the neighbouring segments (the neighbouring segment of F is C1 as shown in Figure 6.3). Therefore, due attention need to be paid to the neighbouring areas related to segment F.

Concerning the axial forces, overall, a higher coefficient of lateral pressure gives larger axial force values, which are also beneficial for the structural section design. For the coefficient range from 0.6 to 0.8, a difference of about 15% might occur, except for JM3 and JM8. With the coefficient’s increase, the axial forces at the waists (around JM3 and JM8) only increase slightly. This can be explained by the fact that JM3, JM8 and the column pillar mainly sustain the vertical load, and therefore are less sensitive to the lateral pressures.

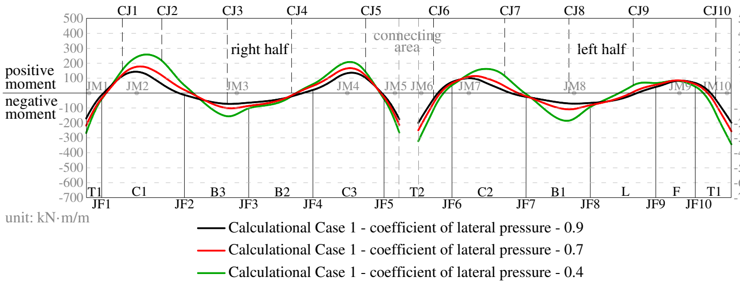

(a)

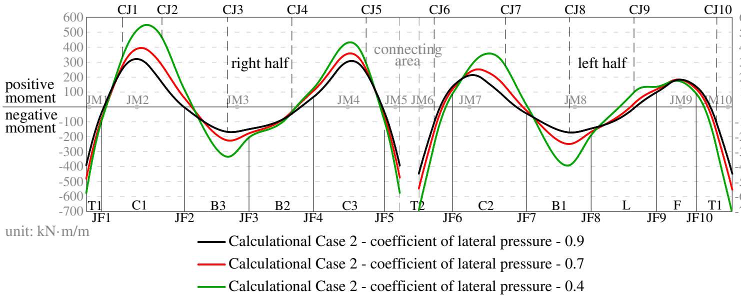

(b)

Figure 6.11 Bending moment under different coefficients of lateral pressure: (a) Calculational Case 1; (b) Calculational Case 2.

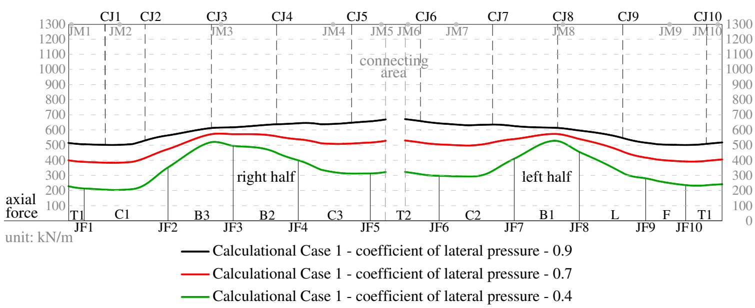

(a)

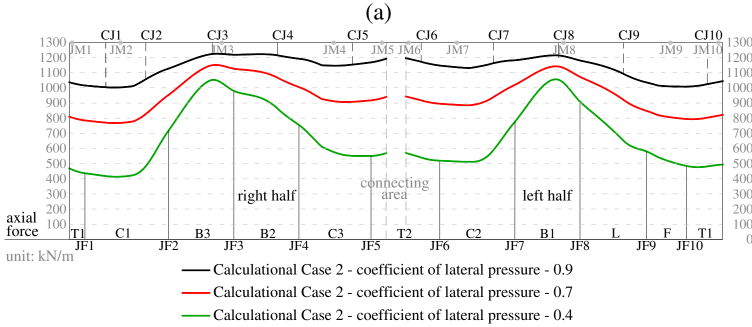

(b)

Figure 6.12 Axial force under different coefficients of lateral pressure: (a) Calculational Case 1; (b) Calculational Case 2.

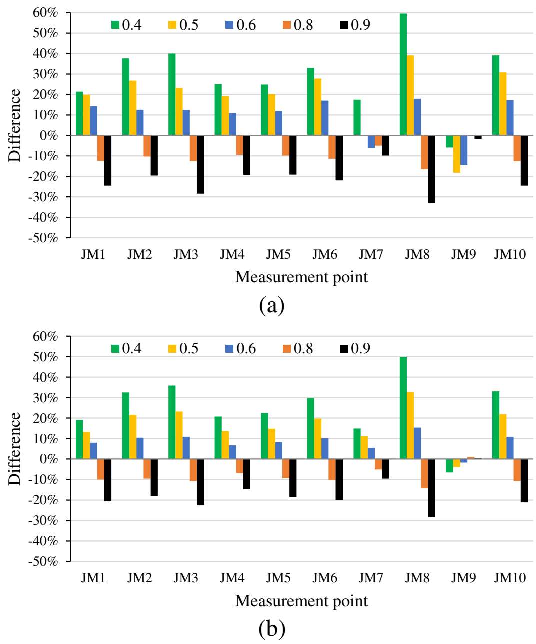

Figure 6.13 Comparison of bending moments at JM1 to JM10 under different coefficients of lateral pressure: (a) Calculational Case 1; (b) Calculational Case 2.

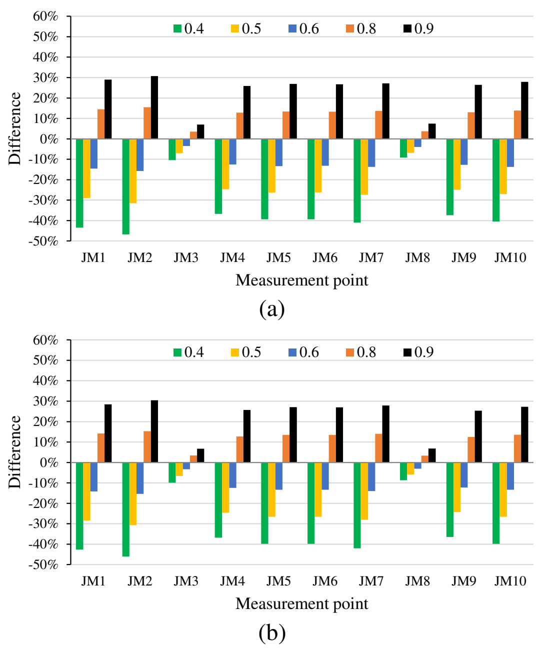

Figure 6.14 Comparison of axial forces at JM1 to JM10 under different coefficients of lateral pressure: (a) Calculational Case 1; (b) Calculational Case 2.

When it comes to the convergence deformations at D1 to D3, the resulting differences are compared in Figure 6.15. It is evident that a large coefficient can decrease the structural deformation, especially at D2 whose measuring direction is aligned with the lateral pressure. If the coefficient changes from 0.6 to 0.8, there is a deformation difference of about 25% at D2 and about 15% at D1 and D3.

Based on the above comparisons, it can be found that the coefficient of lateral pressure can significantly influence the QRST lining's performance. A higher coefficient produces smaller bending moments and deformations, as well as larger axial forces. From the view of design, all of these aspects are beneficial. Hence, a reasonable coefficient is critical, which means a site geological test to decide this coefficient is necessary. In the normal range of the coefficient from 0.6 to 0.8, generally, a 15% variation of the axial force and bending moment might be expected. There is a deformation difference of about 25% at the long axis measurement point D2 and about 15% at the short axes D1 and D3. On the other hand, due to the bending moment transfer, the neighbouring segments C1 sustain the bending moment from segment F as the coefficient changes, resulting in the bending moment in segment F being insensitive to the coefficient change. Correspondingly, sufficient attention should be paid to the bending moment value in segment C1 (the neighbouring segments of F as shown in Figure 6.3).

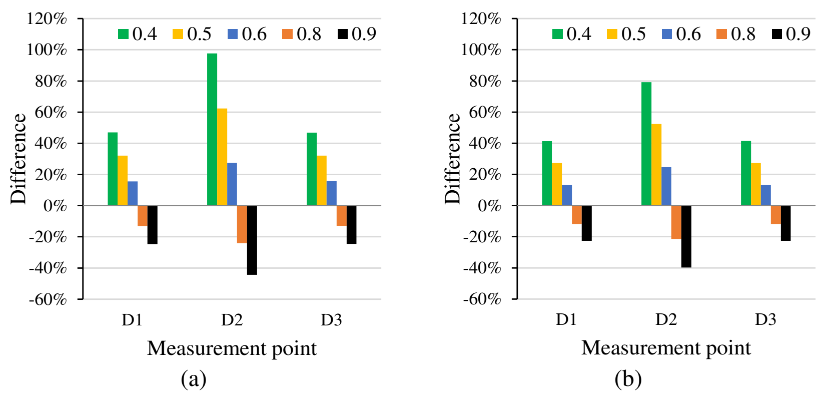

Figure 6.15 Comparison of convergence deformations at D1 to D3 under different coefficients of lateral pressure: (a) Calculational Case 1; (b) Calculational Case 2.

6.5 Influence of coefficient of subgrade reaction

According to the site geological survey, the coefficient of subgrade reaction K_{res} is defined as 5.1 kPa/mm in the current calculational cases. In this section, the coefficient of subgrade reaction is reduced to 1/2, 1/4, 1/8 times the original value in both Calculational Cases 1 and 2, and also the situation with no subgrade reaction is considered. Additionally, the coefficient is also magnified to 2, 4, 8 and 16 times the original value. As such, nine different coefficients of subgrade reaction value (0, 0.6, 1.3, 2.6, 5.1, 10.2, 20.4, 40.8 and 81.6 kPa/mm) are used in the model. These coefficient values can cover peat, organic soil, humus, gravel fills and clayed soil (Bowles, 1996; Akmadžić and Vrdoljak, 2018), and these soil types are the main surrounding soils for the studied QRSTs.

Calculation results from no subgrade reaction and 16 times the original coefficient value (81.6 kPa/mm) are compared with the original results in Figure 6.16 and Figure 6.17. For other coefficient values, the resulting differences from the original subgrade reaction are shown in Figure 6.18 and Figure 6.19. Concerning the bending moment, it can be found that the results are only slightly different when the coefficient is small. Only if the coefficient is magnified to 8 and 16 times, the moment values have a change of more than 15% at most sections. This situation also appears for the axial force. Similar to the effect of the coefficient of lateral pressure, a large coefficient of subgrade reaction can result in relatively small bending moments and large axial forces, and the axial forces at the waists are less susceptible than other areas. Additionally, the moment value in segment F is also insensitive to the changes of coefficient of subgrade reaction. These observations can be explained by the fact that the main essence of these two coefficients is to influence the lateral pressures.

When it comes to the convergence deformations, the result comparisons between different coefficients are shown in Figure 6.20. The small coefficient values have a very limited influence on the deformation. When the coefficient is 8 times the original value, about 20% and 35% of deformation decreases are observed at the short axes (D1 and D3) and the long axis (D2). When the coefficient is 16 times, these deformation decreases are about 30% and 50%. Apparently, the coefficient of subgrade reaction can significantly influence the deformation results, especially for the waists (D2) due to the relatively large subgrade reaction there.

It can be stated that a small coefficient of subgrade reaction, such as below 20 kPa/mm in the current cases, has slight influences on the axial forces, bending moments and convergence deformations. Beyond this range, a large coefficient of subgrade reaction can notably increase the axial forces and decrease the bending moments and convergence deformations, especially for the long axis, resulting in a beneficial effect for design. Therefore a proper coefficient of subgrade reaction is essential.

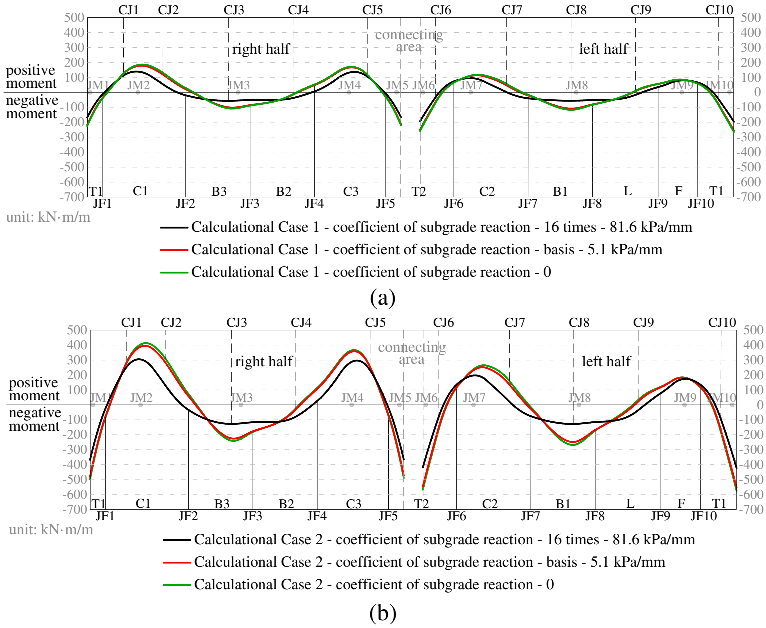

Figure 6.16 Bending moment under different coefficients of subgrade reaction: (a) Calculational Case 1; (b) Calculational Case 2.

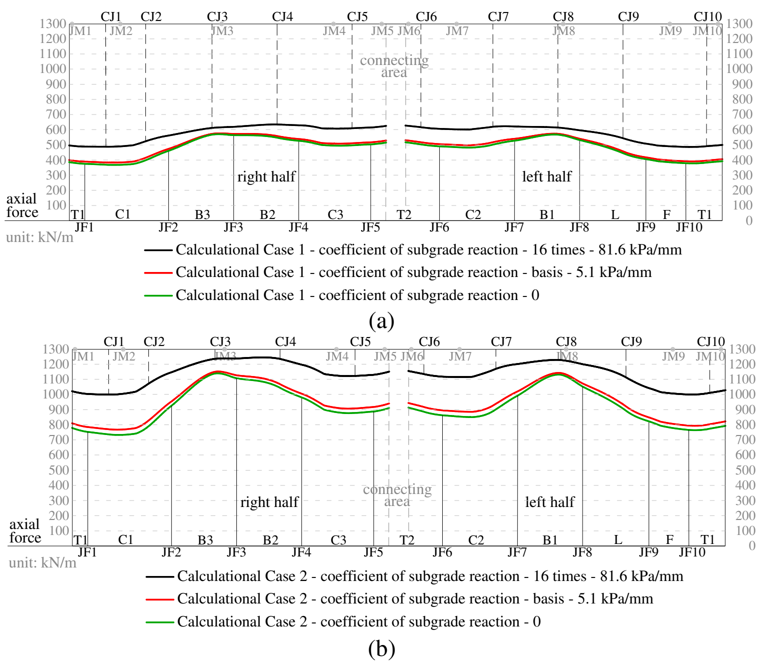

Figure 6.17 Axial force under different coefficients of subgrade reaction: (a) Calculational Case 1; (b) Calculational Case 2.

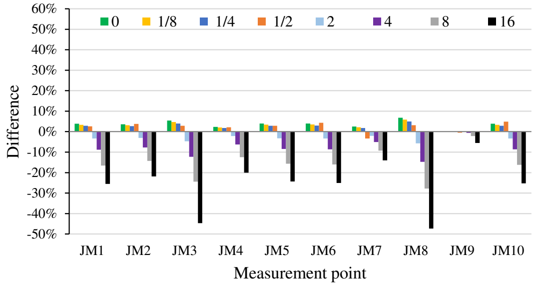

(a)

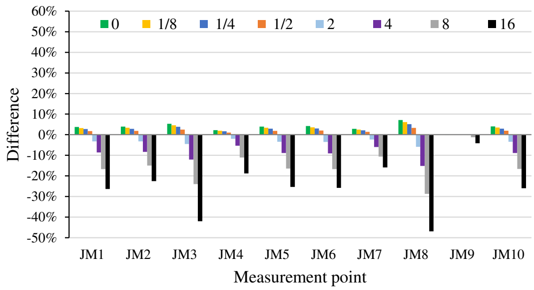

(b)

Figure 6.18 Comparison of bending moments at JM1 to JM10 under different coefficients of subgrade reaction: (a) Calculational Case 1; (b) Calculational Case 2.

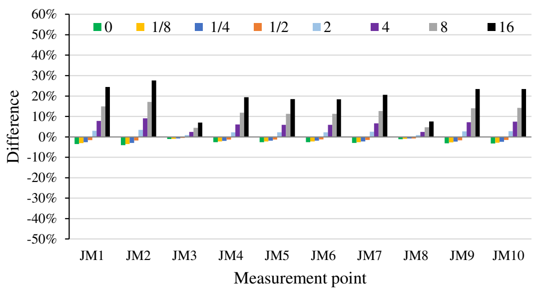

(a)

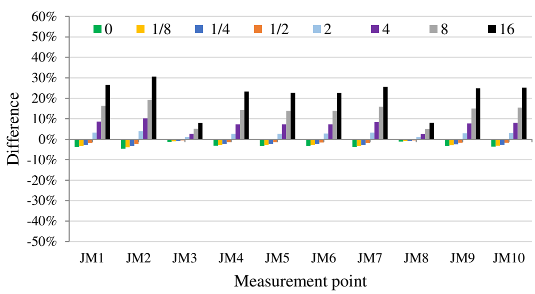

(b)

Figure 6.19 Comparison of axial forces at JM1 to JM10 under different coefficients of subgrade reaction: (a) Calculational Case 1; (b) Calculational Case 2.

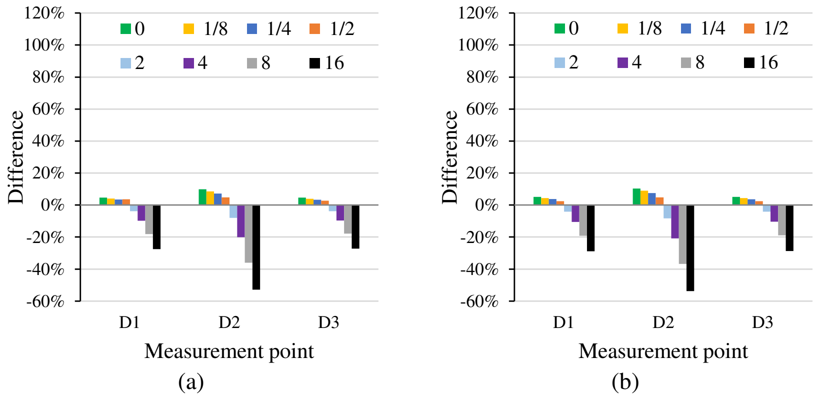

Figure 6.20 Comparison of convergence deformations at D1 to D3 under different coefficients of subgrade reaction: (a) Calculational Case 1; (b) Calculational Case 2.

6.6 Influence of partial offset surcharge

A partial offset surcharge is respectively exerted on the right and left sides of the ground surface in Calculational Cases 1 and 2. The distribution of the partial offset surcharges is shown in Figure 4.6. The surcharge is 30 kPa, and only the lateral pressure at the corresponding side takes account of this surcharge. The soil springs at the bottom and the other side will balance the partial offset surcharge on the ground and the lateral pressure on one side. It means that the bottom pressure and the lateral pressure on the other side can adjust themselves to achieve the structural balance. When the partial offset surcharge is considered, the coefficient of subgrade reaction K_{res} in the model cannot be zero. The calculation results under the partial offset surcharges are compared to the results without the surcharge in Figure 6.21 and Figure 6.22. The differences of the key sections JM1 to JM10 from the non-surcharge situation are shown in Figure 6.23 and Figure 6.24.

Firstly, the changes of axial force are discussed. The left partial offset surcharge increases the left lateral pressure, and thus there is an additional lateral pressure on the right side from the soil springs to resist the left pressure increase. This leads to an overall increase in axial forces. It is also true for the situation with a right partial offset surcharge. However, it can be found that when a left partial offset surcharge is exerted, the left waist (JM3) has a larger axial force increase than the right waist (JM8) and vice versa. The partial offset surcharge at one side is mainly balanced by the bottom soil springs at the corresponding side.

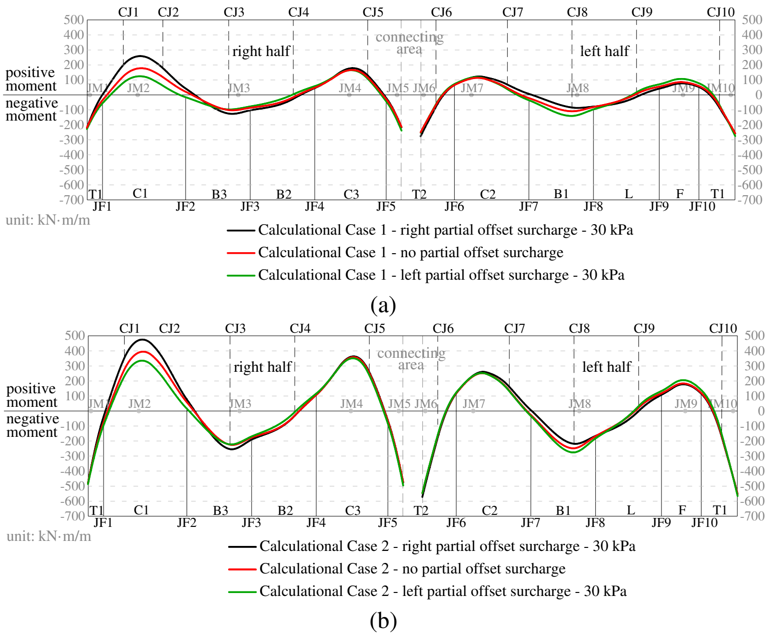

Figure 6.21 Bending moment under right and left partial offset surcharges: (a) Calculational Case 1; (b) Calculational Case 2.

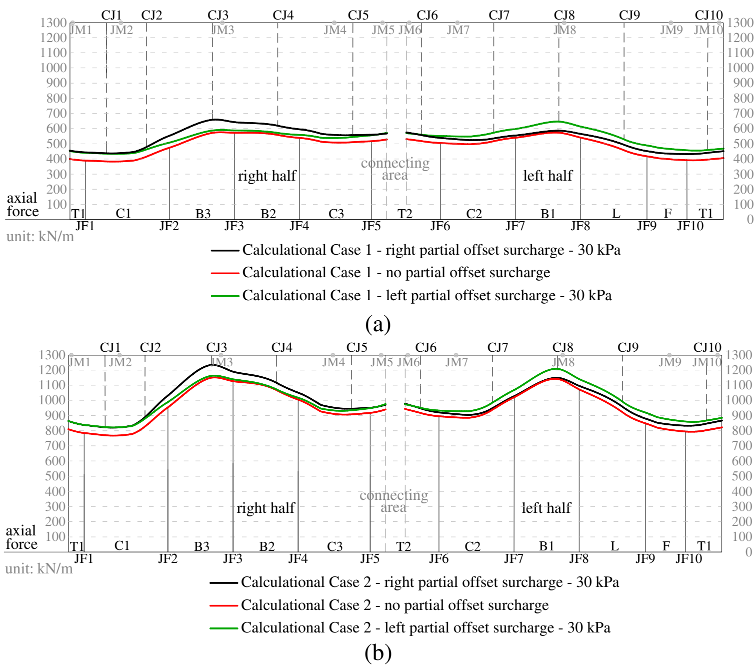

Figure 6.22 Axial force under right and left partial offset surcharges: (a) Calculational Case 1; (b) Calculational Case 2.

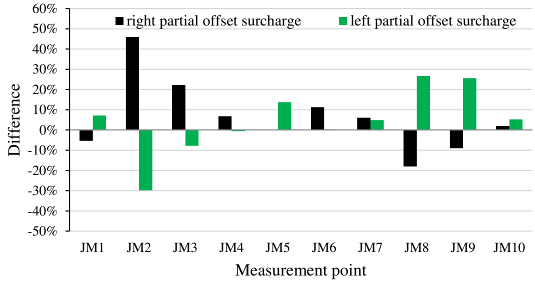

(a)

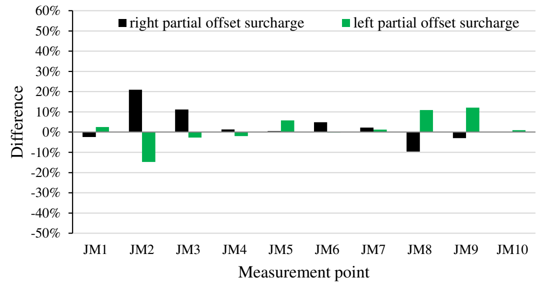

(b)

Figure 6.23 Comparison of bending moments at JM1 to JM10 under right and left partial offset surcharges: (a) Calculational Case 1; (b) Calculational Case 2.

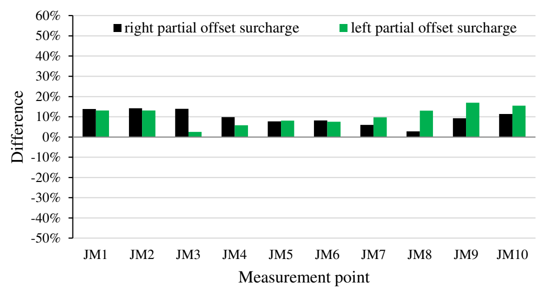

(a)

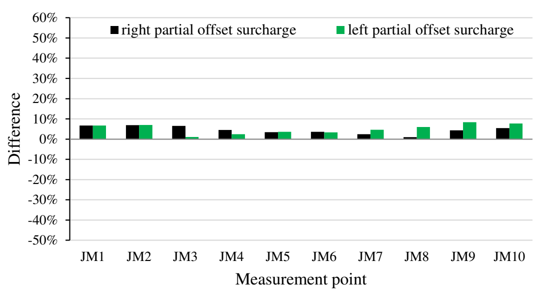

(b)

Figure 6.24 Comparison of axial forces at JM1 to JM10 under right and left partial offset surcharges: (a) Calculational Case 1; (b) Calculational Case 2.

Secondly, concerning the bending moment, the main changes appear at the waists and top, or the sections near JM2, JM3, JM8, JM9, more than in the other areas. When the left partial offset surcharge is considered in the calculation, there is a bending moment increase at JM8 and JM9 (on the left half) and a bending moment decrease at JM2 and JM3 (on the left half). When the right surcharge is exerted, a reverse situation is observed. The phenomenon of the bending moment decrease can be explained by the increase of the lateral pressure at the non-surcharge side for the structural balance. It is similar to the bending moment decrease with an increased coefficient of lateral pressure, as discussed in Section 6.4. However, no matter the surcharge is on the left or right, the right-side bending moment changes caused by the partial offset surcharges (JM2) are always more notable than at the left side (JM9). JM2 is more sensitive than JM9 due to the bending moment transfer. A relatively dangerous situation is exerting the right partial offset surcharge, as shown by the black curve in Figure 6.21a. In this situation, the segment C1 takes the bending moment from the neighbouring rings, resulting in a considerable moment increase at JM2. Correspondingly, segment F transfers its bending moment to the neighbouring rings, resulting in a slight moment increase at JM9. Therefore, when a partial offset surcharge occurs along the tunnel line, segment C1, or JM9, should be carefully considered.

Finally, considering the convergence deformations, the comparisons between the situations with and without the partial offset surcharges are shown in Figure 6.25. For the short axes, it is understandable that the short axis at the same side as the surcharge shows an increase while the other side decreases by a similar percentage. For the long axis, considering the lateral pressure rises due to the surcharge on the ground, the increase of the vertical load only results in a slightly larger horizontal deformation than without the surcharge.

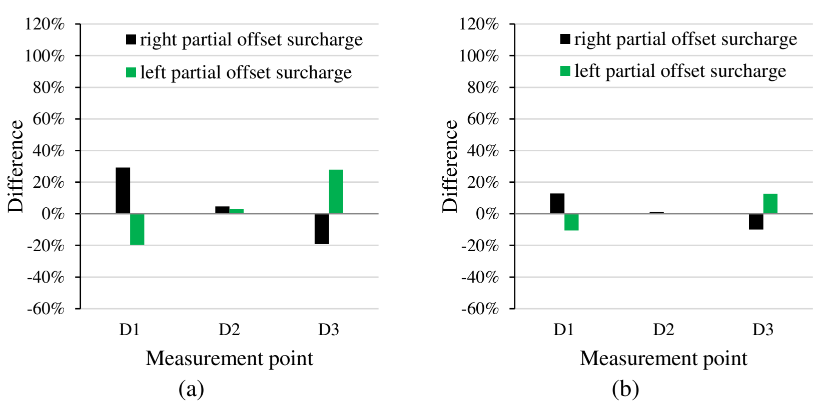

Figure 6.25 Comparison of convergence deformations at D1 to D3 under right and left partial offset surcharges: (a) Calculational Case 1; (b) Calculational Case 2.

To sum up, the partial offset surcharge results in an overall increase of the axial force value. At the same time, the main changes of bending moment only happen at the top and waist areas. The surcharge at one side leads to the increases of the bending moment and the convergence deformation at the same side while decreasing tendencies at the other side. The partial offset surcharge will make segment C1 to sustain an additional bending moment from its neighbouring F segments, and therefore segment C1 should be paid due attention in design.

6.7 Influence of backfilling grouting

The most commonly used BSM and MRM methods regard the tunnel calculation as a planar analysis. Along the tunnel's longitudinal direction, these two methods consider the bending moment transfer by the empirical CBMT and the circumferential joint stiffness, respectively. However, for a segmental lining just pushed out of the shield tail, one of its neighbouring rings is still in the shield while the other is still affected by the grouting process, as presented in Chapter 5. The actual performance of a lining structure at the moment when it is pushed out of a TBM needs a 3D analysis. The TBM can affect its nearby linings, and the linings already pushed out still sustain a decreasing pressure along the tunnel direction. Additionally, the interaction between the grouting process and surrounding soil is unclear. Due to these aspects, the grouting effect is complex. In this section, based on the established QRST model, a preliminary analysis is conducted to investigate the impact of the synchronous backfill grouting.

In the established model, the front ring is regarded as being in the shield tail. Since the effect of the steel brush and grease in the shield tail is small, as presented in Figure 5.5, the pressure caused by them is ignored in the current primary analysis. As such, the front ring is assumed to have only its dead weight as a load. The middle ring sustains the theoretical long-term pressure, as shown in Figure 4.6, and the grouting pressure. The grouting pressure has a cosinusoidal distribution with a 4.32 m influencing area, as introduced in Section 5.4. There are eight grouting holes around the shield tail. Based on the monitoring results in Chapter 5, the grouting pressures of the top four holes are assumed to be equal to the theoretical long-term pressure at the corresponding position, and the grouting pressures of the bottom four holes are 50% of the theoretical long-term pressure. Concerning the back ring, the theoretical long-term pressure and grouting pressure are both considered. However, the grouting pressure is assumed to remain at three different percentages, respectively 100%, 50%, and 0% of the corresponding grouting pressure in the middle ring. Although the grouting process has a certain influencing distance, it is impractical and inconvenient to calculate all the rings within this distance when designing a tunnel. Therefore, in the three-ring model, 100% and 0% of the middle ring's grouting pressure are assigned to the back ring to stand for the situations when the grouting effect attenuates very slowly and quickly. Additionally, a condition where the three rings in the model are all under the theoretical long-term pressure and the full grouting pressure is calculated. Calculational Case 1 is taken as the basis for the analysis, as it has a similar overburden (7m and 20 kPa surcharge) to that of the tunnel project in Chapter 5 (8.3m and no surcharge).

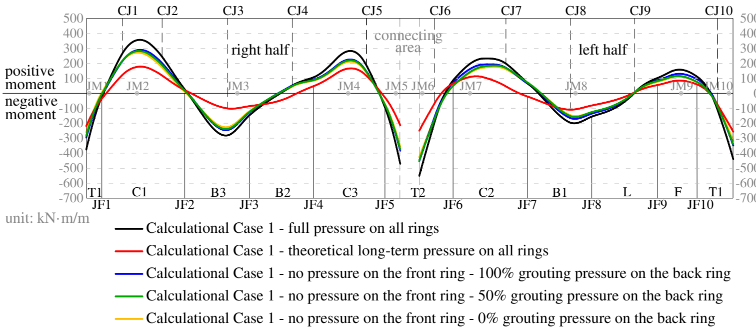

Figure 6.26 Bending moments under different grouting combinations.

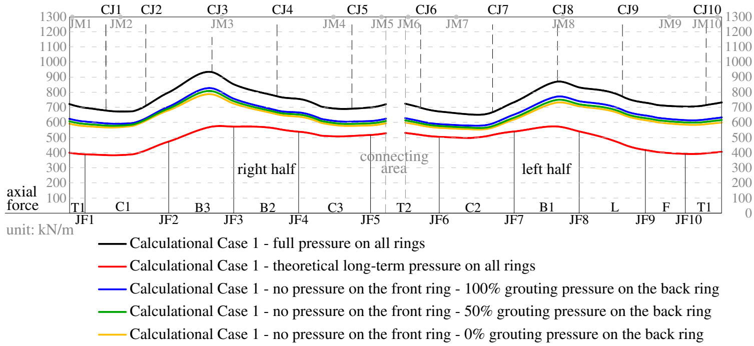

(b)

Figure 6.27 Axial forces under different grouting combinations.

The calculation results of the middle ring are shown in Figure 6.26 and Figure 6.27, and their comparisons of key sections JM1 to JM10 with the standard basis without grouting effect (Calculation Case 1) are presented in Figure 6.28 and Figure 6.29. Overall, the grouting effect leads to the increase of both axial forces and bending moments. The three calculation cases without the pressures on the front ring (blue, green and yellow curves) only have different grouting pressures on the back ring. Compared with the basic case, the bending moment has a larger increase percentage than the axial force, such as JM3 with a 90% increase of moment versus only a 35% increase of axial force, and 80% versus 15% at JM5 and JM6. This indicates that the grouting process is a critical stage for the QRST construction. However, although the grouting pressures on the back ring are different in these three cases, a specific section of the middle ring shows a similar increase rate of both bending moments and axial forces. This means the back ring's grouting effect is limited on the middle ring. Since the pressures around the back ring are larger than or equal to the theoretical long-term pressures, the pressure difference between the middle ring and the back ring is relatively small. Hence, it does not take notable internal forces from the middle ring.

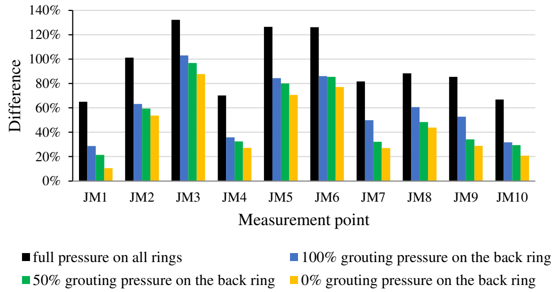

Figure 6.28 Comparison of bending moments at JM1 to JM10 under different grouting combinations.

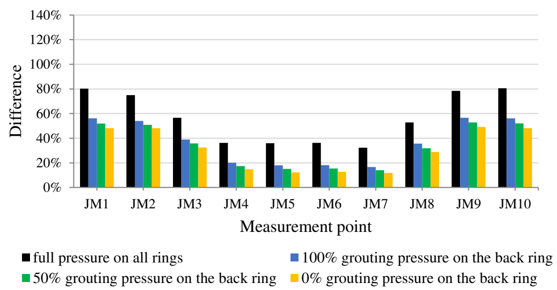

Figure 6.29 Comparison of axial forces at JM1 to JM10 under different grouting combinations.

When it comes to the comparison between the situations with and without the pressures on the front ring (black and blue curves), their only difference is the existence of the pressures on the front ring, but they are quite different from each other. This means that the segmental lining in the shield tail can significantly influence the calculation results of the ring just being pushed out. The load difference between the lining in the shield tail and the lining just getting out is very large. Therefore, the lining in the shield tail (the front ring in the current case) can sustain a reasonably large amount of the internal forces from the ring just pushed out (the middle ring in the current case).

Table 6.13 Convergence deformations under different grouting combinations (unit: mm).

	Grouting pressure combinations	D1	D2	D3	Abs(D3-D1)
1	Theoretical long-term pressure on all rings	-3.49	2.99	-3.67	0.18
2	Full pressure on all rings	-6.88	7.08	-7.22	0.34
3	No pressure on the front ring - 100% grouting pressure on the back ring	-5.68	5.83	-5.85	0.17
4	No pressure on the front ring - 50% grouting pressure on the back ring	-5.53	5.50	-5.59	0.07
5	No pressure on the front ring - 0% grouting pressure on the back ring	-5.31	5.11	-5.19	0.13
	Abs(combination 3-combination 5)	0.37	0.72	0.66	

The middle ring's deformations under different grouting combinations are summarized in Table 6.13, and their comparisons with the basic results are shown in Figure 6.30. When different grouting pressures are exerted on the back ring, the deformations are similar, with a slight difference of up to 0.72 mm. When no pressures and full pressures are considered on the front ring, the deformation differences between them (Grouting pressure combinations 2 and 3) are much larger than those with and without grouting pressures on the back ring (Grouting pressure combinations 5 and 3). These observations are similar to the bending moment comparisons between the different grouting combinations.

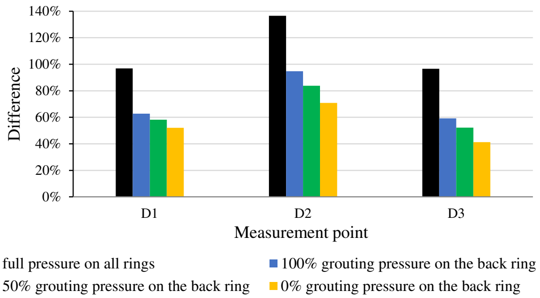

Figure 6.30 Comparison of convergence deformations at D1 to D3 under different grouting combinations.

In contrast to the previous conclusions for the different pressures on the back ring, it is obvious that the pressure difference between the front ring and the middle ring is larger than that between the back ring and the middle ring. The grouting pressures on the back ring only slightly affect the calculation results of the middle ring. It indicates that, at the critical moment when a segmental lining is pushed out, its behaviour is dominated by the pressures around it and the loading situations of its neighbouring lining in the tail. Although the grouting effect's attenuation needs a certain distance, the results from the back ring without any grouting pressures only deviate slightly from the back ring with full grouting pressures. It indicates that the grouting effect of the farther linings has a limited influence on the middle ring. From this perspective, the establishment of more lining rings in the model seems unnecessary, and a three-ring model can already give the overall calculation results for the moment when a ring is pushed out.

It has to been stressed that only a primary analysis for the moment of pushing out is conducted in this section. It aims to give overall predictions and discussions about the grouting effect. Further studies with 3D simulations or on-site verifications are needed to obtain more details about the construction process of a QRST tunnel and to solve the complex problem of pushing out. These aspects are beyond the scope of the current study and might be the subject of a future study. For the 3D simulations, the longitudinal response should be considered, such as with shell or solid elements for the lining modelling. Additionally, the TBM's position and corresponding effect, the interaction between grouting materials and soils, and the interaction between grouting materials and segments are also non-negligible. Each of these aspects needs specific detailed research, which is far beyond the scope of the current study. Actually, the study of shield tunnel construction is a hot topic, but the current research results based on the circular shield tunnels have many limitations due to variability of the soil type, the tunnel buried depth, the tunnel size and shape, the grouting material and the TBM type in each shield tunnel project.

6.8 Conclusions

In this chapter, different pressure settings are assumed to investigate their effects on the QRST's performance. Based on the analyses and discussions in this chapter, the following conclusions can be formulated:

(1) Concerning the deviation between the point loads in the indoor test and the uniform pressures which are assumed in design, the linearly varying lateral pressures lead to higher axial forces at the bottom area than at the top. Gravity has a limited influence on the axial forces and bending moments, up to 7% difference, and a relatively larger influence on the deformations, up to 20% difference. Due to its horizontal position in the indoor experiments, the tested lining ring cannot simulate these effects well. For the conditions without partial offset loads, the indoor point loads generally can give acceptable predictions for the bending moment distributions but smaller axial forces and larger deformations, resulting in a high safety factor for the lining design. Additionally, as the soil reaction is a passive force for the structural equilibrium, the indoor experimental method based

on a horizontal lining position is problematic to simulate a situation with large soil reactions.

(2) The QRST lining structure is divided into two parts by the interior column, and there are different longitudinal joints' location arrangements in each half, resulting in different stiffnesses of these two parts and therefore a non-symmetric distribution of bending moments in the one lining ring. When the pattern of staggered assembly is adopted, the structural deformation decreases notably, and the left and right halves deform uniformly. However, the bending moments from the neighbouring rings are transferred to the middle ring, further enlarging the non-symmetric bending moment distributions between the left and right halves. In the current case study, the bending moment in the neighbouring section related to segment F is roughly twice the bending moment in segment F.

(3) The circumferential joint only takes effect when the stiffness reaches a specific value. The circumferential joint stiffness should be adopted large enough to ensure the moment transfer in design. The increase of the circumferential joint stiffness results in a stronger effect of bending moment transfer. When the magnification factor changes, the CBMRs overall fall into the range from 0.2 to 0.4. Hence 0.3 can be recommended as the CBMR value to evaluate the moment in the segment body in design, but the CBMR of JF5 can be slightly higher around 0.4, while that of JF3 can be slightly lower around 0.2.

(4) The MRM method empirically adjusts the bending moment distributions through a CBMT and structural deformations through an SRF. This method gives overestimated bending moments for some joint sections and unacceptable design moments for segment sections, such as overestimating CJ3 and CJ8 and underestimating JM2. Besides, different SRFs are needed for the deformation calculations of D1 to D3. The MRM method cannot directly produce acceptable values for a QRST design. It is recommended to be used only for a preliminary calculation and an overall evaluation of the QRSTs.

(5) The coefficient of lateral pressure can significantly influence the QRST lining's performance. A higher coefficient produces smaller bending moments and deformations, as well as larger axial forces, producing a beneficial effect for lining design. A reasonable coefficient from a site geological test is critical. Due to the bending moment transfer, the neighbouring segments C1 sustain the bending moment from segment F, resulting in the bending moment in segment F insensitive to the coefficient change. Correspondingly, the bending moment value in segment C1 (neighbouring segments of F) should draw attention.

(6) A small coefficient of subgrade reaction, such as below 20 kPa/mm in the current cases, has slight influences on the structural performance. Beyond this range, a large coefficient of subgrade reaction can notably increase the axial forces and decrease the bending moments and deformations, especially for the long axis, resulting in a beneficial effect for design. A proper coefficient of subgrade reaction is essential.

(7) The partial offset surcharge results in an overall increase of the axial forces. The main changes of bending moment only happen at the top and waist areas. The surcharge at one side leads to the increases of the bending moment and the convergence deformation at the same side while it decreases at the other side. Among all the segments, segment C1 is the most sensitive to the partial offset surcharge, under which it sustains a notable bending moment transfer from its neighbouring F segments.

(8) When a segmental lining is pushed out of the shield tail, its behaviour is dominated by the pressures around it and the loading situations of its neighbouring lining in the tail. Although the grouting effect's attenuation needs a certain distance, the results from the back ring without any grouting pressures only deviate slightly from the back ring with full grouting pressures. The grouting effect of the farther linings has a limited influence on the ring just being pushed out, and the establishment of more lining rings in the model seems unnecessary. A three-ring model can already give acceptable overall calculation results for the pushing-out moment.

Chapter 7

Conclusions and future perspectives

7.1 General conclusions

This research aims to perform a comprehensive analysis of the mechanical behaviour of a QRST lining, covering the joints' behaviour, a calculation model, pressure distributions, and parametric analyses. In this final chapter, the conclusions drawn from each chapter are summarised, and some significant points of interest are highlighted. Finally, perspectives for further research are given.

7.1.1 Flexural and shear behaviours of longitudinal joints

In the Ningbo QRST, a specific type of longitudinal joints with embedded DIJPs is used in QRSTs. Their flexural and shear behaviours under varying axial forces are investigated. Concerning the flexural characteristic, full-scale joint tests and FEM simulations are conducted to detect the damage process of the longitudinal joints with different bolt positions. The proposed joint model provides an efficient approach for exploring the influence of the internal forces in the joint's vicinity, the concrete strength class, the bolt elongation resistance, and the joint structural details. In addition, the area influenced by the existence of the longitudinal joint and a comparison of joint deflections with the BSM method are investigated. The following conclusions can be drawn:

(1) The failure of the joints is initiated by concrete cracking at the core section and is terminated by concrete crushing. The bolts only yield after concrete crushing. The failure mode of the joint type is similar to that of a column cross-section subjected to a normal force with small eccentricity. The joint's resistance to cracking and the ultimate bearing capacity are both enhanced after bolt position

improvements. Additionally, during the damage process, the connecting reinforcements between DIJPs and concrete can guarantee the DIJPs' anchorage in the concrete, and the components of the DIJPs and their connections in this new joint type are proven to be reliable. The joint with DIJPs has an acceptable safety factor in the practical use and shows good performance within the moment range at the normal service level. The studied joint pattern is expected to be qualified to be applied in QRSTs.

(2) For a given axial force, the joint stiffness changes with increasing bending moments and its behaviour can be divided into three stages. At the first stage, the whole joint core section is under compression, and the bolts do not contribute to the rotation resistance. The joint behaviour is governed by the structural details of the core section. At the second stage, the bolts start being tensioned. The bolt stress increases fairly quickly while the rotational stiffness decreases gradually. At the third stage, the lever arm exceeds the distance from the edge of the joint's outer section to the joint's central axis. The evolutions of the joint rotation and the bolt stress appear to be almost linear.

(3) Although an increase of the concrete strength class or the bolt elongation resistance has a positive influence on the joint rotation, a change of the joint section to increase the lever arm between the bolts and the compression zone can improve the joint behaviour the most effectively, resulting in a decrease of the bolt stresses, as well as an increase of the joint rotation stiffness and the joint bearing capacity. This improvement direction should be preferably considered when designing a joint section. It can be achieved through bolt repositioning or increasing the joint's core section height based on the practical applicability.

(4) In the area within a 200 mm distance to the joint section, the stresses along the thickness direction change considerably, and there are notable differences between slices along the width direction of the joint segment. This means the stresses are non-uniformly distributed in the segment width direction, which is different from the assumption in the analysis of the joint without DIJPs that the stress along this direction is regarded as being uniform. Beyond 300 mm to the joint section, the stresses along the thickness show an overall linear distribution. In the positive bending moment case, the area influenced by the joint section is about 400 mm. In the negative bending moment case, the decrease of the concrete section caused by bolt installing holes results in an overall higher stress distribution and a larger influenced area of 500 mm. In addition, although the use of DIJPs makes a flexible joint layout and bolt position arrangement possible, the increased tensile stresses and compressive stress concentrations around DIJPs and bolt installing holes need more attention, and specific stirrup reinforcement is recommended in this area.

(5) The joint deflection caused by the joint rotation accounts for a large proportion of the total deflection, which is direct proof that the joint rotational characteristic is one of the critical factors for shield tunnel lining deformations. A precise description of the joint rotation behaviour is critical in the BSM method. Only then, the BSM method can give good predictions for joint deflections.

(6) A cubic polynomial function is proposed to describe the joint rotation development at each stage for the Type-A and Type-B joints under positive and negative cases. The fitting results show a good consistency with the rotations from the joint model, and the proposed functions serve as an input in the full-ring structural calculation of QRSTs to define the joint’s rotational behaviour.

Regarding the joint’s shear behaviour, full-scale shear resistance tests focusing on the normal service conditions are performed. Although the shear forces in QRSTs are larger than in conventional circular shield tunnels, it follows that the joint dislocation caused by the shear force only accounts for a small proportion of the dislocating requirement and thus will not notably aggravate the dislocation beyond the requirement. Within the axial force range from 500 to 883 kN/m, the stiffness values show an overall linear evolution as the axial force increases. The evolution of the shear stiffness is described by a linear function for the targeted axial force range.

7.1.2 Numerical model for QRST linings

The stiffnesses of the joints in a shield tunnel are related to the level of the joints’ internal forces. For joints in QRSTs, the joints’ rotational and shear deformations are not only affected by bending moments and shear forces in the joints but also by axial forces. Additionally, the longitudinal joints of QRSTs are subjected to a wide range of both bending moments and shear forces. Considering this, a numerical model based on the BSM method is established for this new type of tunnel linings. The main achievements and conclusions include:

(1) An iterative incremental method is presented to simulate the stiffness changes caused by the joint’s moment-axial force and shear-axial force interaction behaviour. The applicability of the numerical model is verified by comparing the bending moments and deformations in the lining to the results of unique indoor full-scale ring experiments.

(2) The iterative incremental method provides acceptable results for different load levels, while a constant stiffness based analysis does not.

(3) The joint stiffness increase through joint improvement can decrease the stiffness difference between the T segments and other areas, resulting in larger moments at the waist areas, while smaller moments occur in the T segments. The joint improvement can also decrease the stiffness difference between the right half and the left half, resulting in larger moments in the joints in the left half while smaller in the right one. Generally, for the overall internal forces in the lining, the effect of the joint improvement is limited, but it can effectively moderate the lining's convergence deformations.

(4) A parametric study reveals that not only the joint's rotational stiffness but also the joint's shear stiffness significantly affects the structural response. They are the most sensitive parameters for a QRST lining, especially for the lining's deformation. Further optimising the structural performance by adjusting only one parameter is difficult, and a combination of the choices for the parameters is important for the practical design of QRST linings.

7.1.3 Pressure distributions around QRSTs

Three in-situ monitoring tests with different grouting situations for QRSTs in soft soils under shallow overburdens are conducted. Based on the measured temporal and spatial distributions of the pressures around the lining structure, the following conclusions for QRSTs can be drawn:

(1) The steel brushes and plates in the shield tail have small contributions to the lining pressures. When the lining is pushed out of the shield tail, peak pressures appear, and these pressures are primarily caused by the injected grout. The peak pressures at the waists are smaller than those at the crown and the bottom, where the grouting holes are concentrated. Comparing the ratios between the peak pressures and the stable values in the case with a relatively normal grouting situation, the ratio at the top areas could reach a value of 2 while these ratios at the bottom and the waist areas were about 1.5 and 1.3.

(2) Non-uniformly distributed top pressures are observed in all tests, and these might result in large local bending moments at the crown area. Unsymmetrical pressure distributions appear on the sides of the lining. The left-right unsymmetrical grout assignment would augment this phenomenon. It might cause an overall rotational tendency of the lining structure and lead to an additional torque during the construction. These potential risks are unique concerns for QRSTs and should be specially considered.

(3) The effect of the grouting process happening at the shield tail attenuates quickly in the longitudinal direction as the peak pressures decrease a lot once the

tested ring is pushed out. The grouting process during tunnel construction has an influential range of 9 rings. Beyond this range, most pressure fluctuations during TBM drillings are smaller than 5% of the corresponding measured pressures. From the long-term perspective, the pressure distributions tend to stabilise at a similar state, and different grouting strategies will not affect the final pressure distributions.

(4) The varying and temporary loads of the back-up equipment and carriages inside the tunnel influence the pressures outside the linings. This kind of load seems to lead to an overall downward tendency of the lining structure and to result in a pressure decrease at the top and an increase at the bottom. By evaluating the lining buoyancy from the monitoring results, the calculated buoyancy fluctuates around the average weights of the tunnel at different stages and changes with a coincident pace of construction activities. The pressures around the lining perform as a counterforce to resist the load from the tunnel, rather than an active force exerted on the segments, such as when the lining was pushed out, and the surrounding soils would behave like an elastic foundation to hold the tunnel.

(5) For the shallow buried QRSTs in soft soils, the applicability of the proposed load distributions referring to the design model of circular tunnels is proven through comparison with long-term monitoring results. The speed of the pressure changes slows down with the increase of time after the linings are constructed. The influence of the grouting process or other construction loads on the lining pressures needs about 50 days to be relieved.

(6) A pressure mode combining cosinusoidal pressures and theoretical long-term pressures is proposed. It can give relatively good predictions for the grouting pressures when lining segments are pushed out, and it is expected to guide the segment design for the construction stage.

7.1.4 Analysis and discussion of QRST linings based on the developed numerical model

Different pressure settings are assumed to investigate their effects on the QRST's performance. Based on the analyses and discussions in this chapter, the following conclusions can be formulated:

(1) Concerning the deviation between the point loads in the indoor test and the uniform pressures which are assumed in design, gravity leads to higher axial forces at the bottom area than at the top. Due to its horizontal position, the tested lining ring cannot well simulate the gravity effect, resulting in smaller axial forces at the bottom area, up to 25% difference from the vertically standing layout. For the

conditions without partial offset loads, generally, the indoor point loads can give acceptable predictions for the bending moment distributions and deformations. However, as the soil reaction is a passive force for the structural equilibrium, the indoor experimental method based on a horizontal lining position is problematic to simulate a situation with large soil reactions.

(2) The QRST lining structure is divided into two parts by the interior column, and there are different longitudinal joints' location arrangements in each half, resulting in different stiffnesses of these two parts and therefore a non-symmetric distribution of bending moments in the one lining ring. When the pattern of staggered assembly is adopted, the structural deformation decreases notably, and the left and right halves deform uniformly. However, the bending moments from the neighbouring rings are transferred to the middle ring, further enlarging the non-symmetric bending moment distributions between the left and right halves. In the current case study, the bending moment in the neighbouring section related to segment F is roughly twice the bending moment in segment F.

(3) The circumferential joint only takes effect when the stiffness reaches a specific value. The circumferential joint stiffness should be adopted large enough to ensure the moment transfer in design. The increase of the circumferential joint stiffness results in a stronger effect of bending moment transfer. When the magnification factor changes, the CBMRs overall fall into the range from 0.2 to 0.4. Hence 0.3 can be recommended as the CBMR value to evaluate the moment in the segment body in design, but the CBMR of JF5 can be slightly higher around 0.4, while that of JF3 can be slightly lower around 0.2.

(4) The MRM method empirically adjusts the bending moment distributions through a CBMT and structural deformations through an SRF. This method gives overestimated bending moments for some joint sections and unacceptable design moments for segment sections, such as overestimating CJ3 and CJ8 and underestimating JM2. Besides, different SRFs are needed for the deformation calculations of D1 to D3. The MRM method cannot directly produce acceptable values for a QRST design. It is recommended to be used only for a preliminary calculation and an overall evaluation of the QRSTs.

(5) The coefficient of lateral pressure can significantly influence the QRST lining's performance. A higher coefficient produces smaller bending moments and deformations, as well as larger axial forces, producing a beneficial effect for lining design. A reasonable coefficient from a site geological test is critical. Due to the bending moment transfer, the neighbouring segments C1 sustain the bending moment from segment F, resulting in the bending moment in segment F insensitive

to the coefficient change. Correspondingly, the bending moment value in segment C1 (neighbouring segments of F) should draw attention.

(6) A small coefficient of subgrade reaction, such as below 20 kPa/mm in the current cases, has slight influences on the structural performance. Beyond this range, a large coefficient of subgrade reaction can notably increase the axial forces and decrease the bending moments and deformations, especially for the long axis, resulting in a beneficial effect for design. A proper coefficient of subgrade reaction is essential.

(7) The partial offset surcharge results in an overall increase of the axial forces. The main changes of bending moment only happen at the top and waist areas. The surcharge at one side leads to the increases of the bending moment and the convergence deformation at the same side while it decreases at the other side. Among all the segments, segment C1 is the most sensitive to the partial offset surcharge, under which it sustains a notable bending moment transfer from its neighbouring F segments.

(8) When a segmental lining is pushed out of the shield tail, its behaviour is dominated by the pressures around it and the loading situations of its neighbouring lining in the tail. Although the grouting effect's attenuation needs a certain distance, the results from the back ring without any grouting pressures only deviate slightly from the back ring with full grouting pressures. The grouting effect of the farther linings has a limited influence on the ring just being pushed out, and the establishment of more lining rings in the model seems unnecessary. A three-ring model can already give acceptable overall calculation results for the pushing-out moment.

7.2 Perspectives and recommendations for further research

7.2.1 Effect of shear-moment-axial interaction in the longitudinal joints

The special-section shield tunnels may generate a non-negligible shear force in some longitudinal joints due to cross-section geometry. A joint in this condition is typically subjected to a combination of shear, moment and axial forces. In the current study, the internal forces in joints are separated into moment-axial force and shear-axial force interactions, and they are considered separately. However, as presented in Chapter 2, as the joint keeps opening with increasing bending moment, the compressive area is changing at the same time, indicating the actual area sustaining the shear force is not as idealised as being under full-section compression. On the other hand, the shear force possibly leads to a joint dislocation, resulting in an imperfect symmetry in the rotational behaviour of the segments beside a joint section. Therefore, the rotational stiffness of the longitudinal joints might be influenced by the sustained shear force, and the bending moment could also affect the shear stiffness. As such, the shear-moment-axial force interaction potentially has a negative effect on the bolt stress, the cracking moment and the joints' bearing capacity. However, the interactive effect of these three forces is a complex problem, especially considering the possible cross combinations of positive and negative bending moments and outward and inward shear forces. A reasonable testing facility and a feasible test design are needed to be developed for the shear-moment-axial force scenario. Meanwhile, the circumferential joint might also sustain this kind of force combination, whose effect on the QRSTs with staggered assembly is unclear. Research related to this aspect is very limited, to the author's knowledge, and is expected to be a subject of future research.

7.2.2 Needs for the 3D modelling

This current study covers some basic aspects of the structural performance of a QRST segmental lining, such as the joint behaviour, the applicability of the BSM method and the pressure distributions in shallow buried soft soils. However, the QRST considered, has a new shield tunnel pattern, and the established BSM model for the QRST can only solve some simple three-dimensioned problems. More aspects related to the 3D modelling have not been studied in detail. Based on the objects considered in the 3D modelling, potential further research directions might include:

(1) 3D modelling for full ring segments. The current study focuses on the lining's behaviour under the elastic stage. A full ring 3D modelling can be used to obtain its performance when the materials develop into the plastic stage. On other hand, due to the high cost of indoor full ring experiments, a simulation approach can help to evaluate the lining's bearing capacity and the effects of further improvements in segment design. For example, an increase in the haunch size of the T segments might postpone the cracking of nearby concrete or shear damage of these segments, and then increase the ultimate bearing capacity of the whole lining structure.

(2) 3D modelling for the tunnel construction process. The construction of shield tunnels is complicated, which is a critical stage for the tunnel lining. The TBM's position can influence the thrust force on the newly placed lining and the forces from grease and brushes in relation to the distance between the shield and the segment extrados. The former is along the tunnel direction, while the latter is a

radial force. At the same time, the lining ring just pushed out is sustaining the backfilling grouting pressure. Based on the experience of the construction of circular shield tunnels, segment damages might occur during this period. The behaviour of the QRST linings under such complex loading conditions is unclear. A 3D simulation is necessary to solve this problem and can help to analyse the lining behaviour in other risky situations, such as the changes of the thrust force from pushing jacks caused by lining assembly, TBM position adjustment, tunnel axis with a curve and/or slope, and unacceptable segment assembly tolerance occurring. Research on these aspects can contribute a lot to the rapid construction of the QRSTs, as the current QRST construction speed (highest speed of six rings per day as shown in Chapter 5) is much lower than that for traditional circular tunnels (more than ten rings per day).

(3) 3D modelling of the tunnel's longitudinal behaviour. When a newly assembled ring is pushed out of the shield tail, fluid grout is ejected to backfill the tail void between the lining and TBM. The resulting buoyancy might have a lifting effect or tendency on the lining rings near the TBM, causing a moment in the tunnel's longitudinal direction. However, at the same time, the TBM needs to balance this moment and to drive along the designed route. Therefore, the force from the jacks in the TBM is not evenly distributed on the tunnel's transverse section. Unexpected joint openings or concrete cracking could occur. A 3D model can consider this effect and simulate the behaviour of the newly pushed-out linings and the faraway linings.

(4) 3D modelling of ground subsidence. Environmental influence control is also an important aspect of the QRST application. The grouting material hardens, consolidates and serves as a permanent filling between the segmental linings and the surrounding soils. Its backfilling pressure and long-term mechanical characteristic affect the ground settlement. With the approach of 3D simulations, it will be of particular interest to investigate the settlement difference between one QRST line and two traditional circular tunnel lines.

(5) 3D modelling of seismic effect. Many studies have focused on the response of circular shield tunnels under seismic stimulation. However, the seismic effect on a QRST has not been investigated yet. The special shape and the interior column might make it more sensitive and more vulnerable than circular tunnels. It will be interesting to conduct a simulation work related to earthquake action.

References

A.A.S.H.T.O. (American Association of State Highway and Transportation Officials). Technical manual for design and construction of road tunnels - civil elements. Washington, DC, USA, 2010.

A.F.T.E.S. (Association Française des Tunnels et de L'espace Souterrain). Recommendation for the Design, Sizing and Construction of Precast Concrete Segments Installed at the Rear of a Tunnel Boring Machine (TBM). Paris, France, 2005.

Abaqus. Abaqus (2018) User's Manual. Abaqus Inc: RI, USA, 2018,

Akmadžić, V.;Vrdoljak, A. Determination of the soil reaction coefficient value–software solution. *e–Zbornik: Electronic collection of papers of the Faculty of Civil Engineering* 2018, *8*, 22-29.

Anh, T.P.;Sugimoto, M. The Effects of Tangential Ground–Lining Interaction on Segmental Lining Behavior Using the Beam-Spring Model. *Applied Sciences* 2020, *10*, 1084.

Arnau Delgado, O. Structural response of precast concrete segmental tunnel linings. 2012.

Arnau, O.;Molins, C. Three dimensional structural response of segmental tunnel linings. *Eng. Struct.* 2012, *44*, 210-221.

Arnau, O.;Molins, C.;Blom, C.;Walraven, J. Longitudinal time-dependent response of segmental tunnel linings. *Tunn. Undergr. Space Technol.* 2012, *28*, 98-108.

Atkinson, J.;Potts, D. Stability of a shallow circular tunnel in cohesionless soil. *Geotechnique* 1977, *27*, 203-215.

B.S.I. (British Standards Institute). Tunnel Design - Design of Concrete Segmental Tunnel Linings - Code of Practice. London, UK, 2016.

Bakhshi, M.;Nasri, V. Structural design of segmental tunnel linings, Proceedings of 3rd International Conference on Computational Methods in Tunnelling and Subsurface Engineering: EURO: TUN, 2013, pp. 17-19.

Bakker, K. Structural design of linings for bored tunnels in soft ground. *Heron* 2003, *48*, 33-64.

Bezuijen, A. Grouting the tail void of bored tunnels: the role of hardening and consolidation of grouts, Geotechnical Aspects of Underground Construction in Soft Ground: Proceedings of the 5th International Symposium TC28, Amsterdam, the Netherlands, 2005, pp. 319-325.

Bezuijen, A.;Talmon, A.M.;Kaalberg, F.J.;Plugge, R. Field measurements of grout pressures during tunnelling of the Sophia Rail Tunnel. *Soils Found.* 2004, *44*, 39-48.

Bilotta, E.;Russo, G. Internal forces arising in the segmental lining of an earth pressure balance-bored tunnel. *J. Geotech. Geoenviron. Eng.* 2013, *139*, 1765-1780.

Blom, C. Design philosophy of concrete linings for tunnels in soft soils. Delft University of Technology, The Netherlands, 2002.

Blom, C.;Van der Horst, E.;Jovanovic, P. Three-dimensional structural analyses of the shield-driven “Green Heart” tunnel of the high-speed line south. *Tunn. Undergr. Space Technol.* 1999, *14*, 217-224.

Blom, C.B.M. Design philosophy of concrete linings for tunnels in soft soils. Doctor, Delft University of Technology, Delft, The Netherlands, 2004.

Bowles, L. Foundation analysis and design. McGraw-hill, 1996,

Brabant, J.-D.;Duhme, R. Hard rock TBM tunnelling—Technical developments and recent experience, Proceedings of the 2017 World Congress on Advances in Structural Engineering and Mechanics (ASEM17), Ilsan, Seoul, Korea.

Buyukozturk, O.;Bakhoum, M.M.;Michael Beattie, S. Shear behavior of joints in precast concrete segmental bridges. *Journal of Structural Engineering* 1990, *116*, 3380-3401.

Cao, Y.;Wang, P.;Jin, X.;Wang, J.;Yang, Y. Tunnel structure analysis using the multi-scale modeling method. *Tunn. Undergr. Space Technol.* 2012, *28*, 124-134.

Caratelli, A.;Meda, A.;Rinaldi, Z.;Giuliani-Leonardi, S.;Renault, F. On the behavior of radial joints in segmental tunnel linings. *Tunn. Undergr. Space Technol.* 2018, *71*, 180-192.

Chen, R.-P.;Chen, S.;Wu, H.-N.;Liu, Y.;Meng, F.-Y. Investigation on deformation behavior and failure mechanism of a segmental ring in shield tunnels based on elaborate numerical simulation. *Engineering Failure Analysis* 2020, *117*, 104960.

Chen, R.-p.;Meng, F.-y.;Ye, Y.-h.;Liu, Y. Numerical simulation of the uplift behavior of shield tunnel during construction stage. *Soils Found.* 2018, *58*, 370-381.

Chow, B. Double-O-tube shield tunneling technology in the Shanghai Rail Transit Project. *Tunn. Undergr. Space Technol.* 2006, *21*, 594-601.

Code for Construction and Acceptance of Shield Tunnelling method [GB50446]. Ministry of Housing and Urban-Rural Development of the People's Republic of China (MOHURD). Beijing, China (in Chinese), 2017.

Code for Design of Concrete Structures [GB50010]. Ministry of Housing and Urban-Rural Development of the People's Republic of China (MOHURD). Beijing, China (in Chinese), 2011.

Code for Design of Metro [GB50157]. Ministry of Housing and Urban-Rural Development of the People's Republic of China (MOHURD). Beijing, China (in Chinese), 2013.

Deutscher Ausschuss fur Unterirdisches Bauen. Recommendations for the design, production and installation of segmental rings. Berlin: Deutscher Ausschuss für unterirdisches Bauen e. V, Cologne, Germany, 2013.

Ding, W.;Duan, C.;Zhu, Y.;Zhao, T.;Huang, D.;Li, P. The behavior of synchronous grouting in a quasi-rectangular shield tunnel based on a large visualized model test. *Tunn. Undergr. Space Technol.* 2019, *83*, 409-424.

Ding, W.;Gong, Y.;Qiao, Y.;Gong, C. Experimental investigation on mechanical behavior of segmental joint under combined loading of compression-bending-shear. *Tunn. Undergr. Space Technol.* 2020, *98*, 103346.

Ding, W.;Yue, Z.;Tham, L.;Zhu, H.;Lee, C.;Hashimoto, T. Analysis of shield tunnel. *Int. J. Numer. Anal. Methods Geomech.* 2004, *28*, 57-91.

Do, N.-A.;Dias, D.;Oreste, P. Three-dimensional numerical simulation of mechanized twin stacked tunnels in soft ground. *Journal of Zhejiang University SCIENCE A* 2014a, *15*, 896-913.

Do, N.-A.;Dias, D.;Oreste, P.;Djeran-Maigre, I. Three-dimensional numerical simulation of a mechanized twin tunnels in soft ground. *Tunn. Undergr. Space Technol.* 2014b, *42*, 40-51.

Do, N.A.;Dias, D.;Oreste, P.;Djeran‐Maigre, I. A new numerical approach to the hyperstatic reaction method for segmental tunnel linings. *Int. J. Numer. Anal. Methods Geomech.* 2014c, *38*, 1617-1632.

Duddeck, H. Guidelines for the design of tunnels. *Tunn. Undergr. Space Technol.* 1988, *3*, 237-249.

Duddeck, H.;Erdmann, J. Structural design models for tunnels in soft soil. *Underground Space* 1985, *9*, 246-259.

Gall, V.E.;Marwan, A.;Smarslik, M.;Obel, M.;Mark, P.;Meschke, G. A holistic approach for the investigation of lining response to mechanized tunneling induced construction loadings. *Underground Space* 2018, *3*, 45-60.

Galván, A.;Peña, F.;Moreno-Martínez, J.Y. Effect of TBM advance in the structural response of segmental tunnel lining. *Int. J. Geomech.* 2017, *17*, 04017056.

Gil Lorenzo, S. Structural behaviour of concrete segmental lining tunnels: towards design optimisation. Doctor's Thesis, University of Cambridge, 2018.

Gil Lorenzo, S. Longitudinal beam response of concrete segmental linings simultaneously backfilled with bicomponent grouts. *Tunn. Undergr. Space Technol.* 2019, *90*, 277-292.

Gong, C.;Ding, W.;Mosalam, K.M.;Günay, S.;Soga, K. Comparison of the structural behavior of reinforced concrete and steel fiber reinforced concrete tunnel segmental joints. *Tunn. Undergr. Space Technol.* 2017, *68*, 38-57.

Groeneweg, T. Shield driven tunnels in ultra high strength concrete: Reduction of the tunnel lining thickness. Master Thesis, Delft University of Technology, Delft, The Netherlands, 2007.

Gruebl, F. Segmental Ring Design: New Challenges with High Tunnel Diameters. AITES/ITA, 2012,

Guo, R.;He, C.;Su, Z.;Peng, Z. Study of shearing mechanical properties of segment joints of shield tunnels. *Xiandai Suidao Jishu* 2011, *48*, 72-77.

Han, L.;Ye, G.-l.;Chen, J.-j.;Xia, X.-h.;Wang, J.-h. Pressures on the lining of a large shield tunnel with a small overburden: a case study. *Tunn. Undergr. Space Technol.* 2017, *64*, 1-9.

Hashimoto, T.;Konda, T.;Brinkman, J.;Feddema, A.;Kano, Y. Simultaneous backfill grouting, pressure development in construction phase and in the long-term. *Tunnelling. A Decade of Progress. GeoDelft 1995-2005* 2005, 101.

Hashimoto, T.;Ye, G.;Nagaya, J.;Konda, T.;Ma, X. Study on earth pressure acting upon shield tunnel lining in clayey and sandy grounds based on field monitoring, Geotechnical Aspects of Underground Construction in Soft Ground: Proceedings of the 6th International Symposium (IS-Shanghai 2008). CRC Press, 2008, pp. 307.

Hu, X.;Zhang, Z.;Teng, L. An analytical method for internal forces in DOT shield-driven tunnel. *Tunn. Undergr. Space Technol.* 2009, *24*, 675-688.

Huang, J. Research of suitable synchronous grouting technology for rectangular-shaoed shield. *China Municipal Engineering* 2016, 53-56.

Huang, X.;Huang, H.;Zhang, J. Flattening of jointed shield-driven tunnel induced by longitudinal differential settlements. *Tunn. Undergr. Space Technol.* 2012, *31*, 20-32.

Huang, X.;Liu, W.;Zhang, Z.;Wang, Q.;Wang, S.;Zhuang, Q.;Zhu, Y.;Zhang, C. Exploring the three-dimensional response of a water storage and sewage tunnel based on full-scale loading tests. *Tunn. Undergr. Space Technol.* 2019, *88*, 156-168.

I.T.A. Working Group NO.2 (International Tunneling and Underground Space Association). Guidelines for the design of shield tunnel lining. Tunn. Undergr. Space Technol., 2000 303-331.

I.T.A. Working Group NO.2 (International Tunneling and Underground Space Association). Guidelines for the design of segmental tunnel linings. Longrine, Place Carnot, Avignon, France, 2019.

J.S.C.E. (Japan Society of Civil Engineers). The design and construction of underground structure. 1977.

J.S.C.E. (Japanese Standard for Shield Tunneling). Standard Specifications for Tunneling-2006: Shield Tunnels. 2007.

J.S.C.E. (Japan Society of Civil Engineers). Standard Specifications for Tunneling–2016: Shield Tunnels. Tokyo, Janpan, 2016.

Japan Society of Civil Engineers. Japanese Standard for Shield Tunneling (Zhu, W. translates). China Construction Industry Press, Beijing, China (in Chinese), 2001.

Jiang, H.;Chen, L.;Ma, Z.J.;Feng, W. Shear behavior of dry joints with castellated keys in precast concrete segmental bridges. *Journal of Bridge Engineering* 2015, *20*, 04014062.

Jin, Y.;Ding, W.;Yan, Z.;Soga, K.;Li, Z. Experimental investigation of the nonlinear behavior of segmental joints in a water-conveyance tunnel. *Tunn. Undergr. Space Technol.* 2017, *68*, 153-166.

Kashima, Y.;Kondo, N.;Inoue, M. Development and application of the DPLEX shield method: results of experiments using shield and segment models and application of the method in tunnel construction. *Tunn. Undergr. Space Technol.* 1996, *11*, 45-50.

Kasper, T.;Meschke, G. A 3D finite element simulation model for TBM tunnelling in soft ground. *Int. J. Numer. Anal. Methods Geomech.* 2004, *28*, 1441-1460.

Kassem, M.;El-Shafeiy, T.;Hussein, M.;Afefy, H.;Hassan, A. Shear behaviour of SHCC dry joints in precast construction, Proc., Int. Conf. on Advances in Structural and Geotechnical Engineering, ICASGE, 2017, pp. 27-30.

Kavvadas, M.;Litsas, D.;Vazaios, I.;Fortsakis, P. Development of a 3D finite element model for shield EPB tunnelling. *Tunn. Undergr. Space Technol.* 2017, *65*, 22-34.

Kim, H.;Eisenstein, Z. Prediction of tunnel lining loads using correction factors. *Engineering Geology* 2006, *85*, 302-312.

Klappers, C.;Grübl, F.;Ostermeier, B. Structural analyses of segmental lining–coupled beam and spring analyses versus 3D-FEM calculations with shell elements. *Tunn. Undergr. Space Technol.* 2006, *21*.

Koyama, Y. Present status and technology of shield tunneling method in Japan. *Tunn. Undergr. Space Technol.* 2003, *18*, 145-159.

Koyoma, Y.;Nishimura, T. The design of lining segment of shield tunnel using a beam-spring model. *Railway Technical Research Institute, Quarterly Reports* 1998, *39*.

Lan, X.;Lu, L.;Liu, L. Experimental study on mechanical properties for segment joints of super tunnel lining. *Structural Engineers* 2009, *25*, 110-114.

Lee, K.;Ge, X. The equivalence of a jointed shield-driven tunnel lining to a continuous ring structure. *Can. Geotech. J.* 2001, *38*, 461-483.

Lee, K.;Hou, X.;Ge, X.;Tang, Y. An analytical solution for a jointed shield - driven tunnel lining. *Int. J. Numer. Anal. Methods Geomech.* 2001, *25*, 365-390.

Leung, C.;Meguid, M. An experimental study of the effect of local contact loss on the earth pressure distribution on existing tunnel linings. *Tunn. Undergr. Space Technol.* 2011, *26*, 139-145.

Li, F.;Hu, Y.;Li, L. Assembling technology for partial segment of shield with horseshoe-shaped cross-section *Tunnel Construction* 2017, *37*, 1162-1166.

Li, X.;Yan, Z.;Wang, Z.;Zhu, H. Experimental and analytical study on longitudinal joint opening of concrete segmental lining. *Tunn. Undergr. Space Technol.* 2015a, *46*, 52-63.

Li, X.;Yan, Z.;Wang, Z.;Zhu, H. A progressive model to simulate the full mechanical behavior of concrete segmental lining longitudinal joints. *Eng. Struct.* 2015b, *93*, 97-113.

Li, Z.;Soga, K.;Wang, F.;Wright, P.;Tsuno, K. Behaviour of cast-iron tunnel segmental joint from the 3D FE analyses and development of a new bolt-spring model. *Tunn. Undergr. Space Technol.* 2014, *41*, 176-192.

Li, Z.;Soga, K.;Wright, P. Behaviour of cast-iron bolted tunnels and their modelling. *Tunn. Undergr. Space Technol.* 2015c, *50*, 250-269.

Liang, Y.;Zhang, J.;Lai, Z.;Huang, Q.;Huang, L. Temporal and spatial distribution of the grout pressure and its effects on lining segments during synchronous grouting in shield tunnelling. *Eur. J. Environ. Civ. Eng.* 2017, 1-18.

Lin, C.;Wu, S.;Xia, T. Design of shield tunnel lining taking fluctuations of river stage into account. *Tunn. Undergr. Space Technol.* 2015, *45*, 107-127.

Liu, C.;Bezuijen, A.;Yang, M.;Cachim, P. Elastic analysis of ground movements around a tunnel considering a buoyant lining moving upwards. *Int. J. Numer. Anal. Methods Geomech.* 2019, *43*, 1562-1575.

Liu, J.;Hou, X. Shield driven tunnel. Bejing: China Railway Publishing House, 1991,

Liu, X.;Bai, Y.;Yuan, Y.;Mang, H.A. Experimental investigation of the ultimate bearing capacity of continuously jointed segmental tunnel linings. *Struct. Infrastruct. Eng.* 2016, *12*, 1364-1379.

Liu, X.;Dong, Z.;Bai, Y.;Zhu, Y. Investigation of the structural effect induced by stagger joints in segmental tunnel linings: First results from full-scale ring tests. *Tunn. Undergr. Space Technol.* 2017a, *66*, 1-18.

Liu, X.;Liu, Z.;Ye, Y.;Bai, Y.;Zhu, Y. Mechanical behavior of quasi-rectangular segmental tunnel linings: Further insights from full-scale ring tests. *Tunn. Undergr. Space Technol.* 2018a, *79*, 304-318.

Liu, X.;Liu, Z.;Yuan, Y.;Zhu, Y. Quasi-Rectangular Shield Tunneling Technology in the Ningbo Rail Transit Project. *High Tech Concrete: Where Technology and Engineering Meet* 2018b, 2765-2773.

Liu, X.;Sun, Q. Case analysis on progressive collapse of shield tunnel linings. *Journal of Tunnelling and Hazard Control* 2020, *2*, 21-30.

Liu, X.;Ye, Y.;Liu, Z.;Huang, D. Mechanical behavior of Quasi-rectangular segmental tunnel linings: First results from full-scale ring tests. *Tunn. Undergr. Space Technol.* 2018c, *71*, 440-453.

Liu, X.;Zhang, C.;Zhang, C.;Yuan, Y. Ultimate load‐carrying capacity of the longitudinal joints in segmental tunnel linings. *Struct. Concr.* 2017b, *18*, 693-709.

Lu, L.;Lu, X.;Fan, P. Full-ring experimental study of the lining structure of Shanghai Changjiang tunnel, 4th International Conference on Earthquake Engineering, Taipei, Taiwan. Citeseer, 2006, pp.

Maidl, B.;Herrenknecht, M.;Maidl, U.;Wehrmeyer, G. Mechanised shield tunnelling. John Wiley & Sons, 2013,

Majdi, A.;Ajamzadeh, H.;Nadimi, S. Investigation of moment-rotation relation in different joint types and evaluation of their effects on segmental tunnel lining. *Arab. J. Geosci.* 2016, *9*, 512.

Mashimo, H.;Ishimura, T. Evaluation of the load on shield tunnel lining in gravel. *Tunn. Undergr. Space Technol.* 2003, *18*, 233-241.

Mashimo, H.;Ishimura, T. Numerical modelling of the behavior of shield tunnel lining during assembly of a tunnel ring. *Earth* 2005, *60*, 100-100.

Mo, H.;Chen, J. Study on inner force and dislocation of segments caused by shield machine attitude. *Tunn. Undergr. Space Technol.* 2008, *23*, 281-291.

Moriya, Y. Special shield tunneling methods in Japan. *Proceedings of the International Conference on Tunnels and Underground Structures* 2000, 249-225.

Nakamura, H.;Kubota, T.;Furukawa, M.;Nakao, T. Unified construction of running track tunnel and crossover tunnel for subway by rectangular shape double track cross-section shield machine. *Tunn. Undergr. Space Technol.* 2003, *18*, 253-262.

Ngan Vu, M.;Broere, W.;Bosch, J.W. Structural analysis for shallow tunnels in soft soils. *Int. J. Geomech.* 2017, *17*, 04017038.

Nomoto, T.;Imamura, S.;Hagiwara, T.;Kusakabe, O.;Fujii, N. Shield tunnel construction in centrifuge. *J. Geotech. Geoenviron. Eng.* 1999, *125*, 289-300.

Ö.V.B.B. (Österreichische Vereinigung für Beton und Bautechnik). Guideline Concrete Segmental Lining Systems. Wien, Austria, 2011a.

Ö.V.B.B. (Österreichische Vereinigung für Beton und Bautechnik). Guidelines concrete segmental lining system. 2011b.

Peck, R.B.;Hendron, A.;Mohraz, B. State of the art of soft-ground tunneling. *International Proceedings of the North American Rapid Excavation and Tunneling Conference* 1972, *1*, 259-286.

Qiao, Y.;Zhao, T.;Ding, W. Simulating Synchronous Grouting in Shield Tunnels with the Consideration of Evolution of Grouting Pressure, GeoShanghai International Conference. Springer, 2018, pp. 23-31.

Schmid, J. Statische Grenzprobleme in kreisförmig durchörtertem Gebirge. PhD Thesis, ETH Zurich, Zürich, Switzerland, 1926.

Schreyer, J.;Winselmann, D. Suitability tests for the lining for the 4th Elbe tunnel tube–Results of large-scale tests. *Tunnel* 2000, *1*, 34–44.

Shirlaw, J.N.;Richards, D.P.;Ramond, P.;Longchamp, P. Recent experience in automatic tail void grouting with soft ground tunnel boring machines, Proceedings of the ITA-AITES World Tunnel Congress, Singapore, 2004, pp. 22-27.

Sramoon, A.;Sugimoto, M.;Kayukawa, K. Theoretical model of shield behavior during excavation. II: Application. *J. Geotech. Geoenviron. Eng.* 2002, *128*, 156-165.

Sun, W.;Guan, L.;Wen, Z. Mechanical analysis and application of large rectangular cross-section shield tunnel. *Tunnel Construction* 2015, *35*, 1028.

Suwansawat, S. Earth Pressure Balance (EPB) Shield Tunneling in Bangkok: Ground Response and Prediction of Surface Settlements Using Artificial Neural Networks. Doctoral Thesis, Massachusetts Institute of Technology (MIT), 2002.

Talmon, A.;Bezuijen, A. Simulating the consolidation of TBM grout at Noordplaspolder. *Tunn. Undergr. Space Technol.* 2009, *24*, 493-499.

Talmon, A.;Bezuijen, A. Analytical model for the beam action of a tunnel lining during construction. *Int. J. Numer. Anal. Methods Geomech.* 2013a, *37*, 181-200.

Talmon, A.;Bezuijen, A. Calculation of longitudinal bending moment and shear force for Shanghai Yangtze River Tunnel: Application of lessons from Dutch research. *Tunn. Undergr. Space Technol.* 2013b, *35*, 161-171.

Tang, Y. The mechanism study of the staggering assembly of shield-driven tunnel. M. Phil. thesis, Tongji University, Shanghai, China, 1988.

Tassios, T.P.;Vintzēleou, E.N. Concrete-to-concrete friction. *Journal of Structural Engineering* 1987, *113*, 832-849.

Teachavorasinskun, S. Evaluation of liner responses due to non-uniform tail void grouting pressure. *Geomechanics and Geoengineering* 2018, *13*, 226-232.

Teachavorasinskun, S.;Chub-uppakarn, T. Influence of segmental joints on tunnel lining. *Tunn. Undergr. Space Technol.* 2010, *25*, 490-494.

Technical Specification for Concrete Structure of Tall Building [JGJ3-2010]. Ministry of Housing and Urban-Rural Development of the People's Republic of China (MOHURD). Beijing, China (in Chinese), 2010.

Thewes, M.;Budach, C. Grouting of the annular gap in shield tunnelling–An important factor for minimisation of settlements and production performance, ITA-AITES World Tunnel Congress, 2009, pp.

Windels, R. Kreisring im elastischen Kontinuum. *Der Bauingenieur* 1967, *42*, 429-439.

Wood, A.M. The circular tunnel in elastic ground. *Geotechnique* 1975, *25*, 115-127.

Xiao, L.;Linxing, G.;Zhuyin, W.;Wei, S.;Xian, L. Experimental Study of Structural Performance of Segmental Lining of Rectangular Shield Tunnel during Construction: A Case Study of Underground Connection Gallery in Hongqiao District of Shanghai. *Tunnel Construction* 2016a, *36*, 9.

Xiao, L.;Linxing, G.;Zhuyin, W.;Wei, S.;Xian, L. A Method for Force Analysis of Rectangular Shield Tunnel Lining Structure Considering Whole Construction Process: Principle and Application. *Tunnel Construction* 2016b, *38*, 10.

Yan, Z.;Peng, Y.;Ding, W.;Zhu, H.;Huang, F. Load tests on segment joints of single lining structure of shield tunnel in Qingcaosha water conveyance project. *Chin. J. Geotech. Eng* 2011, *33*, 1385-1390.

Yang, Z.;Shen, Z.;Zhu, Y.;Huang, D. Research on the design scheme of quasi-rectangular shield tunnel. *Mod. Tunn. Technol* 2016, *53*, 89-97.

Ye, F.;Gou, C.-f.;Sun, H.-d.;Liu, Y.-p.;Xia, Y.-x.;Zhou, Z. Model test study on effective ratio of segment transverse bending rigidity of shield tunnel. *Tunn. Undergr. Space Technol.* 2014, *41*, 193-205.

Ye, G.;Hashimoto, T.;Shen, S.;Zhu, H.;Bai, T. Lessons learnt from unusual ground settlement during Double-O-Tube tunnelling in soft ground. *Tunn. Undergr. Space Technol.* 2015, *49*, 79-91.

Ye, Y. Reseach on mechanical behavior and overall safety of lining structures for quasi-rectangular sheield tunnel. Master Thesis, Tongji University Shanghai, China, 2018.

Yu, H.;Yuan, Y.;Chen, Z.;Yu, G. Numerical simulation for large-scale seismic response analysis of long-distance water-conveyance shield tunnel, *ICPTT 2009: Advances and Experiences with Pipelines and Trenchless Technology for Water, Sewer, Gas, and Oil Applications*, 2009, pp. 1197-1211.

Yu, H.;Yuan, Y.;Qiao, Z.;Gu, Y.;Yang, Z.;Li, X. Seismic analysis of a long tunnel based on multi-scale method. *Eng. Struct.* 2013, *49*, 572-587.

Zhang, H.;Fu, D.;Guo, C. Study on load test of segment joint in shield driven tunnel. *Mod. Tunn. Technol* 2002, *39*, 28D34.

Zhang, J.-L.;Vida, C.;Yuan, Y.;Hellmich, C.;Mang, H.A.;Pichler, B. A hybrid analysis method for displacement-monitored segmented circular tunnel rings. *Eng. Struct.* 2017, *148*, 839-856.

Zhang, J.L.;Mang, H.A.;Liu, X.;Yuan, Y.;Pichler, B. On a nonlinear hybrid method for multiscale analysis of a bearing - capacity test of a real - scale segmental tunnel ring. *Int. J. Numer. Anal. Methods Geomech.* 2019a.

Zhang, W.;De Corte, W.;Liu, X.;Taerwe, L. Influence of Rotational Stiffness Modeling on the Joint Behavior of Quasi-Rectangular Shield Tunnel Linings. *Applied Sciences* 2020, *10*, 8396.

Zhang, W.;Wang, J.;Jin, M.;Koizumi, A. Numerical analysis of DRC segment under inner water pressure based on full-scale test verification for shield tunnel. *Tunn. Undergr. Space Technol.* 2016, *56*, 157-167.

Zhang, Z.;Zhu, Y.;Huang, X.;Zhu, Y.;Liu, W. 'Standing'full-scale loading tests on the mechanical behavior of a special-shape shield lining under shallowly-buried conditions. *Tunn. Undergr. Space Technol.* 2019b, *86*, 34-50.

Zhong, X.;Zhu, W.;Huang, Z.;Han, Y. Effect of joint structure on joint stiffness for shield tunnel lining. *Tunn. Undergr. Space Technol.* 2006, *21*, 406-407.

Zhou, L.;Zhu, H.-h.;Yan, Z.-g.;Shen, Y.;Meng, H.;Guan, L.-x.;Wen, Z.-y. Experimental testing on ductile-iron joint panels for high-stiffness segmental joints of deep-buried drainage shield tunnels. *Tunn. Undergr. Space Technol.* 2019, *87*, 145-159.

Zhu, Y. Stuely on Engineering Technology of Quasi-Rectangular Shield Tunnel. China Communications Press Co.,Ltd.: Beijing, China, 2018,

Zhu, Y.;Zhang, C.;Liu, X.;Dong, Z. Experimental study on shear property of circumferential joint in general ring segment under the staggered assembling. *China Journal of Railway Science and engineering, China* 2017, *14*, 315-324.

Zhu, Y.;Zhu, Y.;Huang, D.;Li, P. Development and application of the technical system for quasi-rectangular shield tunnelling. *Mod. Tunn. Technol* 2016, *53*, 1-12.

Zou, J.;Zuo, S. Similarity solution for the synchronous grouting of shield tunnel under the vertical non-axisymmetric displacement boundary condition. *Adv. Appl. Math. Mech.* 2017, *9*, 205-232.

List of Figures

List of Tables

Curriculum Vitae

Personal information

Name	Weixi Zhang
Date of birth	September 29th, 1991
Place of birth	Henan, China
Email	Weixi.Zhang@Ugent.be

Education

2017-2021	Ph.D. candidate: Civil Engineering Magnel-Vandepitte Laboratory Department of Structural Engineering and Building Materials Faculty of Engineering and Architecture Ghent University, Ghent, Belgium
2014-2017	Master: Architectural and Civil Engineering College of Civil Engineering Tongji University, Shanghai, China
2010-2014	Bachelor: Civil Engineering College of Civil Engineering Zhengzhou University, Zhengzhou, China

Publication

Zhang, W.; De Corte, W.; Liu, X.; Taerwe, L. Influence of Rotational Stiffness Modeling on the Joint Behavior of Quasi-Rectangular Shield Tunnel Linings. Applied Sciences. 2020, 10, 8396.

Zhang, W.; De Corte, W.; Liu, X.; Taerwe, L. Optimization Study on Longitudinal Joints in Quasi-Rectangular Shield Tunnels. Applied Sciences. 2021, 11, 573.

Zhang, W.; Liu, X.; Liu, Z.; Zhu, Y.; Huang, Y.; Taerwe, L.; De Corte, W. Investigation of the pressure distributions around quasi-rectangular shield tunnels in soft soils with a shallow overburden: a field study. Tunnelling and Underground Space Technology. (under review)

Zhang, W.; Liu, X.; De Corte, W.; Taerwe, L. Investigation of the rotational stiffness of longitudinal joints in quasi-rectangular segmental tunnel linings. Proceedings of the fib Symposium 2019: Concrete - Innovations in Materials, Design and Structures, 2019, pp. 1180-1185.

Zhang, W.; De Corte, W.; Liu, X.; Taerwe, L. Optimization study on the rotation-resistance performance of longitudinal joints in quasi-rectangular segmental tunnel linings. Proceedings of the fib Symposium 2021: Concrete Structures: New Trends for Eco-Efficiency and Performance, 2021, pp. 2235-2244.

Quasi-Rectangular Shield Tunnels in Ningbo, China.